Study of a high Reynolds number flow around a two dimensional airfoil at stall; an approach coupling a RANS framework and bifurcation theory

Denis Busquet

INSTITUT POLYTECHNIQUE DE PARIS

NNT : 2020IPPAX027

Thèse de doctorat

ONERA
THE FRENCH AEROSPACE LAB

ÉCOLE POLYTECHNIQUE
IP PARIS

Study of a high Reynolds number flow around a two dimensional airfoil at stall; an approach coupling a RANS framework and bifurcation theory

Thèse de doctorat de l'Institut Polytechnique Paris
préparée à l'École Polytechnique

École Doctorale de l'Institut Polytechnique de Paris (EDIPP)
École doctorale n°626
Spécialité de doctorat: Mécanique des fluides et des solides, acoustique

Thèse présentée et soutenue à Meudon, le 24 Juin 2020, par

Denis BUSQUET

Members of the jury :

Mr. Luc Pastur, Professor ENSTA Paris, France	President
Mrs. Laurette Tuckerman, Research director ESPCI Paris, France	Reviewer
Mr. Esteban Ferrer, Professor Universidad Politécnica de Madrid, Spain	Reviewer
Mr. Anthony Gardner, Expert engineer German Aerospace Lab (DLR), Germany	Examiner
Mr. Olivier Marquet, Research master ONERA, France	Examiner
Mr. Francois Richez, Research master ONERA, France	Examiner
Mr. Denis Sipp, Research director ONERA, France	Thesis supervisor
Mr. Matthew Juniper, Professor University of Cambridge, United Kingdom	Thesis co-supervisor
Mr. Franck Hervy, Expert engineer DGA, France	Guest
Mr. Christopher Hutchin, Expert engineer Dstl, United kingdom	Guest

UNIVERSITY OF CAMBRIDGE

[dstl]

DGA

Acknowledgements / Remerciements

Un an et neuf mois de plus que les trois années initialement prévues auront été nécessaires pour finaliser les résultats présentés dans ce manuscrit. Cependant, plus qu'au temps consacré, cette thèse doit son aboutissement aux conseils et au soutien des nombreuses personnes rencontrées au cours de cette aventure ou connues de plus longue date.

Je tiens à remercier la DGA et la Dstl qui ont financé ce projet et sans qui cette aventure n'aurait pu débuter. Je remercie les membres du jury d'avoir accepté d'évaluer mon travail. Je les remercie aussi pour les discussions de qualité que nous avons eues le jour de la soutenance. Toute ma gratitude va à Luc Pastur pour avoir accepté de présider ce jury de thèse et d'avoir géré à merveille l'organisation de cette soutenance dans des conditions toutes particulières. Je remercie Laurette Tuckerman et Esteban Ferrer d'avoir accepté de relire ce manuscrit, de leurs retours positifs et, surtout, de toutes leurs suggestions qui ouvrent de nombreuses perspectives à ce travail. Enfin, merci à Tony Gardner pour ses remarques éclairées sur la possibilité de valider expérimentalement les résultats théorico-numériques présentés dans ce mémoire.

J'ai la chance d'avoir eu pas moins de quatre encadrants pour superviser ce travail. Chacun par ses qualités scientifiques et personnelles m'a permis d'avancer dans ce projet et de maintenir le cap. Denis, merci d'avoir dirigé ces travaux de la meilleure des façons qui soit. Tes explications, griffonnées dans le coin de feuilles déjà bien remplies, ont débloqué plusieurs situations et à plusieurs reprises, tu as su trouver les mots pour me remobiliser quand je stagnais. Matthew, *first of all*, je ne te remercierai jamais assez de m'avoir accueilli un an à l'Université de Cambridge. Cela a été pour moi une expérience humaine et scientifique extraordinaire. Merci également d'avoir tant de fois lu, écouté et corrigé mon anglais approximatif (sans oublier de te moquer gentiment de mon accent français !). Mes progrès en la matière te doivent beaucoup. Et, *last but not least*, merci de m'avoir toujours encouragé à simplifier au maximum les problèmes avant de les étudier : le modèle de décrochage a vu le jour grâce à ce conseil précieux. Enfin, François et Olivier, merci d'avoir suivi l'avancée de mes travaux quasiment au quotidien même quand plusieurs centaines de kilomètres séparaient nos bureaux. Le duo très complémentaire que vous formez m'aura beaucoup appris. Olivier, tu n'as jamais transigé sur la qualité de mon travail, tant sur le fond que sur la forme et ton exigence m'aura poussé à donner le meilleur de moi-même. François, tu as su être toujours là pour me remotiver et m'encourager à voir le côté positif des choses (en particulier après certaines réunions au cours desquelles le niveau d'exigence d'Olivier atteignait des sommets que je pensais inaccessibles !). Merci également de m'avoir très souvent aiguillé lorsqu'il a fallu que je plonge dans les limbes des lignes de codes qui composent elsA.

Réaliser le travail de cette thèse dans deux laboratoires différents a été l'occasion de rencontrer un grand nombre de doctorants, stagiaires et permanents qui ont tous enrichi cette aventure. Merci beaucoup Samir de la très grande patience dont tu as fait preuve pour répondre à mes nombreuses sollicitations concernant l'outil de stabilité que tu as développé. Merci également à Edoardo et Nicolas, eux aussi utilisateurs

de cet outil, avec qui j'ai pu partager les difficultés techniques liées à ce script mais aussi appréhender tout son potentiel. Merci à Nick, Jos, Jack, Hans, José et Peter de l'accueil que vous m'avez réservé à Cambridge et de m'avoir fait découvrir cette magnifique ville (et ses pubs !). Merci à Johan et Lucas d'avoir maintenu une constante bonne humeur dans le bureau que nous avons partagé à l'ONERA ainsi qu'à Arnold pour les discussions sur le sport qui ont animé nos repas. Il est difficile de citer tout le monde mais je tiens à remercier toutes les personnes que j'ai côtoyées au cours de mes années à l'ONERA ou à Cambridge et que je n'ai pas mentionnées ici.

En entrant à l'ENS de Cachan, je n'envisageais pas de poursuivre mes études après l'obtention de mon diplôme. Cependant, la qualité de l'enseignement reçu dans cette école et surtout les rencontres que j'y ai faites m'ont fait changer d'avis. Merci au groupe de Normaliens qui s'est lancé dans une thèse en même temps que moi et avec qui j'ai pu partager tous mes enthousiasmes et mes déboires de doctorant : Thomas, Valou, Bapt, Andrei, Arnaud C. et une mention particulière à Quentin M. qui m'aura initié à l'optimisation multi-objectif et soufflé l'idée de l'algorithme NSGA-II. Merci aussi, Jules, Arnaud T. et Arthur, d'avoir suivi nos aventures de doctorants même si vous avez quitté le monde de la recherche.
Je reste persuadé que pour mener à bien un tel projet il est nécessaire d'avoir une échappatoire en dehors du laboratoire. Je l'ai trouvée au Paris Basket 15, club dans lequel j'ai commencé à jouer en même temps que je débutais ma thèse. J'y ai fait de nombreuses rencontres et vécu de très bons moments sur et en dehors du terrain. Merci Thibaut de m'avoir accompagné dans cette nouvelle étape basketballistique. Merci Baki de m'avoir accepté comme colocataire à mon retour d'Angleterre. Et surtout, merci Dub pour tous tes conseils sur Illustrator qui m'ont permis de réaliser les schémas présentés dans ce manuscrit.
"Tu soutiens quand ?". Les dernières années de cette thèse ont été marquées par cette question posée un nombre incalculable de fois. Bien qu'assez irritante sur l'instant, elle m'a surtout permis de ne jamais oublier l'objectif final. Donc, à tous mes amis qui m'ont posé cette question : je vous ai maudit hier et je vous remercie du fond du cœur aujourd'hui. Au-delà de cet aspect anecdotique, merci de m'avoir soutenu pendant toutes ces années. Merci Caro, Raph et Hugo d'avoir amené une part de l'âme du Sud-Ouest à Paris. Merci Antoine, Axel, Cyril et Quentin pour tous les WE de ressourcement à Bordeaux et d'être là pour moi depuis (presque) toujours.

Finir cette thèse en même temps que je découvrais mon nouvel emploi aurait été très difficile sans le soutien de ma famille. Je ne pourrai jamais assez remercier mes parents pour leur confiance sans faille et leur aide logistique qui m'ont permis de me consacrer à 100% à la finalisation de ce projet. Un grand merci également à Valentine, ma petite sœur, toujours là pour soutenir son grand frère. Si tu décides toi aussi de faire une thèse, j'espère que je saurai te rendre la pareille.

Enfin, Amanda, merci d'avoir été là pour moi pendant la partie la plus difficile de ma thèse. Ta bonne humeur quotidienne, ton enthousiasme et ta capacité à toujours croire en moi et en cette thèse m'ont permis de surmonter mes doutes mais aussi de vivre des moments exceptionnels. *Tack för att du alltid är där för mig.*

Abstract / Résumé

Le phénomène de décrochage est souvent décrit comme une chute soudaine de portance lorsque l'angle d'incidence augmente. Ce phénomène est préjudiciable aux avions et aux hélicoptères et limite leur enveloppe de vol. Plusieurs études numériques et expérimentales, particulièrement centrées sur le décrochage statique (i.e. pour des ailes fixes), ont révélé des phénomènes apparaissant proche de l'angle de décrochage : des oscillations basses fréquences et une hystérésis des coefficients aérodynamiques. Le premier phénomène se traduit par une oscillation de la portance entre une valeur maximale et une valeur minimale obtenues quand l'écoulement est respectivement attaché ou détaché. Le nombre de Strouhal associé ($\mathrm{St} \sim 0.02$) est habituellement un ordre de grandeur plus faible que le nombre de Strouhal ($\mathrm{St} \sim 0.2$) du lâcher tourbillonnaire qui apparaît pour de plus grandes incidences. Le second phénomène est caractérisé par l'existence de solutions moyennées en temps autour de l'angle de décrochage qui diffèrent selon que l'angle d'attaque est augmenté ou diminué.

L'objectif de cette thèse est d'avoir une meilleure compréhension de l'origine du décrochage et de ces deux phénomènes grâce à des simulations numériques d'écoulements turbulents modélisés par une approche RANS (Reynolds-Averaged Navier-Stokes). Une combinaison de diverses approches numériques et théoriques (simulations instationnaires, continuation de solutions stationnaires, stabilité linéaire et analyse de bifurcation) est développée et appliquée dans le cas du décrochage d'un profil 2D de pale d'hélicoptère, le OA209, à bas nombre de Mach ($\mathrm{M} \sim 0.2$) et haut nombre de Reynolds ($\mathrm{Re} = 1.8 \times 10^6$).

Des solutions stationnaires sont calculées pour différents angles d'attaque en considérant le modèle de turbulence de Spalart-Allmaras et en utilisant des méthodes de continuation (continuation naüve et méthode du pseudo-arclength). Les résultats mettent en évidence une branche supérieure (à haute portance), une branche inférieure (à basse portance) et, entre les deux, une branche intermédiaire. Pour un même angle d'attaque, des solutions coexistent proche de l'angle de décrochage sur chacune des branches, ce qui est caractéristique d'un phénomène d'hystérésis. Des analyses de stabilité linéaire réalisées autour de ces états d'équilibres révèlent l'existence d'un mode instable basse fréquence associé au décrochage. L'évolution des valeurs propres associées à ce mode le long des branches stationnaires nous permet d'établir une première version du diagramme de bifurcation. Afin de le compléter, des calculs RANS instationnaires sont réalisés et des solutions stables sous forme de cycles limites basse fréquence sont identifiées sur une plage réduite d'angles d'attaque proches du décrochage. Ces solutions périodiques sont caractérisées par des valeurs de portance maximales et minimales plus grandes et plus petites que celles des solutions stationnaires à haute et basse portance associées, respectivement. Pour clarifier la formation et la disparition de ces cycles limites basse fréquence quand l'angle d'attaque varie, un modèle à une équation reproduisant les caractéristiques linéaires du phénomène est proposé. Ce modèle non-linéaire doit également permettre une meilleure compréhension du scénario de bifurcation proche du décrochage. Il est calibré sur les états stationnaires calculés par des méthodes de continuation couplées à un formalisme RANS. Le comportement linéaire des états stationnaires, obtenus grâce à l'analyse de stabilité linéaire globale,

est également pris en compte dans le processus de calibration. Une étude du comportement non-linéaire de ce modèle révèle un scenario possible qui pourrait conduire à l'apparition et à la disparition du cycle limite basse fréquence. Finalement, les cas d'un OA209 à nombre de Reynolds $\mathrm{Re} = 0.5 \times 10^6$ et d'un NACA0012 à nombre de Reynolds $\mathrm{Re} = 1.0 \times 10^6$ sont considérés pour valider la robustesse du scenario identifié.

Contents

Chapter 1

Context of the study and state of the art

Contents

1.1 The stall phenomenon: origins and interest

1.1.1 A sudden change of flow topology

An airfoil immersed in a fluid in motion is subject to a force generated by the circulation of the air around the profile. The intensity and direction of this force is driven by several parameters such as the shape of the airfoil, its inclination, the flow speed

and the properties of the fluid. For instance, in the case of an airfoil designed for airplanes, whose objective is to generate lift, the shape and inclination are meant to create a depression on the suction side of the airfoil. At first, an increase of the angle of attack of the airfoil generates a linear increase of the lift. This linear increase lasts until a critical angle of attack α_c, which depends on the geometry of the airfoil and the flow conditions, is reached. Before this particular angle, the boundary layer is attached on most of the suction side while, afterwards, a massive separation of the flow occurs. These two states of the flow are illustrated in Figure (1.1) that presents the flow around a NACA 64010 at Reynolds number $\mathrm{Re} = 0.5 \times 10^4$ for (a) $\alpha = 5.00°$, when the flow is mostly attached and (b) $\alpha = 10.00°$, when the flow is mostly separated (the photos are from the ONERA database, taken by Henri Werle). This change of topology, responsible for a large variation of the circulation around the airfoil, is what is called *stall*. Stall can occur more or less suddenly but is always accompanied by a breakdown of the aerodynamic performance: decrease of the lift, decrease of the pitching moment and increase of the drag. The angle of attack for which it occurs is called the stall angle and, for given flow conditions, depends on the shape of the airfoil. Consequently, it is of interest for industrialists to correctly model this phenomenon and to take it into account in the design process to ensure the best aerodynamic performance.

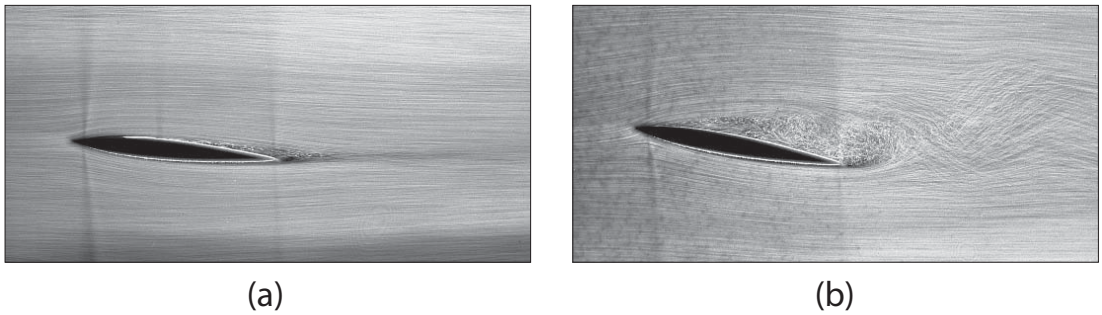

FIGURE 1.1: Visualization of the flow around an airfoil with two different inclinations. (a) Before stall ($\alpha < \alpha_c$), the flow is mostly attached. (b) After stall ($\alpha > \alpha_c$), the flow is massively separated. (from the ONERA database, taken by Henri Werle).

Stall is encountered in many aeronautical applications such as airplane wings, helicopter blades, turbines, etc. Thus, the importance of understanding this phenomenon and the various cases in which it is encountered explains the large number of papers dedicated to this subject. The work presented in this manuscript is related to helicopter blades and emphasis will be put on the impact of stall in this particular case. The introduction of this problematic is also the perfect opportunity to introduce *dynamic stall*. The above description of stall was from a static point of view. However, dynamical phenomena can be coupled to stall, which increases the level of complexity.

1.1.2 Helicopter blades and dynamic stall

Let us consider a helicopter in forward speed, whose blades are anticlockwise rotating, seen from above. Let us introduce the local coordinates of the blade (x, y) where x

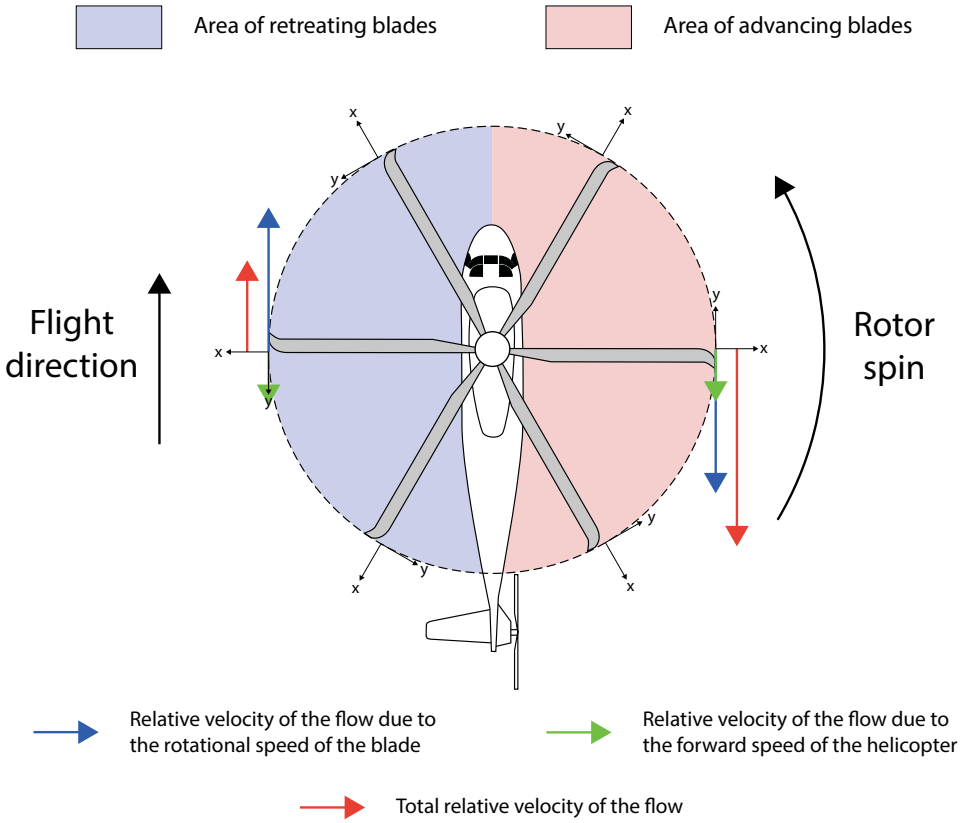

FIGURE 1.2: Top view of a helicopter in forward advance. Influence of the rotational speed of the blade and the forward speed of the helicopter in the total relative velocity of the flow around the blade. Helicopter schema from [74].

is the direction of the blade and y the perpendicular direction (such as illustrated in Figure (1.2)). It appears that during one rotation, a blade faces different aerodynamic conditions. Indeed, the relative velocity of the flow is the sum of the forward speed of the helicopter and the rotational speed of the blade. In the reference frame of the blade, the first one evolves during the rotation and the second one is constant during the rotation (always along the y axis). It results that, on the right side of the helicopter, the blade speed and the y component of the forward speed are in the same direction and the blade is said to be *advancing* (pink area in Figure (1.2)) while on the left side of the helicopter, the blade speed and the y component of the forward speed are in opposite directions and the blade is said to be *retreating* (violet area in Figure (1.2)). Consequently, for the advancing blades, the aerodynamic conditions are based on the sum of the two speeds while for the retreating blades, they are based on the difference between the two speeds. This difference of speed is illustrated in Figure (1.2) for two extrema cases in which the blades are perpendicular to the direction of advance of the helicopter. For these particular configurations, the speed is maximum for the advancing blade and can be close to the speed of sound at the extremity of the blade (Mach number $M \approx 1$) while the velocity is minimum for the retreating

blade and can reach very low values (Mach number M ≈ 0.15). Between these extrema positions, the relative speed of the flow sinusoidally evolves based on the evolution of the y component of the forward speed. Considering a blade with a fixed inclination, this differences of relative flow speed would generate a lift value evolving during the rotation of the blade. Schematically, the lift would be larger for the blade in advancing configuration (pink area in Figure (1.2)) than in retreating configuration (violet area in Figure (1.2)), which would generate a rolling moment of the helicopter. To ensure a lateral equilibrium of the helicopter, the solution is to allow the blade to rotate around the x axis: this is the blade *flapping*. Thus, during one revolution, when the relative speed of the flow increases, the lift force generated lifts up the blade and reduces its angle of attack while, when the relative speed of the flow decreases, the reduction of the lift force makes the blade naturally fall back, increasing its angle of attack. In the end, during one revolution, the blade sinusoidally oscillates around a mean angle of attack (as demonstrated by McCroskey and Fisher [101]), the maximum angle of attack being observed for retreating blades while the minimum one for advancing blades.

The retreating blade configuration is very opportune for stall to occur with its very low speed and high angle of attack. However, due to its periodicity, this phenomenon is called dynamic stall in contrast to the static stall described in section 1.1.1. The differences between the two kinds of stall are illustrated in Figure (1.3) that presents the evolution of the lift coefficient as a function of the angle of attack in the case of static and dynamic stalls for an OA209 airfoil at the Reynolds number $\mathrm{Re} = 1.8 \times 10^6$. The evolution of the lift coefficient in the dynamic case exhibits three main differences compared to the evolution of the lift coefficient in the static case:

- By increasing the angle of attack of the blade, one can observe that the maximum lift coefficient reached is larger in the dynamic case than the one reached in the static case. This is due to inertias effects caused by the movement of the airfoil.

- By decreasing the angle of attack from the maximum angle of attack, an increase of the lift coefficient is observed, which delays stall. This is due to the appearance of vortices at the leading edge. The evacuation of this vortices at the trailing edge causes a sudden massive flow separation, which leads to stall and an abrupt drop of lift.

- For the same inclination of the airfoil, two different flow topologies are identified, depending on whether the position was reached by increasing or decreasing the angle of attack. In the part of the curve of high lift coefficient values, obtained by increasing the angle of attack, the flow is almost fully attached while, in the part of the curve with low lift coefficient values, obtained by decreasing the angle of attack, the flow is massively separated because of the evacuation of the vortices generated at the leading edge.

This cyclic switch between a stalled and unstalled state causes aeroelastic constraints on the structure that are very damaging for the blade. The solution to prevent the appearance of such constraints is to limit the maximum angle of attack in order to avoid stall. The direct implication is the limitation of the forward speed or maximum thrust of the helicopter that are directly responsible for the inclination of the blade during the revolution. This being said, one easily understands the interest of studying

stall in this particular case as it directly impacts the performance of the helicopter and its flight envelope.

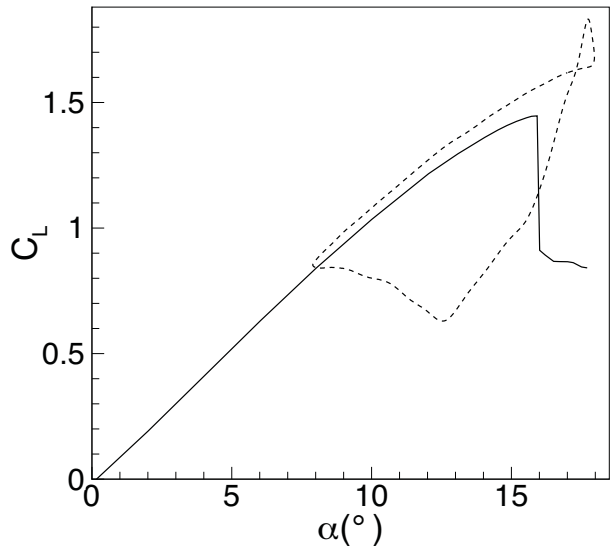

FIGURE 1.3: Evolution of the lift coefficient as a function of the angle attack for an OA209 airfoil at $\mathrm{Re} = 1.8 \times 10^6$ in the case of static stall (full line) and dynamic stall at the frequency of oscillation $f = 3.5Hz$ (dashed line) from Pailhas *et al.* [121].

Dynamic stall appears to be more complex than static stall. However, Piziali [128] demonstrated that although the dynamic stall curve can be more or less close to the static stall curve, the dynamic stall angle is driven by the static stall angle in any case. Consequently, an improvement of the static stall characteristics would lead to an improvement in the dynamic stall properties. That is why, an approach to study the stall problematic in helicopters is to consider a static stall configuration with aerodynamic conditions corresponding to the critical case of a retreating blade. This method, which neglects the dynamic effects, is the one chosen in this manuscript.

1.2 Stall mechanisms and laminar separation bubbles

1.2.1 Quick reminder of the boundary layer separation

Subsection 1.1.1 explained how stall is characterized by a massive flow separation. Before explaining this phenomenon more in detail, it appears necessary to provide a quick reminder on the mechanism leading to a separation of the boundary layer. Prandtl, more than one century ago, was the first to address this problematic of boundary layer separation. Nowadays, the phenomenon is clearly understood and attributed to the action of the *adverse pressure gradient*.

Let us consider the flow passing over the suction side of an airfoil, as represented in Figure (1.4) (adapted from the book of Chassaing [28]), which describes the evolution

of the boundary layer and velocity profiles along the airfoil. The flow is, first, accelerated due to the increase of thickness of the airfoil. In the mean time, to ensure energy conservation, the static pressure decreases and, consequently, the pressure gradient is negative: $\frac{\partial P}{\partial x} < 0$ (x being the direction of the streamwise velocity of the flow). The gradient is said to be *favorable*. In contrast, after the point of maximum thickness is reached, the airfoil starts shrinking causing a decrease of the velocity and an increase of the pressure leading to a positive pressure gradient : $\frac{\partial P}{\partial x} > 0$. The gradient is said to be *adverse*. These notions of favorable and adverse pressure gradient are key to understanding boundary layer separation. By definition, the speed in the boundary layer is non constant in the direction perpendicular to the wall: the no slip-condition imposes a zero speed at the surface of the wall, while the edge of the boundary layer tends to the free stream mean velocity as illustrated in all the velocity profiles depicted in Figure (1.4). The velocity profile B presents the evolution of the speed in the boundary layer without the effects due to pressure gradient. A favorable pressure gradient helps to counter the decelerating effects of the fluid's viscosity, resulting in a faster transition to the free stream mean velocity and a slow evolution of the boundary layer thickness (velocity profile A). On the contrary, an adverse pressure gradient (APG) acts with the fluid's viscosity to slow down the flow, resulting in a slower transition to the free stream mean velocity and a faster evolution of the boundary layer thickness (velocity profile C). In the worst case scenario, a strong enough pressure gradient can even be sufficient to reverse the direction of the flow in the boundary layer (velocity profile E). The inflection point beyond which the flow starts reversing is known as the separation point (velocity profile D). Note that by increasing the angle of attack of the airfoil, the APG becomes stronger leading to an earlier separation of the flow. Also, more generally, any parameter affecting the pressure distribution will have an impact on the separation of the boundary layer.

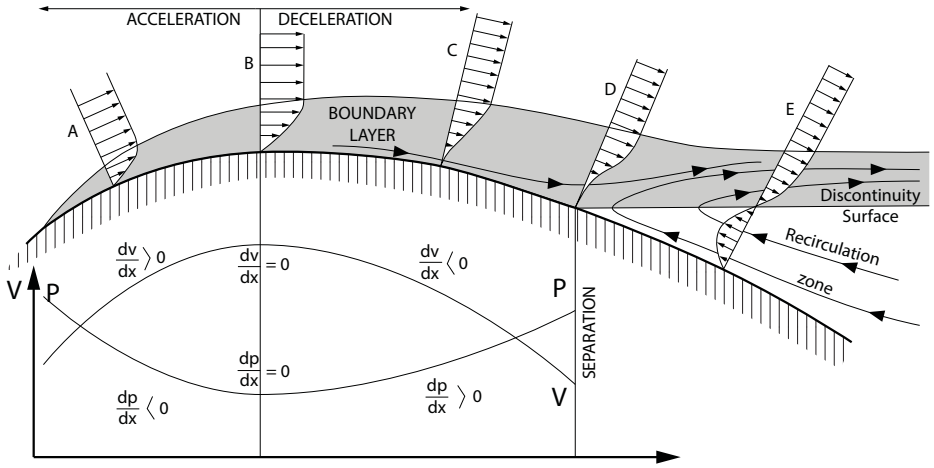

FIGURE 1.4: Schematized visualization of a boundary layer on the suction side of an airfoil and associated evolution of the velocity and pressure. Adapted from the book of Chassaing [28].

The separation of the boundary layer plays a key role in the stall phenomenon. However, this separation is not always as simple as just described. Indeed, for almost

a century, several stall mechanisms have been identified. The next section is dedicated to the description of these mechanisms.

1.2.2 Different mechanisms responsible for stall

The mechanisms responsible for stall have been a topic of research for almost a century with the will of gaining understanding on this touchy subject. Almost simultaneously, Millikan and Klein in 1933 [109] and Jones in 1933 [79] and in 1934 [80] clearly identified the role of the boundary layer (and to some extent, the role of the Reynolds number, the turbulence level in the farfield and the shape of the airfoil) in the mechanisms leading to stall. Millikan and Klein performed several experiments in wind tunnels by varying the turbulence level of the inflow. They observed that, for a given airfoil at a particular Reynolds number, the sooner the transition to a turbulent boundary layer (directly related to a higher turbulence level of the inflow), the higher the maximum lift coefficient. Jones, in his papers, described a series of experiments performed in wind tunnels and in inflight airplanes with several airfoils and wings. The results revealed three different mechanisms leading to stall. Each one exhibits a particular evolution of the flow topology, which is associated with a specific evolution of the lift coefficient as the angle of attack of the airfoils varies. These three types of stall were later named and described more in details by McCullough and Gault in 1951 [102]. Those different types of stall are illustrated in Figure 1.5, which presents a schematized vision of the different mechanisms from the book of Torenbeek [164]. For each type of stall, the evolution of the lift coefficient as a function of the angle of attack is presented on the right and four different states are indicated on it (marked A, B, C and D). The middle pictures presents a schematized vision of the flow at these states and, on the left, the evolution of the pressure coefficient on the suction side of the airfoil for these different states.

• **Trailing edge stall**: this type of stall, depicted in Figure (1.5)(a) occurs mostly for airfoils with a thickness/chord ratio of 15% and above. At low angles of attack (state A), the flow is perfectly attached on the airfoil. The pressure coefficient exhibits a small negative peak at the leading edge and, afterwards, a small increase until the trailing edge, resulting in a small positive adverse pressure gradient. As the angle of attack increases, the leading edge pressure coefficient peak increases, as well as the APG, causing the turbulent boundary layer to separate close to the trailing edge (state B). Although the flow separates, the lift coefficient still linearly increases until it reaches the maximum lift value (state C). For this state, the leading edge peak of pressure coefficient and the APG are even larger resulting in a displacement of the separation point towards the leading edge (at approximately 50% of the chord). Afterwards, the separation point keeps moving upstream and the lift coefficient smoothly decreases (state D). The evolution of the pressure coefficient is very characteristic of a fully detached flow : a small peak at the leading edge followed by a flattened form on the remainder of the airfoil. To summarize, this type of stall is characterized by a separation of the flow starting from the trailing edge, and propagating upstream. It results in a smooth evolution of the lift coefficient.

• **Leading edge stall**: this type of stall, depicted in Figure (1.5)(b) occurs mostly for airfoils with a thickness/chord ratio between 9% and 15%. At low angles of attack

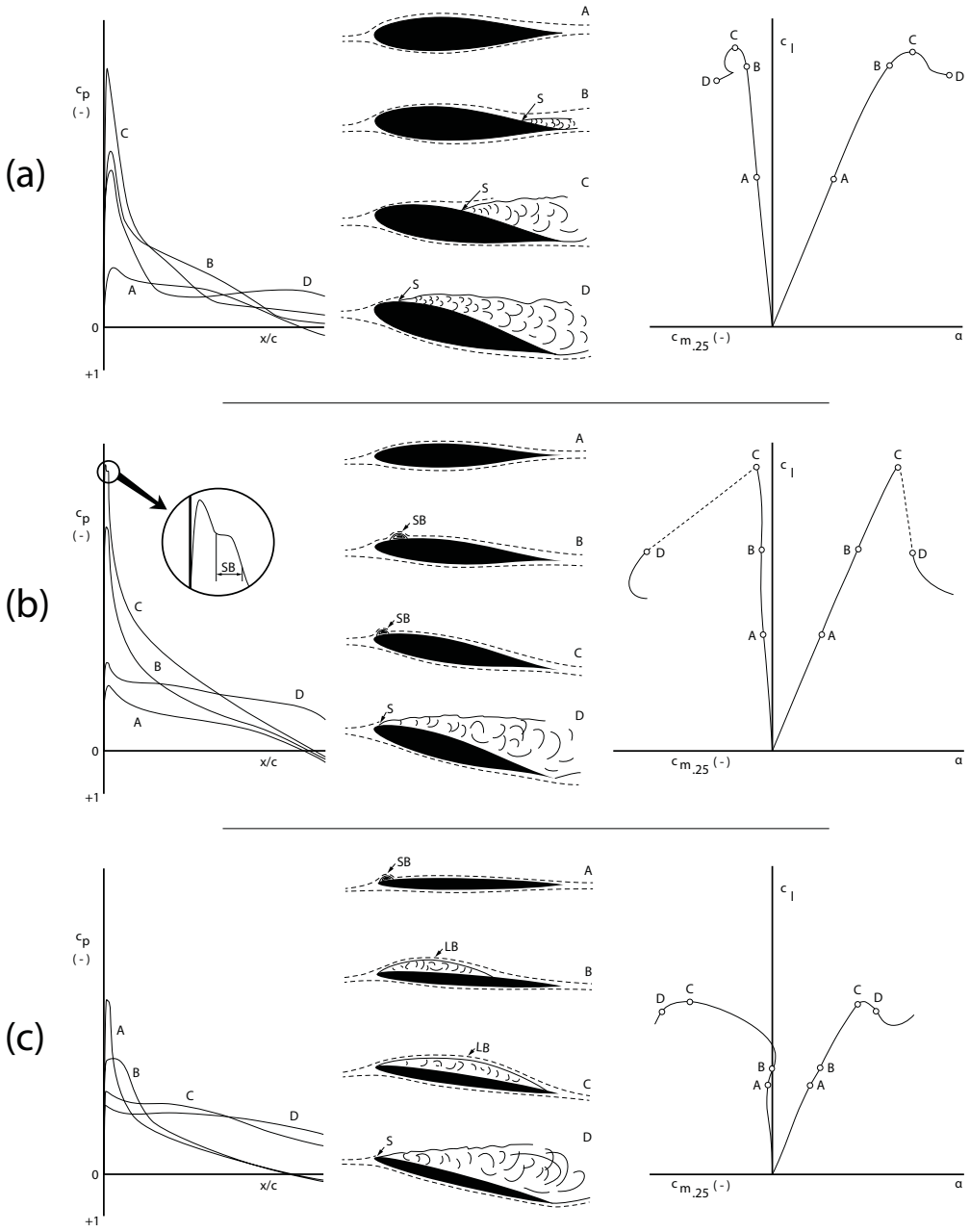

FIGURE 1.5: Representative types of airfoil stall adapted from the book of Torenbeek [164]. (*a*) Trailing edge stall. (*b*) Leading edge stall. (*c*) Thin airfoil stall. For each stall mechanism, the suction side pressure distribution, the evolution of the boundary layer and the evolution of the lift coefficient are represented. Note that the drawings are schemas and not meant to be exactly at scale. On the schemas of the flow around the airfoils: S = separation point, SB = small separation bubble, LB = long separation bubble.

(state A), the flow is perfectly attached on the airfoil. The pressure coefficient exhibits a small leading edge negative peak and a slow increase until the trailing edge. It results in a small positive adverse pressure gradient, which, as a matter of comparison,

is larger than for airfoils exhibiting a trailing edge stall mechanism, particularly on the first half of the airfoil. As the angle of attack increases, the leading edge peak of pressure coefficient becomes even stronger, as well as the adverse pressure gradient. It leads to a separation of the laminar boundary layer close to the leading edge (state B), which triggers transition of the boundary layer. Once the boundary layer becomes turbulent, its kinetic energy becomes strong enough to counter the APG and ensure the reattachment of the boundary layer. The result is a small laminar separation bubble (LSB) located close to the leading edge of the airfoil. This bubble is characterized by a very small plate of pressure coefficient located just after the leading edge peak. Increasing further the angle of attack, the leading edge pressure coefficient peak and the adverse pressure gradient become even higher, which triggers the laminar separation even earlier and causes the displacement of the laminar separation bubble towards the leading edge (state C). From states A to C, the laminar recirculation bubble is small enough ($\approx 1\%$ of the chord) to affect only locally the pressure distribution and ensure that it does not alter the circulation. Moreover, the inclination of the airfoil generates a local overspeed of the flow at the leading edge resulting in an increase of the lift coefficient. However, at some point, the LSB reaches a zone of sharp airfoil curvature and the turbulent boundary layer fails to reattach leading the flow to become massively separated. The small laminar separation bubble is said to burst. It is characterized by a collapsing of the leading edge pressure coefficient peak followed by a flattened distribution of pressure coefficient on the remainder of the suction side. The consequence of such a pressure distribution is an abrupt drop of lift coefficient (state D) at stall. To summarize, leading edge stall is characterized by the appearance of a small laminar separation bubble that bursts causing a sudden drop of lift.

• **Thin airfoil stall**: this type of stall, depicted in Figure (1.5)(c) occurs mostly for airfoils with a thickness/chord ratio below 9%. Due to the extremely small thickness of the airfoil concerned by this mechanism, the adverse pressure gradient is small enough to force the laminar boundary layer to separate and create a small laminar separation bubble located close to the leading edge even at very low angles of attack (state A). As the angle of attack increases, the reattachment point of the laminar separation bubble moves downstream, towards the trailing edge generating a longer separation bubble (state B). The maximum lift coefficient (state C) is reached when the flow reattaches just before the trailing edge. The separation bubble has the same length as the airfoil. Further increasing the angle of attack, the flow no longer reattaches, which causes a massive separation of the flow from the trailing edge (state D). It is characterized by a smooth drop of lift coefficient. One can also observe another increase of the lift coefficient after stall occurred: it is due to vortices appearing in the wake (state not represented).

As a complement to the previous description of stall mechanisms, a few additional points (which can be observed in Figure (1.5)) are worth mentioning. Higher maximum lift values can be obtained for the trailing edge and leading edge types of stall than for the thin airfoil type of stall. The after stall values of lift coefficient are the largest for the trailing edge stall, for which the decrease is very small. The after stall values of the lift coefficient are almost similar for the leading edge stall and for the thin airfoil stall type although the first stall mechanism reached a high maximum value. Consequently,

the leading edge type of stall is the one with the largest drop of lift.

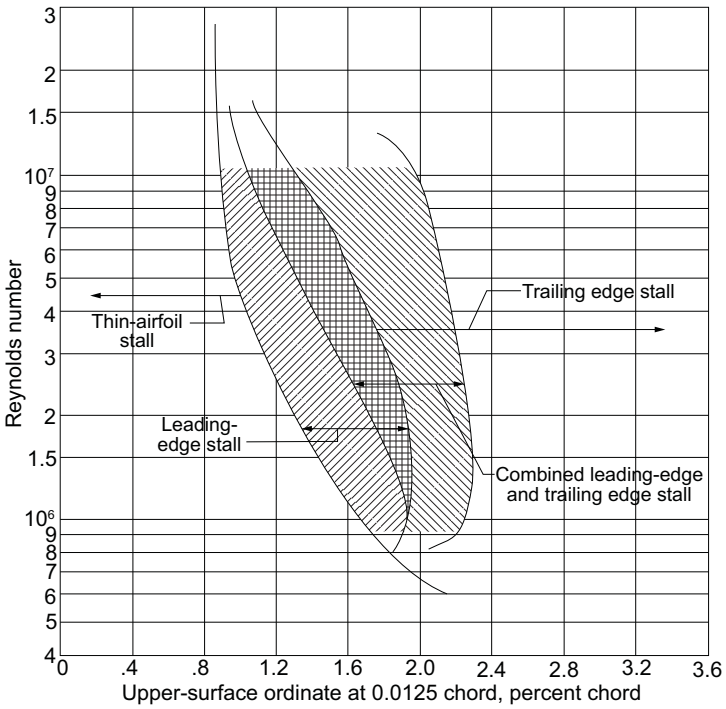

FIGURE 1.6: Identification of regions of existence of the different stall mechanisms in the Reynolds number/relative airfoil thickness plan. Adapted from Gault [58].

Nevertheless, these three types of stall are not meant to be an absolute truth regarding the classification of airfoils: combinations of two types of stall can be encountered as McCullough and Gault mention at the end of their paper [102]. Several experimental studies (such Bonnet and Gleyzes [18] at ONERA) confirmed how the trailing edge and leading edge types of stall can be combined into a fourth stall mechanism. For example, the laminar separation bubble located at the leading edge can increase the size of the turbulent boundary layer, facilitating its separation at the trailing edge. Yet, the trailing edge separation of the turbulent boundary layer modifies the circulation around the airfoil and, consequently, the pressure distribution on the suction side which can affect the characteristics of the laminar separation bubble. A few years after the paper in collaboration with McCullough, Gault dedicated a paper to this fourth type of stall [58]. He tried to find a relation between the Reynolds number, the airfoil nose geometry and the type of stall. He easily identified three zones, each driven by one of the *pure* stall mechanisms described in Figure (1.5). But, between the leading edge stall and the trailing edge stall zones, two more zones appeared: one in which leading edge stall and a coupled leading edge/trailing edge stall can occur and one in which trailing edge stall and a coupled leading edge/trailing edge stall can occur. These zones are pictured in Figure (1.6) in the Reynolds number/relative airfoil thickness plan. According to Gault, the combined type of stall is a *transitional type*, which may or may not occur depending on the flow condition. In the end, this classification is

not always obvious and the boundaries between the different stall types are extremely thin. However, most of the authors dealing with stall refer to it in order to describe the phenomena they observed.

Finally, it was shown how the appearance (or not) and the disappearance of the laminar separation bubble drives the stall mechanism. Next subsection will put emphasis on this complex phenomenon and the different hypotheses regarding the mechanisms that might lead to its formation and disappearance.

1.2.3 Laminar separation bubble

1.2.3.1 General mechanism of the LSB

A laminar separation bubble is formed when the adverse pressure gradient in the laminar boundary layer is strong enough to cause flow separation (see section 1.2.1). The newly formed separated shear layer undergoes a transition from a laminar to a turbulent state. When the kinetic energy generated by the turbulent mixing is strong enough to counter the adverse pressure gradient, the shear layer reattaches into a turbulent boundary layer. This process of separation and reattachment creates a zone, under the shear layer, called a laminar separation bubble. This zone is characterized by "dead-air" that extends from the separation point to the transition point and a reverse flow vortex at the rear of the bubble, between the transition and the reattachment points. This phenomenon is schematized in Figure (1.7), adapted from Horton [68] that exhibits the boundary layer formed at the curved surface of an airfoil leading edge. The laminar boundary layer separates at the line noted SS'', generating a curve $ST'R$ that separates the LSB from the shear layer. Transition occurs at the line $TT'T''$ dividing the shear layer into two zones: the laminar shear layer upstream this line and the turbulent shear layer downstream from this line. Finally, the flow reattaches at the line RR'' resulting in a fully attached turbulent boundary layer. This laminar separation bubble can be identified by a plateau on the pressure distribution as was shown in Figure (1.5), which describes the leading edge and thin airfoil stall mechanisms. More precisely, this plateau is identified between the separation point S and the transition point T and a sudden drop of pressure between the transition point T and the reattachment point R, as shown in Figure (1.7), which exhibits the pressure distribution coefficient with and without LSB from Horton [68]. Owen and Klanfer [119] noted that mostly two types of bubbles could exist: short LSB and long LSB. The second ones are at least one order of magnitude longer than the first ones. Gaster [56] noted that the laminar parts of the shear layers are similar for short or long bubbles and always correspond to the dead air region of the LSB. By contrast, the turbulent part of the shear layer extends as the velocity of the flow decreases. He also observed that a high frequency phenomenon is associated with the short bubble, while high and low frequency phenomena coexist at the same time for long LSB. Hatman and Wan [65] studied the mechanisms of the types of bubbles more in details and confirmed that the transition is similar in both cases. They also provided more insight on the structure of the bubbles: the two types of bubbles reattach after the transition occurred but, in the case of the long bubble, this reattachment is immediately followed by a new separation resulting, in the end, in a longer bubble.

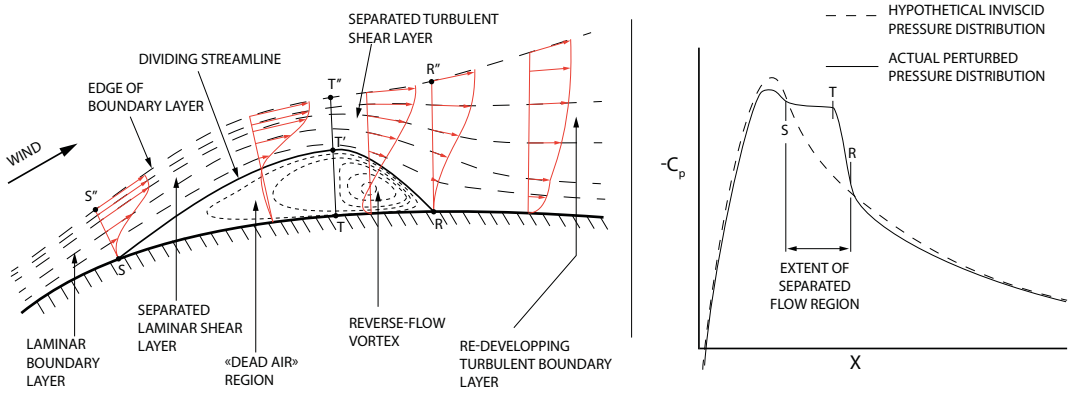

FIGURE 1.7: Left: schematized sectional view of a two dimensional laminar separation bubble (not meant to be at scale). Right: corresponding surface pressure distribution. Pictures adapted from [68].

As mentioned in section 1.2.2 detailing the origin and different types of stall, the appearance and disappearance of the laminar separation bubble plays a key role in stall appearance. That explains why this topic has always been of first interest for aerodynamicist. More particularly, if the appearance of the LSB is quite well understood nowadays, its bursting is still way less understood. The first researches focused on trying to understand the physics behind this phenomenon and establish criterions that would trigger bubble bursting. The works of Tani [158], who proposed one of the first survey on this topic and of Gaster [56] who proposed one of the most cited bursting criterion based on two parameters are worth mentioning. However, these studies failed to clearly identify the mechanisms responsible for the bubble to burst and to define a unique criterion. That is why, since then, the study of laminar separation bubble is still an active topic of research and there is still, at this time, no consensus on the reason leading to bursting. The next subsection is dedicated to the presentation of the main studies related to this topic and the different ideological movements trying to explain bubble breakdowns.

1.2.3.2 Bursting: a phenomenon whose origin is still discussed

A large variety of methods were used to study the bursting of laminar separation bubble: experiments, numerical computations, theoretical criterion, stability analysis, etc. The different approaches for numerical computations are briefly reminded later in this manuscript in section 1.4. The general concept of linear stability consists in observing the evolution of the flow in response to a small initial perturbation: either the perturbation does not have any effect and the flow is said stable or the perturbation strongly modifies the flow topology and it is said unstable. The local stability analysis was first introduced in the field of fluid dynamics. It is limited to parallel or quasi-parallel flows but has a relatively low computational cost. The global stability analysis offers no limitations in terms of flow topology but requires a higher computational cost, which explains its late emergence. An instability is defined as an amplifier if it filters or amplifies the external disturbances of the flow and as an oscillator if it is related to

the flow own dynamics and do not need any external force to be triggered. The stability analysis is discussed more in detail in section 1.6 and the global stability analysis framework is defined in section 5.2.1.

The bursting of laminar separation bubble, that eventually leads to a drop of the aerodynamic performance was originally defined by Gaster [56] as the switch from a short laminar separation bubble to a long separation bubble due to a small variation of the flow conditions. Actually, for finite dimensional shapes (such as airfoil), the reattachment of the flow can actually never occur and it results in a fully separated flow. Many criteria have been proposed and discussed to predict bubbles breakup as well as associated phenomena such as the onset of unsteadiness or the three-dimensionalization of the originally two dimensional LSB. But, none of the existing criteria have found general acceptance so far [43] and the mechanisms responsible for these phenomena have started to become clearer only recently. After a lot of experimental and numerical studies (mostly carried out on flat plates), two types of instabilities of the LSB are identified: amplifier and oscillator.

The amplifier behavior of the LSB was discovered before the oscillator behavior [62] [44]. Indeed, at first, this mechanism was investigated mostly experimentally and, even in very careful experiments, the external disturbances amplitude level, though very small, may be high enough to influence the dynamic of the flow. This amplifier character is also identified in numerical studies by imposing an external forcing in the shape of waves. It is usually considered to account for the onset of two dimensional unsteadiness. However, it failed to explain all the phenomena at stake (such as the three-dimensionalization of the flow). Several papers suggested that those phenomena had an other origin: absolute instabilities [167]. However, they could not prove it with the tools available at the time and it was not before the drastic improvements of global stability analysis [160] [150] that another type of behavior was proposed. In 2000, Theofilis *et al.* [162] were the first ones to properly apply the global stability analysis framework to a separation bubble formed on a flat plate. Two absolute instabilities were discovered: a two dimensional K-H instability and a three dimensional stationary instability. The first one was due to the amplifier behavior of the LSB while the other one was the result of the own dynamic of the flow revealing that the LSB also had an oscillator behavior. Since then, many studies legitimately tried to determine which one occurs first and which one is preponderant in certain flow conditions. Rodriguez *et al.* [139] demonstrated that for flat-plate LSBs, the primary instability is the steady three-dimensionalisation of the bubble rather than the two-dimensional vortex shedding.

In the end, major improvements have been made on the understanding of laminar separation bubble since the first studies. However, although two mechanisms leading to change of flow topology have been identified, several points remain unclear. At this point, no one can systematically predict which mechanism will be dominating the physics of the flow. Consequently, it remains impossible to model and anticipate how a configuration exhibiting a LSB will behave. Also, the link between those behaviors and LSB bursting is not directly established and fail to explain, for instance, the switch from short to long LSB. As a consequence, the global comprehension of laminar separation bubble remains insufficient to completely explain and predict stall. Moreover, the

literature shows the appearance of complex phenomena that seem to be related to the behavior of LSB close to stall such as static hysteresis and low frequency oscillations. Several studies have been conducted on those phenomena but similarly to LSB and stall, their exact origin and behavior remain unclear.

1.3 Particular phenomena related to stall

In this section, we intend to present two phenomena that sometime appear around static stall and that seem to be strongly related to the existence and behavior of laminar separation bubble.

1.3.1 Static hysteresis

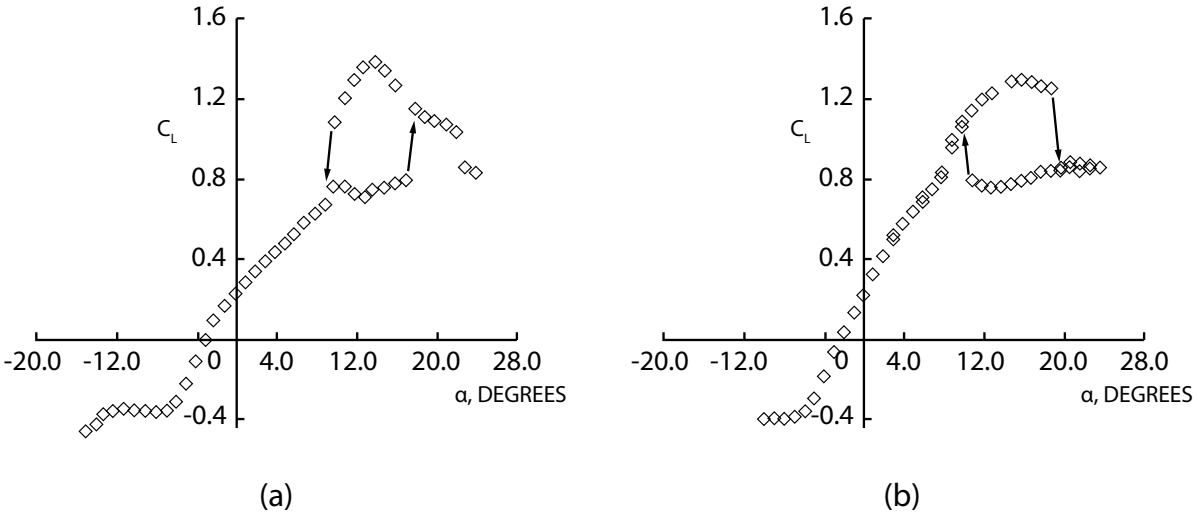

FIGURE 1.8: Evolution of the lift coefficient for: (*a*) a Miley M06-13-128 airfoil (adapted from Pohlen *et al.* [129]) and (*b*) a Lissaman 7769 airfoil (adapted from Mueller *et al.* [114]) at Reynolds number Re = 150000. The black arrows indicate the evolution of the angle of attack.

A very particular phenomenon associated with stall is the capacity of the flow to "remember" its past history and for given aerodynamic conditions have different behavior depending on the previous state of the flow. This phenomenon is called hysteresis. Dynamic hysteresis (which is illustrated by the dashed line in Figure (1.3)) is an example of this particular capacity of the flow as the lift values are different whether the angle of attack is increased of decreased. This case of hysteresis has been studied extensively as it is of first interest in the design of helicopters (see for instance the literature review of McCroskey [100]). However, a more reduced number of researches focused on the hysteresis appearing in the static stall process. The first mention of this phenomenon can be attributed to Schmitz [146] in his study of model of airplane wings. A classic example of static hysteresis is presented in Figure (1.8), which exhibits the evolution of the lift coefficient as a function of the angle of attack from (*a*) Pohlen *et al.* [129] and (*b*) Mueller *et al.* [114] for two different airfoils (respectively Miley

M06-13-128 and Lissaman 7769) at Reynolds number Re = 150000. The black arrows indicate the evolution of the angle of attack. One can observe that depending if the angle of attack is increased or decreased, different states (i.e. flow topology, lift and drag coefficients, ...) are obtained. The main difference between the two curves comes from the fact that Figure (*a*) illustrates an anticlockwise hysteresis (in which the highest lift value is obtained for a decreasing angle of attack) while Figure (*b*) illustrates a clockwise hysteresis (in which the highest lift value is obtained for an increasing angle of attack). Note that in general, most of the studies exhibit a clockwise hysteresis. In this manuscript, except if the contrary is explicitly mentioned, hysteresis will refer to clockwise hysteresis. Mueller [113] suggested that this phenomenon is strongly related to laminar separation bubbles, laminar to turbulent transition and flow separation on airfoils. According to him, this would be an explanation to the inconsistency of appearance of hysteresis (i.e. different results for a same airfoil and Reynolds number reported by different authors) and the difficulty to catch it. Indeed, it was proven that a change in the freestream turbulence intensity, acoustic perturbation or Reynolds number affects the appearance of static hysteresis and the size of the hysteresis loop [94]. These parameters are also well known to be driving the laminar to turbulent transition and LSB formation. The influence of the freestream turbulence level on hysteresis was later quantified by Hoffman [67] on a NACA0015 at Reynolds number Re = 250000. He proved that an increase of the freestream turbulence level tends to reduce the hysteresis size. Different influences of the Reynolds number on the hysteresis were reported: for instance, Marchman *et al.* [93] and Mueller *et al.* [113] observed that the size of hysteresis reduces with an increasing Reynolds number, while Mizoguchi *et al.* [111] and Selig *et al.* [147] observed the opposite for different airfoils. The aspect ratio of the wing seems also to play a key role in the formation of a hysteresis loop as proven by Marchman *et al.* [94] or Mizoguchi *et al.* [111]. Assuming that laminar separation bubbles are strongly related to hysteresis as suggested by many authors, the fact that the aspect ratio has an influence on the hysteresis is consistent with the results on LSB that shows how a three dimensionnalization of the LSB is possible. The first attempt to link the behavior of the aerodynamic coefficients to the flow topology was by Yang *et al.* [169] who, extending the work of Hu *et al.* [71], studied a GA(W)-1 airfoil at Reynolds number Re = 160000. They identified a hysteresis loop and found that for increasing angles of attack, the flow is mostly attached and exhibits a laminar separation bubble located at the leading edge, which causes stall when it bursts. On the other hand, for decreasing angles of attack, the flow is first massively separated and coupled to strong vortices and turbulent structures that periodically shed in the wake. With the decrease of the angle of attack, the flow tries to reattach but the strong reversing flow from the trailing edge prevents it at the stall angle identified for increasing angles of attack. In the end, reattachment occurs for an angle of attack much lower than the first stall angle identified, resulting in a hysteresis loop. All the aforementioned studies observed this phenomenon for relatively low Reynolds numbers (Re $<$ 600000). However, a few recent papers mention hysteresis at relatively high Reynods numbers. For instance, Broeren *et al.* [26], who observed it on a CRM65 semispan wing at Reynolds number Re $= 1.6 \times 10^6$ or Hristov and Ansell [70], who observed a hysteretic behavior of the aerodynamical coefficients for a NACA0012 at Reynolds number Re $= 1.0 \times 10^6$.

In the end, this complex phenomenon appeared to be strongly related to the airfoil

shape, the Reynolds number and the quality of the flow (i.e. freestream turbulence level, acoustic noise,...) rendering its study very complicated. Although the exact causes of this phenomenon are not understood at the moment, three phenomena seem to be preponderant in its appearance: laminar to turbulent transition, laminar separation bubbles and unsteadiness occurring when the flow is separated.

1.3.2 Low frequency oscillations

The phenomenon known as low frequency oscillations (LFO) has been identified since almost a century as Jones [79] reported violent fluctuations of lift and drag occurring around the angle of maximum lift at very low frequencies. However, it was only half a century later that studies dedicated to this phenomenon were conducted. Zaman *et al.* [172], studying the effects of acoustic excitation on flow over an airfoil at low Reynolds number, detected a periodic wake flow structure oscillating at a Strouhal number based on the sine of the chord ($\mathrm{St} = \frac{f \cdot c \cdot \sin(\alpha)}{U_\infty}$) an order of magnitude lower than the usual bluff body vortex shedding. The name of the phenomenon comes from the comparison of Strouhal numbers. In an attempt to study this phenomenon more in depth, Zaman *et al.* [173] dedicated an experimental study to this phenomenon and identified its main features. Three airfoils, exhibiting different stall mechanisms based on McCullough and Gault classification [102], were tested at low Reynolds number ($0.15 \times 10^4 < \mathrm{Re} < 3.0 \times 10^5$). The first noticeable result is that with a *clean* wind tunnel, they failed to reproduce the results observed in [172]. They had to increase the intensity of the free-stream turbulence or to trip transition to observe these low frequency oscillations. Then, they proved that this phenomenon has an hydrodynamic origin, ruling out the possibility that it is due to a standing acoustic wave, a structural resonance or a blower instability. Based on this study the main features of this phenomenon were observed or conjectured. (a) No matter the Reynolds number investigated, the Strouhal number based on the sine of the chord remains almost constant $\mathrm{St} \approx 0.02$ and an order of magnitude lower than the usual bluff body vortex shedding $\mathrm{St} \approx 0.2$ identified in several studies including the famous paper of Rohsko [142]. (b) Large amplitude oscillations (50% of lift coefficient variation). (c) The airfoil stall type (as defined by McCullough and Gault [102]) influences the appearance of this phenomenon contrary to the vortex shedding unsteadiness that is independent of the airfoil type. Broeren *et al.* [24] compared twelve different shapes of airfoils and observed that LFO were inexistant for trailing edge and leading edge stalls but could be identified for thin airfoil stall. However, the largest amplitude oscillations were observed for airfoils exhibiting coupled thin airfoil and trailing edge stall mechanisms. (d) Zaman *et al.* suggested that LFO could not coexist with the hysteresis phenomenon. Broeren *et al.* [24] argued the same in their study of twelve different types of airfoil. (e) They pointed out the leading edge as the origin of the phenomenon and observed that the flow fluctuations are intense on the suction side of the airfoil but rapidly decay downstream. (f) Although observed at relatively low Reynolds numbers, they argued that there is no reason for this phenomenon to disappear at higher Reynolds number. Bragg *et al.* [20] [19] confirmed this hypothesis by observing this phenomenon up to $\mathrm{Re} = 1.4 \times 10^6$. They also identified that the Strouhal number of the unsteadiness slightly increases with the Reynolds number and significantly increases with the angle of attack. (g) This is a two dimensional phenomenon as confirmed by Broeren *et al.*

[25] who focused on the three dimensional phenomena occurring around stall. They linked the type of stall to the appearance of either LFO (thin airfoil stall or coupled thin airfoil/trailing edge stall) or stall cells [170] (trailing edge or leading edge stall). (*h*) They suggested that this phenomenon is linked to a transitional state and cannot appear for a laminar or fully turbulent state, which, according to them, is an explanation of why it is so sensitive to freestream conditions.

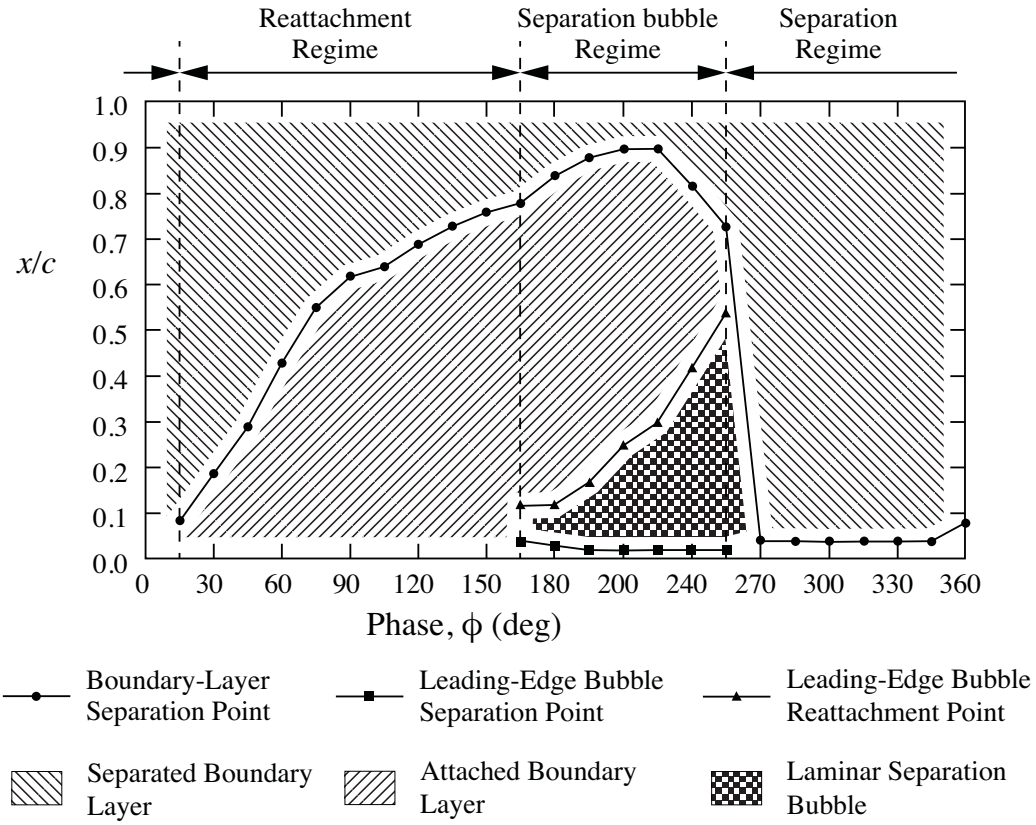

FIGURE 1.9: Evolution of separation and reattachment points on the suction side of the airfoil for one oscillation of low frequency oscillation. Adapted from the paper of Broeren *et al.* [23].

After all these studies on the general features, and thanks to the improvements of measurement techniques, many studies focused on the mechanism ocuring during these large amplitude low frequency oscillations. Broeren *et al.* [22] [23] identified that an oscillation can be decomposed into three regimes that are presented in Figure (1.9) (adapted from the work of Broeren [23]) showing the evolution of separation and reattachment points on the airfoil as a function of the phase over a period. The first regime (reattachment regime) extends from $\Phi = 0°$ to $\Phi = 165°$. It starts from a flow in a fully separated state with a separation point located almost at the leading edge ($\sim 10\%$ of the chord). As the phase evolves, the separation point starts to move towards the trailing edge, reducing the size of the separated boundary layer. The second phase (separation bubble regime) occurs from $\Phi = 165°$ to $\Phi = 255°$. It is characterized by the appearance and expansion of a laminar separation bubble at the leading edge of the airfoil. In the mean time, the separation point kept moving towards the trailing

edge, reaching a maximum at $\Phi = 225°$ and reversed direction, moving upstream. The third regime (separation regime), occurring from $\Phi = 255°$ to $\Phi = 360°$, starts when the separation point of the boundary layer moving towards the leading edge and the reattachment point of the laminar separation bubble moving towards the trailing edge collide, creating a massively separated flow. In the end, it results in an evolution of the flow over a period that switches from a stalled state (fully separated flow) to an unstalled state (mostly attached flow). Note that this scenario is a combination of trailing edge and thin airfoil stall mechanisms combination that is known to be the one with the highest amplitude. For the airfoils exhibiting thin airfoil stall mechanism only, the switch between stalled and unstalled states is only generated by the expansion, bursting and shrinkage of the laminar separation bubble. Although very interesting, these observations do not provide insight on the mechanism that lead the flow to reattach and the laminar separation bubble to form and expand again. A lot of the aforementioned studies suggested that this phenomenon is linked to the shear layer flapping and the low frequency unsteadiness identified for laminar separation bubbles (see subsection 1.2.3.2). Several studies on iced airfoils conducted by Ansell and Bragg [5] [6] [7] confirmed this theory as they identified a low frequency shear layer flapping dominating the upstream portion of the airfoil and a low frequency oscillation of the global circulation. However, no link could be made between these two phenomena. The first attempt to precisely explain how the flow separates and reattaches was provided by Tanaka [157] who, extending the work of Rinoie and Takemura [138], noted that when the flow becomes massively separated, a large vortex is generated at the leading edge. This vortex tends to bend the shear layer towards the airfoil surface, introducing the freestream into the separated boundary layer and tending to make the flow reattach. Finally, very recently, Hristov and Ansell [70] proved that the statement made by Zaman *et al.* [173] and Broeren *et al.* [24] about the coexistence of hysteresis and low frequency oscillations might be wrong: they observed, for a NACA0012, a hysteresis loop and a low frequency phenomenon coexisting. However, the results presented more in details in Hristov PhD [69], one shall note that the amplitude of the oscillations seems to be less large than the ones reported in most of the studies.

In the end, this complex phenomenon, similarly to hysteresis, is strongly related to the airfoil shape and aerodynamic conditions, which both affect the airfoil stall type, as well as the existence and behavior of laminar separation bubbles. Despite the aforementioned studies on the subject, its origin and the mechanisms responsible for the onset of this unsteady phenomenon could not be clearly identified.

1.4 Numerical studies of stall and related phenomena

Stall and associated phenomena were described in the previous sections. It is now legitimate to wonder how numerics can help to gain an understanding of all these complex mechanisms. This is the point of this section.

Numerical simulations of complex flows are of first interest as it might offer the possibility of studying a flow without setting up an experiment. In the particular case of stall, assuming a perfect modeling of the flow, it could help predict the angle of attack

at which it might occur. However, this area is still a work in progress as complicated mechanisms are very time and resources costly to be exactly reproduced numerically. On the other hand, alternative methods, developed to reduce the computational time and cost, are not mature enough and fail to be reliable in all flow configurations. In the end, fluid dynamicists have to choose between computational cost and precision. In this section, we intend to present the different methods to numerically reproduce the behavior of a fluid, the reasonable possibilities that can be used in the case of static stall and, finally, how hysteresis and low frequency oscillations are treated numerically in the literature.

1.4.1 General matters

The Navier–Stokes equations (see equations 2.1 in chapter 2) are partial differential equations that drive the motion of a fluid, including the turbulent ones. Direct Numerical Simulation (DNS) consists in numerically solving these equations for all the scales of the flow. However, it faces a major drawback: in order to catch the whole physics of the flow, all the structures, even the smallest, have to be carefully resolved. Yet, Kolmogorov showed that the size of these smallest structures diminishes as the Reynolds number increases, leading to an increase of the mesh size. Based on space and time integration consideration, it is commonly said that the computational time for DNS is driven by the factor Re^3. In view of the nature of the flow studied in the industry, which are almost all high Reynolds number flows, this method is only marginally used. An alternative method to reduce the computational cost is to filter the smallest structures and to resolve only the largest ones. However, in order to take their effect into account, the smallest scales, usually associated with the turbulent ones, are modeled using a subgrid-scale model. This method is named Large Eddy Simulation (LES): its computational cost is reduces compared to DNS but remains quite high. Another approach is to consider a time averaged solution and model the effects of the small fluctuations of the flow. This is the Reynolds Averaged Navier–Stokes (RANS) approach. The influence of the fluctuations is taken into account using a turbulence model. This method is the most commonly encountered in the industry because of its reduced computational time. The main drawback of modeling a part of the flow is that the models used are usually case dependent: they might be very effective in one precise configuration but irrelevant in the other. Moreover, turbulence models show some limitations as they successfully predict bypass transition but fail to reproduce a natural transition. An alternative to improve the modeling of natural transition is the use of a so called transition model in addition to a turbulence model. However, these models are difficult to calibrate and significantly increase the difficulty of the computation. All these reasons explain why turbulence and transition models are still an active topic of research. Finally, *hybrid* methods also exist: they consist in applying one of the aforementioned method in one zone of the flow and another in another zone of the flow.

A large number of numerical studies related to stall can be found in the literature. There is no consensus on a particular method to be used in this configuration and the choice is always a trade-off between precision and computational time. In the case of stall occurring at low Reynolds number, DNS can be considered. For instance, Rodriguez *et al.* [140] studied the flow over a NACA0012 at $\mathrm{Re} = 5 \times 10^4$. The LES

approach is also well adapted to this type of flow as demonstrated by Almutairi and Alqadi on the same flow [2] or even at slightly higher Reynolds number $\mathrm{Re} = 1.3 \times 10^5$ by Almutairi *et al.* [3]. Finally, higher Reynolds number flows are resolved using a RANS approach as in the work of Mittal and Saxena [110] who studied the flow around a NACA 0012 at $\mathrm{Re} = 1.0 \times 10^6$ or a hybrid approach as in the work of Richez *et al.* [135] who investigated the flow around an OA209 airfoil at $\mathrm{Re} = 1.0 \times 10^6$. The present work is dedicated to the study of stall at high Reynolds number with a RANS approach. As a consequence, in the remainder of the section, emphasis is put on the studies related to stall through this approach and, particularly, on the capacity of turbulence models to correctly identify and predict stall as well as static hysteresis and low frequency oscillations. However, an abundant literature, not detailed in the present manuscript, exists on numerical studies of stall at low Reynolds number.

1.4.2 RANS modeling of stall

One of the most studied engineering application of stall at high Reynolds number in the literature is rotating helicopter blades. This explains why most of the studies of stall through a RANS approach focuses on dynamic stall. Most of them compares several turbulence models to experimental data, trying to identify a turbulence model that would correctly predict stall. Srinivasan *et al.* [154] compared some of the most commonly used and simplest turbulence models at this time (algebraic turbulence models and one-equation transport turbulence models). In the end, they concluded that although most of the turbulence models investigated successfully caught the global dynamics of the flow, they all failed to correctly predict it. Some are better to model separated flows and other to model attached flows, but none catch all the complexity of the different flow topologies existing during the stall process. However, they noted that the one-equation turbulence models provided better results than the algebraic ones. Later, Ekaterinaris *et al.* [48] extended the comparison to several transport turbulence models (Spalart–Allmaras [151], Baldwin-Barth [9], $k-\epsilon$ [81], $k-\omega$ [168] and modified versions of the $k-\omega$ model, BSL and SST by Menter [107]). The conclusion is mostly similar to the one of Srinivasan *et al.*: none of the investigated turbulence models correctly predicted stall due to their limited range of application. However, they argued that the $k-\omega$ SST turbulence model was the one providing the better results (an illustration of the limitation of the turbulence models is shown in Figure (3.6) in chapter 3). Finally, they noticed that, in the case of the flow is not tripped at the leading edge, the laminar to turbulent transition plays a key role in the mechanisms occurring at stall (as for example the formation of a laminar separation bubble). By nature, the turbulence models, which consider a fully turbulent flow, fail to model this region of the flow. Indeed, a turbulent flow is less sensitive to adverse pressure gradient that could lead to separation than a laminar flow. Consequently, the fact that the flow is already turbulent at the leading edge overestimate the capacity of the flow to remain attach delaying or even preventing a separation that is necessary to the appearance of a laminar separation bubble. However, Ekaterinaris *et al.* claimed that even the most basic transition model, which considers a laminar part of the boundary layer, drastically improved the results. The conclusion of the RANS approach on modeling dynamic stall (correctly reproduce it but poorly predict it no matter the turbulence model) was also demonstrated in several papers for static stall [144] [137]. Finally, it is

worth noticing the work of Gleize *et al.* [61] on static stall (further extended by Szydlowski *et al.* [156] and Richter *et al.* [137] on dynamic stall). They demonstrated the effect of the mesh refinement for different turbulence models, exhibiting an extremely slow mesh convergence and a large dispersion of the results. It indicates that numerical studies have to be carefully conducted and that the results have to be conscientiously verified. Indeed, coarse meshes might give results that seem in better agreement with experiments than the ones obtained with refined mesh. However, in such a case, this is a bias that might lead to wrong interpretation of the results.

1.4.3 Numerical studies of stall related phenomena

Although hysteresis was attributed in the literature to laminar to turbulent transition of the boundary layer and to laminar separation bubbles, hysteresis was surprinsingly observed in some numerical studies performed with fully RANS computations. Mittal and Saxena [110] computed the flow around a NACA0012 at Reynolds number $\mathrm{Re} = 1.0 \times 10^6$ with the Baldwin-Lomax turbulence model. The unsteady RANS computations were carried out for several angles of attack and the time-averaged values of the aerodynamic coefficients were considered. They observed a static hysteresis of the aerodynamic coefficients in fair agreement with the experiments of Thibert *et al.* [163]. By comparing the flow visualisation at a same angle of attack, they also observed stronger unsteadiness for low lift flow than for high lift flow. Richez *et al.* [133] computed steady solutions of a flow around an OA209 airfoil at Reynolds number $\mathrm{Re} = 1.8 \times 10^6$ with a $k-\omega$ turbulence model (Kok's version with SST correction from Menter) and observed a hysteresis of steady solutions around the stall angle. One shall note that this hysteresis is slightly different from the ones previously described. Indeed, in experiments or in the computation performed by Mittal, the values of aerodynamic coefficients plotted are time-averaged values deduced from unsteady solutions contrary to Richez *et al.* who presented values obtained from steady solutions. A similar hysteresis of the steady solutions was also observed by Wales *et al.* [166] on a NACA0012 airfoil at Reynolds number $\mathrm{Re} = 1.85 \times 10^6$ and higher with the Edwards–Chandra modification of the Spalart–Allmaras turbulence model.

According to the author's knowledge, there is only one paper mentioning the appearance of low frequency oscillations with URANS computations. Iorio *et al.* [76] observed it on a NACA0012 airfoil at Reynolds number $\mathrm{Re} = 6.0 \times 10^6$ and with the Spalart–Allmaras turbulent model. However, several numerical studies conducted at lower Reynolds number with LES approach provides interesting insight on the mechanisms of LFO at low Reynolds number. For more details, one can refer for instance to the works of Eljack *et al.* [49] and the references therein.

In the end, note that although RANS and URANS computations suffer some limitation in correctly predicting stall, more often overestimating the stall angle, they successfully identify stall but also static hysteresis and low frequency oscillations. Moreover, contrary to DNS or LES, the RANS approach offers the possibility to compute steady solutions. This specific feature makes it the perfect candidate to be coupled to bifurcation theory for which steady solutions are a first requirement.

1.5 Bifurcation theory

Bifurcation theory was introduced in the $XVII^{th}$ century by Newton in his study of the motion of the earth around the sun. Since then, several breakthroughs (one can cite for instance Poincaré in the XIX^{th} century and Lorenz in the 1960's) made this theory dedicated to the study of dynamical system very popular in a lot of very different fields: physics, biology, electronics, chemistry, engineering, etc. The main objective of this theory is to identify the dependency of the system on some parameters: how do they affect the steady states of the system, their linear stability or even the appearance of limit cycles? Every time a qualitative change occurs in the dynamics of the system, it is said that the system faces a *bifurcation* and the parameter values for which it happens are named the bifurcation points. Finding the bifurcation points of a system is of first interest in order to identify the different behaviors of the system and eventually defining a functioning range or finding the parameters triggering the onset of a specific mechanism.

One has surely noticed that in the description of stall phenomenon made so far, the evolution of the aerodynamic coefficients or of the flow topology has always been considered has a function of the angle of attack. In our attempt to study stall phenomenon, it would be extremely useful to identify particular values of α corresponding to sudden changes in the flow around the airfoil: instability, onset of oscillations, hysteresis, etc. To do so, bifurcation theory will be considered with the angle of attack as a parameter. Several types of bifurcations will be encountered in this manuscript, such as saddle-node bifurcations of steady states and limit cycles, Hopf bifurcations and homoclinic bifurcations as well as the notions of attractors and repellers. One can find a detailed description of these notions in the abundant literature on this topic and for instance to the books of Strogatz [155] or Gilmore [60].

Bifurcation theory was applied to fluid dynamics to understand the physics of flow in many configurations. An extensive review of bifurcation theory applied to Navier–Stokes equations and the discoveries resulting from this formalism can be found in the review of Dijkstra *et al.* [41]. As examples, one can mention several papers who addressed the different behaviors of flows by varying the Reynolds number: Barkley *et al.* [11] on a circular cylinder, Nagata [115] on a plane Couette flow, Mamun and Tuckerman [92] on a spherical Couette flow, Fabre *et al.* [51] on a sphere and a flat disk, Meliga *et al.* [105] on a flat disk or Cui *et al.* [34] who, based on the polar curves obtained by Mueller [113] on a Lissaman 7769, identified the bifurcation leading to the formation of hysteresis. Moreover, several studies are directly related to the study of stall considering the angle of attack as the bifurcation parameter. Dimitriadis and Li [42] adressed the question of stall flutter, identifying different flow behavior as the angle of attack varies. Wales and Gaitonde [166] studied static stall on a NACA0012 at high Reynolds number and partially established the bifurcation diagram by computing the steady solutions using continuation methods identifying a hysteresis of steady solutions and two saddle-node bifurcations.

As stated by Tuckerman and Barkley [165], any CFD code is sufficient to perform a bifurcation analysis of a flow. Indeed, a stable state (steady or limit cycle) can be

reached after a long enough time and by gradually shifting a control parameter, one can observe when the flow changes and identify the bifurcation points. However, it suffers several limitations: the impossibility to reach unstable steady states, the difficulty to identify specific phenomena such as unstable limit cycles, and, particularly, it might be extremely time costly to wait for stabilization or destabilization of certain states. To overcome these difficulties, several specific tools, dedicated to bifurcation theory were developed. For instance, continuation methods, linear stability analysis, Floquet stability analysis or nonlinear stability analysis, respectively used for the computation of steady states, the study of their stability, the study of limit cycles stability and the determination of bifurcation criticality. Note that the implementation of all these methods in the RANS framework is not an easy task.

1.6 Global linear stability analysis

Linear stability analysis is a very powerful tool in the bifurcation theory framework. It was proven to be very useful in the study of laminar separation bubble (as detailed in subsection 1.2.3.2) and, coupled with a RANS approach, it is expected to provide very interesting insights on stall, static hysteresis and LFO. In this section we intend to detail the global stability analysis principles (briefly detailed in subsection 1.2.3.2) as well as its application to turbulent flows modeled with a RANS approach.

The concept of instabilities in fluid mechanics has been existing for over a hundred years and the most famous examples are probably the Kelvin-Helmotz instability and the Benard-von Karman vortex street. The concept of linear stability analysis, developed to study those instabilities, is very commonly used in the field of dynamical systems. It consists in determining how a small perturbation of the initial condition affects a system: does it or does it not change its actual state? If, after a long time, the perturbation has not affected the system, it is said stable, otherwise the system is said unstable. Considering the flow as a system, such an analysis applied to the field of fluid dynamics shall help to have a better understanding of the onset of unsteady phenomena. At first, the *local stability analysis* was considered due to its reduced computational time (see for example the works of Batchelor and Gill [12] or Crighton and Gaster [31]). This approach considers that the flow does not vary in the streamwise direction and a crosswise profile completely describe the flow topology. This way, only the cross-stream direction of the flow is to be considered and discretized. However, it also limits its domain of application to parallel and quasiparallel flows, which wavelength of the unsteady phenomena is short compared to the typical streamwise scale of the flow. Studying the propagation of the local instabilities, Huerre and Monkewitz [72] classified them into two categories: absolutely unstable or convectively unstable. For absolute unstable flows, the perturbation remains located at its origin and only expands upstream and downstream without moving while for convective unstable flows, the perturbation is convected far away from the source while expanding. With the increase of computational power, a new approach was recently considered: the *global stability analysis* (also referred as Bi-Global or Tri-Global stability in some paper for respectively two and three dimensional flows). This approach has been widely used in the field of fluid dynamics (see for instance the literature reviews of Theofilis [160] [161], Sipp *et al.* [150] or Chomaz [29]) as it can be used for any flow configuration

contrary to the local stability analysis. However, the computational cost is obviously higher. A mathematical description of this theory is given in section 5.2.1. Huerre and Monkewitz [72] also adressed the question of comparing local and global approaches. They argued that an absolute local instability is a necessary condition for the existence of a global instability. Another very commonly used classification associated with linear stability analysis is the distinction between oscillators and amplifiers. A flow is said to act as an oscillator if it imposes its own dynamic at a very particular frequency, independent of the external noise. This type of instability is associated with an unstable global mode (defined by Drazin [45] as a state variable in which the dynamic of the system is driven by coherent oscillations). A flow is said to act as an amplifier if the external disturbances coming from upstream are filtered or amplified when convected downstream. This type of instability is associated with a global stable mode which requires other techniques to be identified (see for instance the work of Cossu [30]).

Although being in constant development with the increase of the computational capacities, global stability analysis still suffers computational limitations to study complex three dimensional configurations. The mathematical framework presented in section 5.2.1 is perfectly usable for three dimensional flows and several studies, which have successfully performed global stability analysis of three-dimensional configurations, exist in the literature (see for instance Tezuka and Suzuki [159] Bagheri *et al.* [8] or more recently Paladini [122]). However, results found in the literature demonstrated that all the phenomena that we intend to study can be identified with a two dimensional study. Consequently, in order to reduce the computational cost, the choice is made to study the global stability of a two dimensional flow.

One of the main question related to the linear stability analysis is: around which flow the equations should be linearized? Stability of dynamical systems considers the steady state of the system as base flow around which the equations are linearized. This approach is mathematically more accurate. However, in the case of the Navier–Stokes equations, experiments and Direct Numerical Simulation do not permit to consider such a base flow. In these cases, mean flows (i.e. time averaged solutions) are usually considered, which raises a lot of questions in the field of stability analysis applied to fluid mechanics. Several studies showed surprisingly good results with global stability analysis of mean flows (for instance Barkley [10] or Piot *et al.* [127]) and extended studies were dedicated to the identification of conditions for the use of mean flows (for instance Sipp and Lebedev [149] or Beneddine *et al.* [15]). The case of linear stability analysis applied to RANS flows is a bit different but raises the same kind of questions. Indeed, it is possible to compute steady RANS solutions around which perform linear stability analysis. However, because of the inherent properties of the RANS approximation, a steady solution of the RANS equations is not necessarily a steady solution of the Navier–Stokes equations as it is already a time averaged solution. If the theoretical framework and rigorous validation for the use of linear stability analysis coupled with RANS approach has not been established, several studies exhibited very good results for various configurations such as the buffet (which has been one of the most studied topic with for instance the works of Crouch *et al.* [32] [33], Sartor *et al.* [145], Iorio *et al.* [75], Paladini *et al.* [123],...) or the deep cavity flow by Mettot *et al.* [108]. Finally, the work of Iorio *et al.* [76] is worth mentioning: their main objective was the global

stability analysis of a turbulent flow around a complex multielements airfoil but, in a validation step of the method, they presented very interesting insights on the stability analysis of a turbulent flow around a NACA0012 at low Mach number M = 0.15 and Reynolds number Re = 6.0×10^6 with the Spalart–Allmaras turbulence model. The analysis revealed an unstable global mode (illustrated in Figure (1.10)) which associated frequency is very low. The existence of such an unsteadiness was confirmed with unsteady RANS computations with an excellent agreement between the frequencies.

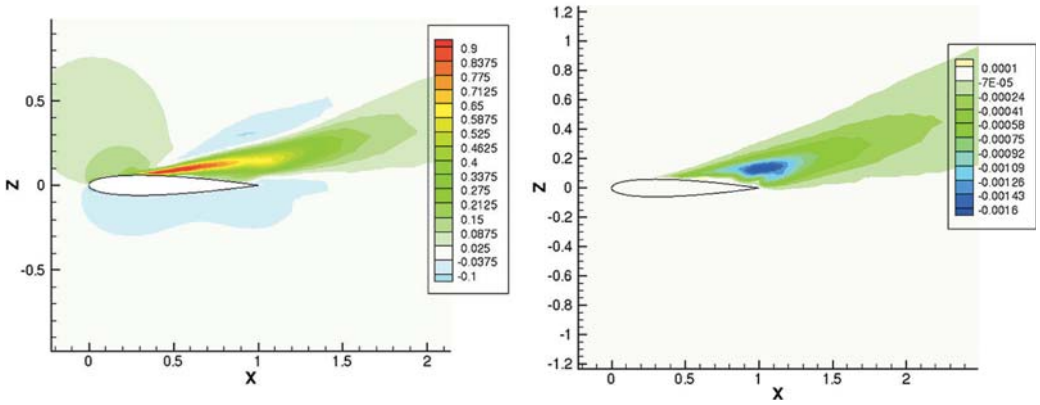

FIGURE 1.10: Structure of the unstable global mode found for the flow around a NACA0012 at low Mach number M = 0.15 and Reynolds number Re = 6.0×10^6 with the Spalart–Allmaras turbulence model. (*a*) Streamwise velocity component (*b*) Turbulent component. From the paper of Iorio *et al.* [76].

If the global stability analysis allows the user to identify the type of instability governing the flow, the most sensitive regions of the flow are a very useful information to obtain and several methods were developed for this purpose. The adjoint mode is the easiest information to obtain from a linear global stability analysis. For each global mode (also called direct mode), a corresponding eigenvalue, which real part corresponds to the growth rate and imaginary part to the angular frequency of the instability, is found. It is also possible to determine a so-called associated adjoint mode (the mathematical formalism of the adjoint mode is introduced in section 5.2.5.1). The physical meaning of the adjoint mode is the designation of the zones where an external forcing will be the most effective to amplify or damp the instability of the associated direct mode [148]: the most receptive regions of the flow. Consequently, it is of first interest when intending to control the instability mechanism. Emphasis were also put on finding the regions of the flow that affect the most the eigenvalue (i.e. the temporal properties of the instability). With that goal in mind, Huerre and Monkewitz [72] proposed the concept of wavemaker, which was extended by Giannetti and Luchini [59] who proposed a formalism that nowadays meet consensus in the community. In the same spirit, Paladini *et al.* [123], extending the work of Marquet and Lesshaft [95], proposed an alternative tool based on the decomposition of the linear operator instead (by opposition to the approach of Giannetti and Luchini [59] who considered a perturbation of the linear operator). The method, called eigenvalue contribution, provides a density function which real (respectively imaginary) part shows the influence of the

flow on the growth rate (respectively angular frequency). The contribution of the flow can be either positive or negative contrary to the wavemaker function which is defined as a norm. Furthermore, it is proven in the PhD of Paladini [122] that from the eigenvalue contribution, it is possible to determine the wavemaker function highlighting the link between the two approaches. These two tools are mathematically introduced in subsection 5.2.5.1.

1.7 The OA209 airfoil

The previous sections introduced the problematic of stall, its link with helicopter performance and the limitations of our comprehension of this phenomenon as well as static hysteresis and LFO. The different methods that can be used to model this phenomenon were also introduced, as well as bifurcation theory and linear stability analysis widely used in the field of fluid dynamics nowadays. In our attempt to apply those tools to the specific case of stall, a particular helicopter blade airfoil is used: the OA209. This section intends to present the results that can be found in the literature on this airfoil in the aerodynamic conditions considered (i.e. a retreating blade configuration at Mach number $M = 0.16$ and Reynolds number $Re = 1.8 \times 10^6$).

The OA209 is a helicopter blade airfoil that was designed in the 70's at ONERA. This airfoil is still in service on several helicopters. As explained in section 1.1.2, dynamic stall plays a key role in helicopters performance. This explained why so many studies were carried out on this topic at ONERA. For many of them, the OA209 airfoil was used, which gives us a lot of information about the flow topology, the aerodynamic performance and the phenomena occurring. Although the aim was to study dynamic stall, many studies address the question of static stall as it is very helpful to understand the complex dynamical phenomena. At first, an experimental database was formed by Pailhas [121] *et al.* and widely extended by Le Pape *et al.* a few years later [125]. Several Reynolds numbers were investigated ($Re = 0.5 \times 10^6$, $Re = 1.0 \times 10^6$ and $Re = 1.8 \times 10^6$). It appeared that a diminution of the Reynolds number leads to a diminution of the stall angle and the maximum lift coefficient. Also, the two lowest values revealed the appearance of a laminar separation bubble at the leading edge. They noted that the higher the Reynolds number, the lower the size of the recirculation bubble (which is in agreement with the observations of O'Meara and Mueller [118]). According to them, this diminution of the size with the increase of the Reynolds number is the reason why this LSB is not identified at $Re = 1.8 \times 10^6$ as they suggested that the pressure probes refinement might be too large to identify a tiny LSB ($< 1\%$ of the chord) in that case. They also noted that a very classic laminar to turbulent transition is associated with this LSB. Richez *et al.* [134] performed a hybrid RANS/LES computation at $Re = 1.8 \times 10^6$ on a prior stall configuration and confirmed the appearance of a laminar separation bubble at the leading edge (although they suggested that its size is overestimated in their computation). Several numerical studies on a post-stall configuration at $Re = 1.0 \times 10^6$ [136] [135] and $Re = 1.8 \times 10^6$ [136] revealed the appearance of vortex shedding occurring at $St \approx 0.2$ when the flow is fully detached. In terms of modeling, two points are worth noticing. First, Jain *et al.* [78] demonstrated that the fully turbulent RANS approach constantly overestimates the

stall angle and the Spalart–Allmaras turbulence model appears to be even worse than the $k-\omega$ model (note that the overprediction was already noticed by Richter *et al.* [137] for the Spalart–Allmaras model). Second, Kaufman *et al.* [85] noted on a flow at $\mathrm{Re} = 1.0 \times 10^6$ that, with the Spalart–Allmaras model, only a trailing edge separation appeared, characteristic of a trailing edge stall, contrary to experiments that exhibit a coupled leading edge/trailing edge stall. Finally, Richez *et al.* [133] computed steady RANS solutions with the $k-\omega$ turbulence model and identified a static hysteresis of steady solutions around stall. Figure (1.11) illustrates this hysteresis by showing the evolution of the lift coefficient of steady solutions as a function of the angle of attack close to stall angle: for several values of α, a high lift solution coexists with a low lift solution. Note that this hysteresis is different from the one illustrated in Figure (1.8): this one is a hysteresis of steady solutions while the other one is a hysteresis of time-averaged unsteady solutions.

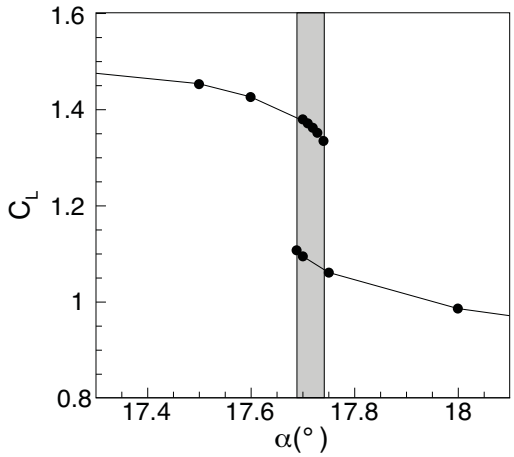

FIGURE 1.11: Evolution of the lift coefficient as a function of the angle of attack. Obtained from steady RANS computations with the $k-\omega$ turbulence model for an OA209 at $\mathrm{M} = 0.16$ and $\mathrm{Re} = 1.8 \times 10^6$. Identification of a static hysteresis of steady solutions close to stall angle. Adapted from Richez *et al.* [133].

1.8 Objectives and outline

The aim of the present study is to provide more insight into stall phenomenon in an attempt to improve helicopters' performance. By opposition to static stall (encountered in the case of airplanes for instance), the blades of a helicopter face dynamic stall, which is caused by inertia effects generated by the variation of theirs angles of attack during one rotation. It is shown in the literature that the dynamic stall characteristics of an airfoil are driven by its static stall properties [128]. In the present work, the choice is made to neglect the dynamic effects of stall and to focus on static stall, which also remains not well understood. The aerodynamic conditions corresponding to the case of

a retreating blade perpendicular to the helicopter fuselage are used for the static computations because they correspond to the most critical configuration regarding stall. It is characterized by a low Mach number and high Reynolds number flow, which raises the question of the numerical approach to be considered in this work. Because of the high Reynolds number, the choice of a RANS approach is made in order to be able to compute several solutions at a reasonable computational cost and in a realistic time. The turbulence model chosen is the Spalart–Allmaras model and no transition model is used, which is well known to provide decent results in the case of static stall [121], although not as good as the $k-\omega$ model coupled with a transition model for instance [48]. Two main reasons motivated this choice: the relative simplicity of the turbulence model (one equation), which facilitates the implementation part and the fact that low frequency oscillations and static hysteresis can be identified with this turbulence model [166] [76], which allows us to gain an understanding of those phenomena even with this *simple* modeling.
Moreover, the present work also intends to take advantage of the capacity of the RANS formalism to compute steady solutions, which are a prerequisite to perform a study through bifurcation theory. Although the first steps of a bifurcation scenario around stall were proposed in several papers, a complete bifurcation diagram was never drawn. One can refer to Wales *et al.* [166] who computed steady solutions around stall using continuation methods and study their linear stability but did not focus on the bifurcations occurring or to Iorio *et al.* [76] who identified a low frequency stable mode close to stall but only focused on the study of high lift solutions and did not track the mode all along the curve. In the present work, it is intended to go further with the following strategy: (*i*) couple continuation methods to the RANS formalism (*ii*) conduct a more careful linear global stability analysis of the steady solutions (*iii*) perform unsteady RANS computations to investigate the nonlinear behavior of the flow and (*iv*) create a one-equation stall model to gain an understanding of the nonlinear phenomena that cannot be identified with the standard unsteady RANS computations. With such an approach, we intend to answer several questions: does an unstable mode responsible for stall exist? How does this mode evolve along the polar curve as the angle of attack varies? What are the most sensitive regions of the flow at stall? How may the low frequency oscillations and hysteresis, which are mentioned in several studies in the literature, be linked to the behavior of this mode? Can we explain why these phenomena sometimes appear at stall and sometimes not? And, can we draw a bifurcation diagram that would logically link all these phenomena?

To answer these questions, the particular case of a two dimensional OA209 airfoil in retreating blade configuration (i.e. $\mathrm{M} = 0.16$ and $\mathrm{Re} = 1.8 \times 10^6$) is considered at first. The RANS approach coupled with the Spalart–Allmaras turbulence model [151] is retained to perform this study of this high Reynolds number flow. Chapter 2 is dedicated to the presentation of the numerical tools used: RANS formalism, turbulence model, numerical schemes and definition of residuals.
Chapter 3 is dedicated to confirm that stall, static hysteresis and low frequency oscillations, which were all identified for different flow configurations, airfoils or turbulence model, can be observed with the Spalart–Allmaras turbulence model in the configuration studied by varying the angle of attack from $\alpha = 12.00°$ and $\alpha = 22.00°$. The standard time stepping methods implemented in the CFD solver *elsA* [27] is used. A

local time stepping approach is used to compute steady solution: the results obtained with the Spalart–Allmaras model are similar to the ones found in the literature. Moreover, it is proven that the static hysteresis identified in this configuration with the $k-\omega$ turbulence model by Richez *et al.* [133] is also caught with the Spalart–Allmaras turbulence model. Similarly to Iorio *et al.* [76] on a NACA0012 at $\mathrm{Re} = 6.0 \times 10^6$, an unsteady RANS computations with the Spalart–Allmaras turbulence model reveal a low frequency oscillation for one particular angle of attack in the high lift configuration close to stall. Finally, this chapter is also the opportunity to highlight the limitations of time steppers to study stall.
Once it has been proven that stall, static hysteresis and low frequency oscillations can be found in this configuration with the Spalart–Allmaras turbulence model, the main question is to know if it is possible, similarly to the work of Wales and Gatonde [166] on a NACA0012, to identify a branch of unstable steady solutions, unaccessible with the local time stepping approach, which would link the two branches of respectively high lift steady solutions and low lift steady solutions. To answer this question, continuation methods are necessary. These methods will also allow us to override the convergence problems of time steppers close to stall angle. Chapter 4 introduces the formalism of two continuation methods (the naive continuation method and the pseudo arclength method [86]) and their implementation in association with the CFD solver *elsA* [27].
These methods are applied to the flow configuration mentioned by considering the angle of attack α as the parameter of the study. The results, presented in the first part of chapter 5, show that it is possible to identify a branch of steady solutions that link the two already computed upper and lower branches, similarly to the results of Wales *et al.* [166]. The stability analysis of each steady solution in the range of $12.00° < \alpha < 22.00°$ is investigated. The second part of chapter 5 is dedicated to the presentation of the two unstable modes encountered: a stall mode (similar to the one identified by Iorio *et al.* [76]) and a vortex shedding mode. Their associated adjoint modes and different sensitivity analysis [91] [123] are also presented. In the last part of chapter 5, the evolution of the stall mode along the polar curve is presented and several bifurcations are identified.
Chapter 6 is dedicated to the identification and tracking of unsteadiness and limit cycles with URANS simulations: a large low frequency limit cycle is encountered around stall and a vortex shedding unsteadiness is identified for high angles of attack, both in good agreement with the results of the linear stability analysis. A first proposition of bifurcation scenario taking limit cycles into account is made but the lack of information available with this method is highlighted.
It was mentioned in section 1.5 that studying the bifurcations of a system with time steppers is possible but quite limited [165]. Ideally in order to complete the information obtained in chapter 6, it would be interesting to develop a tool able to track limit cycles [39]. However, in order to avoid the development of a supplementary tool a one-equation stall model is used. This nonlinear model, presented in chapter 7 is based and calibrated on the evolution of the steady states and their linear behavior described in chapter 5. The study of the nonlinear behavior of this models is supposed to replace the tracking of the limit cycles identified with URANS computations and provide us additional information. This approach is a considerable gain of time and computational ressource as specific softwares and plugin, such as Matcont [39], already exist to study in detail the bifurcations of simple systems such as this one. Based on this

one-equation model, a plausible complete bifurcation scenario involving saddle-node bifurcations, subcritical Hopf bifurcations and Homoclinic bifurcations that would link stall, low frequency oscillations and hysteresis is proposed. Another advantage of this approach is the possibility to study slightly different cases at a very low computational cost by varying the constants of the model, which allowed us to propose alternative bifurcation scenarios.
Finally, in chapter 8, a different Reynolds number and a different airfoil are investigated to verify if the bifurcation scenario observed can be encountered in different configurations.

Chapter 2

Standard tools to study stall through RANS approximation

Contents

The principle advantages and drawbacks of the RANS approach have been discussed in the introduction. In this chapter we intend to introduce the mathematical formalism of the approach as much as the Spalart–Allmaras turbulence model. The solver and the numerical schemes used to perform time marching computations are introduced for steady and unsteady computations.

2.1 The RANS formalism

2.1.1 Compressible Navier–Stokes equations

In continuum mechanics theory, which implies that the smallest scale of the flow is larger than the molecular scale, the Navier–Stokes equations are believed to describe the physics of all fluid flows including the turbulent ones. They were introduced in the mid XIXth century by the mathematician Henry Navier and the physicist George Gabriel Stokes. In the case of a compressible, viscous and heat conductor flow and by

neglecting the effects of the gravity, the local form of these equations can be written as shown in equations (2.1) in cartesian coordinates using the Einstein notation. These equations describe respectively the mass conservation, the momentum equation and the energy conservation.

$$\begin{cases} \dfrac{\partial \rho}{\partial t} + \dfrac{\partial}{\partial x_j}(\rho u_j) = 0 \\ \dfrac{\partial}{\partial t}(\rho u_i) + \dfrac{\partial}{\partial x_j}(\rho u_i u_j) = -\dfrac{\partial p}{\partial x_i} + \dfrac{\partial \tau_{ij}}{\partial x_j} \qquad i = 1,2,3 \\ \dfrac{\partial}{\partial t}(\rho E) + \dfrac{\partial}{\partial x_j}\left[(\rho E + p)u_j\right] = \dfrac{\partial}{\partial x_j}(\tau_{ij} u_i) - \dfrac{\partial q_j}{\partial x_j} \end{cases} \tag{2.1}$$

where t is the time variable and x_i the i^{th} spatial coordinate. The variables ρ designate the density, u_i the i^{th} component of the flow speed, p the static pressure, τ_{ij} a component of the the stress tensor , q_i the i^{th} component of the heat flux and E the total energy. To close this system, the expression of some variables needs to be set.

2.1.1.1 Energy

The total energy E is defined as the sum of the internal energy e and the kinetic energy per mass unit.

$$E = e + \frac{1}{2} u_i u_i \tag{2.2}$$

2.1.1.2 Ideal gas law

In the case where the fluid can be considered as an ideal gas, the ideal gas law links the pressure p with the density ρ in equation (2.3) where T designates the temperature of the fluid, r the ratio of the universal gas constant $R = 8.3145 J.mol^{-1}.K^{-1}$ to the molar mass M of the flow considered ($r = \frac{M}{R}$).

$$p = \rho r T \tag{2.3}$$

This law also links the pressure p to the internal energy e in equation (2.4) where γ is the ratio of isobaric to isochoric heat capacities ($\gamma = \frac{C_p}{C_v}$). For a diatomic gas, $\gamma = 1.4$.

$$p = \rho(\gamma - 1)e \tag{2.4}$$

2.1.1.3 Stress tensor

The hypothesis of a Newtonian fluid is made to express the stress tensor τ. It means that the tensor is linked to the strain tensor (depending on the velocity derivatives

with respect to the position) through a viscosity tensor that does not depend on the stress state and velocity of the field. In the case of an isotropic fluid, this viscosity tensor can be reduced to two real coefficients. It leads to equation (2.5) where μ and λ are the coefficients of the viscosity tensor.

$$\tau_{ij} = \lambda \frac{\partial u_k}{\partial x_k}(\delta_{ij}) + \mu \left(\frac{\partial u_i}{\partial x_j} + \frac{\partial u_j}{\partial x_i} \right) \tag{2.5}$$

The Stokes hypothesis is considered verified and a link between the two coefficients can be made : $\lambda + \frac{2}{3}\mu = 0$.

$$\tau_{ij} = -\frac{2}{3}\mu \frac{\partial u_k}{\partial x_k}(\delta_{ij}) + \mu \left(\frac{\partial u_i}{\partial x_j} + \frac{\partial u_j}{\partial x_i} \right) \tag{2.6}$$

Finally, the coefficient μ can be deduced from the Sutherland's law. It links the viscosity to the temperature only, respecting the Newtonian fluid hypothesis.

$$\mu(T) = \mu_0 \left(\frac{T}{T_0} \right)^{\frac{3}{2}} \frac{T + 110.4}{T_0 + 110.4} \tag{2.7}$$

where $T_0 = 273.16K$ and $\mu_0 = 1.711 \times 10^{-5} kg.m^{-1}.s^{-1}$ for air.

2.1.1.4 Heat flux

Fourier's law links the heat flux to the temperature gradient as shown in equation (2.8).

$$q_i = -\kappa \frac{\partial T}{\partial x_i} \tag{2.8}$$

where κ is set by using the definition of the Prandtl number (equal to $\mathrm{Pr} = 0.72$ for air), which is a dimensionless number characterizing the ratio between the viscous diffusion rate and the thermal diffusion rate. It leads to equation (2.9) where μ and C_p have already been defined.

$$\kappa = \frac{\mu C_p}{\mathrm{Pr}} \tag{2.9}$$

2.1.2 The Reynolds Averaged Navier–Stokes formalism

At high Reynolds number, the use of Direct Numerical Simulations (DNS) to solve the Navier–Stokes equations (2.1) is extremely costly, which makes this method almost impossible, particularly for industrial problems. One alternative is the Reynolds Average Navier–Stokes (RANS) approach, which consists in modeling the lowest scales of the turbulence with a so called turbulence model. This section is dedicated to the decomposition of the Navier–Stokes equations (presented in (2.1)) into the Reynolds Averaged Navier–Stokes equations. The average operator as defined first by Reynolds

[132] is introduced, as well as the decomposition applied to the Navier–Stokes equations. The reader can refer to the book of Gatski and Bonnet for more details about this formalism [57].

2.1.2.1 Average operator

The RANS approach considers turbulence as a random phenomenon that can be studied from a statistical point of view. The main hypothesis of this approach is that each variable f of the flow can be decomposed into a mean part $\langle f \rangle$ and a fluctuating part f'.

$$f = \langle f \rangle + f' \tag{2.10}$$

where $\langle f \rangle$ is the ensemble average of the variable f, which corresponds to the mean value of the variables f_k after a number N of independent realizations in the same conditions.

$$\langle f \rangle = \frac{1}{N} \sum_{k=1}^{N} f_k \tag{2.11}$$

To be formally exact, one should consider $N \to \infty$. However, such a limit considerably complexifies the mathematical framework besides being not realistic, as in practice, a finite number of experiments would have to be considered. This operator follows Reynolds properties (a being a scalar and ψ a time or space variable) :

$$\begin{array}{lll} \langle f' \rangle = 0 & \langle f+g \rangle = \langle f \rangle + \langle g \rangle & \langle a.f \rangle = a.\langle f \rangle \\ \langle \langle f \rangle \rangle = \langle f \rangle & \langle fg \rangle = \langle f \rangle \langle g \rangle + \langle f'g' \rangle & \langle \dfrac{\partial f}{\partial \psi} \rangle = \dfrac{\partial \langle f \rangle}{\partial \psi} \\ & \langle \langle f \rangle g \rangle = \langle f \rangle \langle g \rangle & \end{array}$$

2.1.2.2 Averaged equations

Equation (2.10) was introduced by Reynolds for turbulent incompressible flows. However, in order to simplify the notations for the case of compressible flows, the Favre average [53] [54] is introduced :

$$f = \tilde{f} + f'' \quad \text{with} \quad \tilde{f} = \frac{\overline{\rho f}}{\overline{\rho}} \tag{2.12}$$

By applying this decomposition to the system (2.1), it becomes:

$$\begin{cases} \dfrac{\partial \overline{\rho}}{\partial t} + \dfrac{\partial}{\partial x_j}(\overline{\rho}\tilde{u}_i) = 0 \\ \dfrac{\partial \overline{\rho}\tilde{u}_i}{\partial t} + \dfrac{\partial}{\partial x_j}(\overline{\rho}\tilde{u}_i\tilde{u}_j + \overline{p}\delta_{ij} - \tilde{\tau}^*_{ij}) = -\dfrac{\partial}{\partial x_j}(\widetilde{\overline{\rho}u''_i u''_j}) + \dfrac{\partial}{\partial x_j}(\overline{\tau}_{ij} - \tilde{\tau}_{ij}) \\ \dfrac{\partial}{\partial t}(\overline{\rho}\tilde{E}) + \dfrac{\partial}{\partial x_j}(\overline{\rho}\tilde{E}\tilde{u}_j + \overline{p}\tilde{u}_j - \tilde{\tau}^*_{ij}\tilde{u}_i + \tilde{q}^*_j) = -\dfrac{\partial}{\partial x_j}(\overline{(\rho e'' + p)u''_j}) \\ \qquad -\dfrac{\partial}{\partial x_j}(\widetilde{\overline{\rho}u''_i u''_j}\tilde{u}_i) + \dfrac{\partial}{\partial x_j}(\overline{\tau_{ij}u''_i}) + \dfrac{\partial}{\partial x_j}(\overline{\tau}_{ij}\tilde{u}_i - \tilde{\tau}^*_{ij}\tilde{u}_i) \\ \qquad +\dfrac{\partial}{\partial x_j}\left(\dfrac{1}{2}\overline{\rho u''_i u''_i u''_j}\right) - \dfrac{\partial}{\partial x_j}(\overline{q}_j - \tilde{q}^*_j) \end{cases} \tag{2.13}$$

with:

$$\overline{\rho}\tilde{E} = \overline{\rho}\tilde{e} + \frac{1}{2}\overline{\rho}\tilde{u}_i\tilde{u}_i + \frac{1}{2}\overline{\rho}\widetilde{u''_i u''_i} \tag{2.14}$$

$$\tilde{\tau}^*_{ij} = -\frac{2}{3}\mu(\tilde{T})\frac{\partial \tilde{u}_k}{\partial x_k}\delta_{ij} + \mu(\tilde{T})\left(\frac{\partial \tilde{u}_i}{\partial x_j} + \frac{\partial \tilde{u}_j}{\partial x_i}\right) \tag{2.15}$$

$$\tilde{q}^*_i = -\kappa(\tilde{T})\frac{\partial \tilde{T}}{\partial x_i} \tag{2.16}$$

In order to simplify the set of equations (2.13), two hypotheses are made : the influence of viscosity fluctuations in the viscous stress tensor is neglected as well as the effects of the fluctuations of the density [112]. It leads to the following set of equations:

$$\begin{cases} \dfrac{\partial \overline{\rho}}{\partial t} + \dfrac{\partial}{\partial x_j}(\overline{\rho}\tilde{u}_i) = 0 \\ \dfrac{\partial \overline{\rho}\tilde{u}_i}{\partial t} + \dfrac{\partial}{\partial x_j}(\overline{\rho}\tilde{u}_i\tilde{u}_j + \overline{p}\delta_{ij} - \tau^*_{ij}) = -\dfrac{\partial \tau^R_{ij}}{\partial x_j} \\ \dfrac{\partial}{\partial t}(\overline{\rho}\tilde{E}) + \dfrac{\partial}{\partial x_j}(\overline{\rho}\tilde{E}\tilde{u}_j + \overline{p}\tilde{u}_j - \tilde{\tau}^*_{ij}\tilde{u}_i + \tilde{q}^*_j) = -\dfrac{\partial \tilde{q}^R_{t_j}}{\partial x_j} - \dfrac{\partial}{\partial x_j}(\tilde{\tau}^R_{ij}\tilde{u}_i) \end{cases} \tag{2.17}$$

where $\tilde{\tau}^R_{ij}$ is the Reynolds stress tensor and $\tilde{q}_t i^R$ the viscous heat flux defined by:

$$\tilde{\tau}^R_{ij} = -\widetilde{\overline{\rho}u''_i u''_j} \tag{2.18}$$

$$\tilde{q}_t i^R = \overline{(\rho e'' + p)u''_j} \tag{2.19}$$

Note that at this stage, this system has more unknowns than equations: closure equations are required to solve system (2.17). The simplest closure equations are first order models. The concept is to add a set of equations that links the two turbulent

variables $\tilde{\tau}_{ij}^R$ and $\tilde{q}_t i^R$ to the mean values of the flow instead of computing them with costly transport equations. The first order Boussinesq approximation is chosen in our case for the Reynolds stress tensor:

$$\tilde{\tau}_{ij}^R = \mu_t \left(\frac{\partial \tilde{u}_i}{\partial x_j} + \frac{\partial \tilde{u}_j}{\partial x_i} - \frac{2}{3} \frac{\partial \tilde{u}_k}{\partial x_k} \delta ij \right) - \frac{2}{3} \overline{\rho} k \delta_{ij} \tag{2.20}$$

where k is the kinetic energy of the viscous fluctuations, such as: $k = \frac{1}{2} \tilde{u_i'' u_i''}$. For the turbulent heat flux, a Reynolds analogy is used:

$$\tilde{q}_{t_j} = -\kappa_t \frac{\partial \tilde{T}}{\partial x_i} \tag{2.21}$$

where κ_t is defined using the Prandtl number:

$$\kappa_t = -\frac{\mu_t C_p}{\mathrm{Pr}_t} \tag{2.22}$$

Finally, the variable μ_t is the only unknown that remains to be defined in this set of equations. The point of turbulence models is to provide additional equations to define this quantity. Two types of turbulence models exist: algebraic turbulence model and transport equations turbulence model. In this PhD thesis, the Spalart–Allmaras model, which is a one equation transport turbulence model, is used. The next section is dedicated to its description.

2.1.3 Spalart–Allmaras turbulence model

This turbulence model, designed especially for aeronautic application, is based on a single transport equation for the kinetic eddy turbulent viscosity and was created by Spalart and Allmaras [151] and adapted to compressible flows by Deck [38]. The equation is built empirically, using dimensional analysis and studying four different flows to add more complexity to the model. It starts with simple free shear flows from which the simplest version of the model is designed based on the general form: Convection = Production − Dissipation + Diffusion. Correction terms were added to obtain a logarithmic velocity profile in the near wall region at high Reynolds number. Then, additional corrections were made to correctly describe the buffer layer and viscous sublayer at low Reynolds number. Finally, some terms were provided to trip the boundary layer transition and trigger turbulence. Equation (2.23) presents the final form of the model in the compressible case.

$$\begin{cases} \mu_t = \rho \tilde{\nu} f_{v1} \\ \\ \dfrac{D(\rho\tilde{\nu})}{Dt} = C_{b1}(1 - f_{t2})\tilde{S}\rho\tilde{\nu} + \dfrac{C_{b2}}{\sigma} \dfrac{\partial \rho\tilde{\nu}}{\partial x_j} \dfrac{\partial \tilde{\nu}}{\partial x_j} \\ \qquad - (C_{w1} f_w - \dfrac{C_{b1}}{\kappa^2} f_{t2}) \rho \dfrac{\tilde{\nu}^2}{d^2} - \dfrac{\partial}{\partial x_j} \left[\dfrac{1}{\sigma} (\mu + \rho\tilde{\nu}) \dfrac{\partial \tilde{\nu}}{\partial x_j} \right] \end{cases} \tag{2.23}$$

where the terms used are described as follow (d being the distance to the wall) :

$$f_{v1} = \frac{\chi^3}{\chi^3 + C_{v1}^3} \qquad f_{t2} = C_{t3} e^{C_{t4}\chi^2} \qquad \chi = \frac{\rho\tilde{\nu}}{\mu}$$
$$\tilde{S} = ||\overrightarrow{rot}\overrightarrow{U}|| + \frac{\tilde{\nu}}{\kappa^2 d^2} f_{v2} \qquad f_{v2} = 1 - \frac{\chi}{1 + \chi f_{v1}}$$
$$f_w = g\left(\frac{1 + C_{w3}^6}{g^6 + C_{w3}^6}\right) \qquad g = r + C_{w2}(r^6 - r) \qquad r = \frac{\tilde{\nu}}{\tilde{S}\kappa^2 d^2}$$

with the recommended values for the constants :

$$C_{b1} = 0.1355 \qquad C_{b2} = 0.622 \qquad \sigma = \frac{2}{3} \qquad \kappa = 0.41$$
$$C_{w1} = \frac{C_{b1}}{\kappa^2} + \frac{(1 + C_{b2})}{\sigma} = 0.3 \qquad C_{w2} = 2 \qquad C_{v1} = 7.1 \qquad C_{t1} = 1$$
$$C_{t2} = 2 \qquad C_{t3} = 1.1 \qquad C_{t4} = 2$$

This model offers a good balance between simplicity and efficiency. Its one equation form leads to reduced computational time and it was proven to be very robust. However, it shows some limits in complex configurations.

2.1.4 Edwards–Chandra modification of the Spalart–Allmaras turbulence model

The modification of the Spalart–Allmaras turbulence model proposed by Edwards and Chandra [46] was originally made to solve convergence issues close to the leading edge stagnation point. The singular behavior of the source term S in the near-wall region and the implicit formulation of the equation on the $\tilde{\nu}$ variable (see equation (2.23)) are the main reason of such convergence issues. The modification consists in redefining the source term $\tilde{S}$ and the parameter r as presented in equations (2.24) to (2.26). Also, the f_{t2} term is ignored.

$$\tilde{S} = \overline{S}^{\frac{1}{2}}\left[\frac{1}{\chi} + f_{v1}\right] \tag{2.24}$$

with

$$\overline{S} = \left(\frac{\partial u_i}{\partial x_j} + \frac{\partial u_j}{\partial x_i}\right)\frac{\partial u_i}{\partial x_j} - \frac{2}{3}\left(\frac{\partial u_k}{\partial x_k}\right)^2 \tag{2.25}$$

$$r = \frac{\tanh\left(\frac{\hat{\nu}}{\tilde{S}^2\kappa^2 d^2}\right)}{\tanh(1.0)} \tag{2.26}$$

2.2 Numerics

2.2.1 elsA, a finite volume software

There are several possibilities to resolve numerically partial derivative equations (PDE): finite volume method, finite element methods, finite difference, ... The CFD solver used at ONERA, *elsA* [27], is based on the finite volume method. Contrary to the finite difference method, based on an approximation of the derivative, the finite volume and element methods are based on approximations of integrals. The finite volume method uses the *strong form* of the equations whereas the finite element method uses the *weak form* of the equations. Using the Green-Ostrogadski theorem, the integral form of equations (2.1) and (2.23) can be written under the generic integral form presented in equation (2.27).

$$\frac{d}{dt}\int_{\Omega(t)} \boldsymbol{q} d\Omega + \oint_{\partial\Omega(t)} \left[\mathcal{F}^c + \mathcal{F}^d\right] \cdot \boldsymbol{n}(t) d\Sigma = \int_{\partial\Omega(t)} \boldsymbol{T} d\Omega \tag{2.27}$$

where $\Omega(t)$ is the computation domain, $\partial\Omega(t)$ the boundary of outer normal $\boldsymbol{n}(t)$, $\mathcal{F}^c$ and $\mathcal{F}^d$ the convective and diffusive fluxes respectively, $\boldsymbol{T}$ designates the source terms and $\boldsymbol{q} = [\rho, \rho u, \rho v, \rho w, \rho E, \rho\tilde{\nu}]$ the solution of the compressible Navier–Stokes equations in the RANS framework coupled with the Spalart–Allmaras turbulence model. The approximation of a fixed and unalterable domain is also set. The point of the finite volume method is to obtain an approximated solution of the equation (2.27) by using a mesh made of several separated finite volumes, which once reunited correspond to the whole domain. The equation is solved in each domain (cell) Ω_{cell} of volume $V(\Omega_{cell})$ and of boundary surface (resp. line) Σ_i defined such as :

$$V(\Omega_{cell}) = \int_{\Omega_{cell}} d\Omega \quad \text{and} \quad \partial\Omega_{cell} = \sum_{i=1}^{N} \Sigma_i$$

where N corresponds to the number of adjacent cells. The structural solver of the CFD code *elsA* is used in this PhD thesis. Consequently, for the remainder of the section, the cells will be considered to be hexahedra. Each surface Σ_i has a normal $\boldsymbol{n}$ and the outer norm of the cell is defined such as $\boldsymbol{N}_{\Sigma_i} = \int_{\Sigma_i} \boldsymbol{n} d\Sigma$. In the case of the cell-centered formulation, considered in *elsA*, the values of the variables of $\boldsymbol{q}$ the fluxes and the source terms are constant in each cell and are defined such as:

$$\begin{cases} \boldsymbol{q}_{cell} = \dfrac{1}{V(\Omega)} \displaystyle\int_{\Omega_{cell}} \boldsymbol{q} d\Omega & (2.28) \\ \boldsymbol{F}_{\Sigma_i} = \displaystyle\oint_{\Sigma_i} \left[\mathcal{F}^c + \mathcal{F}^d\right] \cdot \boldsymbol{n} d\Sigma & (2.29) \\ \boldsymbol{T}_{cell} = \dfrac{1}{V(\Omega)} \displaystyle\int_{\partial\Omega_{cell}} \boldsymbol{T} d\Omega & (2.30) \end{cases}$$

Finally, equation (2.27) becomes (2.31) for a cell :

$$V(\Omega)\frac{d}{dt}\boldsymbol{q}_{cell} = -\mathcal{R}_{cell} \quad \text{with} \quad \mathcal{R}_{cell} = \sum_{i=1}^{N} \boldsymbol{F}_{\Sigma_i} - V(\Omega)\boldsymbol{T}_{cell} \tag{2.31}$$

$\mathcal{R}$ being the local residual of the cell. The method presented offers several advantages and drawbacks briefly introduced here. The finite volume method in itself offers the advantage of being completely independent of the mesh. However, the attributes of the mesh are of first importance in the correct evaluation of the fluxes. The cell-centered method offers the advantage of a good precision on the results as the volume used in the integral correspond exactly to the volume of the mesh. However, it requires an interpolation to apply the boundary condition. A key step in the success of this method is the method of computation of the fluxes. Several methods exist and in the next subsection, the ones used in our case are introduced.

2.2.2 Spatial discretisation

In order to simplify the indexation, the numerical schemes are presented in this section for the case of a one dimensional mesh pictured on figure (2.1). The center of the reference cell i is at a position x_i. The boundaries of the cell are at positions $x_{i-1/2}$ and $x_{i+1/2}$ (corresponding to the position of the nodes).The index $_{i+1/2}$ is used to refer to any quantity at the boundary in $x_{i+1/2}$.

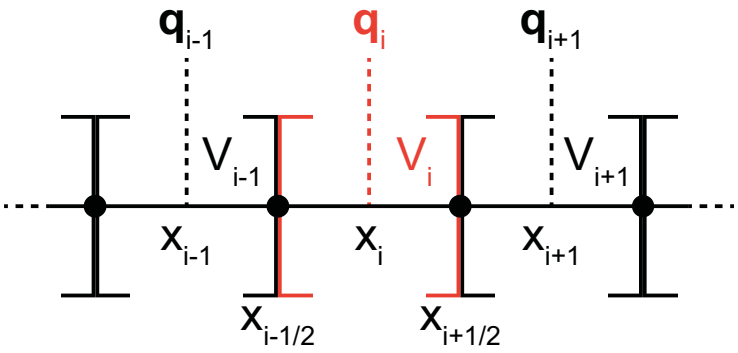

FIGURE 2.1: Cell-centered discretization in a one dimensional case.

2.2.2.1 Convective fluxes for conservative variables

The convective fluxes of the conservative equations (2.1) are discretized using the AUSM+(P) scheme [47], a modified version of the AUSM+ scheme. The name of the original scheme stands for Advection Upstream Splitting Method, which, practically, means that the flux is considered to have two physically distinct parts: convective and pressure fluxes. Several modification were introduced to improve the robustness and the accuracy of the model as much as the applicability domain (speed-regimes, phases,...). The AUSM+(P) ensures a good precision for all flow speeds (from supersonic to low Mach number configurations). However, in our configuration of low Mach

number, the capture of shock properties is useless and so a modified version of original AUSM+(P) scheme, from [99], is used in order to reduce the computational time. Finally, the expression of the flux at the boundary $x_{i+1/2}$ is defined in equation (2.32).

$$\boldsymbol{F}^c_{i+1/2} = \frac{1}{2}U_1(\boldsymbol{W}^L_{i+1/2} + \boldsymbol{W}^R_{i+1/2}) - \frac{1}{2}|U_{dis}|(\boldsymbol{W}^R_{i+1/2} - \boldsymbol{W}^L_{i+1/2}) + \boldsymbol{P} \tag{2.32}$$

where exponents ^{R} and ^{L} refers to the interpolating values on the right and on the left of the boundary respectively, U_1 is the flow speed at the interface, $\boldsymbol{W}$ is a state vector such as $\boldsymbol{W} = (\rho, \rho u, \rho v, \rho w, \rho E{+}p)$, the pressure term $\boldsymbol{P}$ is defined by $\boldsymbol{P} = (0, \frac{(p^L+p^R)}{2}, 0, 0, 0)$ and U_{dis}, introduced as a local flow speed, characterizes the numerical dissipation acting on the velocity components. These quantities are defined by :

$$\begin{cases} U_1 = \dfrac{1}{2}(u^L + u^R) - c_2(p^R - p^L) \\ U_{dis} = max\left(\dfrac{1}{2}|u^L + u^R|, c1\right) \\ \boldsymbol{W}^L_{i+1/2} = \boldsymbol{W}_i + \dfrac{1}{6}\left[2(\boldsymbol{W}_{i+1} - \boldsymbol{W}_i) + (\boldsymbol{W}_i - \boldsymbol{W}_{i-1})\right] \\ \boldsymbol{W}^R_{i+1/2} = \boldsymbol{W}_{i+1} - \dfrac{1}{6}\left[2(\boldsymbol{W}_{i+1} - \boldsymbol{W}_i) + (\boldsymbol{W}_{i+2} - \boldsymbol{W}_{i+1})\right] \end{cases}$$

The term $c_2(p^R - p^L)$ in the expression of U_1 is a stabilization term introduced to improve the velocity/pressure coupling in the low mach number regions. c_1 and c_2 are two constant values set to $c_1 = c_2 = 0.04$ in order to minimize dissipation and ensure stability as recommended in the PhD Thesis of Mary [98] (which also contains a precise analysis of the behavior of this numerical scheme). The expressions of the left and right interpolated values are defined by using the reconstruction scheme MUSCL developed by Van Leer [90] (standing for Monotonic Upstream Schemes for Conservation Laws), in the case of a partially non-centered third order scheme.

2.2.2.2 Convective fluxes for turbulent variables

In order to discretize the fluxes appearing in the turbulent equation (2.23), the noncentered Roe scheme is used [141]. This scheme is based on a linearisation of the Riemann problem. The expression of the flux at the boundary $x_{i+1/2}$ is defined in equation (2.33):

$$\boldsymbol{F}^c_{i+1/2} = \frac{1}{2}\left[\mathcal{F}^c(\boldsymbol{q}^L_{i+1/2}) + \mathcal{F}^c(\boldsymbol{q}^R_{i+1/2}) - |\boldsymbol{A}^{Roe}|(\boldsymbol{q}^L_{i+1/2} + \boldsymbol{q}^R_{i+1/2})\right] \tag{2.33}$$

Where A^{Roe} is the diagonalisable Jacobian matrix such that $|\boldsymbol{A}^{Roe}| = \boldsymbol{M}|\lambda_i|\mathcal{I}\boldsymbol{M}^{-1}$, λ_i designating the eigenvalues of A^{Roe} and $\boldsymbol{M}$ the transformation matrix. However, too low eigenvalues could lead to nonentropic solutions. To prevent such a behavior, Harten and Hyman [64] proposed a modification of the scheme such as the entropy issue is fixed.

2.2.2.3 Diffusive fluxes

The diffusive fluxes are by definition easier to compute. The same cell-centered scheme based on a five points stencil is used for the conservative and turbulent equations. In the case of the one dimensional formalism introduced in Figure (2.1), it leads to:

$$\begin{aligned} \boldsymbol{F}^d_{i+1/2} &= \frac{1}{2}(\boldsymbol{F}^d_{i+1} + \boldsymbol{F}^d_i) \\ \boldsymbol{F}^d_{i-1/2} &= \frac{1}{2}(\boldsymbol{F}^d_i + \boldsymbol{F}^d_{i-1}) \end{aligned} \tag{2.34}$$

The gradients required to compute the source terms are estimated at cell centers using the Ostrogradski formula:

$$\left.\frac{\partial \boldsymbol{F}^d}{\partial x_k}\right|_i \approx \frac{1}{V(\Omega)} \iiint_{\Omega_i} \frac{\partial \boldsymbol{F}^d}{\partial x_k} d\Omega_i = \frac{1}{V(\Omega)} \iint_{\Sigma_i} \boldsymbol{F}^d \boldsymbol{n} d\Sigma_i \tag{2.35}$$

2.2.3 Temporal approach

2.2.3.1 Schemes

Two approaches can be considered for the numerical time integration of the Navier–Stokes equations : explicit or implicit methods. The first one calculates the solution at an iteration $n+1$ from the state at iteration n. It results an easy formulation and implementation and a reduced computational cost. However, the explicit methods requires small time steps Δt in order to ensure the stability of the scheme. The implicit method is more complex as it requires to solve a system in which the current state at iteration n and the expected solution at iteration $n+1$ are coupled. It results in a much more difficult implementation and a higher computational cost. However, this scheme is unconditionally stable, which leads to the possibility to use higher time steps than the explicit method.

In the case of the explicit method, the time step Δt is chosen by using the Courant-Friedrich-Lewy condition (CFL) defining in equation (2.36). It links the size of mesh Δx to the time step Δt via V the the modulus of the mean velocity in the cell, c the local sound speed in the cell and some fluid parameters already defined. The CFL condition, defined in these terms, takes into account the convective and dissipative parts of the flow (two terms in the *min* operator) and only the most critical is used to determine the step time Δt. The CFL parameter is also introduced: it is a coefficient that must satisfy CFL$\langle$1 in the case of an explicit scheme.

$$\Delta t \leq \mathrm{CFL} \times min \left[\frac{\Delta x}{V + c} \ , \ \frac{\rho(\Delta x)^2}{2\gamma \left(\frac{\mu}{\mathrm{Pr}} + \frac{\mu_t}{\mathrm{Pr}_t} \right)} \right] \tag{2.36}$$

With such a condition on the explicit schemes, one can obviously notice that small cells will lead to small time steps. Yet, to correctly model the physics of the boundary

layer with a RANS approach, very small cells are required. This observation leads us to consider an implicit approach.

The computation of steady solutions (RANS) is performed by considering an unsteady computation with a local time stepping approach. It means that, as the history of the solution is not of interest, different time step Δt are used for each cell, directly determined from the CFL condition. It means that small time steps are used in small cells and larger time steps are used in larger cells. It allows the destruction of unsteadiness that could lead to oscillatory phenomena and a reduced computational time. We choose CFL = 30 to scale the local time step Δt in our RANS computations.

In the case of unsteady computations (URANS), the history of the flow is required and consequently the method of local time stepping is useless. Note that in that case, the choice of an explicit scheme would have been even more critical as the choice of the time step Δt is global and scaled on the smallest cell of the mesh. In the case of an implicit scheme, we just ensure that the time step is small enough compared to the frequency of the physical phenomena we intend to observe.

Finally, two different implicit schemes are chosen for the steady and unsteady cases. First, a backward Euler scheme (first order scheme presented in equation (2.37) obtained from equation (2.31)) is used for steady computations.

$$\frac{\boldsymbol{q}_{cell}^{n+1} - \boldsymbol{q}_{cell}^{n}}{\Delta t} V(\Omega) = -\mathcal{R}_{cell}^{n+1} \tag{2.37}$$

Second, a Gear scheme (second order scheme presented in equation 2.38 obtained from equation (2.31)) is used for unsteady computations .

$$\frac{3\boldsymbol{q}_{cell}^{n+1} - 4\boldsymbol{q}_{cell}^{n} + \boldsymbol{q}_{cell}^{n-1}}{2\Delta t} V(\Omega) = -\mathcal{R}_{cell}^{n+1} \tag{2.38}$$

In both cases, we intend to find the solution $\boldsymbol{q}^{n+1}$ at iteration $n+1$ corresponding to a time $(n+1)\cdot\Delta t$ (local or global depending on the type of computation) by considering $\boldsymbol{q}^{n}$ and $\boldsymbol{q}^{n-1}$ known. The residual $\mathcal{R}_{cell}^{n+1}$ is defined as the some of the all the fluxes and production terms of the cell (see equation (2.31)). In both cases, it leads to a system of the form :

$$\mathcal{G}(\boldsymbol{q}^{n+1}) = 0 \tag{2.39}$$

where $\boldsymbol{q}^{n+1}$ is a vector of dimension $N_{variables} \times N_x \times N_y \times N_z$

2.2.3.2 Resolution of the non linear problem

Steady case

To resolve equation (2.37), the residual $\mathcal{R}_{cell}^{n+1}$ is first linearized in equation (2.40).

$$\mathcal{R}_{cell}^{n+1} = \mathcal{R}_{cell}^{n} + \frac{\partial \mathcal{R}_{cell}^{n}}{\partial \boldsymbol{q}}(\boldsymbol{q}^n)\left[\boldsymbol{q}^{n+1} - \boldsymbol{q}^n\right] + \boldsymbol{O}(\Delta t^2) \tag{2.40}$$

Then the expression of the residual is replaced by the expression of the linearized residual in equation (2.37).

$$\left[\frac{V(\Omega)}{\Delta t}\mathcal{I} + \mathcal{J}(\boldsymbol{q}^n)\right](\boldsymbol{q}^{n+1} - \boldsymbol{q}^n) = -\mathcal{R}_{cell}^{n} \tag{2.41}$$

where $\mathcal{J}$ is the Jacobian of the system defined such as :

$$\mathcal{J}(\boldsymbol{q}^n) = \frac{\partial \mathcal{R}_{cell}^{n}}{\partial \boldsymbol{q}}(\boldsymbol{q}^n) \tag{2.42}$$

Unsteady case

In the case of unsteady computations, the system presented in equation (2.39) is solved using a Newton's method to find $\boldsymbol{q}^{n+1}$. the reader is invited to refer to section 4.1.1 in which the Newton's method is described more in detail. For each iteration n a number M of sub-iterations are performed to converge the resolution of the Newton's method. The Jacobian of the system at sub-iteration m is defined in equation (2.43).

$$\mathcal{J}(\boldsymbol{q}^{n+1,m}) = \frac{\partial \mathcal{G}}{\partial \boldsymbol{q}}(\boldsymbol{q}^{n+1,m}) \tag{2.43}$$

Jacobian approximation

In both cases, a system of the form $\mathcal{M} \cdot \Delta\boldsymbol{q} = \boldsymbol{b}$ needs to be solved. However, instead of solving this system with the exact Jacobians previously introduced, this system is solved by using the LU - SSOR method (standing for LU decomposition with Symmetric Successive Over Relaxation) introduced by Yoon and Jameson [171]. This methods consists, first, in a LU decomposition of the Jacobian in three matrices : one upper triangular matrix $\mathcal{U}$, one diagonal matrix $\mathcal{D}$ and one lower triangular matrix $\mathcal{L}$. The system becomes :

$$(\mathcal{L} + \mathcal{D} + \mathcal{U}) \cdot \Delta\boldsymbol{q} = \boldsymbol{b} \tag{2.44}$$

Then the second step is the application of the SSOR method to solve this new system. The system is decomposed into two steps repeated at each relaxation cycle. The number of relaxation cycles is a user parameter and in our case, four cycles are

considered in the steady case and two in the unsteady case. By introducing the number of the cycle p, the final system to be solved is :

$$\begin{cases} (\mathcal{L}+\mathcal{D})\cdot\Delta\boldsymbol{q}^{p+1/2} = \boldsymbol{b}-\mathcal{U}\cdot\Delta\boldsymbol{q}^{p} & (2.45) \\ (\mathcal{D}+\mathcal{U})\cdot\Delta\boldsymbol{q}^{p+1} = \boldsymbol{b}-\mathcal{U}\cdot\Delta\boldsymbol{q}^{p+1/2} & (2.46) \end{cases}$$

2.2.4 Residuals

Depending on the type of computation, *elsA* can provide several types of residual, which are introduced in the present subsection.

2.2.4.1 Explicit residual

The explicit residual, is based on the definition of the residual of the cell as the sum of all the fluxes and production terms of the cell introduced in equation (2.31). A scalar value of the residual for each variable q_i of the solution vector $\boldsymbol{q}$ is obtained by considering the square root of the mean value of the squared local residual value $\mathcal{R}^i_{cell}$ weighted by the volume of the cell $V(\Omega)$ as shown in equation (2.47).

$$Res^{n+1}_{explicit}(q_i) = \sqrt{\frac{1}{N}\sum_{k=1}^{N}\left(\frac{\mathcal{R}^i_{cell}}{V(\Omega)}\right)^2} \tag{2.47}$$

2.2.4.2 Implicit residual

The explicit expression of the residual might struggle to correctly estimate the real convergence of the computation when an implicit method with large time steps are used. An alternative definition of the residual based on the solution increment instead of an evaluation of the right hand side is considered and leads to equation (2.48). This is the type of residual used to analyze convergence in our unsteady computations.

$$Res^{n+1}_{implicit}(q_i) = \sqrt{\frac{1}{N}\sum_{k=1}^{N}\left(\frac{q^{i,n+1}_{cell}-q^{i,n}_{cell}}{\Delta t}\right)^2} \tag{2.48}$$

2.2.4.3 Explicit/implicit residual

A third option, coupling both approaches is also possible. This explicit/implicit version, available for RANS computations with a transport equations turbulent model, consists in using the explicit definition of the residual for the conservative equations and the implicit definition of the residual for the turbulent equations. This way, the application of limiters on the turbulence variables, which is possible only with the implicit computation, can be taken into account. This is the type of residual used to analyze convergence in our steady computations.

Chapter 3

The OA209 airfoil in stall configuration: a standard tools approach

Contents

In this chapter, we intend to apply the methods and tools described in chapter 2 (i.e. a time stepping approach in the RANS formalism coupled with the Spalart–Allmaras turbulence model). The particular case of a two dimensional OA209 airfoil at $\mathrm{Re} = 1.8 \times 10^6$ and $\mathrm{M} = 0.16$, corresponding to a retreating helicopter blade configuration, is investigated. The objective is to identify a stall mechanism by varying the angle of attack of the airfoil. First, the airfoil, the mesh and the boundary conditions are introduced. Then, the results of the steady and unsteady computations are presented and analyzed. Finally, the limitations of this approach are discussed.

3.1 Nondimensionalization, mesh and boundary conditions

For the aforementioned aerodynamic conditions, we intend to solve the Navier–Stokes equations (2.13) coupled with the Spalart–Allmaras turbulence model (2.23). This system is written in the form $\frac{d\boldsymbol{q}}{dt} = \boldsymbol{R}(\boldsymbol{q})$ where the vector solution $\boldsymbol{q}$ has the following

variables $\boldsymbol{q} = (\rho, \rho u, \rho v, \rho E, \rho\tilde{\nu})^T$. Where ρ is the density, u the streamwise velocity in the horizontal axis ($\boldsymbol{x_0}$), v the cross-stream velocity in the vertical axis ($\boldsymbol{y_0}$), E the internal energy and $\tilde{\nu}$ the turbulent variable (the axes $\boldsymbol{x_0}$ and $\boldsymbol{y_0}$ are introduced in Figure (3.1) and detailed below). All the quantities are made non-dimensional with respect to the chord c and the speed of sound $A = 340m \cdot s^{-1}$ and are presented as unitless in this manuscript except if explicitly mentioned.

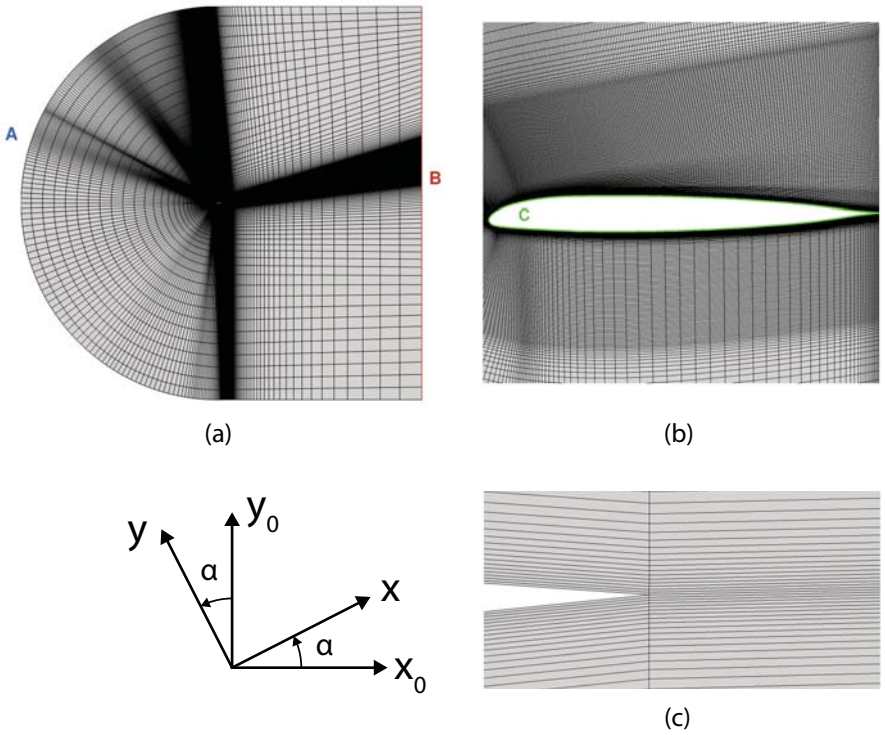

FIGURE 3.1: Visualization of the mesh around a two dimensional OA209 airfoil. (a) Whole domain with boundary conditions A and B. (b) Zoom in close to the airfoil with boundary condition C. (c) Zoom in close to the trailing edge, highlighting the sharp angle.

Figure (3.1) shows three views of the mesh used : (a) exhibits the whole domain (of approximately twenty times the chord length on each direction), (b) shows a zoom in close to the airfoil and (c) presents a zoom in close to the trailing edge. Particular attention has been paid to the refinement close to the airfoil (as shown in Figure (3.1)(b)) in order to correctly capture the physics of the boundary layer. Also, an effort has been made to try to ensure as much as possible the local perpendicularity between the lines starting from the airfoil and the boundary C. In the end, this mesh is made of 144352 cells. Also, looking at the bottom right picture of Figure (3.1), one can observe how the trailing edge has a sharp angle. Such a geometry is not representative of the real geometry but this approximation of a zero thickness of the trailing edge is made in order to simplify the remainder of the study. Finally, the airfoil reference frame ($\boldsymbol{x_0}, \boldsymbol{y_0}$) is also defined in Figure (3.1) as well as the flow reference frame ($\boldsymbol{x}, \boldsymbol{y}$). This second reference frame is introduced to model the inclination of the airfoil. Indeed, we intend to compute solutions for a large range of angles of attack ($12.00° < \alpha < 22.00°$) and, instead of rotating the airfoil and generating a new mesh for each value of α,

the inclination of the airfoil is modeled through the boundary conditions. On the boundary condition A, a compressible inlet condition is set, such that the flow speed is $\boldsymbol{u_\infty} = U_\infty \boldsymbol{x}$. This leads to the following flow quantities on A in the airfoil reference frame $(\boldsymbol{x_0}, \boldsymbol{y_0})$:

$$\boldsymbol{q}_\infty = \begin{pmatrix} \rho_\infty \\ U_\infty \cos(\alpha) \\ U_\infty \sin(\alpha) \\ E_\infty \\ \tilde{\nu}_\infty \end{pmatrix} \tag{3.1}$$

where $\rho_\infty = 1$ (deduced from the Reynolds number and Sutherland's law (2.7) before being non-dimensionalized to be equal to one), $U_\infty = 0.16$ (non-dimensionalized by A such that $U_\infty = M_\infty$), E_∞ is deduced from the equations of the total energy (2.2) and the ideal gas law (2.4) (non-dimensionalized by the square of the speed of sound A^2) and $\tilde{\nu}_\infty = 3\nu_\infty$, based on the recommendation from Spalart and Rumsey [152] and non-dimensionalized by ρ_∞, A_∞ and the chord. In the end, the boundary condition A is driven by the angle of attack α and can be written $\boldsymbol{q}_\infty = f(\alpha)$. On the boundary condition B, a compressible outlet condition is set and an adiabatic wall condition is imposed on boundary condition C. One shall note that the computations are performed in the airfoil reference frame $(\boldsymbol{x_0}, \boldsymbol{y_0})$ but all the results are presented in the flow reference frame $(\boldsymbol{x}, \boldsymbol{y})$.

In order to identify the capacity of the mesh to capture the physics of the boundary layer, one can evaluate the number of cells in the viscous sublayer by using the dimensionless parameter y^+ defined in equation (3.2) where y is the height of the first cell, τ_w the wall shear stress, ρ the density and ν the viscosity.

$$y^+ = \frac{y u_\tau}{\nu} \qquad \text{where} \qquad u_\tau = \sqrt{\frac{\tau_w}{\rho}} \tag{3.2}$$

The evolution of the $y+$ value around the airfoil is plotted as a function of the percentage of the chord on the pressure side (dashed line) and the suction side (solid side) for four angles of attack ($\alpha = 12.00°$, $\alpha = 16.00°$, $\alpha = 18.00°$ and $\alpha = 22.00°$) in Figure (3.2).

Note that the condition $y^+ < 1$ is always validated on the suction side permitting an accurate computation of the viscous sublayer. The values on the pressure side are slightly higher but remain correct ($y^+ < 2.5$) as the characterization of the pressure side is not as critical as the suction side.

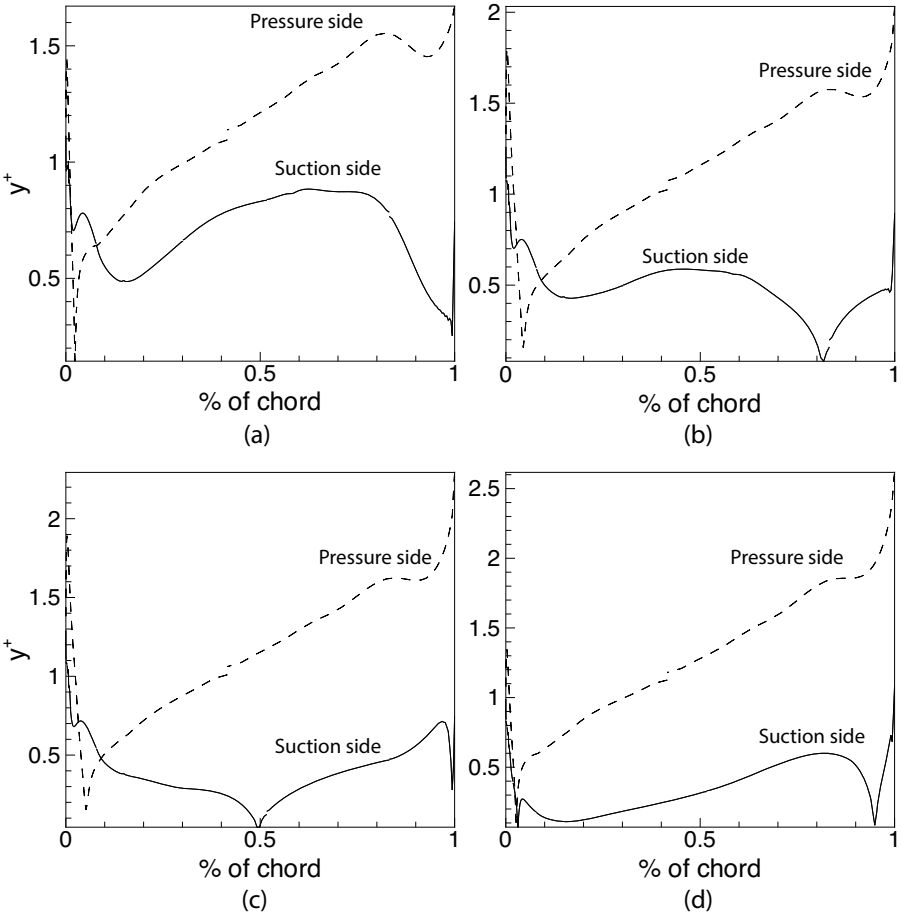

FIGURE 3.2: Evolution of the $y+$ value as a function of the percentage of the chord for the flow around a OA209 airfoil at Re $= 1.8 \times 10^6$ and M $= 0.16$. (a) $\alpha = 12.00°$. (b) $\alpha = 16.00°$. (c) $\alpha = 18.00°$. (d) $\alpha = 22.00°$.

3.2 Steady solutions of the RANS equations coupled with the Spalart–Allmaras model

3.2.1 General overview of the solutions

Figure (3.3) shows the ρu field (left) and the $\rho\tilde{\nu}$ field (right) for different angles of attack. In each picture, the limit of the recirculation bubble, if existing, is plotted in a black line. For each case, the position of the corresponding angle of attack is indicated with a red dot on the middle picture showing the evolution of the lift coefficient as a function of the angle of attack. This curve is presented and discussed more in details in Figure (3.4). The first angle of attack investigated in pictures (a) and (b) is $\alpha = 12.00°$. For this value of α, the flow is fully attached and there is no recirculation bubble. The wake is relatively thin and the level of turbulence in it is extremely low. The second case, $\alpha = 16.00°$, depicted in pictures (c) and (d), exhibits the appearance of a tiny recirculation bubble at the trailing edge. The thickness of the wake, the level of turbulence as well as the lift coefficient increase with the angle of attack. The next configuration, $\alpha = 17.50°$, presented on pictures (e) and (f) corresponds to a maximum

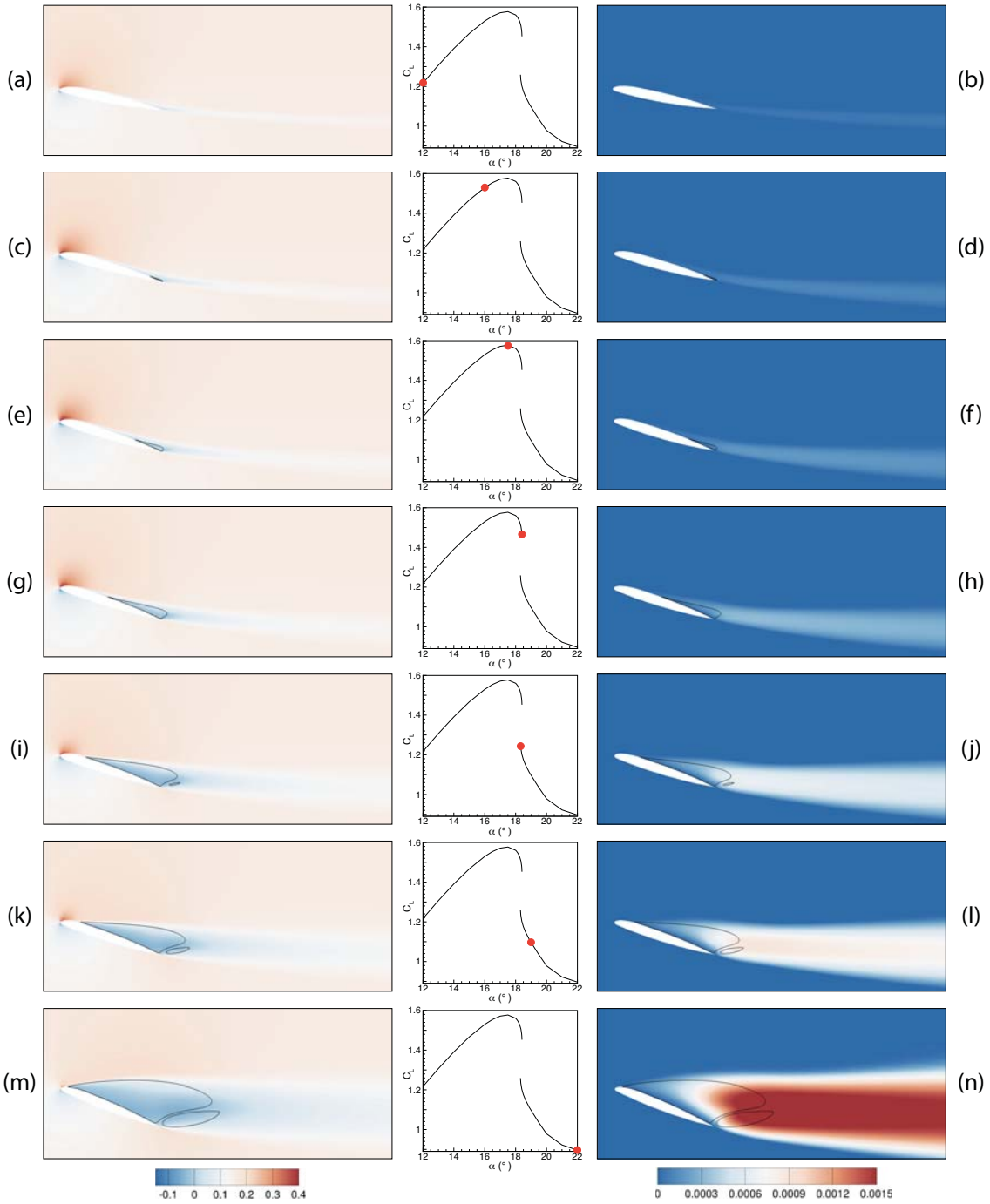

FIGURE 3.3: Flow topology for different angles of attack: (a) and (b) $\alpha = 12.00°$. (c) and (d) $\alpha = 16.00°$. (e) and (f) $\alpha = 17.50°$. (g) and (h) $\alpha = 18.35°$ on the upper branch. (i) and (j) $\alpha = 18.35°$ on the lower branch. (k) and (l) $\alpha = 19.00°$. (m) and (n) $\alpha = 22.00°$. Left pictures: ρu field. Middle pictures: position of the steady solution in the (α, C_L) plan. Right pictures: $\rho\tilde{\nu}$ field.

value of lift coefficient. The separation point of the recirculation bubble has moved backward, in the direction of the leading edge, resulting in an increase of the recirculation bubble size and the thickness of the wake. Pictures (g) and (h) present the fields

for $\alpha = 18.35°$ just before a sudden drop of lift. The separation point kept moving towards the leading edge and the recirculation bubble size as well as the thickness of the wake increased. The same angle of attack $\alpha = 18.35°$ is presented in pictures (i) and (j) but the flow topology is completely different : the flow is now massively separated, resulting in a much bigger recirculation bubble and wake thickness as well as a larger turbulence level in the wake. Also, a second small recirculation bubble appears at the trailing edge. The coexistence of these steady solutions was introduced in chapter 1 and was expected considering the work of Richez *et al.* [133]. A new interpretation, enlightened by the continuation method approach, is presented in detail afterwards in subsection 5.1.2. Then, the case $\alpha = 19.00°$ is presented in pictures (k) and (l). The evolution of the recirculation bubble and the wake is similar to the one observed so far. Moreover, the small recirculation zone at the trailing edge also grows and, by doing so, pushes the reattachment point of the large recirculation bubble towards the leading edge. Finally, the highest angle of attack investigated, $\alpha = 22.00°$, is presented in pictures (m) and (n). The flow is now massively separated from almost the leading edge and the modelled turbulence level is high. In the end, the evolution of the flow topology is characteristic of a trailing edge stall as the separation point moves toward the leading edge as the angle of attack is increased. This result is in good agreement with the prediction of Kaufman *et al.* who noticed that computations performed with a fully turbulent Spalart–Allmaras model caught the trailing edge separation but omitted the laminar separation bubble at the leading edge suggesting a trailing edge stall mechanism instead of a coupled leading edge/trailing edge stall.

From all these solutions, it is possible to extract some aerodynamic coefficients that can be plotted as a function of the angle of attack and provide a quantitative evolution of the flow. These coefficients are defined in appendix A.

3.2.2 Presentation of the polar curves

Figure (3.4) shows the evolution of the lift coefficient (a) and (b), the drag coefficient (c) and (d) and the pitching moment coefficient (e) and (f). The three left pictures (a), (c) and (e) show the evolution of the coefficients for $12.00° < \alpha < 22.00°$ while the middle pictures (b), (d) and (f) exhibit a zoom in for the area $18.28° < \alpha < 18.43°$. One can first observe in pictures (a), (c) and (e), a linear increase of the lift, drag and pitching moment coefficients for the lowest values of angles of attack (from $12.00°$ to $17.50°$ approximately). Then stall occurs, characterized by a sudden drop of lift and pitching moment coefficients and a sudden increase of the drag coefficient. Finally, the lift and pitching moment coefficients keep decreasing more slowly after stall occurs while the drag coefficient keeps increasing. One can observe a discontinuity of the evolution of the three aerodynamic coefficients computed from the steady solutions. This discontinuity occurs precisely at stall. Based on this discontinuity, two different branches of the curve are defined: the upper branch that corresponds to steady solutions between $\alpha = 12.00°$ until stall and the lower branch that corresponds to steady solutions between stall and $\alpha = 22.00°$. The name of the branches is based on the value of the lift coefficient that is generally larger for the upper branch than for the lower branch. Moreover, a very interesting phenomenon is observed close to stall (presented in pictures (b), (d) and

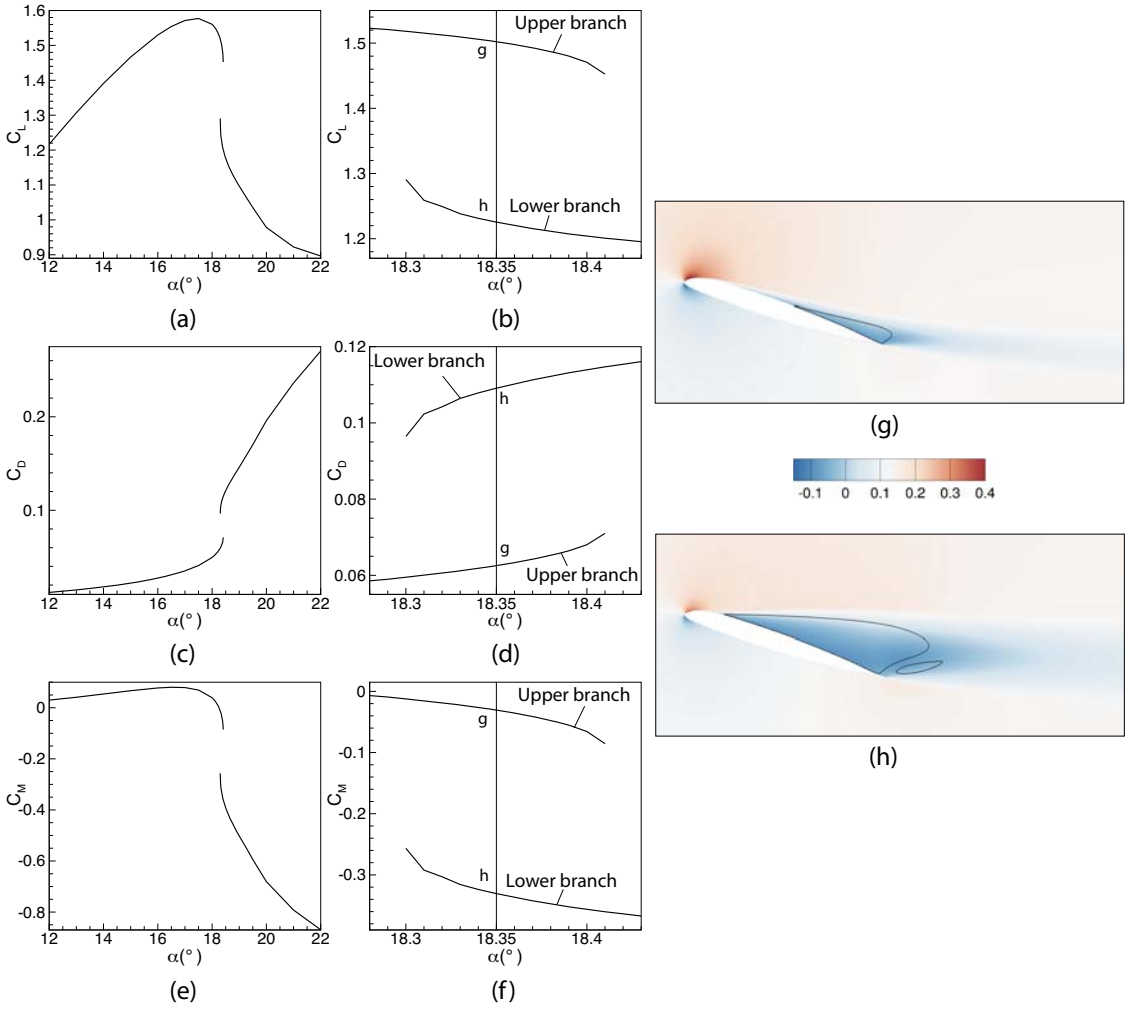

FIGURE 3.4: Evolution of several flow topology related values of steady solutions as a function of the angle of incidence. (a) and (b) Evolution of the lift coefficient. (c) and (d) Evolution of the drag coefficient. (e) and (f) Evolution of the pitching moment coefficient. (g) and (h) Flow visualisation of the ρu field for $\alpha = 18.35°$ on the upper branch (g) and the lower branch (h).

(f)), at the discontinuity: the two branches overlap for $18.30° < \alpha < 18.41°$ for all the aerodynamic coefficients. It means that, for this range of angles of attack, two different steady solutions coexist for each value of α. This is illustrated in pictures (g) and (h), which show the flow for the ρu variable for $\alpha = 18.35°$ on the upper and lower branches. The associated aerodynamic coefficients associated with these two solutions are marked in pictures (b), (d) and (f). The numerical procedure to identify such a phenomenon is based on the initialization of the RANS computations: to compute the upper (respectively lower) branch, one shall first compute a steady solution for an angle of attack α lower (respectively higher) than the angles of attack for which two steady solutions coexist. Then a steady solution is computed for $\alpha + \Delta\alpha$ (respectively $\alpha - \Delta\alpha$) and so on until the end of the branch is reached. It is considered done when, for a small enough increment $\Delta\alpha$, the computation for $\alpha + \Delta\alpha$ gives a steady solution

on the other branch. This means that, by numerically increasing the angle of attack (upper branch) or by numerically decreasing it (lower branch) different solutions are reached, which is typical of a hysteresis phenomenon.

3.2.3 Convergence of the steady solutions

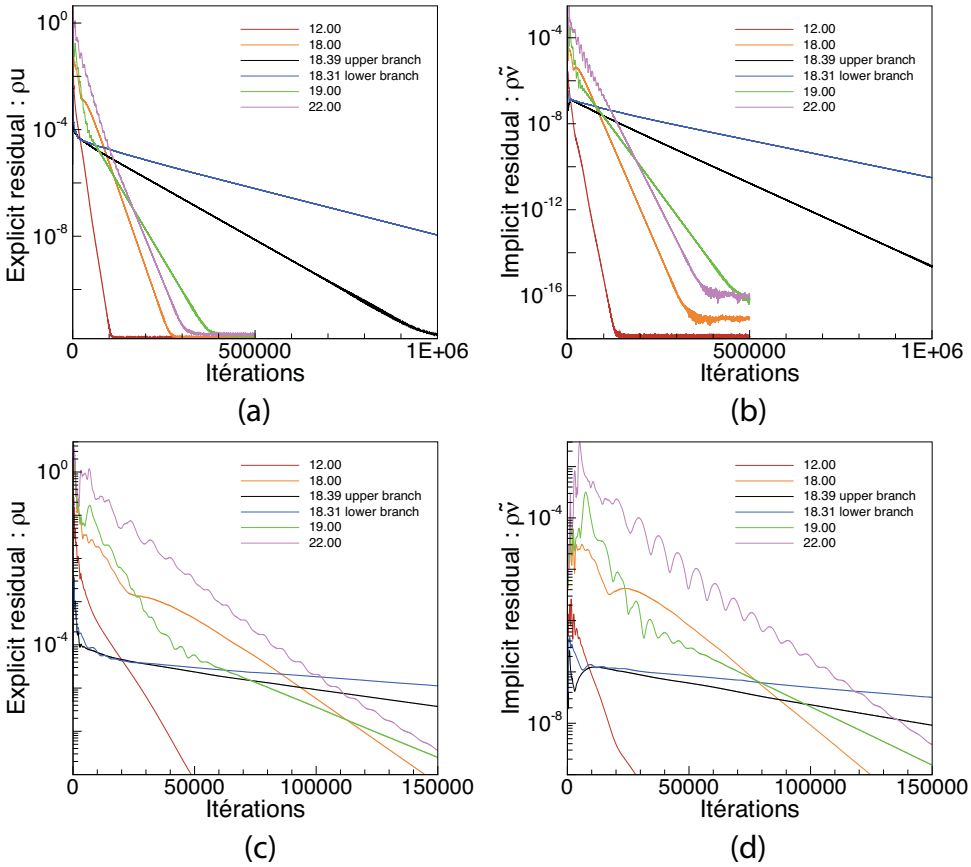

FIGURE 3.5: Evolution of the residual for the variables ρu (explicit) and $\rho\tilde{\nu}$ (implicit) for six different values of α on a log scale. (a) and (b): evolution for 10^6 iterations. (c) and (d) evolution for the beginning of the computation.

Figure (3.5) presents the evolution of the explicit residual of the variable ρu and the implicit residual of the variable $\rho\tilde{\nu}$ on a log scale for several angles of attack. As a reminder, for the local time stepping computations, the residual type used is the explicit/implicit type, which means the explicit residuals is considered for the conservative variables, while the implicit residual is considered for the turbulent variable (more details on the residual types are available in section 2.2.4 of chapter 2). The procedure is the following: 500000 iterations are considered for every angle of attack. If the computation is not converged, the computation is restarted from where it stopped and 500000 more iterations are performed, and so on until convergence of the computation. The two upper pictures present the evolution of the residuals for the first 10^6 iterations while the lower ones present a zoom on the first iterations to highlight

a particular phenomenon. First, one can observe how the residual decreases and reach a plateau for all the angle of attack (of approximately 10^{-12} for the conservative variable and 10^{-16} for the turbulent variable). Even for the blue ($\alpha = 18.31°$) and black ($\alpha = 18.39°$) curves, although it is not represented in Figure (3.5). Such an evolution of the residual is characteristic of well converged computations. Second, note how the convergence is much slower close to stall ($\alpha = 18.31°$ and $\alpha = 18.39°$) and requires many more iterations to converge. On the contrary, for the lowest angle of attack, the convergence is extremely fast and the 500000 iterations considered were not required. Finally, on the lower branch, one can observe how the residual oscillates at the beginning of the computation. The amplitude of these oscillations is high as the angle of attack increases.

3.2.4 Discussion of the results obtained

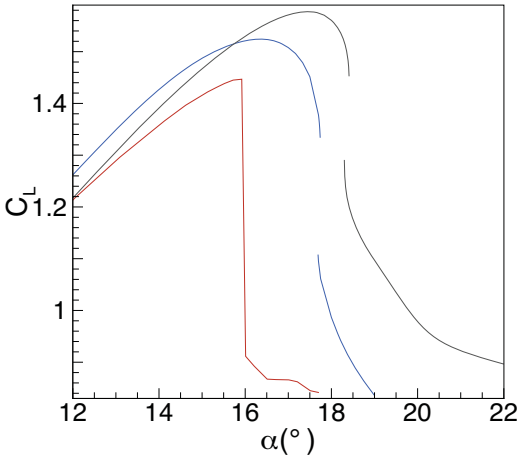

FIGURE 3.6: Comparison of the evolution of the lift coefficient as a function of the angle attack for a two dimensional OA209 airfoil at Re = 1.8×10^6. Red curve: experimentally (from Le Pape *et al.* [125]). Blue curve: numerically from steady RANS solutions with the $k - \omega$ model (from Richez *et al.* [133]). Black curve: numerically from steady RANS solutions with the Spalart–Allmaras model (from the present study).

The results obtained are compared with those in the literature. The stall angle, as well as the maximum lift coefficients are overestimated with the Spalart–Allmaras model (as illustrated in Figure 3.6), compared to the RANS computations with a $k-\omega$ model and with the experiment. The same phenomenon was observed by Richter *et al.* [137] and Jain *et al.* [78]. The inability of the Spalart–Allmaras turbulence model to identify the leading edge LSB was also noted, as suggested by Kaufman *et al.* [85] who argued that computations performed with the Spalart–Allmaras suggested a trailing edge stall mechanism instead of the coupled leading edge/trailing edge stall mechanism identified in the experiments. However, it was demonstrated that an hysteresis of steady solutions existed around stall, similarly to what was found by Richez *et al.* with the $k - \omega$ turbulence model.

3.3 Unsteady RANS computations

The steady RANS computations with the Spalart–Allmaras model proved to be able to identify stall although the stall angle was overestimated. Moreover, hysteresis of the steady solutions was identified in the region of sudden drop of lift. These results are in good agreement with the literature and particularly with the paper of Richez *et al.* [133]. We are now interested in investigating the unsteady behavior of the flow in the stall region. To do so, unsteady RANS computations are performed for several angles of attack close to stall. These computations are initialized with the steady RANS solutions previously presented. For the angles of attack at which two steady solutions coexist, two different computations are performed, each one initialized with a different steady solution.

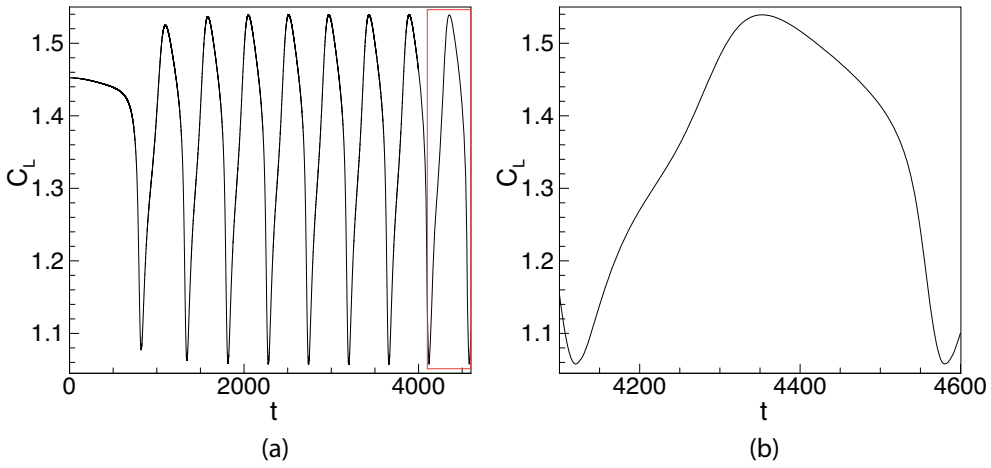

FIGURE 3.7: Time evolution of the lift coefficient for $\alpha = 18.41°$. Results from an unsteady RANS computation initialized with the steady solution at the same angle of attack on the upper branch. (a) Full curve. (b) Zoom in on a period.

Figure (3.7) presents the evolution of the lift coefficient as a function of the time for the computation initialized with $\alpha = 18.41°$ on the upper branch (extrema of the upper branch): an oscillatory phenomenon appears. Picture (a) shows the evolution of the lift coefficient over several periods while picture (b) zooms in on one period of oscillation. The unsteadiness observed highlights a large variation of lift coefficient: $1.54 < C_L < 1.06$ approximately that rapidly converges to a limit cycle. As a comparison, the two steady solutions at this particular angle of attack have values of $C_L = 1.29$ on the lower branch and $C_L = 1.54$ on the upper branch. This large amplitude lift coefficient variation occurs at a very low frequency: $f = 0.00217$. The associated Strouhal number based on the chord length weighted by the sine of the angle of attack is computed using equation (3.3):

$$\mathrm{St} = \frac{\omega \cdot c \cdot \sin(\alpha)}{2\pi \cdot U_\infty} \tag{3.3}$$

It is equal to $\mathrm{St} = 0.00429$. This value, two orders of magnitude lower than the usual vortex shedding frequency $\mathrm{St} = 0.2$, is similar to the Strouhal number of the low

frequency oscillations (LFO) presented in chapter 1. The alternation between high lift coefficient values and low lift coefficient values is also characteristic of LFO. The zoom over a period, presented in picture (b) of Figure (3.7), highlights the non-symmetry of the lift coefficient evolution during one oscillation. Considering an oscillation starting from a low lift coefficient value, an almost linear increase occurs in the first half, until the maximum lift coefficient value is reached. Afterwards, the lift coefficient slowly reduces before suddenly dropping just before the end of the period. Finally, it is worth noticing that this unsteadiness was found only for this particular angle of attack and only when the computation was initialized from the steady solution on the upper branch.

Figure (3.8) presents snapshots of the flow at different times over a period. Left pictures depict the ρu field on which the recirculation bubble is plotted in black line. The pictures in the middle shows the evolution of the lift coefficient as a function of the time over a period (corresponding to picture (b) of Figure (3.7)). The red dot indicates the instantaneous value of the lift coefficient at the corresponding time. The pictures on the right present the turbulent variable field, $\rho\tilde{\nu}$, on which, the instantaneous recirculation region is delimited with a black line. The period starts from a low lift solution (pictures (a) and (b)): the flow is massively separated on the suction side of the airfoil, which gives birth to a large recirculation bubble. A smaller bubble also exists at the trailing edge of the airfoil. Also, the value of $\rho\tilde{\nu}$ is very high in all the wake, which is wide in this case. This state is similar to the fully separated steady flows identified for high angles of attack (picture (k),(l), (m) and (n) of Figure (3.3)). Then, the lift coefficient evolves almost linearly ((c), (d), (e) and (f)) until it reaches a maximum value over the period (pictures (g) and (h)). In the meantime the separation point moves toward the trailing edge and the size of the recirculation bubble drastically decreases, as does the value of $\rho\tilde{\nu}$ and the thickness of the wake. In the second half of the period, the lift coefficient starts decreasing linearly (with a smaller slope than in the first half-period) (pictures (i) and (j)). At the end of the period, there is a sudden break of the slope and an abrupt drop of lift is observed (pictures (k) and (l)). This point seems to correspond to the appearance of the second smaller recirculation bubble at the trailing edge. This sudden decrease of the lift coefficient is associated with a drastic increase of the recirculation bubble size and by an increase of the turbulence eddy viscosity. Note that the smaller recirculation bubble appearing close to the trailing edge has a recirculation direction opposite to the main recirculation region.

Although low frequency oscillations have always been linked to laminar recirculation bubble at the leading edge, it seems that this fully turbulent unsteady RANS computation with the Spalart–Allmaras model captures LFO without the formation of a laminar separation bubble at the trailing edge. All the characteristics of the phenomenon are identified: low Strouhal number (St ≈ 0.02) compared to the Strouhal number of a bluff body vortex shedding, high amplitude oscillations and a switch between stalled and unstalled states. One shall note that for the angles of attack higher than stall angle tested, ($\alpha < 19°$) no vortex shedding was identified.

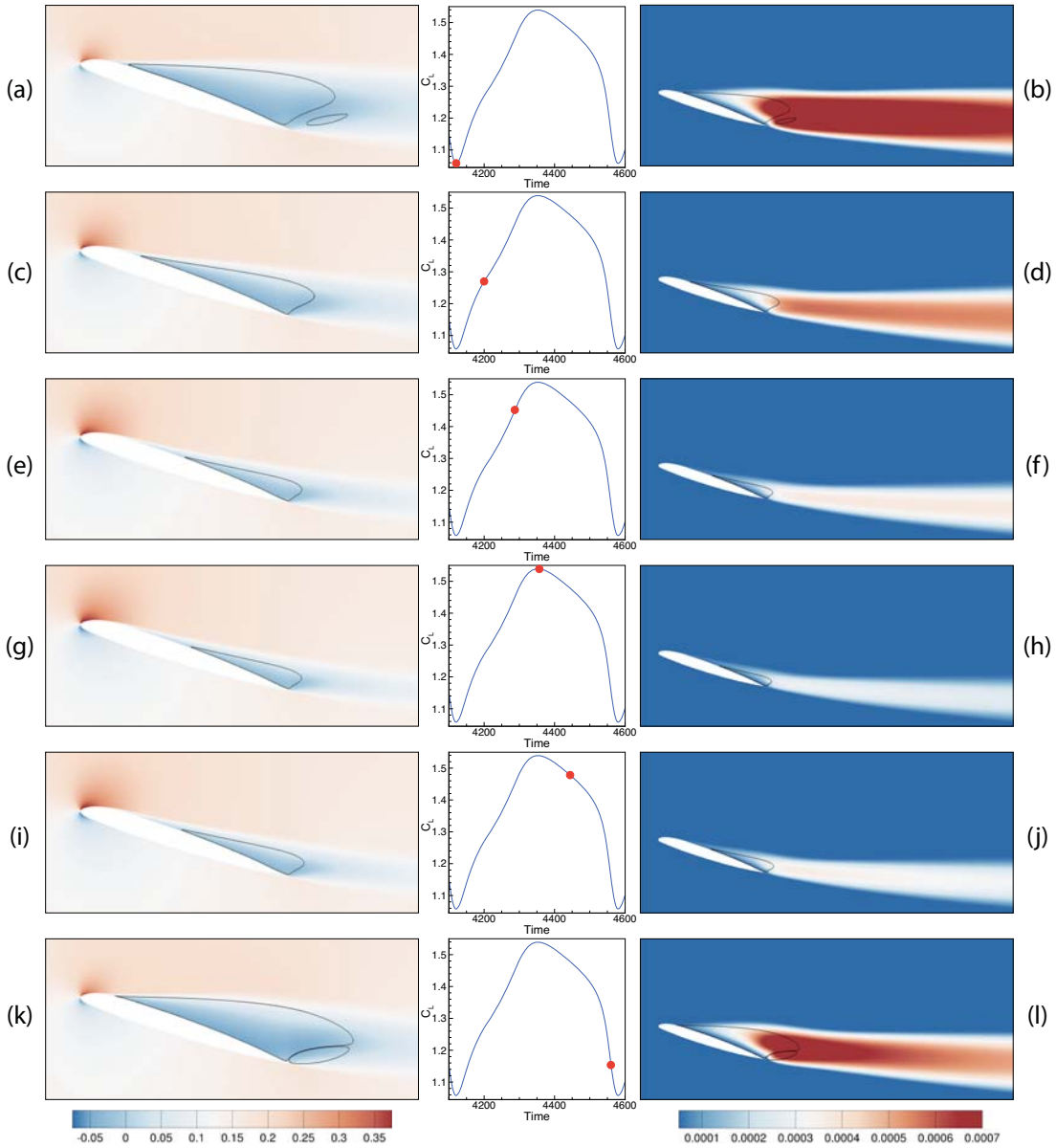

FIGURE 3.8: Flow visualisation over a period for six times t such as $t \in [0; T]$ and $\alpha = 18.41°$. Left : ρu field. Right : $\rho\tilde{\nu}$ field. Middle : evolution of the lift coefficient over a period. Red dot : position of the visualized flow on the polar curve.

3.4 Conclusion

The study of an OA209 airfoil in a retreating helicopter blade configuration (Re $= 1.8 \times 10^6$ and M $= 0.16$) with a RANS approach coupled with the Spalart–Allmaras model was carried out. The standard local time stepping method was used to compute steady solutions. The polar curve of these solutions shows a sudden drop of lift signifying stall. However, the limitations of this approach are also highlighted as the angle of attack is overestimated compared to the experiment and even compared to the two equations $k - \omega$ turbulence model. These observations are in agreement with the difficulties in predicting stall addressed for example by Ekaterinaris and Menter [48].

Moreover, careful computations performed close to stall reveal that several solutions can coexist for the same angle of attack in this area. This result was also observed with RANS computations performed with the $k-\omega$ turbulence model for the same airfoil in the same aerodynamic conditions by Richez *et al.* [133]. The extremely low convergence rate observed close to stall made this study quite long. Finally, unsteady RANS computations revealed the appearance of low frequency oscillations for one particular angle of attack.

Although the RANS approach, particularly with the use of the Spalart–Allmaras model, fails to predict stall qualitatively, one can observe that it successfully captures stall and associated phenomena widely described in the literature: hysteresis of steady solutions and LFO. This study intends to shed light on the appearance and coupling of these three phenomena. The first step of our work is based on the results presented by Wales *et al.* [166] that demonstrated on a NACA0012 that upper and lower branches can be linked revealing two saddle-node bifurcations located at the end of each branch. He also demonstrated that this middle branch, which links the two saddle-node bifurcations, cannot be computed with the standard methods introduced in chapter 2 and used in this chapter. Consequently, the next chapter introduces alternative methods that offer the possibility to compute a middle branch in our case and, also, allows us to compute faster solutions close to stall.

Chapter 4

Continuation methods for computing steady RANS solutions

Contents

In this chapter, continuation methods are introduced to compute steady solutions of the Reynolds Averaged Navier Stokes (RANS) equations when varying the angle of attack of the wing section. The naive continuation method is first introduced. It is based on the resolution of the nonlinear equations with the Newton's method, this iterative algorithm being initialized with a known solution obtained for another value of the angle of attack. Compared to the more classical local time-stepping approach, it drastically reduces the number of iterations and thus the computational time to achieve convergence. This is particularly true for angles of attack close to stall, where the local time-stepping method is very slow, as shown in chapter 3. Although this naive continuation method allows us to compute a branch of steady solutions in a limited computational time, it does not allow us to go through turning points in a branch of steady solutions. To bypass the saddle-node bifurcation occurring at the turning point, the pseudo-arclength method is then introduced, thus allowing to compute the branch of unstable solutions connecting the upper (high-lift) and lower (low-lift) branches of solutions identified in chapter 3.

The chapter is organized as follows. The theoretical framework for the two continuation methods is first introduced. The numerical implementation is then detailed, with a particular attention on the method used to compute the Jacobian matrix. Finally, the two continuation methods are validated at low angles of attack trying to find a solution for $\alpha = 12.20°$ from a solution at $\alpha = 12.00°$.

4.1 Principle of continuation methods

We are interested in solving the compressible Reynolds–Averaged Navier–Stokes equations (defined by (2.17) in chapter 2) with a turbulence model and appropriate boundary conditions. In the present case, the Spalart–Allmaras turbulence model, defined in (2.23), is chosen. The flow variable $\boldsymbol{q} = (\rho, \rho u, \rho v, \rho E, \rho\tilde{\nu})^T$ satisfies these governing equations, which, after spatial discretization with a finite volume method, can be formally written:

$$\frac{d\boldsymbol{q}(\alpha)}{dt} = \boldsymbol{R}(\boldsymbol{q}(\alpha), \alpha) \ , \tag{4.1}$$

where $\boldsymbol{R}$ is the discrete residual vector. At the i^{th} cell of the mesh, the discrete flow variable is $\boldsymbol{q}_i = (\rho, \rho u, \rho v, \rho E, \rho\tilde{\nu})_i^T$ and the residual is denoted $\boldsymbol{R}_i$. The latter includes the definition of the boundary conditions. So, if the i^{th} cells belongs to the inlet of the computational domain, the residual is modified so as to take into account the inflow boundary conditions such as defined by equation (3.1) in chapter 3. As a reminder, the velocity components are defined by:

$$u_i = U_\infty \cos(\alpha) \ , v_i = U_\infty \sin(\alpha) \tag{4.2}$$

This explains the explicit dependence of the residual on the angle of attack in (4.1). A steady solution of these equations, also called the base flow hereafter, satisfies :

$$\boldsymbol{R}(\boldsymbol{Q}(\alpha), \alpha) = 0 \tag{4.3}$$

The objective of any continuation method is to compute a branch of steady solutions $\boldsymbol{Q}(\alpha)$ for a varying parameter, such as the angle of attack, in a range of extreme values $\alpha_{min} \leq \alpha \leq \alpha_{max}$. The computation of an unknown solution $\boldsymbol{Q}(\alpha_1)$ at the angle of incidence α_1 relies on the knowledge of the solution $\boldsymbol{Q}(\alpha_0)$ at another angle of incidence α_0. Once it is determined, the solution $\boldsymbol{Q}(\alpha_2)$ can be obtained from $\boldsymbol{Q}(\alpha_1)$ and so on. This iterative process is generally divided in two steps. The **predictor step** computes a first guess $\hat{\boldsymbol{Q}}(\hat{\alpha})$ for an angle of incidence $\hat{\alpha}$ close to α_1. In the following, the symbol $\hat{}$ is used for guess solution. The **corrector step** aims at computing the solution $\boldsymbol{Q}(\alpha_1)$, starting from the predicted solution $\hat{\boldsymbol{Q}}(\hat{\alpha})$. Distinction between different continuation methods comes from the exact definition of the predictor and corrector steps. In the following, the predictor and corrector steps are detailed first for the *naive* continuation method, and then for the pseudo-arclength method.

4.1.1 Naive continuation method

A schematic view of this continuation method is proposed in Figure (4.1)(a). The flow solution $\boldsymbol{Q}$ being a multi-dimensional variable, we use the lift coefficient C_L (defined in appendix A) to represent its evolution as a function of the angle of incidence. The branch of steady solutions is depicted with the solid curve, while the crosses on that curve are the solutions that we are interested to compute for discrete values of the angles of attack.

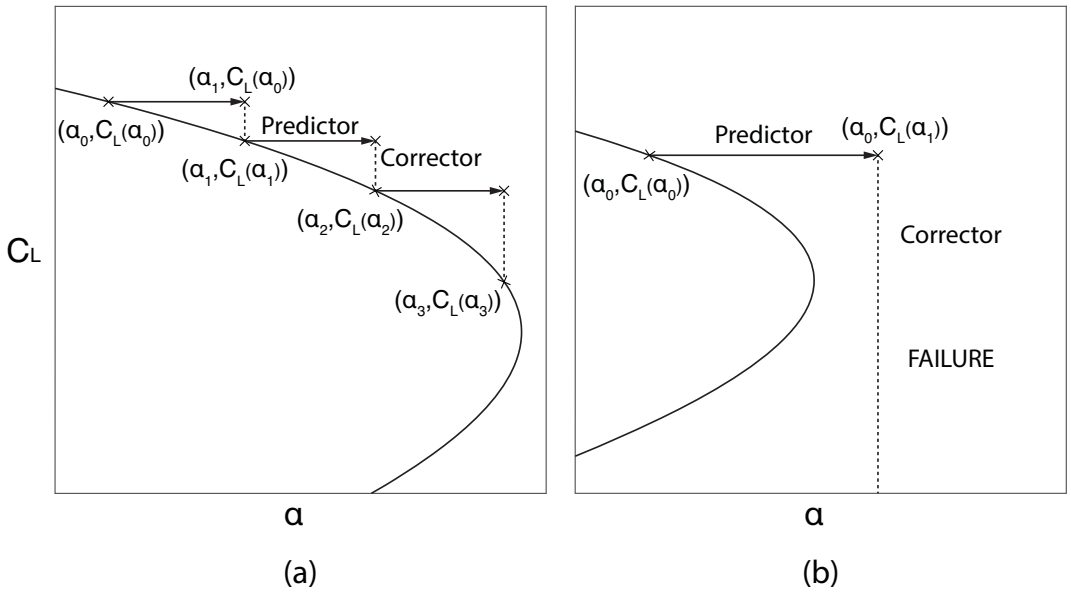

FIGURE 4.1: (a) Schematic view of the naive continuation method, where the lift coefficient C_L is used to represent the flow solution $\boldsymbol{Q}$, as a function of the angle of attack α. Starting from a known steady solution $\boldsymbol{Q}_0$ at α_0, computation of steady solutions on the branch are continued in a two-steps process. (1) Predictor step (solid arrows) and (2) Corrector step (dashed lines). (b) Example of the naive continuation method failing to bypass a turning point.

At each step j of the naive continuation method, the angle of incidence is a fixed parameter. To compute the solution at a fixed α_j, the solution already computed at α_{j-1} is used as a guess value. The **predictor step** is thus rather trivial and is written $\hat{\alpha} = \alpha_{j-1}$ and $\boldsymbol{Q}(\hat{\alpha}) = \boldsymbol{Q}(\alpha_{j-1})$.

Obviously, this guess solution does not satisfy the governing equation (4.3). The **corrector step** allows us to compute that solution from the guess value, as depicted in Figure (4.1)(a). The Newton's method, also known as the Newton–Raphson method, is here used. It was first proposed by Isaac Newton [117] and simplified by Joseph Raphson [131]. Since then, a lot of scientists have studied and improved this approach meant to find the roots of a function. As a consequence, this method is nowadays very common and described in many books and papers (see for instance Kelley [87]).

In the remainder of the subsection, in order to simplify the notations, $\boldsymbol{Q}_j$ will refer to $\boldsymbol{Q}(\alpha_j)$. At the j^{th} iteration of the continuation method, the solution $\boldsymbol{Q}_{j+1}^{k+1}$ for the $(k+1)^{th}$ iteration of the Newton algorithm is decomposed as:

$$\boldsymbol{Q}_{j+1}^{k+1} = \boldsymbol{Q}_{j+1}^{k} + \delta\boldsymbol{Q}. \tag{4.4}$$

Injecting this solution into (4.3) and linearizing gives that the variation $\delta\boldsymbol{Q}$ is solution of the following linear system:

$$\boldsymbol{J}(\boldsymbol{Q}_{j+1}^{k}, \alpha_{j+1})\delta\boldsymbol{Q} = \boldsymbol{R}(\boldsymbol{Q}_{j+1}^{k}, \alpha_{j+1}) \tag{4.5}$$

Where $\boldsymbol{J}(\boldsymbol{Q}_{j+1}^{k}, \alpha_{j+1})$ is the Jacobian of the nonlinear residual $\boldsymbol{R}$ defined as :

$$\boldsymbol{J}(\boldsymbol{Q}_{j+1}^{k}, \alpha_{j+1}) = \left.\frac{\partial \boldsymbol{R}}{\partial \boldsymbol{Q}}\right|_{(\boldsymbol{Q}_{j+1}^{k}, \alpha_{j+1})} \tag{4.6}$$

For the first Newton's iteration ($k = 0$), the initial solution is chosen as the guess value, i.e. $\boldsymbol{Q}_{j+1}^{0} = \boldsymbol{Q}(\alpha_j)$. The solution is said to be converged when:

$$\boldsymbol{R}(\boldsymbol{Q}_{j+1}^{k}, \alpha_{j+1})^T \boldsymbol{R}(\boldsymbol{Q}_{j+1}^{k}, \alpha_{j+1}) < \epsilon \ , \tag{4.7}$$

Where ϵ is a small user-defined parameter. The convergence of the Newton method is quadratic when the guess solution is close to the desired solution, but it may diverge otherwise.

In term of computational cost, the most expensive part of this algorithm is the resolution of the linear system (4.5). More specifically, at each step of the Newton method, the Jacobian matrix is first assembled and then LU factorized, so as to eventually solve the linear system by successive lower and upper triangular resolution. A slightly modified version of this Newton's method, usually named quasi-Newton's method (see [87]), has been implemented to improve the computational time efficiency. Instead of re-assembling the Jacobian matrix at every steps, the Jacobian matrix $\mathcal{J}(\boldsymbol{q}_{j+1}^{k}, \alpha_{j+1})$ computed at step k may be reused at steps $l \leq k$. This deteriorates the convergence speed of the Newton's method but improve the computational-time efficiency of the linear system. The overall computational and storage cost is thus drastically reduced. The exact procedure is explained more in details in subsection 4.2.2.

A specific case where the naive continuation method fails to converge towards a solution is depicted in Figure (4.1)(b). Close to a turning point of the steady branch, the Newton's method used in the corrector step fails to converge towards a steady solution. Indeed, for values over the angle of attack beyond the turning point, there exist no steady solutions in the vicinity of the guess solution at a fixed angle of incidence. To bypass such turning points, the angle of attack should be varied during the corrector step, as in the pseudo-arclength method that is introduced in the next paragraph.

4.1.2 Pseudo-arclength method

Instead of considering the angle of attack to parametrize the branch of steady solutions, the arclength s of this curve is introduced to parametrize these solutions and the angle of attack, that now both depend on the arclength as $(\boldsymbol{Q}(s), \alpha(s))$. The governing equations are thus rewritten:

$$\boldsymbol{R}(\boldsymbol{Q}(s), \alpha(s)) = 0 \tag{4.8}$$
$$N(\boldsymbol{Q}(s), \alpha(s), s) = 0 \tag{4.9}$$

Where the second (scalar) equation is introduced to account for the supplementary unknown $\alpha(s)$. The continuation of the branch beyond a turning point is illustrated in Figure (4.2)(a). At the $(j+1)^{th}$ iteration of the continuation method, we look for a solution $(\boldsymbol{Q}(s_{j+1}), \alpha(s_{j+1}))$ that satisfies the above equations. In the **predictor step** of the algorithm, a guess solution, denoted $(\hat{\boldsymbol{Q}}(s_{j+1}), \hat{\alpha}(s_{j+1}))$, is searched in the direction tangent to the branch of steady solutions at the previous values of the arc length s_j as illustrated in Figure (4.2)(b). Assuming that the tangent vector $\boldsymbol{t}_j = (\boldsymbol{t}_j^Q, t_j^\alpha)^T$ is known, the guess solution is thus given by:

$$\hat{\boldsymbol{Q}}(s_{j+1}) = \boldsymbol{Q}(s_j) + \Delta s\, \boldsymbol{t}_j^Q \tag{4.10}$$
$$\hat{\alpha}(s_{j+1}) = \alpha(s_j) + \Delta s\, t_j^\alpha \tag{4.11}$$

Where Δs is the pseudo-arclength step. Note that this scalar is an approximation of the arc-length between $(\boldsymbol{Q}(s_j), \alpha(s_j))$ and $(\boldsymbol{Q}(s_{j+1}), \alpha(s_{j+1}))$, hence the name of the *pseudo-arclength* method as illustrated in Figure (4.2)(b).

Several strategies, for instance discussed in the book of Govaerts [63], exist to compute the solutions in the **corrector step** of the algorithm. They depend on the additional constraint N (4.9) introduced to solve the steady solution in (4.8). The Keller's method [86] used in the present work, is illustrated in Figure (4.2)(b). The solution $(\boldsymbol{Q}(s_{j+1}), \alpha(s_{j+1}))$ is looked for in the hyperplane perpendicular to the tangent direction $\boldsymbol{t}_j$ at point $(\hat{\boldsymbol{Q}}(s_{j+1}), \hat{\alpha}(s_{j+1}))$. The Newton's method is then used to find the solution of this augmented system composed of equations (4.8) and (4.9).

Details on the computation of the tangent vectors used in the predictor step, and the resolution of the nonlinear system in the corrector step are given in the two next subsections.

4.1.2.1 Tangent vector and predictor step

The coordinates of the tangent vector $\boldsymbol{t}_j = (\boldsymbol{t}_j^Q, t_j^\alpha)^T$ at the point $(\boldsymbol{Q}(s_j), \alpha(s_j))$ of the branch are obtained by differentiating the equation (4.8) with respect to the curvilinear abscissa s, yielding:

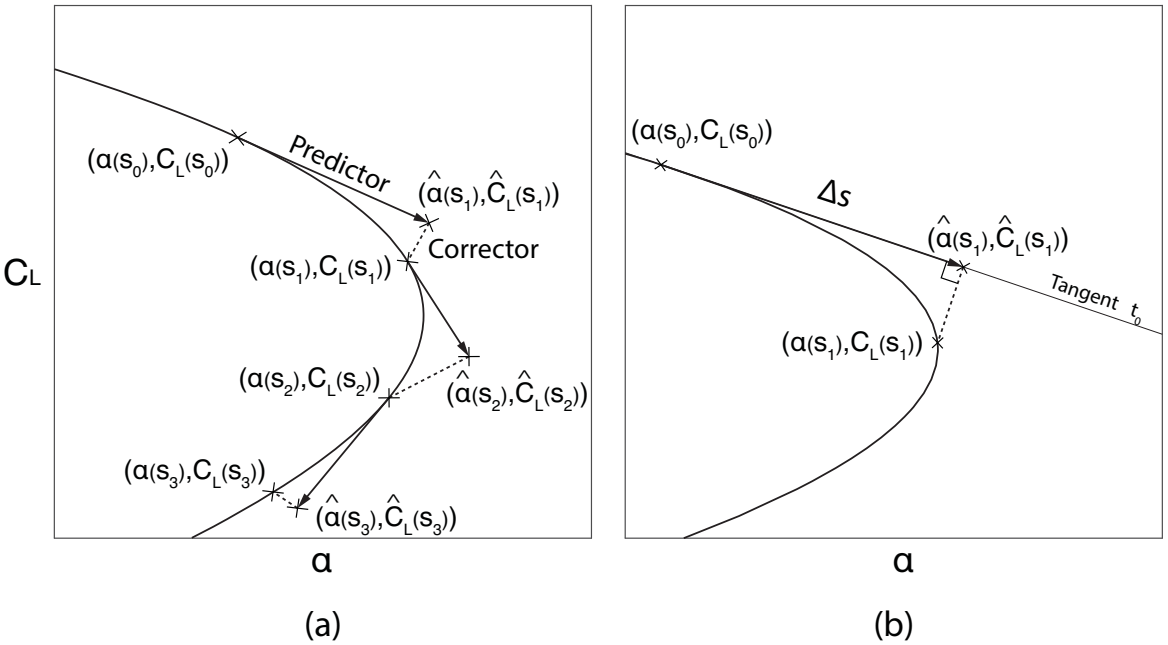

FIGURE 4.2: (*a*) Schematic view of the pseudo-arclength method, where the lift coefficient C_L is used to represent the flow solution $\boldsymbol{Q}$, as a function of the angle of attack α. Starting from a known steady solution $\boldsymbol{Q}(s_0)$ at $\alpha_0(s_0)$, computation of steady solutions on the branch are continued in a two-steps process. (1) Predictor step (solid arrows) and (2) Corrector step (dashed lines). (*b*) Schematic view of the pseudo-arclength method focusing on one iteration: visualisation of the tangent $\boldsymbol{t}_0$, approximation of the arc-length ΔS along the tangent and search of a solution perpendicular to the tangent during the corrector step.

$$\boldsymbol{J}(\boldsymbol{Q}_j, \alpha_j)\, \frac{\partial \boldsymbol{Q}}{\partial s}\bigg|_{s_j} + \boldsymbol{v}(\boldsymbol{Q}_j, \alpha_j) \frac{d\alpha_j}{ds} \;=\; \boldsymbol{0} \tag{4.12}$$

Where $\boldsymbol{Q}_j$ and α_j refers to respectively $\boldsymbol{Q}(s_j)$ and $\alpha(s_j)$ in order to simplify the notation and where the vector $\boldsymbol{v}(\boldsymbol{Q}_j, \alpha_j)$ is defined as:

$$\boldsymbol{v}(\boldsymbol{Q}_j, \alpha_j) = \frac{\partial \boldsymbol{R}}{\partial \alpha}\bigg|_{s_j}. \tag{4.13}$$

In the present case, this is the linearization of the boundary condition (4.2) at the inlet of the computational domain. After identifying the coordinates of the tangent vector in the above equation, we obtain:

$$\mathcal{J}(\boldsymbol{Q}_j, \alpha_j)\, \boldsymbol{t}_j^Q + t_j^\alpha\, \boldsymbol{v}(\boldsymbol{Q}_j, \alpha_j) \;=\; \boldsymbol{0} \tag{4.14}$$

The two coordinates of the tangent vector cannot be determined from this single

equation. To close up the system, the folllwing normalization of this tangent vector with respect to the Euclidean norm is imposed [86] [40]:

$$(t_j^\alpha)^2 + (\boldsymbol{t}_j^Q)^T \boldsymbol{t}_j^Q = 1 \tag{4.15}$$

This choice for the normalization of the tangent vector ensures that Δs remains an approximation of the arc-length. The computation of the tangent coordinates is obtained by solving equations (4.14) and (4.15). To that aim, we first introduce the vector $\boldsymbol{w}_j$, solution of:

$$\mathcal{J}(\boldsymbol{Q}_j, \alpha_j)\, \boldsymbol{w}_j = -\boldsymbol{v}(\boldsymbol{Q}_j, \alpha_j)\,. \tag{4.16}$$

Note that the components of the tangent vector are related by this vector as $\boldsymbol{t}_j^Q = t_j^\alpha \boldsymbol{w}_j$. Introducing that relation into (4.15), one obtains:

$$(t_j^\alpha)^2 \left(1 + \boldsymbol{w}_j^T \boldsymbol{w}_j\right) = 1 \tag{4.17}$$

The tangent vector is thus defined as:

$$t_j^\alpha = h_j \frac{1}{\sqrt{1 + \boldsymbol{w}_j^T \boldsymbol{w}_j}} \quad , \quad \boldsymbol{t}_j^Q = t_j^\alpha \boldsymbol{w}_j \tag{4.18}$$

Where the parameter $h_j = \pm 1$ is used to specify the orientation of the tangent vector at the j^{th} iteration. To ensure that the solution at iteration $j+1$ is searched in the correct direction, it is required to preserve the orientation of the tangent vector from iteration $j-1$ to iteration j of the continuation method, which is done by further imposing that:

$$t_{j-1}^\alpha t_j^\alpha + (\boldsymbol{t}_{j-1}^Q)^T (\boldsymbol{t}_j^Q) > 0 \tag{4.19}$$

Inserting the definitions (4.18) into the above inequality yields:

$$h_j (t_{j-1}^\alpha + (\boldsymbol{t}_{j-1}^Q)^T \boldsymbol{w}_j) > 0 \tag{4.20}$$

The choice of h is particularly important when by passing the turning point where the orientation of the tangent changes. If not set correctly, it might end up being trapped in the iterations and indefinitely compute solutions j (before the saddle-node) and $j+1$ (after the saddle-node) alternatively.

Once the tangent vector is properly defined, the guess solution given by the predictor step is finally:

$$\hat{\boldsymbol{Q}}(s_{j+1}) = \boldsymbol{Q}(s_j) + \Delta s\, t_j^{\alpha}\, \boldsymbol{w}_j \tag{4.21}$$
$$\hat{\alpha}(s_{j+1}) = \alpha(s_j) + \Delta s\, t_j^{\alpha} \tag{4.22}$$

Where the scalar t_j^{α} is defined by (4.18) and $\boldsymbol{w}_j$ is solution of (4.16).

4.1.2.2 Corrector step

In the Keller's method, the additional equation (4.9), introduced to ensure that the number of equations is equal to the number of unknown, should reflect that the solution is sought in the hyperplane perpendicular to the tangent vector $\boldsymbol{t}_j$ at point $(\hat{\boldsymbol{Q}}_j, \hat{\alpha}_j)$. The orthogonality relation is written :

$$\mathcal{N}(\boldsymbol{Q}_{j+1}, \alpha_{j+1}, s_{j+1}) = (\boldsymbol{t}_j^{Q})^T(\boldsymbol{Q}_{j+1} - \hat{\boldsymbol{Q}}(s_{j+1})) + t_j^{\alpha}(\alpha_{j+1} - \hat{\alpha}(s_{j+1})) = 0 \tag{4.23}$$

The corrector step then consists in solving the system of equations (4.8) and (4.9) with the additional equation given by (4.23). Applying the Newton's method to this system of nonlinear equations, the flow solution and angle of attack are decomposed as:

$$\boldsymbol{Q}_{j+1}^{k+1} = \boldsymbol{Q}_{j+1}^{k} + \boldsymbol{\delta Q} \tag{4.24}$$
$$\alpha_{j+1}^{k+1} = \alpha_{j+1}^{k} + \delta\alpha \tag{4.25}$$

Where the variations of the flow solution $\boldsymbol{\delta Q}$ and angle of attack $\delta\alpha$ are solutions of :

$$\begin{pmatrix} \boldsymbol{J}(\boldsymbol{Q}_{j+1}^{k}, \alpha_{j+1}^{k}) & \boldsymbol{v}(\boldsymbol{Q}_{j+1}^{k}, \alpha_{j+1}^{k}) \\ (\boldsymbol{t}_j^{Q})^T & t_j^{\alpha} \end{pmatrix} \begin{pmatrix} \boldsymbol{\delta Q} \\ \delta\alpha \end{pmatrix} = - \begin{pmatrix} \boldsymbol{R}(\boldsymbol{Q}_{j+1}^{k}, \hat{\alpha}_{j+1}^{k}) \\ \\ N(\boldsymbol{Q}_{j+1}^{k}, \alpha_{j+1}^{k}, s_{j+1}) \end{pmatrix} \tag{4.26}$$

Note that, in the left-hand side operator, the tangent vector $\boldsymbol{t}_j$ is independent of the Newton's iteration k. Only the derivative operators (i.e. the Jacobian matrix $\boldsymbol{J}(\boldsymbol{Q}_{j+1}^{k}, \alpha_{j+1}^{k})$ and the vector $\boldsymbol{v}(\boldsymbol{Q}_{j+1}^{k}, \alpha_{j+1}^{k})$) depend on the Newton's iteration k. There exists alternative strategy where the tangent vector is updated in course of the Newton algorithm (see for instance [63]). Finally, this iterative algorithm is initialized with the guess solution given by the predictor step, i.e.:

$$\hat{\boldsymbol{Q}}_{j+1}^{0} = \hat{\boldsymbol{Q}}(s_{j+1}) \quad , \quad \alpha_{j+1}^{0} = \hat{\alpha}(s_{j+1}) \tag{4.27}$$

The algorithm is converged at the k^{th} iteration if the residual satisfies:

$$\boldsymbol{R}^T(\boldsymbol{Q}^k_{j+1}, \alpha^k_{j+1})\boldsymbol{R}(\boldsymbol{Q}^k_{j+1}, \alpha^k_{j+1}) < \epsilon \tag{4.28}$$

$N(\boldsymbol{Q}^k_{j+1}, \alpha^k_{j+1}, s_{j+1})$ being equal to 0 as explicited in equation (4.23).

4.2 Numerical aspects

Once the formalism of the two continuation methods used is defined, a few numerical aspects of the numerical resolution are discussed.

4.2.1 Derivative operators

The main challenge of continuation methods is the computation of the derivative operators (i.e the Jacobian matrix $\mathcal{J}$ and the vector $\mathcal{V}$) appearing during the linearization of the governing equations. Several approaches can be considered and the first step is to chose the linearization method : it can either be *continuous* or *discrete*. In the continuous method, the considered equations are first linearized and then discretized whereas in the discrete method the equations are first discretized and then linearized. Drawbacks and advantages of these two methods are extensively discussed by Peter [77]. Unexhaustively, it can be said that the discrete method is conceptually simpler as the derivative operators can be built from the discrete residual of the equations whereas the continuous framework requires to derivate complicated equations (particularly in the RANS framework). However, the continuous approach has, most of the time, less memory requirements and is easier to implement. In both methods, an analytical computation of the derivative operators is possible but complex. Indeed, in the particular case of the RANS approach, the turbulent equations and boundary conditions involved might be complex to linearize. Moreover, such an approach implies a new formulation for each turbulence model, boundary condition or spatial scheme variation and is consequently not adapted to comparisons. The computation of the derivative operators by finite difference is an interesting alternative to the analytical approach. It consists in approximating the derivatives using differential quotients as described in equations (4.29) and (4.30) that respectively present the evaluation of a component of the Jacobian with a forward finite difference and a central finite difference.

$$\left.\frac{\partial \mathcal{R}_i}{\partial \boldsymbol{Q}_j}\right|_{(\overline{\boldsymbol{Q}},\overline{\alpha})} = \frac{\boldsymbol{R}_i(\overline{\boldsymbol{Q}} + \delta Q_j \boldsymbol{Q}^j, \overline{\alpha}) - \boldsymbol{R}_i(\overline{\boldsymbol{Q}}, \overline{\alpha})}{\delta Q_j} \tag{4.29}$$

$$\left.\frac{\partial \mathcal{R}_i}{\partial \boldsymbol{Q}_j}\right|_{(\overline{\boldsymbol{Q}},\overline{\alpha})} = \frac{\boldsymbol{R}_i(\overline{\boldsymbol{Q}} + \delta Q_j \boldsymbol{Q}^j, \overline{\alpha}) - \boldsymbol{R}_i(\overline{\boldsymbol{Q}} - \delta Q_j \boldsymbol{Q}^j, \overline{\alpha})}{2\delta Q_j} \tag{4.30}$$

In these equations, $(\overline{\boldsymbol{Q}}, \overline{\alpha})$ is the point at which the derivative is evaluated, $\boldsymbol{R}$ is the discrete residual of the system of equations $\mathcal{R}$, δQ_j is a small perturbation of the j^{th} component of $\overline{\boldsymbol{Q}}$ and $\boldsymbol{Q}^j$ is a vector for which the j^{th} component of the vector is equal to one and null everywhere else. This method offers many advantages. First, with such a formulation, the derivative operators can be expressed with the residuals

of the solver, which is a classic output available in all of them. By doing so, all the complexity of the equations (turbulence model, boundary conditions, spatial schemes, ...) is not directly treated but taken into account in the residual. Second, the derivative operators can be computed without interfering with the solver, just using it as a black box and post-processing the residuals in output with an independent tool. Third, once the tool computing the derivative operators has been built, changing a boundary condition, the turbulence model or a numerical scheme do not require any additional implementation that makes this method very convenient for testing multiple turbulence models. However, the main drawback remains that the derivative operators obtained with this method are not exact. Indeed, the method in itself is an *approximation* of the derivatives, consequently, some errors will necessarily be introduced during the computation. The final error is very sensitive to the choice of the small perturbation imposed (δq^j in the example presented in equations (4.29) and (4.30)). This perturbation must be small enough to ensure the validity of the method (neglecting high order terms in the Taylor expansion) but not too small to avoid rounding errors. In its study on Jacobian-free Newton-Krylov methods, Knoll describes this choice *as much of an art as a science* [88]. Following the recommendations of Knoll, Mettot [108] and Beneddine [14] suggested that δq_j should be chosen such as : $\delta q_j = \epsilon_m(|q_j| + 1)$ with q_j the local value of the j^{th} variable. The value of ϵ_m is chosen with respect to the machine precision. H-B. An [4] showed that to minimize this error, one should set $\epsilon_m \approx 10^{-8}$ for a forward finite difference and $\epsilon_m \approx 5 \times 10^{-6}$ for a central finite difference.

In our case, the solver used is the finite volume compressible code *elsA* [27]. A tool that perturbates the flow, collects the residuals and performs the finite difference was created at ONERA by C. Mettot and S. Beneddine (former PhD students). C. Mettot initiated the work and validated it on a deep-cavity case [108]. S. Beneddine improved the tool adding, among others, an automatization of the procedures regarding configurations and parallelization of the perturbation [14]. More details on the perturbation strategy (stencil, parallelization, additional rules on the choice of δq_j, ...) are provided in the previously mentioned references.

4.2.2 Continuation methods

Once the derivative operators are computed, all the difficulty remaining is to solve a system of the shape $A \cdot x = b$ at each iteration of the corrector step. The resolution of this system is performed using PETSc [1] in combination with the direct LU solver MUMPS (MUltifrontal Massively Parallel sparse direct Solver) [120]. The computation and LU decomposition of the matrix are the most time consuming steps of the process. To limit the time of the continuation methods, an alternative approach, based on the quasi-Newton's method concept described in subsection 4.1.1, is considered. The matrices are not computed and LU decomposed at each iteration but every m iterations. m is determined by the convergence rate: the Jacobian is recomputed and LU decomposed when the convergence rate becomes too small. It leads to a drastically reduced computational time even if the number of iterations increased due to the non optimal descent at each iteration.

The convergence of these methods is very sensitive to the initial guess. Practically speaking, the parameter step between two solutions ($\Delta\alpha = \alpha_1 - \alpha_0$ in the method and $\Delta s = s_1 - s_0$ in the pseudo-arclength method) must be carefully chosen. The topology of the solution $\boldsymbol{Q}_0$ must be close to the topology of the searched solution $\boldsymbol{Q}_1$. As an indication, on parts of the polar curve where the flow topology does not change very fast as the angle of attack varies (far away from stall), the steps of the naive continuation method can be chosen $\Delta\alpha = 0.2°$. However, close to stall angle, these steps must be reduced, as a small variation of α implies a larger variation of flow topology. Figure (4.1)(b) summarizes why the naive continuation method fails to bypass a saddle-node bifurcation. However, based on this same figure and assuming a scenario similar to the one described in chapter 3 (with an upper and a lower branches overlapping), one could imagine that the naive continuation method could converge to a lower solution (not represented on the picture). It is actually impossible, as the topology of the initial solution $\boldsymbol{Q}_0$ on the upper branch is too different from the expected solution $\boldsymbol{Q}_1$ on the lower branch. The pseudo-arclength method offers the possibility of bigger steps on the linear parts. Indeed, the tangent predictor is known to offer a better convergence than the trivial predictor. More visually, the initial guess $\hat{\boldsymbol{Q}}_1$ will be evaluated with the tangent and consequently will be closer to the sought solution. However, the stall area still remains critical, and particularly the saddle-node bifurcations around which the direction of the tangent drastically changes for small variations of angle of attack.

In practice, the naive continuation method is to be used as much as possible. Indeed, in the pseudo arclengh method, by adding one line and on column to the Jacobian matrix, the sparsity of the matrix is deteriorated. It leads to either memory issues or an increased allocation time when using PETSc. Consequently, except when it is absolutely required, the naive continuation method is to be preferred.

A simplified view of the different steps of the two continuation methods is presented in Appendix B. Figures (B.1) to (B.3) show three schemas that include the different tools and software used, the interfaces between them and the data exchanged.

4.3 Validation and comparison with local time stepping solutions

The objective is here to validate the implementation of the continuation methods. To do so, time marching computations with local time stepping approach are compared with the results obtained with the continuation methods. Theoretically, the different methods should give the same solution. However, it is demonstrated that some differences appear due to the implementation of the turbulence model in the solver *elsA*.

4.3.1 Naive continuation method

First, the method is applied at an angle of attack $\alpha = 12.00°$ and initialized with a solution converged for the same angle of attack with a local time stepping approach. The convergence of the conservative variable ρ and the turbulent variable is depicted

in Figure (4.3) presenting the evolution of the explicit residual. The other conservative variables follow the same convergence rate as the variable ρ and are not depicted on the picture. Each dot corresponds to a resolution of the system (4.5). The Jacobian matrix is not computed and factorized at each iteration to reduce the computational time. However, it is computed every ten iterations (diamonds in Figure (4.3)) in order to accelerate the convergence as explained in section 4.2.2. Indeed, one can observe an exponential decrease of the convergence speed after each computation of the Jacobian.

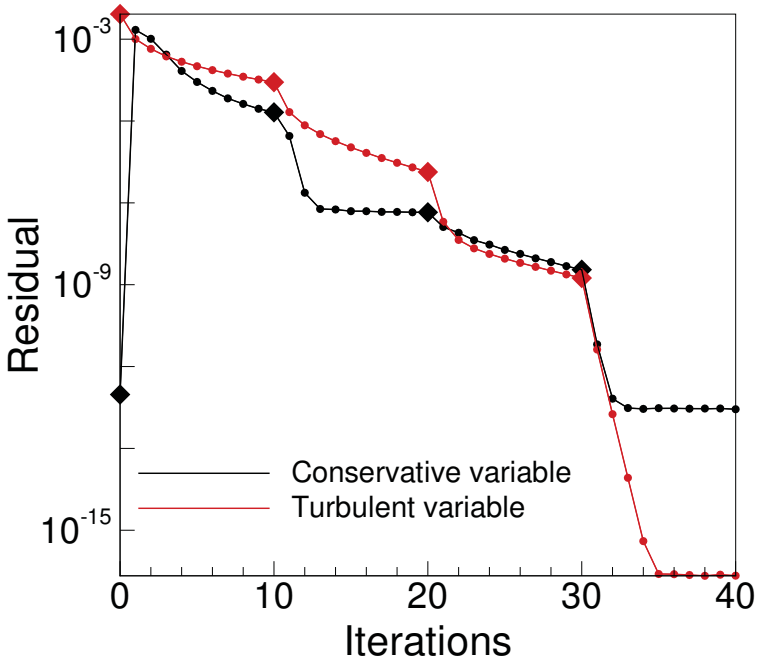

FIGURE 4.3: Evolution of the explicit residual for the conservative variable ρ and the turbulent variable $\tilde{\nu}$ for $\alpha = 12°$ initialized with a solution from a local time stepping computation (with naive continuation method).

The residual of the conservative variable drastically increases at the first iteration and then slowly decreases to more or less the same level of convergence as originally whereas the residual of the turbulent variable directly decreases to values several order of magnitude lower than the original one. One can observe that the original value of the residual of the turbulent variable, which corresponds to the solution computed with the local time stepping approach, is quite high. This high value is due to the implementation of several cutoffs in the Spalart–Allmaras turbulent model equations in *elsA* that are included to ensure the numerical convergence. These cutoffs are applied to the final value of the turbulent viscosity and to intermediate quantities computed in the process of determining the final value of the turbulent variable, such as the production term. However, these cutoffs never appear in the turbulence model equation from which the explicit residual is evaluated. This implies that the solver tries to converge to an exact solution of the equation without cutoffs but, at each step, the cutoffs (if triggered)

prevent the solver to reach this exact solution by directly modifying the quantities computed. This is the reason why the explicit residual remains high. Nevertheless, the original solution, obtained with a local time stepping approach was considered converged based on the implicit residual[1]. Indeed, in *elsA* user guides, it is recommended to consider an explicit residual for conservative variables and an implicit residual for turbulent variables to evaluate the convergence of RANS computations (more details are provided in section 2.2.4 of chapter 2 about the differences between the two types of residuals). On the other hand, continuation methods use the explicit residual of the equations to converge to a solution. The intermediate quantities of the turbulence model are never computed and no cutoffs are applied to it, neither to the final value of $\rho\tilde{\nu}$. Consequently, in the end, continuation methods converge to an exact solution of the turbulent equation such as formulated in the solver. These differences between the local time stepping approach and the continuation methods approach explain the evolution of the residual curve depicted in Figure (4.3). The original values of the residual, corresponding to the local time stepping solution, was just explained. Then, at the first iteration, the turbulent variable is more converged from a mathematical point of view and the equilibrium state found with the cutoffs applied on the turbulent variable is broken. That explains the sudden peak of residual for all the conservative variables. Then, all the variables converge to the exact solutions of the equations implemented in the solver and reaches explicit residual values of 10^{-12} for the turbulent variables and 10^{-17} for the turbulent variable. To evaluate the difference between the solutions, the local relative error between the solutions obtained with the local time stepping approach and the naive continuation method is depicted in the left picture of Figure (4.4). One can observe that the main difference appears on the turbulent variable, on the wake with an error that reaches approximately 15%. The error on the two other conservative variables investigated (the density ρ and the streamwise speed ρu) is also located in the wake but is less high : 0.15% for the first one and 3% for the second one. It seems normal to observe the maximum error on the turbulent variable as this is the one directly affected by the cutoffs.

In order to validate the theory whereby differences between the solutions are due to cutoffs, one more local time stepping computation is performed at $\alpha = 12.00°$. The difference with the original time stepping computation is that the cutoff on the turbulent viscosity is removed. An ideal case would have been to also remove the cutoffs on the intermediate quantities computed during the resolution of the turbulent equation. However, it would require a direct modification of the solver code as there is no user parameter provided to control those cutoffs, contrary to the cutoff on the turbulent variable. In the end, removing the main cutoff on the turbulent viscosity should improve the convergence of the explicit residual of the turbulent variable although not being the perfect comparison configuration. Two cases are investigated and compared with the naive continuation method approach :

- Case 1 (reference case, described in chapter 3): local time stepping computation performed with all the internal cutoffs active and with a cutoff on the minimum value of $\rho\tilde{\nu}$.

[1]The implicit residual evaluates the differences of solutions between the step n and the step $n-1$: the computation is considered converged from an implicit point of view when the solution stops evolving.

- Case 2 (validation case to identify the influence of one cutoff on the solution): local time stepping computation performed with all the internal cutoffs active but without cutoff on the minimum value of $\rho\tilde{\nu}$.

The solution obtained in the second case exhibits an explicit residual for the turbulent equation of approximately $\sim 10^{-6}$ whereas it was $\sim 10^{-2}$ for the case 1. The local relative error between the solution obtained in case 1 and the solution obtained with the naive continuation method is presented in Figures (4.4)(a), (b) and (c), next to the error between the solution obtained in case 2 and the solution obtained with the naive continuation method in Figures (4.4)(d), (e) and (f). The tendency is very similar : the maximum error is obtained for the turbulent variable $\rho\tilde{\nu}$ (c) and (f). However, one can observe that, as expected, the error is smaller when comparing the solution obtained with the naive continuation method to the solution obtained in case 2 ((d), (e) and (f)) than comparing it to the solution obtained case 1 ((a), (b) and (c)) : a diminution from approximately 15% for case 1 (c) to approximately 6% for case 2 (f). This reduction of the error of almost 10% on the turbulent variable tends to prove that removing cutoffs provide solutions closer to the ones obtained with the naive continuation method. Moreover, it implies that the difference of solutions between the two approaches is due to the presence of several cutoffs applied during the local time stepping computation that cannot be set in the naive continuation method. However, the error in the second case is still not null as some cutoffs remain active. In the end, from a pure mathematical point of view, the naive continuation method provides a better resolution of the turbulent equation as the explicit residual is extremely lower while from a numerical and physical point of view, removing some recommended cutoffs might raise some questions as discussed in appendix C.

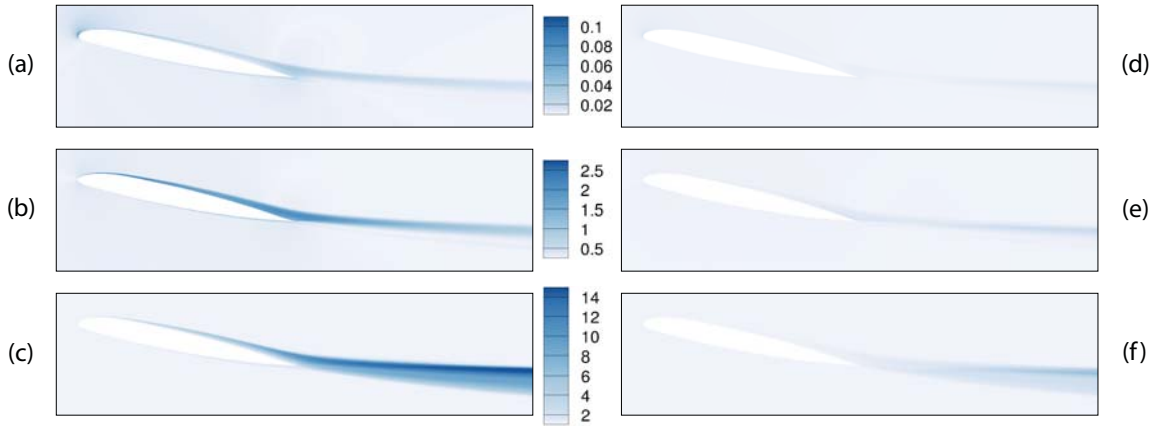

FIGURE 4.4: Local relative error in % between the solution obtained with the naive continuation method and solutions obtained with local time stepping approach ($\alpha = 12.00°$) for three variables ρ (a) and (d), ρu (b) and (e) and $\tilde{\nu}$ (c) and (f). (a), (b) and (c) : with cutoffs on the turbulent variable. (d), (e) and (f) : without cutoffs on the turbulent variable.

The second step of validation of the naive continuation method is to compute a solution for an angle of incidence slightly higher ($\alpha = 12.20°$) from the solution at

$\alpha = 12.00°$. The evolution of the explicit residual of the conservative variable ρ and the turbulent variable $\tilde{\nu}$ is depicted in Figure (4.5). Once again, each dot corresponds to a resolution of the system (4.5) and, although not essential, the Jacobian matrix is computed and factorized every five iterations to accelerate the convergence (diamond symbols on the curves).

Finally, when computing a steady solution with the naive continuation method from a solution obtained with a local time stepping approach at the same angle of attack, a diminution of the residual of 14 orders of magnitude is observed on all the variables. The residuals reach levels of 10^{-12} for the conservative variables and 10^{-17} for the turbulent variable. When computing a steady solution with the naive continuation method from a solution obtained with the naive continuation method at a different angle of attack, a diminution of 7 orders of magnitude is observed on the conservative variables and 6 orders of magnitude on the turbulent variable. The residuals reach levels of 10^{-12} for the conservative variables and 10^{-17} for the turbulent variable. Such an evolution of residuals indicates that the naive continuation method is validated for our configuration.

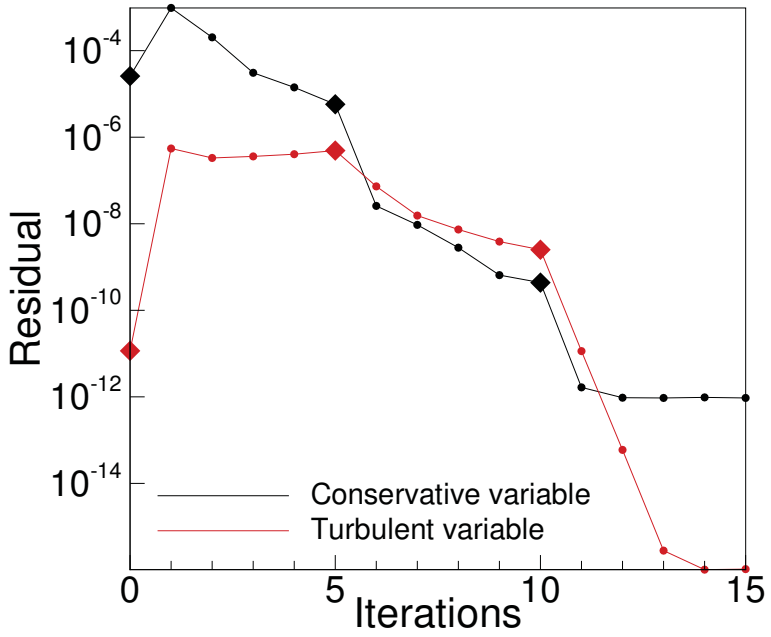

FIGURE 4.5: Evolution of the explicit residual for the conservative variable ρ and the turbulent variable $\tilde{\nu}$ for $\alpha = 12.20°$ initialized with a solution for $\alpha = 12.00°$ (with naive continuation method).

4.3.2 Pseudo-arclength method

The naive continuation method was tested by computing a solution for $\alpha = 12.20°$ from the solution at $\alpha = 12.00°$. However, in the case of the pseudo-arclength, the control

parameter is not the variation of angle of attack but a distance Δs along the tangent approximating the curvilinear length between the two solutions. It means that the variation of angle of attack is not directly controllable. By choosing $\Delta s = 0.652614$, a solution for $\alpha \approx 12.20°$ is reached (with a precision up to 10^{-6}) and will be used for validation. The evolution of the residual of the conservative variable ρ and the turbulent variable $\tilde{\nu}$ is plotted in Figure (4.6). Each dot corresponds to a resolution of the system (4.26) and the diamond symbol at the beginning corresponds to the computation and factorization of the Jacobian Matrix. This time, the convergence is slower than with the naive continuation method but linear. Moreover, by adding one line and one column to the Jacobian matrix, the sparsity of the matrix is ruined and so the factorization time drastically increases due to memory allocation matters.

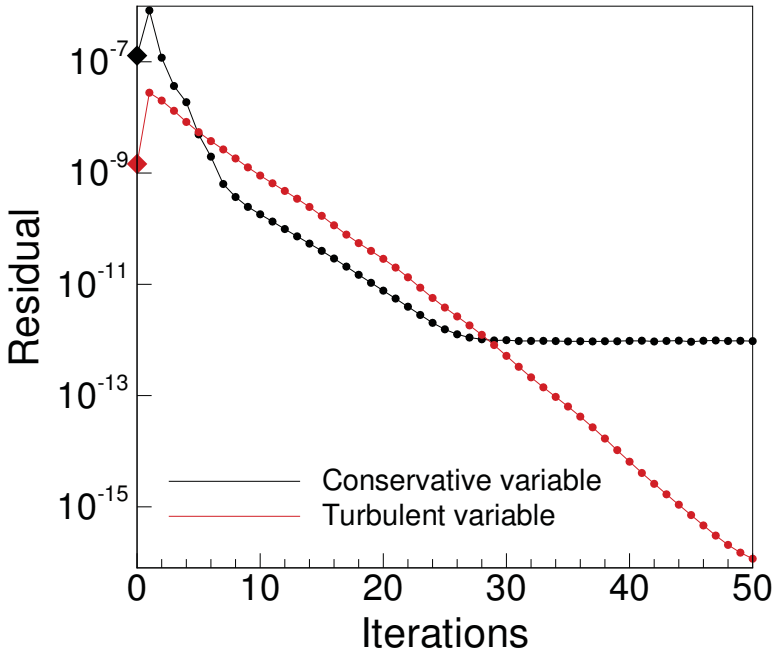

FIGURE 4.6: Evolution of the explicit residual for the conservative variable ρ and the turbulent variable $\tilde{\nu}$ for $\alpha \approx 12.20°$ initialized with a solution for $\alpha = 12.00°$ (with pseudo-arclength method).

Finally, when computing a steady solution with the pseudo-arclength method from a solution obtained with the naive continuation method at a different angle of attack, a diminution of 5 orders of magnitude is observed on the conservative variables and 8 orders of magnitude on the turbulent variable. The residuals reach levels of 10^{-12} for the conservative variables and 10^{-17} for the turbulent variable. Such an evolution of residuals indicates that the pseudo-arclength method is validated for our configuration.

Note that the local relative error between the pseudo-arclength method and the local time stepping approach at $\alpha = 12.20°$ is similar for each variable to the local relative

error depicted in the comparison of the naive continuation method and the local time stepping approach at $\alpha = 12.00°$ and the reasons of such an error are similar.

4.3.3 Summary

Table 4.1 shows the values of the lift and drag coefficients obtained for steady solutions computed at $\alpha = 12.20°$ with four different methods: a local time stepping approach with the recommended cutoffs on the turbulent variable active, a local time stepping approach with no cutoffs on the turbulent variable (but still some inner cutoffs active during the computation of the turbulent variable), a naive continuation method approach and a pseudo-arclength approach. First, one can observe how the naive continuation method and the pseudo-arclength give similar results. Second, by comparing the results obtained with the two continuation methods with the result obtained with the local time stepping approach with all the recommended cutoffs on the turbulent variable active, one can observe a slight difference of lift and drag coefficients. However, the difference between the two steady solutions (already presented in the left pictures of Figure (4.4)) results in an extremely small error on the aerodynamic coefficients ($< 1\%$). Nevertheless, by removing the cutoffs on the turbulent variable, this error on the aerodynamic coefficients decreases by 4 orders of magnitude.

Method	C_L	C_D
Local time stepping with recommended cutoff	1.237283	0.013172
Local time stepping without cutoff	1.247874	0.012333
Naive continuation method	1.247872	0.012332
Pseudo-arclength	1.247872	0.012332

TABLE 4.1: Comparison of the aerodynamic coefficients C_L and C_D for $\alpha = 12.20°$ regarding the computational method used.

Chapter 5

The OA209 airfoil in stall configuration: linear stability analysis of steady RANS solutions

Contents

The turbulent flow around a two dimensional OA 209 airfoil in a retreating blade configuration ($M = 0.16$ and $Re = 1.8 \times 10^6$) is considered. This configuration is similar to that studied in chapter 3 and the mesh used is the same as the one introduced in section 3.1. The study is still performed in the RANS formalism (see chapter 2 for more details) with the Spalart–Allmaras turbulence model [151] (also described in chapter 2) under the assumption of a fully turbulent flow (i.e. no transition model). However, in this chapter, the steady solutions of the Navier–Stokes equations are obtained for different angles of attack (from $\alpha = 12.00°$ to $\alpha = 22.00°$) with continuation methods : naive continuation and pseudo arc-length methods (which are introduced in detail

in chapter 4) instead of time stepping methods presented in chapter 2 and applied on this configuration in chapter 3. Such an approach should allow us to reach solutions that are unaccessible with local time stepping approach and reduces the total computational time. More precisely, a branch of steady solutions linking the upper and lower branches identified in chapter 3 is sought, similarly to the work of Wales and Gaitonde [166].

Next, a stability analysis is performed for each steady solution obtained for different values of α. First, the formalism of the stability analysis is introduced. Then, the two unstable modes observed are introduced : one is a low frequency mode appearing close to stall and the other is a classic bluff-body vortex shedding mode, which appears for higher values of angles of attack and oscillates at a higher frequency. Finally, the complex behavior of the low frequency mode along the steady solution is described close to stall.

5.1 Steady RANS solutions of the flow around an OA209 airfoil

5.1.1 General overview of the solutions

The vector $\boldsymbol{Q} = (\rho, \rho u, \rho v, \rho E, \rho\tilde{\nu})^T$ is introduced as the steady solution of the Navier–Stokes equations $\boldsymbol{R}(\boldsymbol{Q}) = 0$. The conservative variables are : the density ρ, the streamwise velocity along the horizontal axis (x) u, the cross-stream velocity along the vertical axis (y) v and the internal energy E. The vector is completed by the turbulent variable $\tilde{\nu}$ of the Spalart–Allmaras model.

Figure (5.1) shows the ρu field (left) and the $\rho\tilde{\nu}$ field (right) for different angles of attack. On each picture, the limit of the recirculation bubble, if it exists, is plotted in black. For each case, the position of the corresponding angle of attack is indicated with a red dot in the middle picture showing the evolution of the lift coefficient as a function of the angle of attack. This curve is presented and discussed in more detail in Figure (5.2). The first angle of attack investigated in pictures (a) and (b) is $\alpha = 12.00°$. For this value of α, the flow is fully attached and there is no recirculation bubble. The wake is relatively thin and the level of turbulence in it is extremely low. The second case, $\alpha = 16.00°$, depicted in pictures (c) and (d), exhibits the appearance of a tiny recirculation bubble on the trailing edge. The thickness of the wake, the level of turbulence as well as the lift coefficient increase with the angle of attack. The next configuration, $\alpha = 17.50°$, presented in pictures (e) and (f), corresponds to a maximum value of lift coefficient. The separation point of the recirculation bubble moves backward, in the direction of the leading edge, resulting in an increase of the recirculation bubble size and the thickness of the wake. Pictures (g) and (h) present the fields for $\alpha = 18.45°$ just before a sudden drop of lift. The separation point keeps moving towards the leading edge and the recirculation bubble size as well as the thickness of the wake increases. The same angle of attack $\alpha = 18.45°$ is presented in pictures (i) and (j) but the flow topology is completely different : the flow is now massively separated, resulting in a much bigger recirculation bubble and wake thickness as well as a larger

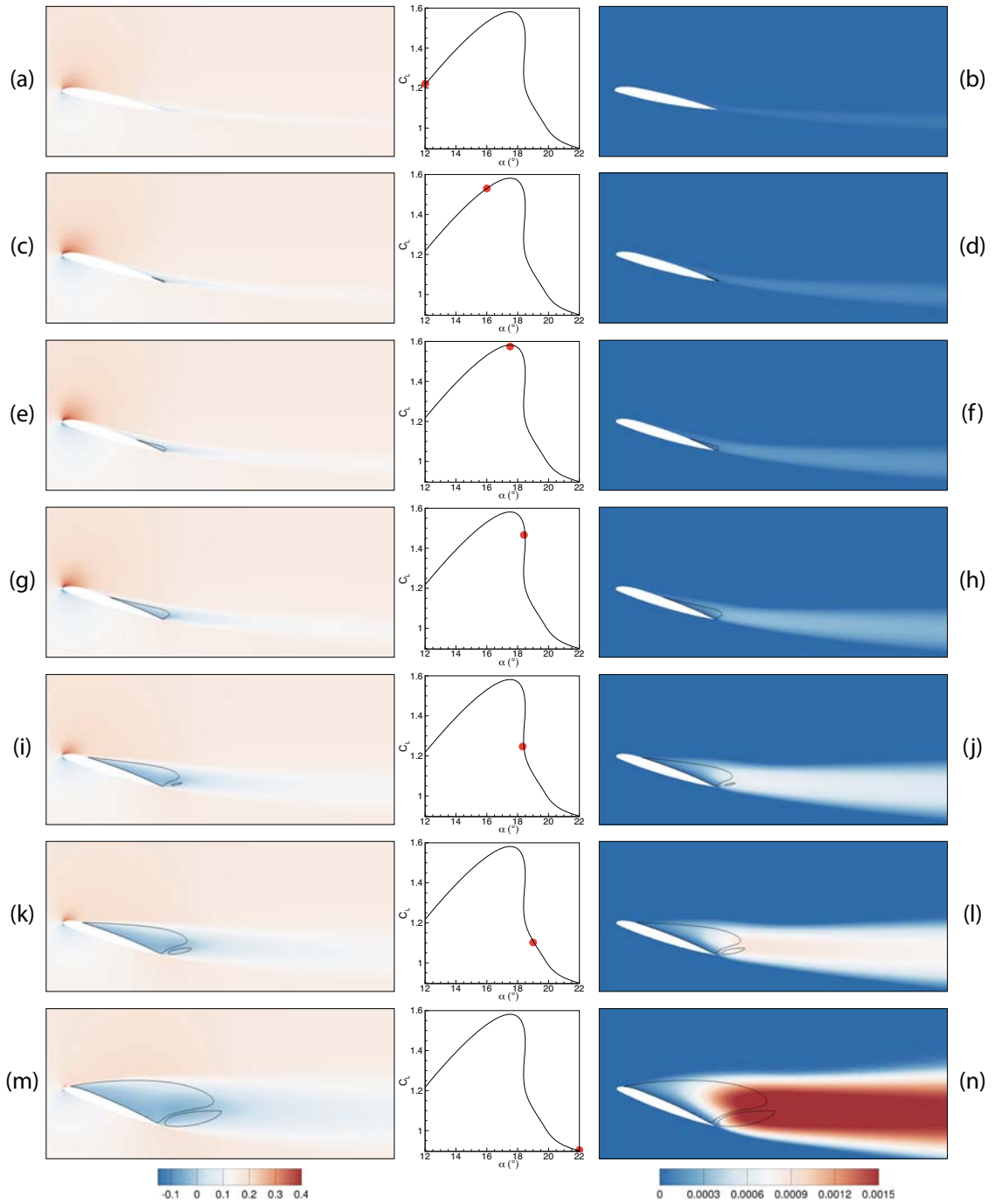

FIGURE 5.1: Flow topology for different angles of attack: (a) and (b): $\alpha = 12.00°$. (c) and (d): $\alpha = 16.00°$. (e) and (f): $\alpha = 17.50°$. (g) and (h): $\alpha = 18.45°$ on the upper branch. (i) and (j): $\alpha = 18.45°$ on the lower branch. (k) and (l): $\alpha = 19.00°$. (m) and (n): $\alpha = 22.00°$. Left pictures: ρu field. Middle pictures: position of the steady solution in the (α, C_L) plane. Right pictures: $\rho\tilde{\nu}$ field.

turbulence level in the wake. Also, a second small recirculation bubble appears at the trailing edge. The coexistence of these solutions was introduced in chapter 3 and a new interpretation, made possible with the use of continuation methods, is presented

in detail afterwards in subsection 5.1.2. Then, the case $\alpha = 19.00°$ is presented in pictures (k) and (l). The evolution of the recirculation bubble and the wake is similar to the one observed so far. Moreover, the small recirculation at the trailing edge also grows and, by doing so, pushes the reattachment point of the large recirculation bubble towards the leading edge. Finally, the highest angle of attack investigated, $\alpha = 22.00°$, is presented in pictures (m) and (n). The flow is now massively separated from almost the leading edge and the turbulence level is high.

From all these solutions, it is possible to extract several interesting variables that can be plotted as a function of the angle of attack and provide a quantitative evolution of the flow. Figure (5.2) shows the evolution of the lift coefficient (a), the drag coefficient (b), the pitching moment coefficient (c) and the evolution of the separation and reattachment points (respectively in full and dashed black lines) to evaluate the recirculation bubble position (d). The curves showing the evolution of the aerodynamic coefficient (introduced in appendix A) were presented in chapter 3 for steady solutions computed with a local time stepping approach: a discontinuity and the coexistence of several solutions for the same angle of attack was identified. This area is indicated on the curves (a), (b), (c) and (d) by a grey area. In the present case, which exhibits solutions obtained with continuation methods, the major difference comes from the continuity of all the quantities plotted as a function of the angle of attack, highlighting the fact that steady solutions that could not be found with a local time stepping approach exist and were successfully identified with the pseudo-arclength method. Apart from this difference, the remaining portions of the different curves are similar. One can first observe a linear increase of the lift, drag and pitching moment coefficients for the lowest values of angles of attack (from $\alpha = 12.00°$ to $\alpha = 17.50°$ approximately). Then, stall occurs, characterized by a sudden drop of lift and pitching moment coefficients and a sudden increase of the drag coefficient. Finally, the lift and pitching moment coefficients keep decreasing more slowly after stall occurred while the drag coefficient keeps increasing. As mentioned in the description of Figure (5.1), the separation point moves from the trailing to the leading edge as the angle of attack increases. The exact position of this point is plotted as a function of the angle of attack with a full black line in picture (d). The position is defined as a fraction of the chord of the airfoil $\frac{x}{c}$: 1 corresponds to the trailing edge and 0 corresponds to the leading edge. For the lowest angles of attack investigated ($\alpha < 13.00°$), the flow is entirely attached. Then, a flow separation appears at the trailing edge, initiating a recirculation bubble, and slowly moves towards the leading edge, expanding the size of this recirculation bubble, which grows faster as the angle of attack is getting closer to the stall area. Before the stall area, the flow never reattaches on the airfoil. However, just before the drop of lift, the flow starts reattaching on the airfoil. The evolution of the position of the reattachment point is plotted with a dashed black line in picture (d). Similarly to the separation point, the reattachment point is also moving towards the leading edge. Note that as the reattachment point moves backward, the size of the second small recirculation bubble identified in Figure (5.1) increases.

To summarize, the phenomena revealed by this analysis are similar to those described in chapter 3, which validates the use of continuation methods in this configuration. A more detailed comparison of the steady solutions obtained with continuation

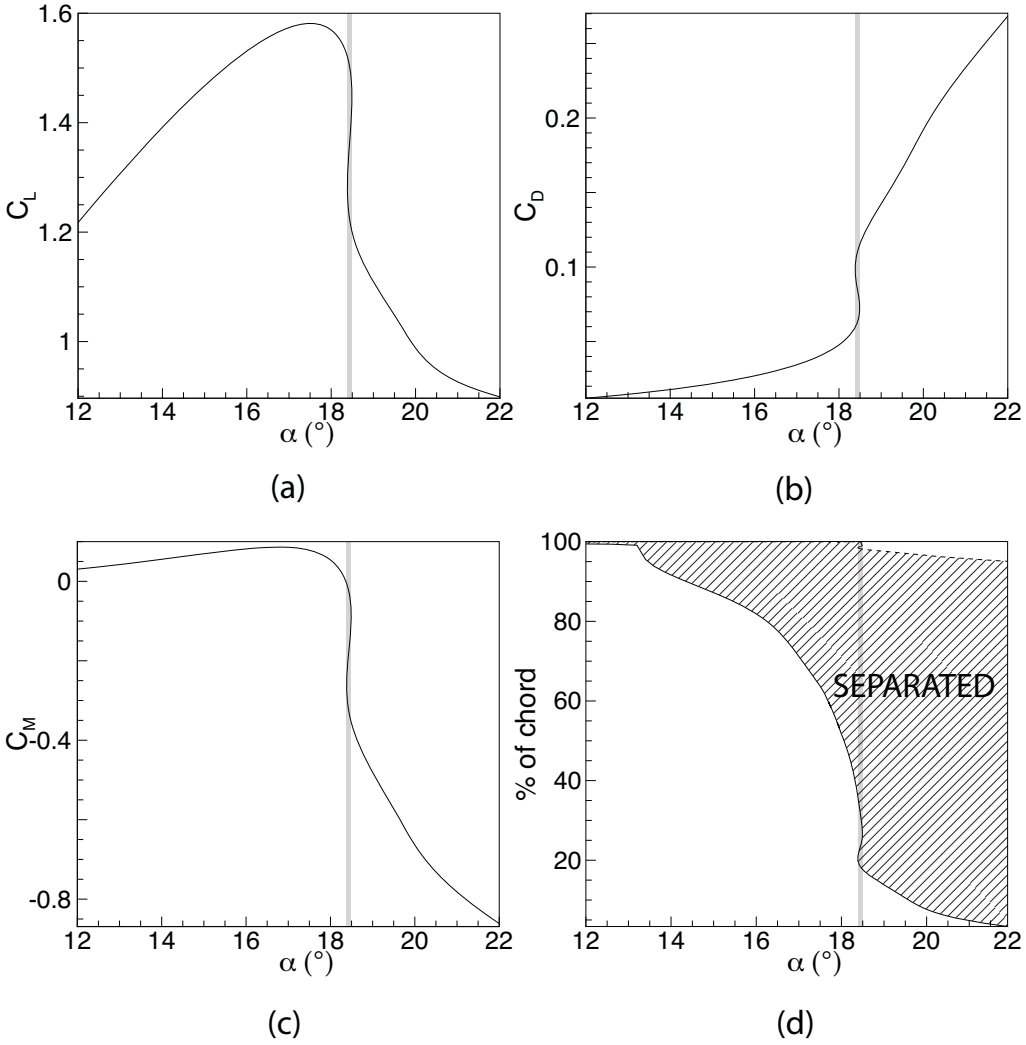

FIGURE 5.2: Evolution of several quantities related to the flow topology of steady solutions as a function of the angle of incidence. (*a*) Evolution of the lift coefficient. (*b*) Evolution of the drag coefficient. (*c*) Evolution of the pitching moment coefficient. (*d*) Evolution of the separation (full black line) and reattachment points (dashed black line) and identification of the separated flow area (hatched region).

methods and with a local time stepping approach is presented in appendix C. The stall mechanism identified is a trailing edge stall characterized by a separation point moving from the trailing edge to the leading edge as the angle of attack increases. The question of the validity of such a stall type for these particular airfoil and configuration is addressed in section 3.2.4. A second small recirculation bubble at the trailing edge for high angles of attack is also identified. The coexistence of several solutions for the same angle of attack is highlighted close to the stall angle similarly to what was observed in chapter 3. However, with the data previously available, stall was associated with an abrupt change of flow topology from the so called upper branch (of high lift) to the so called lower branch (of low lift). With this new approach, it appears that there is actually no discontinuity from one branch to the other as highlighted by the evolution of the aerodynamic coefficients as well the evolution of the recirculation bubble. The

branch that links the upper and lower branches, is named the middle branch. This branch was unaccessible with the classic local time stepping approach but the pseudo arclength method made it possible and, in the end, a result similar to the one of Wales and Gaitonde [166] on a NACA0012 at high Reynolds number is obtained. The next section is dedicated to a more detailed description of this zone of coexisting solutions.

5.1.2 Solutions close to the stall angle

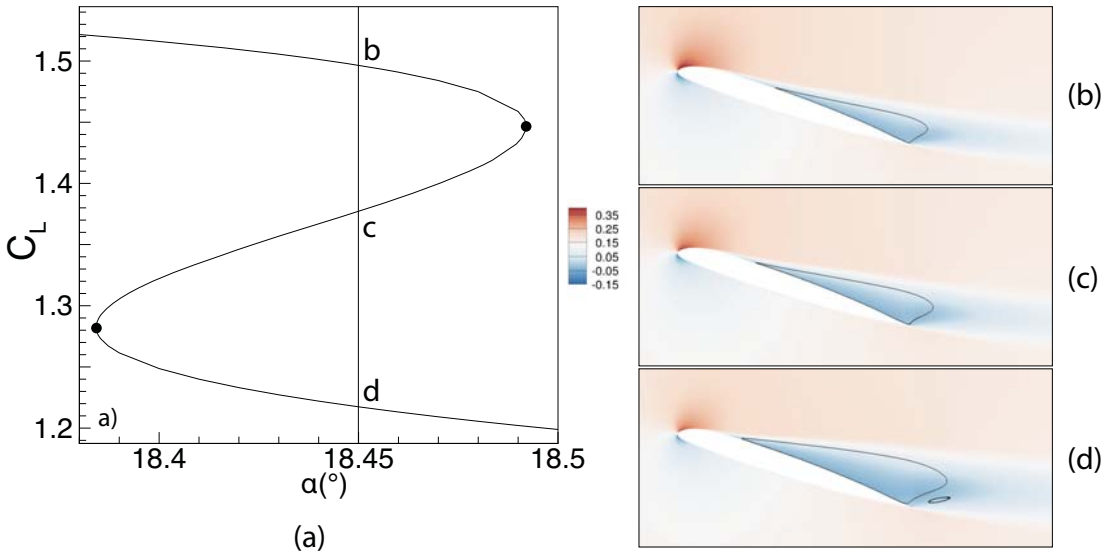

FIGURE 5.3: Visualisation of three steady solutions coexisting for a same angle of attack ($\alpha = 18.45°$). (a) Lift coefficient polar curve zoomed in close to stall. The black vertical line refers to the angle of attack considered. The three different solutions existing for this angle of attack are marked by a letter, which refers to a picture on the right. (b) Upper branch solution. (c) Middle branch solution. (d) lower branch solution.

Now that the continuity of the steady solutions have been demonstrated, it is interesting to focus on the stall area where several solutions coexist. Figure (5.3) shows, on the left, the evolution of the lift coefficient in this area. One can observe how the upper branch, of high lift values, ends in with a saddle-node point (marked by the furthest right black dot). This point also marks the first extremity of the middle branch. The other extremity of the middle branch corresponds to the second saddle-node bifurcation that ends the lower branch (marked by the furthest black dot). In chapter 3, this stall area is characterized by two steady solutions coexisting for a same angle of attack. With the identification of the middle branch, we acknowledge that there are actually three solutions coexisting for each angle of attack in this area. The three pictures on the right of Figure (5.3) illustrate the topologies of these three different steady solutions for the particular value $\alpha = 18.45°$ (marked by a vertical line on the polar curve). Each flow topology is referenced on the polar curve by the corresponding letter : picture (b) corresponds to the high lift solution on the upper branch, picture (c) corresponds to the solution on the middle branch and picture (d) corresponds to the low lift solution on the lower branch. One can observe three different flow topologies for each solution

: (b) exhibits a medium size recirculation bubble, (c) a larger recirculation bubble and (d) and even larger one coupled with the appearance of a second smaller recirculation bubble at the trailing edge.

5.2 Linear global stability analysis of the steady RANS solutions

The steady solutions for several angles of attack between $\alpha = 12.00°$ and $\alpha = 22.00°$ have been computed with continuation methods. Such a range of values allowed us to identify stall and static hysteresis and a perfect continuity of the steady solutions even at stall. The objective is to perform a linear stability analysis of each steady solution in order to see if self-sustained global instabilities can be found for particular angles of attack. Particularly, the identification of a mechanism that could be directly linked to stall will be carefully investigated. First, the formalism of the linear global stability analysis is introduced: particularly, it is shown how this linear study can be written as an eigenvalue problem where the eigenvalue characterizes the temporal behavior of the instability and the eigenmode corresponds to the spatial structure of the instability. Afterwards, the results obtained for the linear stability analysis of the steady solutions computed in section 5.1 are presented. Several tools, used to identify the regions of the flow that could be at the origin of the mechanisms identified, are also introduced.

5.2.1 Formalism and tools

The governing equations of the system are the compressible Navier–Stokes equations (defined by (2.17) in chapter 2) closed with a turbulence model in the RANS framework. In the present case, the Spalart–Allmaras turbulence model, defined in (2.23), is chosen. The flow variable $\boldsymbol{q} = (\rho, \rho u, \rho v, \rho E, \rho\tilde{\nu})^T$ satisfies these governing equations, which, after spatial discretization with a finite volume method, can be formally written:

$$\frac{d\boldsymbol{q}}{dt} = \boldsymbol{R}(\boldsymbol{q}) \tag{5.1}$$

where the vector $\boldsymbol{q}$ refers to variables of the system : $\boldsymbol{q} = (\rho, \rho u, \rho v, \rho E, \rho\tilde{\nu})^T$. A first assumption is made on the form of the solution of the Navier–Stokes equations : they can be written as the sum of a steady solution $\boldsymbol{Q}$ and time dependent perturbation $\boldsymbol{q'}$ of small amplitude ϵ :

$$\boldsymbol{q} = \boldsymbol{Q} + \epsilon\boldsymbol{q'} \tag{5.2}$$

where $\boldsymbol{Q}$ satisfies :

$$\boldsymbol{R}(\boldsymbol{Q}) = 0 \tag{5.3}$$

By replacing decomposition (5.2) into (5.3) and linearizing the equations, the system can be written as :

$$\frac{d\boldsymbol{q'}}{dt} = \mathcal{J}(\boldsymbol{Q})\boldsymbol{q'} \tag{5.4}$$

where $\mathcal{J}(\boldsymbol{Q})$ is the Jacobian of the system $\boldsymbol{R}$ evaluated at $\boldsymbol{Q}$. Details about the computation of this matrix is given in section 4.2.1 of chapter 4. Moreover, the time dependent perturbations are sought under the form of normal modes:

$$\boldsymbol{q'} = \hat{\boldsymbol{q}}\mathrm{e}^{\lambda t} \tag{5.5}$$

where $\hat{\boldsymbol{q}}$ designates the spatial behavior of the mode and $\lambda = \sigma + i\omega$ its temporal behavior (σ its growth rate and ω its angular frequency). A base flow $\boldsymbol{Q}$ is considered asymptotically stable if the perturbation tends to zero for large times, which means $\sigma < 0$ for all modes found. Otherwise, if $\sigma > 0$, a mode is considered asymptotically unstable. The base flow is considered unstable if at least one mode is unstable . Finally, equation (5.4) can be written as an eigenvalue problem where $(\lambda, \hat{\boldsymbol{q}})$ is the eigenvalue/eigenvector combination which verifies:

$$\mathcal{J}(\boldsymbol{Q})\hat{\boldsymbol{q}} = \lambda\hat{\boldsymbol{q}} \tag{5.6}$$

where $\hat{\boldsymbol{q}} = (\hat{\rho}, \hat{\rho u}, \hat{\rho v}, \hat{\rho E}, \hat{\rho\tilde{\nu}})^T$.

The computation of the eigenspectrum is performed using Krylov methods with a shiff-and-invert strategy [143] available in the open source library ARPACK [130]. The direct parallel LU solver MUMPS [120] is used as linear solver. As already mentioned in section 4.2.2, the LU factorization is costly and has high memory requirements. However, in our two dimensional case this is not a limitation. The tools used in the present work to compute the Jacobian matrix and the eigenvalue/eigenvector combination have been validated first by Mettot *et al.* [108] in the case of a two dimensional deep cavity with several turbulence models and numerical schemes and used in several studies afterwards (see for instance Beneddine *et al.* [13], Bonne *et al.* [17] or Paladini *et al.* [123]).

5.2.2 General overview of the stability results

Figure (5.4) exhibits the evolution of the lift coefficient as a function of the angle of attack already presented in Figure (5.2). The dashed portions of the curve correspond to the solutions for which an unstable eigenvalue is found (i.e. an eigenvalue λ with a positive growth rate σ). One can observe two very distinct zones with an unstable mode : a first one close to the stall area ($\alpha \approx 18.45°$) and a second one for high angles of attack ($\alpha > 20.50°$) when the flow is completely detached. It appears that, for each area, it is possible to identify a coherent evolution of the eigenvalue and a similar structure of the eigenmodes for the different angles of attack. However, the angular frequency ω (imaginary part of the eigenvalue λ) and the structure of the modes are drastically different between the two zones. From this point, the mode identified close to the stall angle will be designated as the *stall mode*. The other one, appearing when the flow is massively separated, is actually a bluff body *vortex shedding mode* as will

be shown in the rest of this chapter.

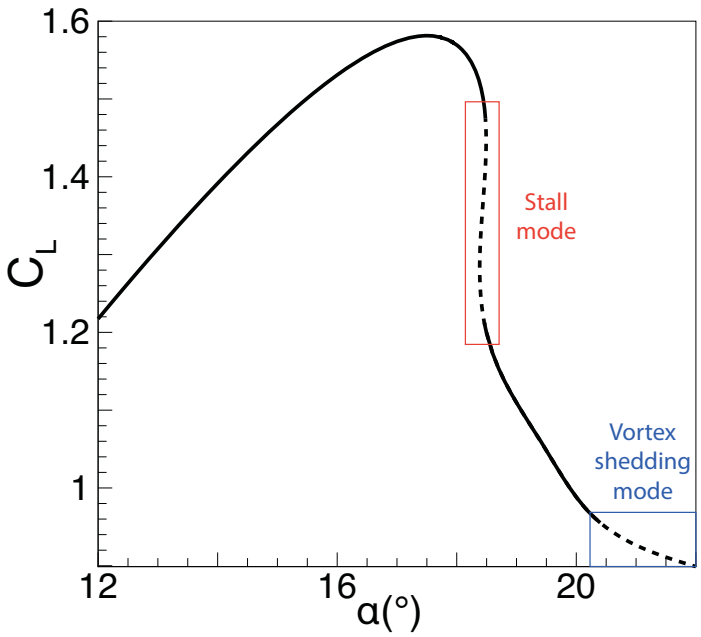

FIGURE 5.4: Lift coefficient curve and associated linear stability state. The angles of attack for which the linear stability analysis of the steady solutions reveals an unstable mode are plotted with a dashed black line. Otherwise, a full black line is used. Two different zones of interest are identified : one close to stall and one for high angles of attack, for which the flow is massively separated.

5.2.3 Eigenspectra

Figure (5.5) shows the unstable eigenvalues identified for a particular angle of attack in each area : (a) presents the results obtained for $\alpha = 18.49°$ on the upper branch (close to stall) and (b) presents the results obtained for $\alpha = 21.00°$ on the lower branch (when the flow is massively separated). The modes are marked by red dots in the complex plane (σ, ω). Note that there are actually two red dots in each figure : one corresponds to the actual mode and the other to its complex conjugate of similar growth rate and opposite angular frequency. The grey areas highlight the zones where the modes are unstable ($\sigma > 0$) and note that the red dots are in these areas.

The main difference between the two pairs of eigenvalues comes from the order of magnitude of their angular frequency ω : for the unstable mode identified close to stall for $\alpha = 18.49°$, $\omega = 0.0086$ (picture (a)) while for the unstable mode identified at higher angles of attack for $\alpha = 21.00°$, $\omega = 0.515$ (picture (b)). This means that the frequency of the phenomenon identified close to stall is two orders of magnitude lower than the bluff body vortex shedding phenomenon. A more common way to quantify unsteady phenomena occurring around airfoils is to consider the Strouhal number base on the chord length weighted by the sine of the angle of attack :

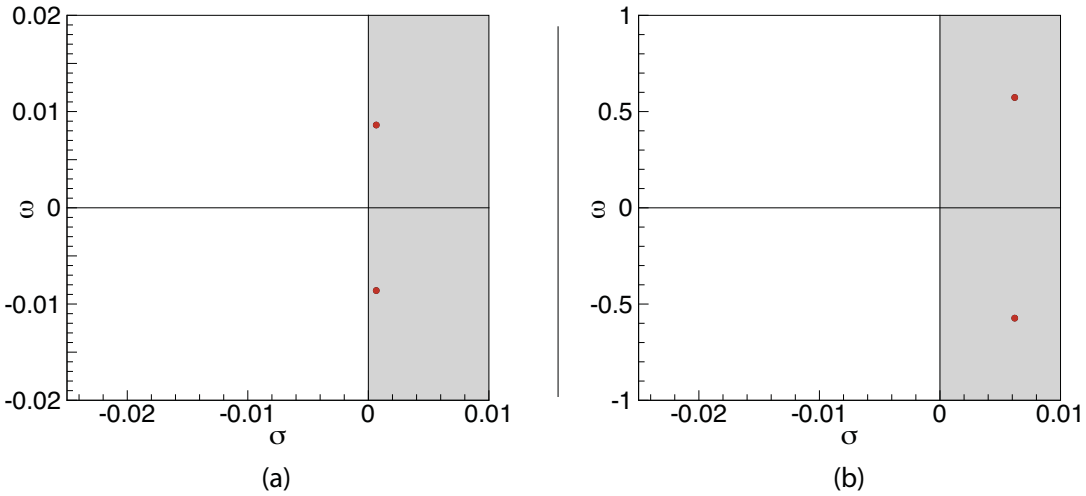

FIGURE 5.5: Visualisation of two eigenspectra for two different angles of attack. (*a*) Stall mode for $\alpha = 18.49°$ on the upper branch, just before stall. (*b*) Vortex-shedding mode for $\alpha = 21.00°$ on the lower branch, when the flow is massively separated. For each spectrum, the leading mode and its associated complex conjugate are represented.

$$\mathrm{St} = \frac{\omega \cdot c \cdot \sin(\alpha)}{2\pi \cdot U_\infty} \tag{5.7}$$

With ω the angular frequency, c the chord of the airfoil, α the angle of attack and U_∞ the far field velocity in the x direction ($U_\infty = 0.16$ in our case). The corresponding values of Strouhal number are summarized in Table 5.1. The vortex shedding mode has a very classic Strouhal number $\mathrm{St} \approx 0.2$, similar to what is usually found in the literature (see for instance [142]). The Strouhal number of the stall mode, $\mathrm{St} = 0.00271$, is two orders of magnitude lower than the Strouhal number of the bluff body vortex shedding mode, which echoes the value found for low frequency oscillations, which appear close to stall (detailed in section 1.3.2).

Mode	α (°)	σ	ω	St
Stall	18.49	6.56×10^{-4}	8.60×10^{-3}	0.0027
Vortex shedding	21.00	6.2×10^{-3}	5.73×10^{-1}	0.20

TABLE 5.1: Components of the eigenvalues for two different types of mode : stall ($\alpha = 18.49°$)and vortex shedding ($\alpha = 22.00°$ modes. Growth rate σ, angular frequency ω and associated Strouhal number St scaled on the chord length weighted by the sine of the angle of attack.

5.2.4 Structure of the mode and influence on the dynamics

Very different orders of magnitude are identified between the angular frequencies of the two pairs of eigenvalues. It is now interesting to examine the respective structures of the associated eigenmodes. First, the structures of the modes are introduced and then the influence on their respective baseflows is presented.

5.2.4.1 Eigenmodes

Figure (5.6) presents the real part of the eigenmodes. Pictures (a) and (c) describe the stall mode ($\alpha = 18.49°$) and pictures (b) and (d) present the vortex shedding mode ($\alpha = 21.00°$). The upper ones correspond to the streamwise velocity $\hat{\rho u}$ component of the modes and the lower ones to the turbulent variable $\hat{\rho\tilde{\nu}}$. On each picture, the recirculation bubble obtained from the associated steady solution is represented by a black line.

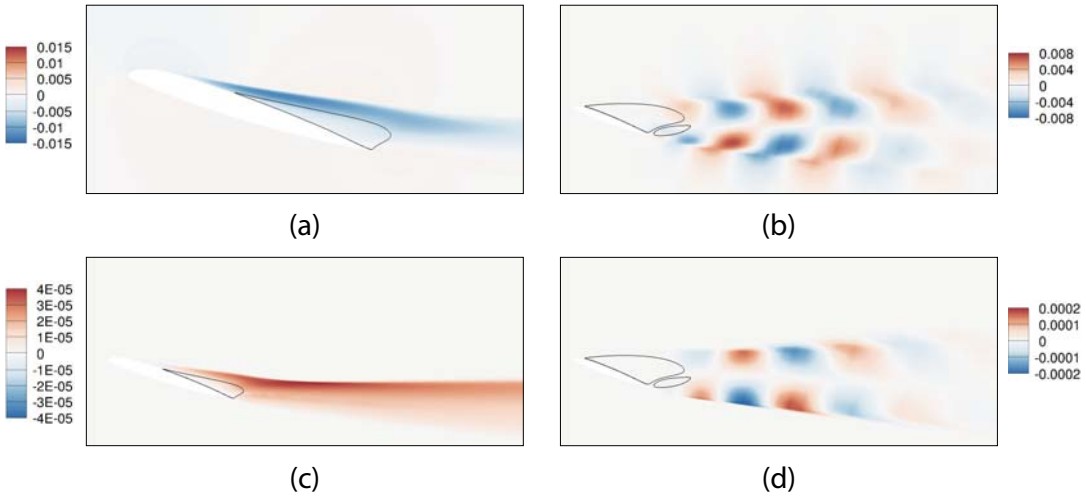

FIGURE 5.6: Visualisation of the structure of the eigenmodes. (a) Real part of the $\hat{\rho u}$ field of the stall eigenmode ($\alpha = 18.49°$). (c) Real part of the $\hat{\rho\tilde{\nu}}$ field of the stall eigenmode ($\alpha = 18.49°$). (b) Real part of the $\hat{\rho u}$ field of the vortex-shedding eigenmode ($\alpha = 21.00°$). (d) Real part of the $\hat{\rho\tilde{\nu}}$ field of the vortex-shedding eigenmode ($\alpha = 21.00°$).

The spatial pattern of the streamwise velocity $\hat{\rho u}$ of the stall mode, presented in Figure (5.6)(a), shows a large pulsating structure starting on the suction edge of the airfoil just before the separation point of the steady solution. The structure extends until the end of the recirculation bubble of the steady solution. The turbulent variable $\hat{\rho\tilde{\nu}}$ exhibits similar pulsating structures but also exists in the wake of the steady solution, downstream from the recirculation region (picture (c)). The amplitude reaches its peak in the upper part of the wake, close to the recirculation region. The shape of this mode is very similar to the one observed around a NACA 0012 at Reynolds number $\mathrm{Re} = 6.0 \times 10^6$ and Mach number $\mathrm{M} = 0.15$ by Iorio [76] presented in Figure 1.10.

The spatial pattern of the streamwise velocity shown in Figure (5.6)(b) is typical of a vortex-shedding eigenmode: two rows of large structure patterns which oscillate out

of phase in the streamwise direction and located in the wake of the flow. The structures reach their largest amplitude downstream from the recirculation region of the steady solution and slowly vanish in the far field. The turbulent variable $\widehat{\rho\tilde{\nu}}$ depicted in Figure (5.6)(d) shows the same kind of structures in the streamwise direction and located downstream from the airfoil although more affected by the wake of the steady solution, whose boundaries are clearly visible on this component.

5.2.4.2 Superimposition of the eigenmodes and the steady solutions

Once the structures of the eigenmodes are well known and understood, it is interesting to observe how these modes could affect the steady solution. A first order approximation of the unsteady solution of the Navier–Stokes equations can be obtained by summing the steady solution $\boldsymbol{Q}$ and the small time dependent perturbation $\boldsymbol{q'}$ (see section 5.2.1 for more details). Equation (5.8) details the expression of the approximated solution with ϵ a small amplitude perturbation, $\hat{\boldsymbol{q}}$ the eigenmode, σ the growth rate of the mode and ω the angular frequency of the mode.

$$\boldsymbol{q}_{approx} = \boldsymbol{Q} + 2\epsilon e^{\sigma t}[\hat{\boldsymbol{q}}_{\boldsymbol{r}} \cos(\omega t) - \hat{\boldsymbol{q}}_{\boldsymbol{i}} \sin(\omega t)] \tag{5.8}$$

Many of those variables are known from the stability analysis. However, the amplitude of the perturbation ϵ remains unknown. The exact determination of this variable in our approach is complicated and would require time-consumming computations. Indeed, as demonstrated by Sipp and Lebedev [149] in the case of the flow past a cylinder at low Reynolds number, an equation for the amplitude might be obtained by originally considering a higher order of approximation of the Navier–Stokes equations: such as $\boldsymbol{q} = \boldsymbol{Q} + \epsilon\boldsymbol{q'} + \epsilon^2\boldsymbol{q''} + ...$ The resolution of this amplitude equation would give us the parameter ϵ. Then, it would be necessary to wait for the phenomenon to slowly be amplified based on the exponential evolution of the growth rate $e^{\sigma t}$ until the phenomenon would become significant. However, even in that case, the solution computed would still be a first order approximation and it would require to investigate the amplitudes of higher order perturbations to obtain the exact solution. In order to avoid such a complexity, we just set an arbitrary amplitude A such that $A = 2\epsilon e^{\sigma t}$. We set the value of A to ensure that significant changes of the base flow can be observed. Such an approach, although quantitatively approximate, provides a useful qualitative overview of the global dynamics of the instabilities and of how the modes affect the baseflow. The values of A used in our cases are referenced in Table 5.2.

	Stall mode	Vortex Shedding mode
A	10	20

TABLE 5.2: Values of the amplitude chosen to compute the approximate unsteady solution $\boldsymbol{q}_{approx}$.

Figure (5.7) presents the approximated solution $\boldsymbol{q}_{approx}$ over a period $T = \frac{2\pi}{\omega}$ (with ω the angular frequency of the mode) for the stall mode at $\alpha = 18.49°$. One can

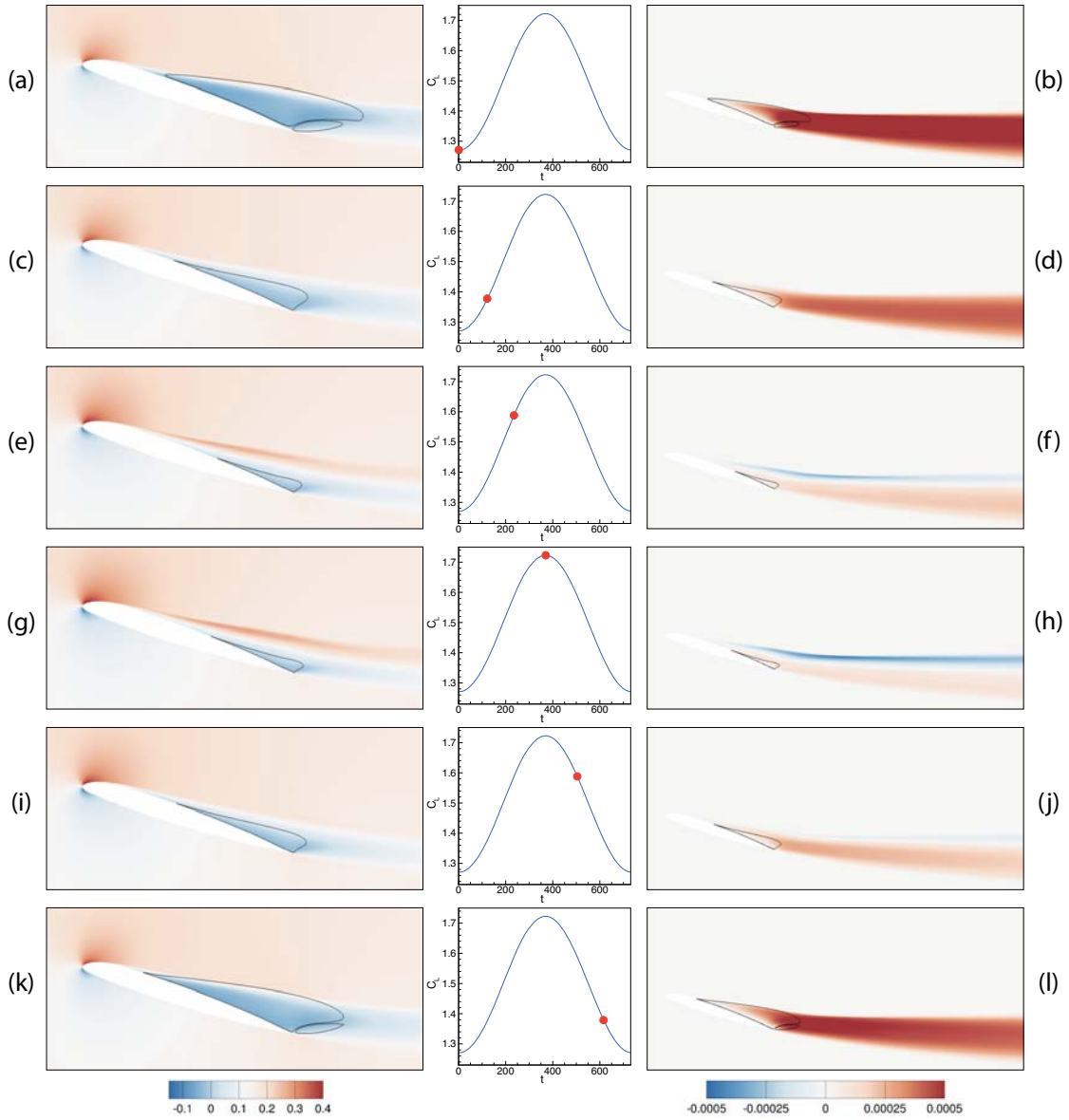

FIGURE 5.7: Visualisation of the effect of the stall eigenmode on the steady solution for $\alpha = 18.49°$ for an arbitrary amplitude $B = 10$. Left pictures: ρu field. Middle pictures: position of the solution in the (t, C_L) plane. Right pictures: $\rho\tilde{\nu}$ field. Six different times are considered over a period T. (a) and (b): $t = 0$. (c) and (d): $t = \frac{T}{6}$. (e) and (f): $t = \frac{T}{3}$. (g) and (h): $t = \frac{T}{2}$. (i) and (j): $t = \frac{2T}{3}$. (k) and (l): $t = \frac{5T}{6}$.

observe the perfect sinusoidal form of the evolution of the lift coefficient over a period. The solution at $t = 0$ (pictures (a) and (b)) corresponds to a minimum of lift value over the period. It exhibits two recirculation bubbles: a large one on the suction side of the airfoil and a smaller one located at the trailing edge. The wake is wide and the turbulent level in it is high. The solution at $t = \frac{T}{6}$ (pictures (c) and (d)), which corresponds to an increase of lift value, presents a displacement of the separation point towards the trailing edge resulting in a smaller recirculation bubble on the suction side of the airfoil. The smaller recirculation bubble located at the trailing edge of the

airfoil no longer exists and the wake is thinner with a lower turbulence level in it. The separation point keeps moving towards the trailing edge as the lift coefficient increases as shown in the solution at $t = \frac{T}{3}$ (pictures (e) and (f)). One can observe a region of higher speed in the streamwise direction just above the recirculation bubble and a region of negative $\tilde{\nu}$ in the upper part of the wake, which is even thiner than previously. The solutions at $t = \frac{T}{2}$ (pictures (g) and (h)) correspond to a maximum of lift value over the period. The topology of the flow is very similar to that observed at $t = \frac{T}{2}$: no visible differences in the size of the recirculation bubble or the thickness of the wake. The main difference comes from an even higher speed above the recirculation bubble and even smaller values of $\tilde{\nu}$. Afterwards, for $t = \frac{2T}{3}$ (pictures (i) and (j)) the lift value starts decreasing. It is characterized on the flow topology by a displacement of the separation point towards the leading edge resulting in an increase of the recirculation bubble size and of the thickness of the airfoil. One can also observe that the two solutions at $t = \frac{T}{3}$ and $t = \frac{2T}{3}$ exhibit similar lift coefficient values but very different topologies (this difference is also observed between the solutions at $t = \frac{T}{6}$ and $t = \frac{5T}{6}$ depicted in pictures (k) and (l)). Indeed, the second one exhibits a larger recirculation zone on the suction side of the airfoil and also a second recirculation bubble located at the trailing edge with a thicker wake. More generally, one can observe that the stall mode, whose structure is located just above the recirculation bubble, tends to affect the size of this recirculation bubble. Therefore, the approximated solution pulsates between a high lift state with a tiny recirculation bubble located at the trailing edge and a low lift state with a very large recirculation bubble on almost all the suction side of the airfoil : stalled and unstalled position are alternatively encountered.

A similar approach is used for the vortex shedding mode and depicted in Figure (5.8). The solution at $t = 0$ (pictures (a) and (b)) corresponds to a maximum of lift over the period. It exhibits two rows of a pattern, which oscillates out of phase (similarly to the structure of the vortex shedding eigenmode). This pattern is identified at any time over the period, and the differences between the flow topologies can be identified by looking at the recirculation bubbles. Three different ones exist at $t = 0$: a large one located on the suction side of the airfoil, a tiny one at the trailing edge (under the large one) and a third one in upstream in the wake. At $t = \frac{T}{6}$ (pictures (c) and (d)), the large one is convected upstream, going over the tiny one that slightly increases while the one already in the wake is convected even more upstream. These displacements of the recirculation bubbles are characterized by a drop of lift. The same tendency is observed at $t = \frac{T}{3}$ (pictures (e) and (f)) with two shrinking bubbles convected upstream in the wake and one becoming bigger at the trailing edge of the airfoil. At $t = \frac{T}{2}$ (pictures (g) and (h)), corresponding to a minimum value of lift over the period, the most upstream recirculation bubble has vanished while the one at the trailing edge is bigger and a new one, of approximately the same size, is appearing above the airfoil. Afterwards, the lift coefficient is increasing again (pictures (i) and (j) corresponding to $t = \frac{2T}{3}$) as the recirculation bubble above the airfoil becomes a large recirculation bubble covering the whole suction side of the airfoil. The other one, located at the trailing edge, is pushed upstream by the size increase of the large one. The same tendency is observed for the last time depicted $t = \frac{5T}{6}$ at which the recirculation bubble on the suction side of the airfoil is even larger while the other one is convected even more upstream. Afterwards, the same behavior is repeated from $t = 0$ with the appearance of a tiny recirculation

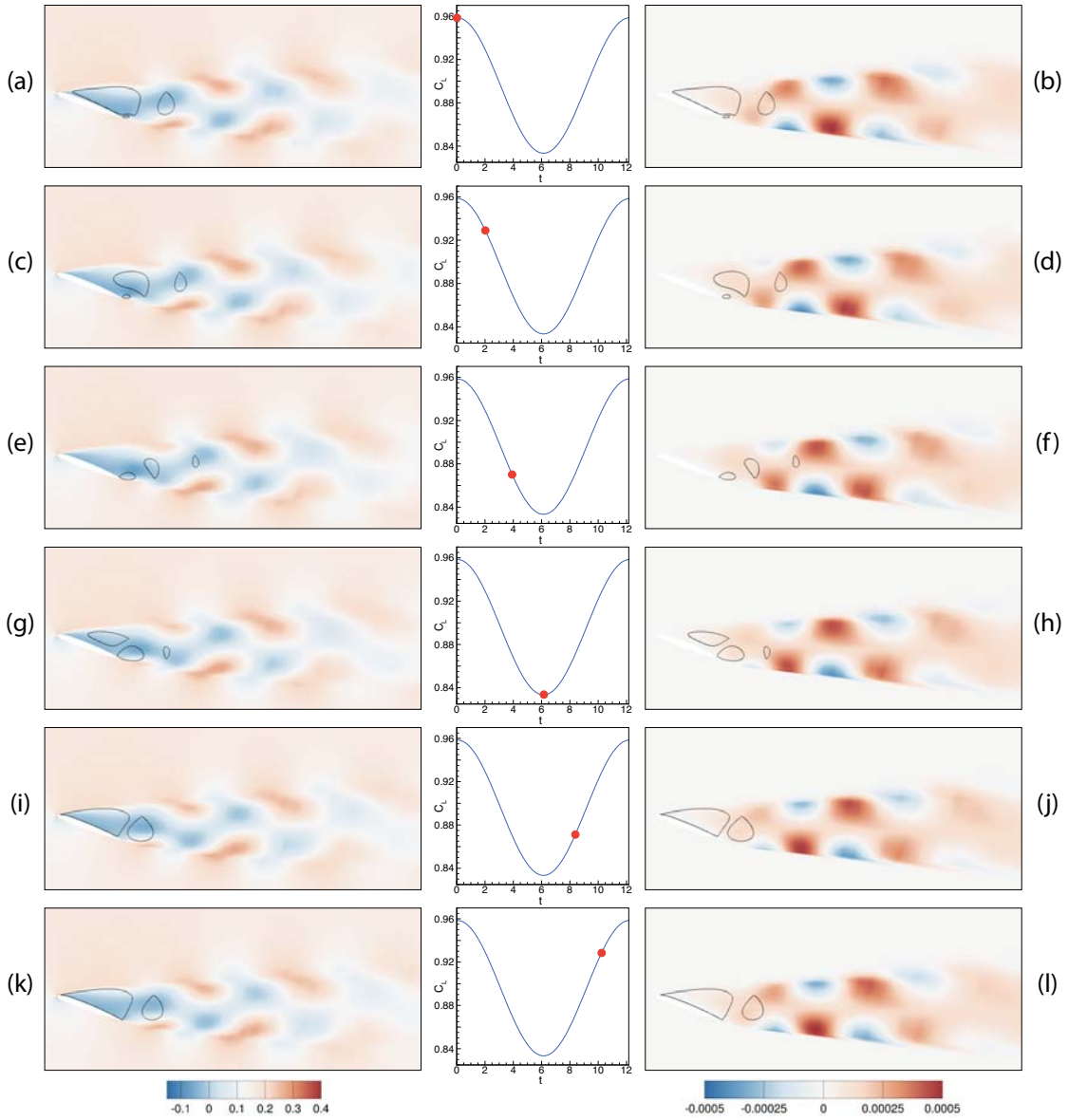

FIGURE 5.8: Visualisation of the effect of the vortex-shedding eigenmode on the steady solution for $\alpha = 21.00°$ for an arbitrary amplitude $B = 20$. Left pictures: ρu field. Middle pictures: position of the solution in the (t, C_L) plane. Right pictures: $\rho\tilde{\nu}$ field. Six different times are considered over a period T. (a) and (b): $t = 0$. (c) and (d): $t = \frac{T}{6}$. (e) and (f): $t = \frac{T}{3}$. (g) and (h): $t = \frac{T}{2}$. (i) and (j): $t = \frac{2T}{3}$. (k) and (l): $t = \frac{5T}{6}$.

bubble under the large one and so on. More generally, one can observe recirculation bubbles convected upstream one after the other: the large one on the suction side of the airfoil and the smaller one located at the trailing edge of the airfoil. It results in two out of phase rows of an oscillating pattern, which generate an oscillating wake similar to a Von Karman street [83] [84].

5.2.5 Adjoint mode, wavemaker and local contribution of the flow

The global stability analysis of the steady solutions revealed the appearance of linearly unstable mechanisms for some values of α. However, although this method gives good insight into the structure, frequency and linear growth of the instability, it does not provide any information about the region of the flow where the instability develops. The concept of *wavemaker* was introduced by Huerre and Monkewitz [73] to locate this region. They defined it as the region where instability waves are intrinsically generated in globally unstable flows. Extending the work of Hill [66], Giannetti and Luchini [59] proposed an alternative approach to define the concept of wavemaker. Their approach relies on the concept of *structural sensitivity*, which characterizes the effects of localized changes of the flow operator on the eigenvalues. This led to the most commonly accepted definition of the wavemaker: the region of maximum structural sensitivity. Hill [66] and Giannetti and Luchini [59] all used it in the case of the flow behind a cylinder, in order to identify the regions where a control cylinder be the most effective. Since then, this approach has been used in many studies to identify the regions of the flow where the self-sustained mechanism induces the largest eigenvalue variation (see for instance [96] [106] or [123]). Note that the definitions introduced by Huerre and Monkewitz [73] and Giannetti and Luchini [59] are for different frameworks: respectively local and global stability analysis frameworks. However, Juniper and Pier [82] proved that the definition of Giannetti and Luchini [59] can be extended in the case of local stability analysis with decent results as long as a weakly nonparallel flow is considered. In the spirit of the wavemaker, Paladini *et al.* [123] proposed an alternative approach based on the decomposition instead of a variation of the linear operator. In an attempt to identify the regions of the flow which contribute the most to the growth rate and the frequency respectively Marquet and Lesshafft [95] proposed a proportional modification of the operator, still based on the concept of sensitivity, which is further described and used in the work of Paladini *et al.* [123][1]. This approach, named *local contribution*, offers the advantage of identifying if the regions of the flow contribute positively or negatively to the linear growth rate and angular frequency of the eigenvalue.

In this subsection, we intend to apply the sensitivity tools developed by Gianetti and Luchini [59] and Paladini *et al.* [123] in order to identify the most sensitive regions of the flow. First, the notion of adjoint mode, which is used in all the aforementioned tools, is introduced. Then, the results obtained with the wavemaker are presented and, finally, the local contribution of the flow to the growth rate and angular frequency is shown.

5.2.5.1 Definition of the adjoint mode

As a reminder, λ is the eigenvalue of the Jacobian matrix $\mathcal{J}(\boldsymbol{Q})$ and $\hat{\boldsymbol{q}}$ its eigenvector, designated as the direct global mode of the steady solution $\boldsymbol{Q}$, which are linked through

[1] A link with the wavemaker function of Giannetti and Luchini [59] as well as a detailed comparison of the two approaches in the case the flow behind a cylinder can be found in the PhD of Paladini [122]

equation (5.6). The adjoint Jacobian matrix $\tilde{\mathcal{J}}(\boldsymbol{Q})$ is introduced such that, for any pair of vectors $\boldsymbol{q_1}$ and $\boldsymbol{q_2}$, condition (5.9) is fulfilled:

$$\langle \boldsymbol{q_1}, \mathcal{J}(\boldsymbol{Q})\boldsymbol{q_2}\rangle_{\boldsymbol{V}} = \langle \tilde{\mathcal{J}}(\boldsymbol{Q})\boldsymbol{q_1}, \boldsymbol{q_2}\rangle_{\boldsymbol{V}} \tag{5.9}$$

where $\langle \cdot, \cdot \rangle_{\boldsymbol{V}}$ designates an inner product based on a real symmetric positive definite matrix $\boldsymbol{V}$ such that two arbitrary vectors $\boldsymbol{q_1}$ and $\boldsymbol{q_2}$ fulfill the relation: $\langle \boldsymbol{q_1}, \boldsymbol{q_2}\rangle_{\boldsymbol{V}} = \boldsymbol{q_1}^* \boldsymbol{V} \boldsymbol{q_2}$. Practically speaking, $\boldsymbol{V}$ is a diagonal matrix for which the terms V_k correspond to the volume of the k^{th} cell. The adjoint Jacobian matrix is therefore defined as:

$$\tilde{\mathcal{J}}(\boldsymbol{Q}) = \boldsymbol{V}^{-1}\mathcal{J}(\boldsymbol{Q})^*\boldsymbol{V} \tag{5.10}$$

where $\mathcal{J}(\boldsymbol{Q})^*$ is the transpose conjugate of the Jacobian matrix. The adjoint mode $\boldsymbol{q}^\dagger = (\rho^\dagger, \rho u^\dagger, \rho v^\dagger, \rho E^\dagger, \rho\tilde{\nu}^\dagger)^T$ is defined in relation (5.11):

$$\tilde{\mathcal{J}}(\boldsymbol{Q})\boldsymbol{q}^\dagger = \lambda^* \boldsymbol{q}^\dagger \tag{5.11}$$

where λ^* is the complex conjugate of the eigenvalue λ. Moreover, the two bases consisting of the entire set of eigenvectors of the Jacobian matrix and the adjoint Jacobian matrix are bi-orthogonal with respect to the defined inner product, which results in:

$$\langle \boldsymbol{q}_i^\dagger, \hat{\boldsymbol{q}}_j\rangle_{\boldsymbol{V}} = \boldsymbol{q}_i^{\dagger *}\boldsymbol{V}\hat{\boldsymbol{q}}_j = \delta_{ij} \tag{5.12}$$

where δ_{ij} is the Kronecker symbol.

Based on these definitions, the stall adjoint mode and the vortex shedding adjoint mode are computed and their real parts are depicted in Figure (5.9). Pictures (a) and (c) show the stall mode ($\alpha = 18.49°$) and pictures (b) and (d), the vortex shedding mode ($\alpha = 21.00°$). The real parts of the streamwise velocity $\rho u^\dagger$ component of the modes are shown in pictures (a) and (b) and the real parts of the turbulent variable $\rho\tilde{\nu}^\dagger$ component of the modes in pictures (c) and (d). On each picture, the recirculation bubble obtained from the associated steady solution is represented by a black line. The stall adjoint mode is made of a thin structure which starts from the stagnation streamline and follows the airfoil curvature until the recirculation bubble on the suction side. The conservative variables, illustrated by the $\rho u^\dagger$ field (picture (a)), exhibits a larger structure than the turbulent field (picture (c)): the structure goes beyond the separation point of the recirculation bubble while it stops just before for the turbulent variable. Similarly to the direct stall mode, the adjoint mode pulses at the low frequency $\omega = -8.60 \times 10^{-3}$. The vortex shedding adjoint mode exhibits a different behavior. The highest levels are identified in an area located between the stagnation point and the separation point (which are very close for this angle of attack). Moreover, an oscillating pattern, which convects the structures backward, is identified upstream. In the case of the conservative variable (picture (b)), these structures are identified around the recirculation bubble and seem to round the recirculation bubble as they are

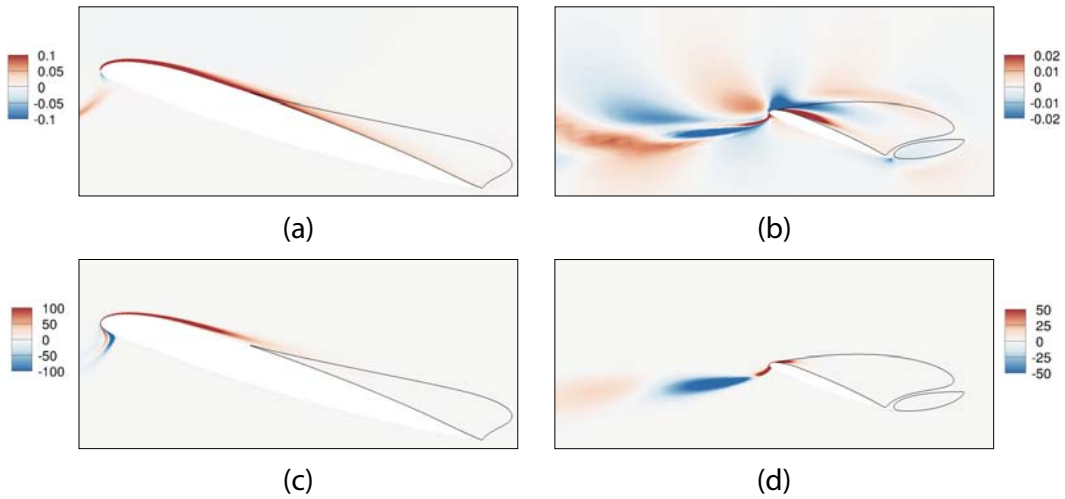

FIGURE 5.9: Visualisation of the structure of the adjoint modes. (a) Real part of the $\rho u^\dagger$ field of the stall adjoint mode ($\alpha = 18.49°$). (c) Real part of the $\rho\tilde{\nu}^\dagger$ field of the stall adjoint mode ($\alpha = 18.49°$). (b) Real part of the $\rho u^\dagger$ field of the vortex-shedding eigenmode ($\alpha = 21.00°$). (d) Real part of the $\rho\tilde{\nu}^\dagger$ field of the vortex-shedding eigenmode ($\alpha = 21.00°$).

convected backward. In the end, similarly to the direct modes, the stall adjoint mode is located close to the airfoil while the vortex shedding adjoint mode is propagated in the freestream.

5.2.5.2 The wavemaker function in the global stability framework

Chomaz [29] noticed for the Ginzburg-Landau equation that the wavemaker can be identified as the overlapping region between the direct and adjoint modes. This approach was extended to open flows by Giannetti and Luchini [59]. The implementation of this concept in this case is to consider a perturbation of the Jacobian matrix by another matrix $\delta\mathcal{J}$. The form of the matrix is considered such that the perturbation only affects the k^{th} cell of the mesh, which results in a diagonal block matrix with all diagonal blocks equal to zero except the one corresponding to the k^{th} cell. In the end, it is shown that, for each cell, the wavemaker function can be written as the product of the p-Euclidian norm of the direct and the adjoint mode:

$$W_{a_k} = ||\hat{\boldsymbol{q}}_k|| \cdot ||\boldsymbol{q}^\dagger{}_k|| \tag{5.13}$$

This function quantifies how the eigenvalue responds to a localized forcing of a given perturbation in the form of an internal forcing. Physically, in this definition, the direct mode (which propagates downstream from the wavemaker region) indicates the region of the flow where the perturbation has a significant amplitude and the adjoint mode (which propagates upstream) indicates the most receptive region of the flow to a forcing. Consequently, with this definition of the wavemaker, the most sensitive regions of the flow are those which simultaneously have a perturbation with a significant amplitude and a significant receptivity to perturbations. Furthermore, according to

Giannetti and Luchini, the regions where eigenvalue changes are the strongest also correspond to the regions where the self-sustained dynamics of the flow starts.

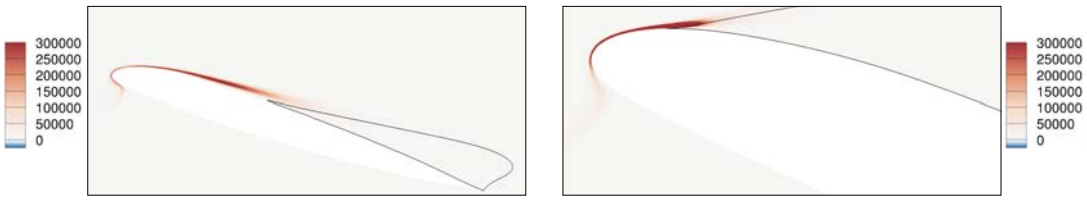

FIGURE 5.10: Visualisation of the structure of the wavemakers W_a. (a) Based on the direct and adjoint stall modes for $\alpha = 18.49°$. (b) Based on the direct and adjoint vortex shedding modes for $\alpha = 21.00°$.

This function is plotted for the two modes in Figure (5.10): picture (a) exhibits the result for the stall mode at $\alpha = 18.49°$ while picture (b) exhibits the result for the vortex shedding mode at $\alpha = 21.00°$. The structure of the wavemaker for the stall mode stretches from the stagnation point to just before the separation point by following the shape of the airfoil. It seems to be driven by the turbulent variable of the adjoint mode as they exhibit very similar structures as can be observed by comparing Figures (5.9)(c) and (5.10)(a). The structure of the wavemaker for the vortex shedding mode stretches from the stagnation point to the separation point. The corresponding area is smaller than the one of the stall mode as the separation point is closer to the leading edge but the intensity in it is higher, particularly close to the separation point.

5.2.5.3 Local contributions of the eigenvalues

The concept of local contribution, introduced by Paladini *et al.* [123], is also investigated. The aim of this approach is to evaluate how each region contributes to the global dynamics of the flow and more particularly to the growth rate and the frequency of the eigenmode. For the k^{th} cell of the mesh, the density function d_k is defined in equation (5.14):

$$d_k = \lambda(\hat{\boldsymbol{q}}_k^* \boldsymbol{q}^\dagger{}_k) \tag{5.14}$$

The local contribution of the flow to the growth rate is defined as the real part of the density d_k: $\Re(d_k)$ and the local contribution of the flow to the angular frequency is defined by the imaginary part of the quantity d_k: $\Im(d_k)$. Note that the growth rate σ and the angular frequency ω are linked to the density d_k by equations (5.15) and (5.16):

$$\sigma = \sum_{k=1}^{N_c} (\Re(d_k) V_k) \tag{5.15}$$

$$\omega = \sum_{k=1}^{N_c} (\Im(d_k) V_k) \tag{5.16}$$

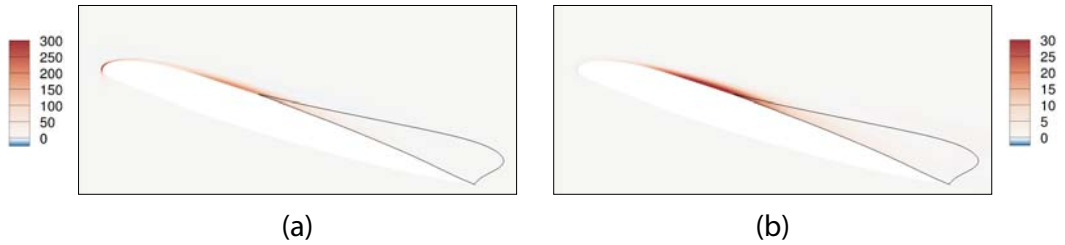

FIGURE 5.11: Visualisation of the sensitivity of the eigenvalue for the stall mode at $\alpha = 18.49°$. (a) Influence on the growth rate ($\Re(d_k)$). (b) Influence on the angular frequency ($\Im(d_k)$).

Figure (5.11) presents the real and imaginary parts of the density d_k for the stall mode: picture (a) exhibits $\Re(d_k)$ and picture (b) $\Im(d_k)$. The regions pointed out, corresponding to the the leading edge and the separation point, are similar to the regions indicated by the wavemaker function in Figure (5.10)(a) although not exactly the same. The contribution to the growth rate (Figure (5.11)(a)) is only positive, which seems to indicate that there is no region of the flow which stabilizes the dynamics. Particularly, the leading edge region is mainly responsible for the positive value of the growth rate while the separation point has a lesser impact on the growth rate. The contribution to the angular frequency (Figure (5.11)(b)) is mostly located on the suction side of the airfoil between the point of maximum thickness of the airfoil and the separation point with a high peak just before the separation point. The contribution is mostly positive as only a very small area of relatively low intensity is identified at the leading edge.

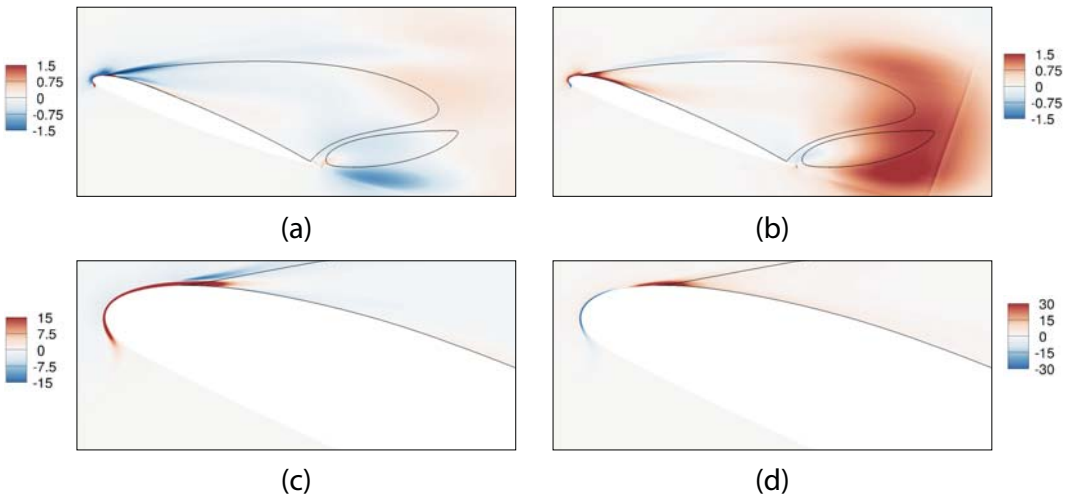

FIGURE 5.12: Visualisation of the sensitivity of the eigenvalue for the vortex shedding mode at $\alpha = 21.00°$. (a) and (c): influence of the growth rate ($\Re(d_k)$). (b) and (d): influence of the angular frequency ($\Im(d_k)$).

The case of the vortex shedding mode is depicted in Figure (5.12). Two different levels of zoom and saturation are depicted: pictures (a) and (b) show a global view

of the airfoil with a low saturation level while pictures (c) and (d) exhibit a zoom in close to the leading edge with a higher saturation level. Pictures (a) and (c) show the contribution of the flow to the growth rate $\Re(d_k)$ while pictures (b) and (d) present the contribution of the flow to the angular frequency $\Im(d_k)$. Two main zones of interest are identified: one close to the leading edge and the other downstream from the recirculation bubbles. The highest levels are identified close to the leading edge (and presented in pictures (c) and (d)). One can note that the contributing regions are more spread for the vortex shedding mode than for the stall mode, which, based on equations (5.15) and (5.16) explains the difference of maximum value of the densities (particularly visible by comparing $\Re(d_k)$ for the two modes). Contrary to the stall mode, the regions of the flow differently contribute to the growth (picture (a) and (c)). Particularly, the thin region located at the leading edge between the stagnation point and the separation point has the highest intensity and a positive contribution while the regions of negative contribution are more spread and with a much lower intensity. The imaginary part of the density $\Im(d_k)$ also reveals a spread region of low intensity located downstream from the two recirculation bubbles and a more condensed region of higher intensity. The first region positively contributes to the angular frequency and strongly recalls the contribution to the angular frequency observed by Paladini *et al.* in the case of a flow around a cylinder [123]. The second region, on the other hand, strongly recalls the stall mode as can be observed by comparing Figures (5.11)(b) and (5.12)(d): a region at the leading edge with a negative contribution and a region at the separation point with a positive contribution.

5.2.5.4 Conclusion on the sensitivity analysis of the flow

In the end, the two sensitivity tools (wavemaker W_a and local contribution to the eigenvalue d_k) used to identify the zones at the origin of the dynamics observed provide mostly similar results. Although a contributing region located downstream from the recirculation bubbles is identified only for the vortex shedding mode, the other contributing regions are similar for the two modes: the leading edge and the separation point. This observation raises some questions regarding the results obtained. Indeed, this region is precisely the one which the RANS approach (and particularly the Spalart–Allmaras model) fails to precisely predict. The main reason for this failure is the fully turbulent approach which prevent the development of a laminar to turbulent transition and possibly of a laminar separation bubble. The use of another turbulence model, possibly coupled to a transition model, would be an interesting path to investigate in future work in order to consolidate those results.

5.3 The complex behavior of the stall eigenmode along the polar curve

The stall eigenmode was described for the particular angle of attack $\alpha = 18.49°$. Actually, this mode is unstable for other values of α as was shown in Figure (5.4) and can be tracked along the curve of steady solutions around stall angle even when the mode is stable. Moreover, it appears that, while the structure of the eigenmode is similar

for each angle of attack at which it exists, the eigenvalues present a complex behavior along the curve of steady solutions.

5.3.1 From Hopf bifurcations to saddle-node bifurcations

In this subsection, we intend to describe the complex behavior of the eigenvalues along the steady solution curve. An easy way to identify the evolution of this pair of eigenvalues is to plot them for different values of α on the same graph. This is the point of Figure (5.13). The union of pictures (a) and (b) to respectively (c) and (d) corresponds to the entire polar curve and the associated entire superimposed spectra.

Starting with pictures (a) and (b), the stall mode and its complex conjugate are first identified for $\alpha = 12.00°$ (not represented on the polar curve in picture (a)). At this angle of attack the mode is stable ($\sigma \approx -0.017$) and unsteady ($\omega \approx 0.024$). The behavior of the eigenvalue remains almost similar until $\alpha \approx 18.35°$. After this angle of attack, by increasing the curvilinear abscissa, the stall mode becomes less and less stable and, in the mean time, its angular frequency decreases. Then, at some point on the upper branch, the stall mode becomes unstable (marked on the polar curve by a switch from full blue line to dashed blue line). Although the mode is now unstable, its angular frequency keeps following the same evolution so that, at some point, it reaches the axis $\omega = 0$. During the whole process, from $\alpha = 12.00°$, the complex conjugate mode follows the exact same behavior in mirror symmetry with respect to the axis $\omega = 0$. This means that the the two unsteady modes merge into a double steady eigenvalue. Then, this double eigenvalue splits into two steady eigenvalue. This state corresponds to the pair of eigenvalues plotted with empty red dots and marked by the dashed red lines on the polar curve (tiny area at the end of the upper branch). Afterwards, one unstable eigenvalue tends to become even more unstable (its value of σ increases) while the other unstable eigenvalue is stabilized. The green dashed line and the green empty dots correspond to the state where an unstable steady eigenvalue coexist with a stable steady eigenvalue. The two extrema steady eigenvalues correspond to the last point of the middle branch plotted in dashed green line in picture (a). The second part of the polar curve is described in pictures (c) and (d). Note that the behavior is similar to one depicted in pictures (a) and (b) but backward. The main difference is that the arc described by the eigenvalues seems to be shifted to the right for the lower branch, which corresponds to a larger range of existence of unstable unsteady modes (blue dashed lines) on the lower branch than on the upper branch. In the end, the stall mode is unstable for a range of angles of attack which seem to correspond to the values for which stall occurs and becomes steady at the very end of the upper and lower branches and on all the middle branch.

To summarize this behavior and introduce the bifurcations that can be deduced, a schematic representation is proposed in Figure (5.14). The left picture is a schematized representation of the hysteretic region of the polar curve. The curve is split into seven different areas marked by a different color code and an associated number. Two zones are labelled 1 and plotted with full blue lines, two others are labelled 2 and plotted with dashed blue, two others are labelled 3 and plotted with red dashed and the last one is labelled 4 and plotted with green dashed line. This color code is similar to that

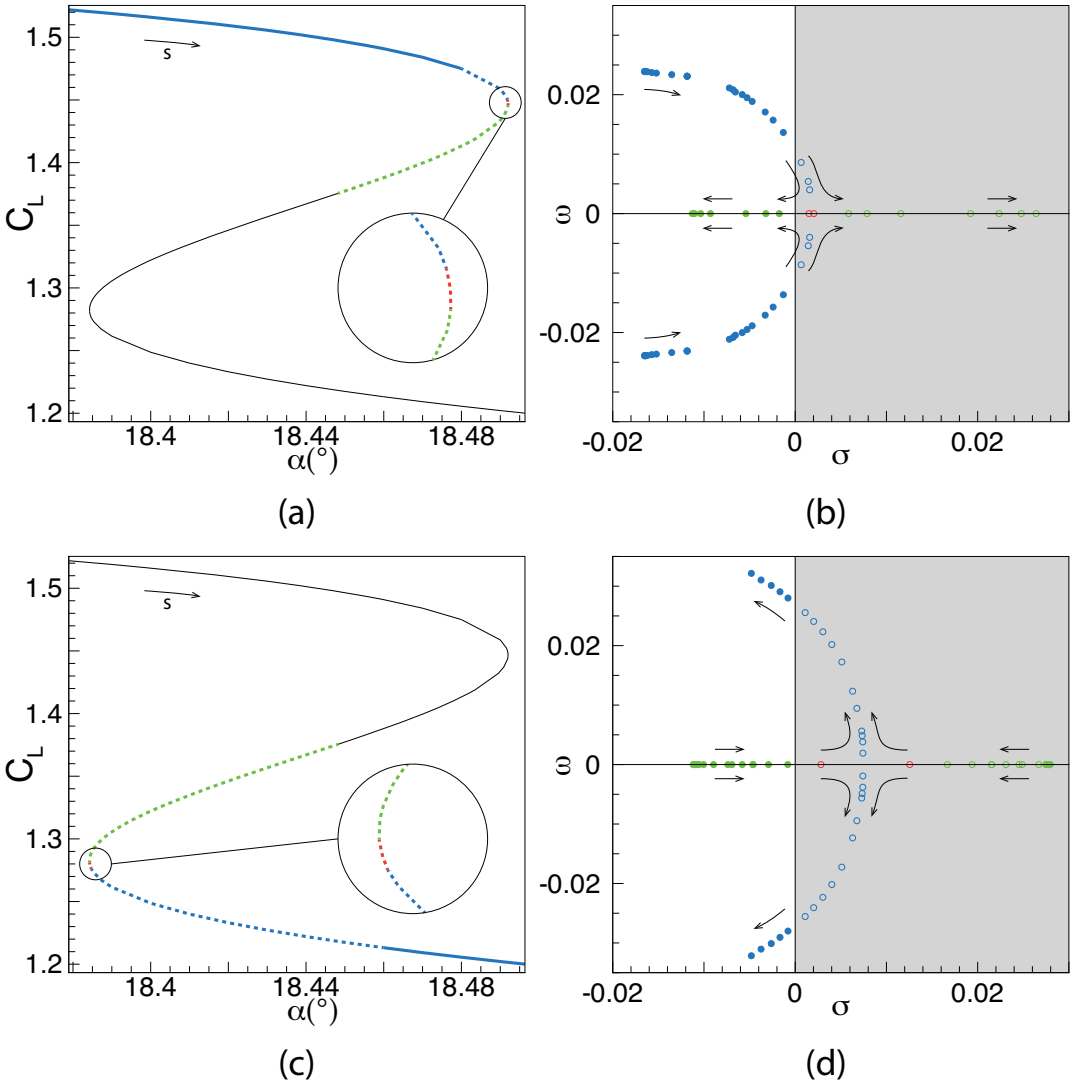

FIGURE 5.13: (a) and (c): lift coefficient polar curves zoomed in close to stall. The colored parts of the curves highlight the angles of attack for which the spectrum is represented. (b) and (d): superimposition of all the eigenspectra of all the angles of attack considered in the complex plane (σ, ω). The arrows associated with the letter s in (a) and (c) indicate the direction of a positive curvilinear abscissa. The arrows in (b) and (d) indicate the evolution of the eigenvalue while moving along the curve of steady solutions with an increasing curvilinear abscissa. The color code matches between the left and right pictures. Full blue line or full blue circle: two unsteady stable modes. Dashed blue line or empty blue circle : two unsteady unstable modes. Dashed red line or empty red circle : two steady unstable modes. Dashed green line or green circle : one unstable steady mode (empty circle) and one stable steady mode (full circle). (a) and (b): from $\alpha = 12.00°$ to $\alpha = 18.46°$ on the middle branch. (c) and (d): from $\alpha = 18.46°$ on the middle branch to $\alpha = 18.80°$.

used in Figure (5.13) and is related to the behavior of the eigenvalues in this area. Delimiters are present between the areas and refer to particular states of the eigenvalues :

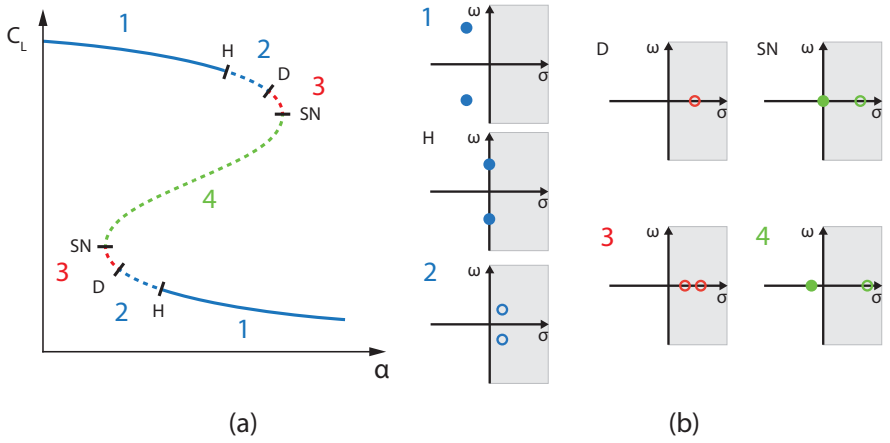

FIGURE 5.14: Schematic scenario of the evolution of the behaviour of the stall mode. (a) Schematic polar curve. (b) Schematic position of the eigenmodes in the complex plane (σ, ω). The color code is similar to the one described in Figure (5.13). Full blue line or full blue circle: two unsteady stable modes. Dashed blue line or empty blue circle : two unsteady unstable modes. Dashed red line or empty red circle : two steady unstable modes. Dashed green line or empty green circle : one unstable steady mode and one stable steady mode.

H corresponds to a Hopf bifurcation, D corresponds to a state for which there are two identical real eigenvalues and SN corresponds to a Saddle Node bifurcation. Picture (b) shows seven diagrams corresponding to the schematized positions of the eigenvalues in the complex plane (σ, ω) for the states 1, 2, 3, 4, H, D and SN. The grey parts of the diagrams correspond to the area where the eigenvalues are unstable.

5.3.2 Evolution of the angular frequency and growth rate of the mode along the curve of steady solutions

The positions of the particular states H, D and SN cannot be exactly determined. However, it is possible to have quite an accurate approximation of their positions by interpolating the behavior of the eigenvalues between the solutions computed. The results are presented in Figure (5.15), which depicts the evolution of the angular frequency ω (a) and the growth rate σ (b) as a function of the angle of incidence. The color code as well as the number referred to the formalism introduced in Figures (5.13) and (5.14). The arrows correspond to a positive evolution of the curvilinear abscissa. A linear evolution of the angular frequency and growth rate is considered between the solutions computed and produces decent results. From these evolutions the positions of the particular points H, D and SN are deduced and summarized in Table 5.3.

Observing the evolution of the angular frequency and the growth rate as a function of the angle of attack it is worth noticing how those quantities drastically evolve close to the ends of branches. The angular frequency, depicted in Figure (5.15)(a), slightly varies in most of the curve and is even almost constant in domain 1 of the upper

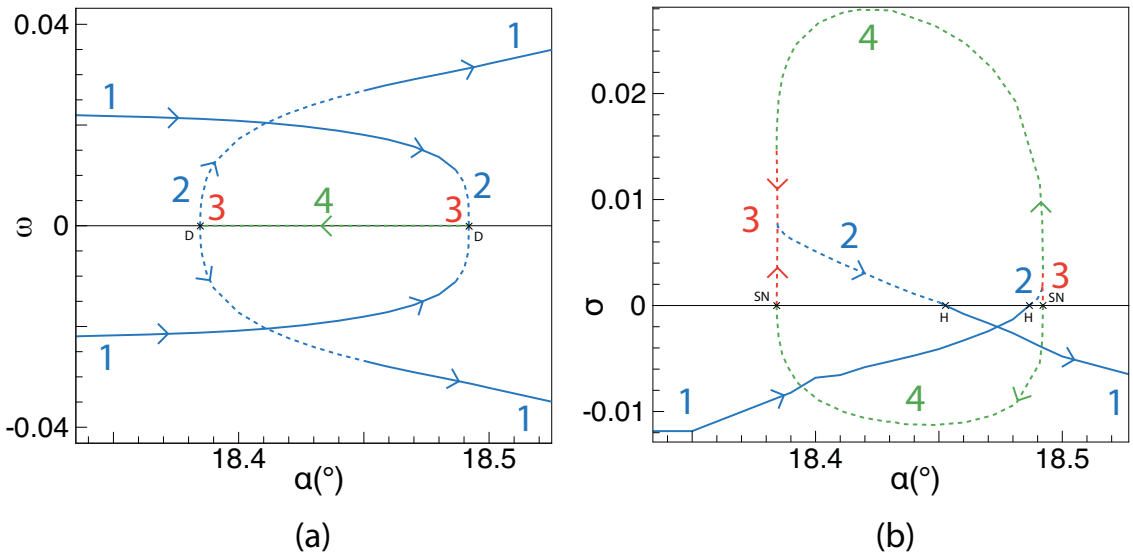

FIGURE 5.15: Evolution of the angular frequency ω and the growth rate σ of the eigenmode as a function of the angle of attack. The color code is similar to the one described in Figure (5.13). Full blue line: two unsteady stable modes. Dashed blue line: two unsteady unstable modes. Dashed red: two steady unstable modes. Dashed green line: one unstable steady mode and one stable steady mode.

brunch. However, at the end of domain 2, on each branch, the angular frequency suddenly tends to 0. The growth rate, depicted in Figure (5.15), evolves linearly in domains 1 and 2 and slightly changes in the middle of domain 4. However, close to the extremities of branches in domains 3 and 4, when the modes are steady, their growth rate suddenly varies. This behavior indicates that, close to the extremities of branches, the eigenvalues are very sensitive to a small change of angle of attack (i.e. of boundary condition).

	Upper branch		Lower branch	
	α (°)	C_L	α (°)	C_L
H	18.4867	1.466	18.4527	1.2153
D	18.4919	1.4496	18.3846	1.277
SN	18.49203	1.4467	18.38423	1.2826

TABLE 5.3: Approximate coordinates of the bifurcation points : Hopf bifurcation H, two identical eigenvalues D and saddle-node bifurcation SN in the (α, C_L) plane.

5.4 Conclusion

This chapter demonstrates the capacity of continuation methods to capture phenomena similar to that observed in chapter 3. The pseudo-arclength methods reveals the existence of a middle branch of steady solutions linking the upper and lower branches.

It results in a range of angles of attack for which three different steady solutions coexist simultaneously. In that sense, the flow around an OA209 airfoil in retreating blade configuration ($\mathrm{Re} = 1.8 \times 10^6$ and $\mathrm{M} = 0.16$) computed with the Spalart–Allmaras turbulence model in the RANS framework behaves similarly to a NACA0012 in several high Reynolds flow configurations described by Wales *et al.* [166]. The global linear stability analysis performed on each steady solution for $12.00° < \alpha < 22.00°$ revealed two different instability mechanisms. The first one appears close to stall and is therefore named the *stall mode*, while the second one appears in the post-stall configuration when the flow is massively separated. This second mode is actually a vortex shedding mode characterized by its classic features: a Strouhal number based on the frontal projected area $\mathrm{St} \approx 0.2$ and large structures located in the trailing edge convected downstream. The Strouhal number of the stall mode appears to be two orders of magnitude lower than the vortex shedding mode: $\mathrm{St} = 0.0027$. It consists of a large structure located above the recirculation bubble on the suction side of the airfoil, which tends to make the recirculation bubble pulsate from tiny to large, generating large variations of lift coefficient. These two features strongly echo the low frequency oscillation phenomenon described in section 1.3.2 and identified with URANS computations in chapter 3. One can note that this mode is very similar to the one observed by Iorio *et al.* [76] for a NACA0012 at higher Reynolds number. By tracking the evolution of the stall mode along the polar curve, a complex evolution of this mode is found. This motion implies Hopf and saddle-node bifurcation and switches between steady and unsteady states. If the saddle-node bifurcations were expected based on the evolution of the steady solutions, the linear stability analysis confirms it with the identification of a steady eigenvalue switching between stable and unstable at these exact positions. This proves that the hysteretic behavior of the polar curve is definitely linked to the behavior of the stall mode.

Finally, the linear global stability analysis is not sufficient to explain several phenomenon. Indeed, although the stall mode presented in this chapter exhibits features very similar to those of the low frequency oscillations presented in chapter 3, it remains unclear why these low frequency oscillations were observed only for a particular value of α while the stall mode appears to be unstable for several angles of attack. Furthermore, there are no explanations on how and when the flow suddenly jumps from one branch to the other. In order to gain an understanding of those two points and based on the discoveries made in this chapter, a more complete study based on unsteady RANS computations is carried out.

Chapter 6

Unsteady RANS simulations of the nonlinear dynamics

Contents

The linear stability analysis of the steady solutions revealed two different unstable modes, one appearing close to stall and the other appearing for high angles of attack. The first one, named stall mode, exists where a hysteresis of the steady solutions is identified. This combination generates a complex evolution of this mode along the steady solution polar curve. The second unstable mode, appearing when the flow is massively separated, is actually a vortex shedding mode. In this chapter, we intend to observe how the linear instabilities identified with the stability analysis grow in time. In particular, the features of the stall mode are very similar to the ones of the low frequency oscillations detailed in 1.3.2. However, although this mode appeared to be unstable for several values of angles of attack, a limit cycle very similar to low frequency oscillations was identified in chapter 3 only for one particular value of α. A more detailed analysis of this limit cycle is carried out in this chapter to address this question. In the continuity of this problematic, the stable state reached by the linearly unstable steady solutions when they do not converge to this large limit cycle is investigated. Particularly, it is interesting to understand in which conditions the flow jumps from one branch to the other.

First, the two limit cycles associated with the two global mechanisms identified with the linear stability analysis are introduced for a particular angle of attack. Then, their range of existence is presented. Finally, a first attempt of bifurcation scenario implying limit cycles is presented and the limitations of the approach are discussed.

A reminder about the initialization of unsteady RANS computations

In this chapter, the results of several unsteady RANS computations are presented. The initialization of these computations may vary depending on the purpose of the computation and, the different methods are briefly summarized. When trying to determine the temporal solution $\boldsymbol{q}(\alpha)$ for a particular angle of attack α, the initialization method depends on the linear stability analysis of the steady solution $\boldsymbol{Q}(\alpha)$ computed at the same angle of attack α.

- If the steady solution $\boldsymbol{Q}(\alpha)$ computed at the angle of attack α is stable, then the unsteady computation performed to determine $\boldsymbol{q}(\alpha)$ is initialized with the steady solution $\boldsymbol{Q}(\alpha + \delta\alpha)$ computed at $\alpha + \delta\alpha$

- If the steady solution $\boldsymbol{Q}(\alpha)$ computed at the angle of attack α is unstable, then the unsteady computation performed to determine $\boldsymbol{q}(\alpha)$ is initialized with the steady solution $\boldsymbol{Q}(\alpha)$ computed at α

Another initialization method is used in this chapter when the objective is to track a stable limit cycle (i.e. when a temporal solution $\boldsymbol{q}(\alpha)$ appears to be a limit cycle and we intend to verify if the temporal solution $\boldsymbol{q}(\alpha + \delta\alpha)$ also exhibits a limit cycle). In such a case, the evolution of the lift coefficient is plotted as a function of time for $\boldsymbol{q}(\alpha)$ and a solution corresponding to a peak of lift (maximum or minimum) is used to initialize the unsteady computation performed to determine $\boldsymbol{q}(\alpha + \delta\alpha)$. This initialization process is presented in more detail in appendix D, which also introduces a quantitative comparison of the results of the linear stability analysis with unsteady RANS computations.

6.1 Identification of limit cycles

6.1.1 A low frequency limit cycle close to stall

An unsteady RANS computation is performed for $\alpha = 18.49°$. The results are presented in Figure (6.1), which shows the evolution of the lift coefficient as a function of time. The lift values of the steady solutions on the upper and lower branches are marked by the dashed lines in Figure (6.1). The simulation is initialized with the high lift steady solution (upper branch), which is, according to the linear stability analysis, unstable. This unstable behaviour is confirmed by the unsteady RANS computation as the lift coefficient quickly departs from the constant value $C_L = 1.459$, which characterizes the high lift solution (upper dashed line in Figure (6.1)). Instead of converging towards a steady value, the lift coefficient oscillates between maximal and minimal values that are larger and smaller than the steady coefficients. This demonstrates the existence of a stable limit cycle, characterized by a low-frequency oscillation of frequency $f = 0.0021$ and of corresponding Strouhal number based on chord length weighted by the sine of the angle of attack $\mathrm{St} = 0.00416$, which surrounds the three steady solutions from the upper, middle and lower branches that coexist at this angle of attack. The temporal behavior of the limit cycle can be compared with the unstable mode found with the linear stability analysis of the steady solution: $f = 0.00137$ and $\mathrm{St} = 0.00271$. Note

that, similarly to the results of unsteady RANS computations introduced in chapter 5, this limit cycle is established only for this very particular angle of attack. However, it is also encountered when initializing the unsteady computation from the middle branch, which was not available in chapter 3 (this case is not represented in Figure (6.1).

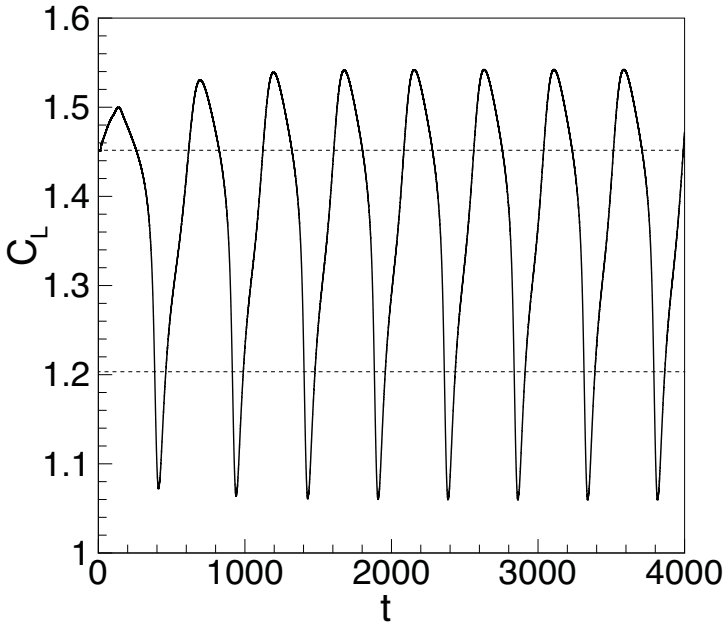

FIGURE 6.1: Full black line : time evolution of the lift coefficient for $\alpha = 18.49°$. Results from an unsteady RANS computation initialized with the steady solution on the upper branch at $\alpha = 18.49°$ (unstable solution in the sense of the linear stability analysis). Dashed lines : value of the lift coefficient of the steady solution on the upper (high lift) and lower branch (low lift).

Figure (6.2) presents the structure of the flow at different times over a period T of oscillation. The pictures on the left depict the ρu field on which the recirculation bubble is plotted in black line. The pictures in the middle shows the evolution of the lift coefficient as a function of time over a period (zoomed from Figure (6.1)). The red dot indicates the instantaneous value of the lift coefficient at the corresponding time. The pictures on the right present the turbulent variable field, $\tilde{\nu}$, on which, the instantaneous recirculation region is delimited with a black line. First, note that when zoomed, the evolution of the lift coefficient is not symmetric over a period (the two half-periods are different). Second, a smaller recirculation bubble located downstream from the larger one appears when the flow is massively separated. However, it seems that this second recirculation bubble only exists in the second half-period. Indeed, when comparing two solutions of same lift value but from different half period (for example the first one (a) and (b) with the last one (o) and (p) or the second one (c) and (d) with the penultimate one (m) and (n)), the solutions of the first half-period only exhibit a large recirculation bubble on the suction side of the airfoil, while the ones of the second half-period exhibit larger recirculation bubbles on the suction side of the airfoil plus a smaller recirculation bubble located at the trailing edge of the airfoil. In more detail, it starts from a low lift

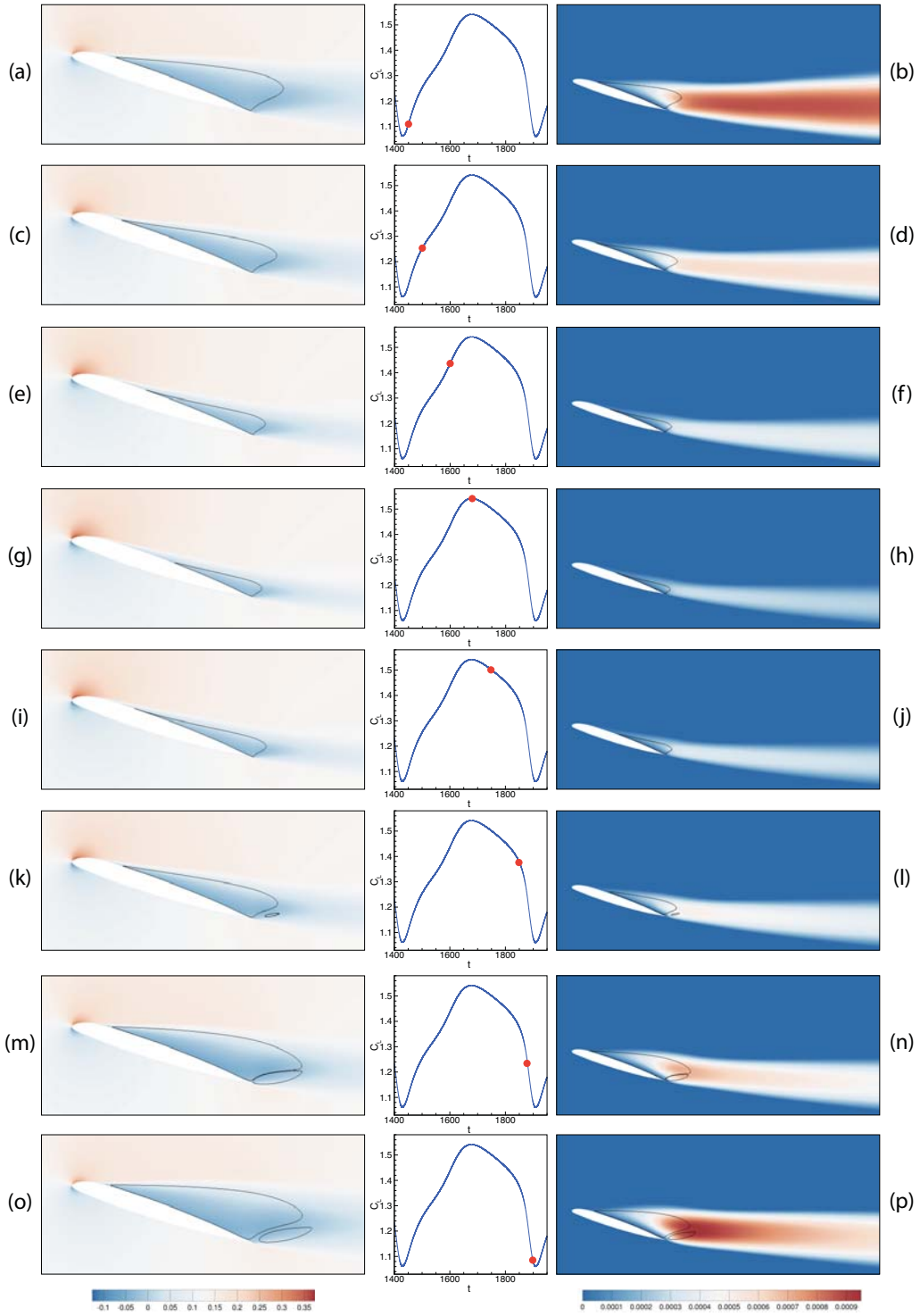

FIGURE 6.2: Flow visualisation over a period for eight different times t such as $t \in [0; T]$. Left : ρu field and $\alpha = 18.49°$. Right : $\tilde{\nu}$ field. Middle : evolution of the lift coefficient over a period. Red dot: position of the visualized flow in the lift coefficient the polar curve.

solution (pictures (a) and (b)): the flow is massively separated on the suction side of the airfoil, which gives birth to a large recirculation bubble. Also, the value of $\tilde{\nu}$ is very

high in all the wake that is wide in that case. Then, the lift coefficient evolves almost linearly until it reaches a maximum value over the period (pictures (g) and (h)). In the meantime the separation point moves toward the trailing edge and the size of the recirculation bubble drastically decreases, as well as the value of $\tilde{\nu}$ and the thickness of the wake. In the second half of the period, the lift coefficient starts decreasing linearly (with a smaller slope than in the first half-period) (pictures (i) and (j)). At the end of the period, there is a sudden break of the slope and an abrupt drop of lift is observed (pictures (k) and (l)). This point seems to correspond to the appearance of the second smaller recirculation bubble at the trailing edge. This sudden decrease of the lift coefficient is associated with a drastic increase of the recirculation bubble size and with an increase of the turbulence eddy viscosity. Note that the smaller recirculation bubble appearing close to the trailing edge has a recirculation direction opposite to the main recirculation region. Finally, the minimum lift coefficient value over the period is reached when the two recirculation bubbles are the largest (pictures (o) and (p)).

To summarize, this unsteady phenomenon is characterized by a large recirculation bubble located on the suction side of the airfoil. This structure pulsates over the period as it alternates between two extrema states : one of low lift, in which the flow is massively separated, the recirculation bubble is big and the wake quite wide and, another, in which the flow is only separated on the half chord, the recirculation bubble very small and the wake very thin. It seems that the appearance of a second recirculation bubble at the bottom of the main one tends to accelerate the lift variation over a period. The evolution of the flow depicted in Figure (6.2) is very similar to the approximated solution computed in section 5.2.4.2 and depicted in Figure (5.7). Indeed, this approximated solution computed from the base flow and the eigenmode also showed a flow that switched between a stalled and an unstalled state. However, the evolution of the lift coefficient was a perfectly sinusoidal while the one depicted in Figure (6.1) exhibits a oscillatory behavior with several subharmonics due to the nonlinear effects taken into account in the URANS computations. Also, this switch between stalled and unstalled state combined to the low frequency computed tend to confirm that this mechanism correspond to a low frequency oscillation phenomenon described in section 1.3.2.

6.1.2 A high frequency limit cycle when the flow is massively separated

An unsteady RANS computation performed for $\alpha = 22.00°$ and initialized with the unstable steady solution at $\alpha = 22.00°$ reveals a high frequency limit cycle. At this angle of attack, the steady solution exhibits a flow mostly separated with a large recirculation bubble and the linear stability analysis revealed an unstable mode with a frequency of $f = 0.0827$ and an associated Strouhal number based on the chord length weighted by the sine of the angle of attack $\mathrm{St} = 0.1935$. This mode was found to be unstable from $\alpha = 20.00°$ and was presented for $\alpha = 21.00°$ in section 5.2.3 of chapter 5. This unstable mode was identified as a very classic bluff body vortex shedding mode because of its very typical value of Strouhal number $\mathrm{St} \approx 0.2$ and because of the structure of the mode made of two rows of patterns in the streamwise direction that oscillate in phase opposition. The evolution of the lift coefficient as a function of time is presented in

figure 6.3. The lift coefficient value at the time $t = 0$ corresponds to the value of lift of the steady solution. One can observe that, from the steady solution, the lift coefficient starts oscillating and, as the time increases, the amplitude of the oscillations, as well as the mean value, increases. Finally, a stable state is reached when the lift coefficient oscillates between the two extrema of a limit cycle that extends from $C_L \approx 1.1$ to $C_L \approx 1.3$. The mean frequency of this limit cycle is $f = 0.0877$ and the associated Strouhal number based on the chord length weighted by the sine of the angle of attack is $\mathrm{St} = 0.205$. This value is in good agreement with the Strouhal number of the unstable mode found with the linear stability analysis for $\alpha = 22.00°$. One can also notice that the time-averaged value of the lift coefficient in the limit cycle significantly defers from the lift value of the steady solution. Indeed, the mean lift coefficient value in the limit cycle is $C_L \approx 1.2$ while the lift coefficient associated with the steady solution is $C_L \approx 0.9$.

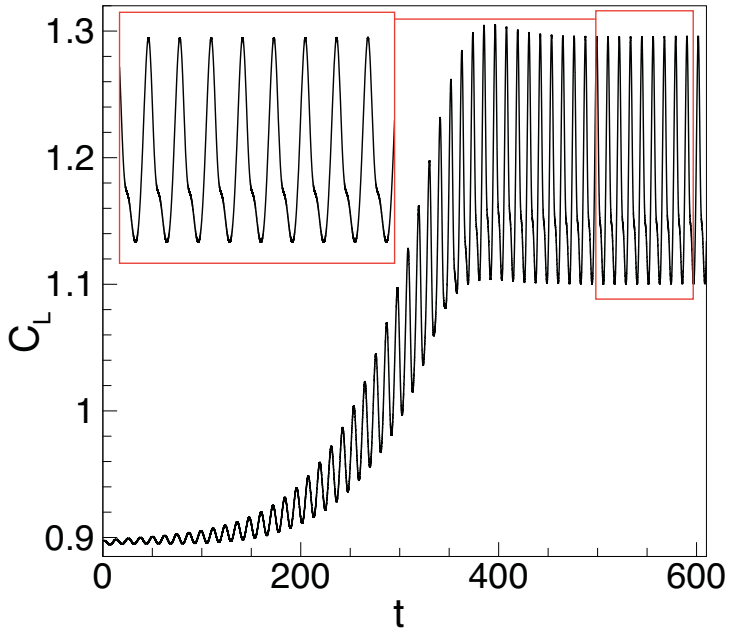

FIGURE 6.3: Time evolution of the lift coefficient for $\alpha = 22.00°$. Results from an unsteady RANS computation initialized with the steady solution (linearly unstable solution)

The structure of the this unsteady phenomenon is presented in Figure (6.4) which shows snapshots of the ρu field and the $\tilde{\nu}$ field at different times over a period. The top pictures ((a) and (b)) of the figure correspond to the maximum lift coefficient solution. It exhibits a large recirculation bubble on almost all the suction side of the airfoil and two tiny recirculation bubbles : one located at the trailing edge and one in the wake. On can also observe a very classic Von Karman vortex street. A vortex, with a high level of turbulence is identified at the trailing edge, just upstream the larger recirculation bubble. Afterwards, the larger recirculation is shrinking and moving upstream forming a new vortex located higher than the first on. The two vortices are convected upstream (pictures (c), (d), (e) and (f)). The turbulence level in the second vortex becomes higher as it moves upstream. In the meantime, the tiny recirculation bubble

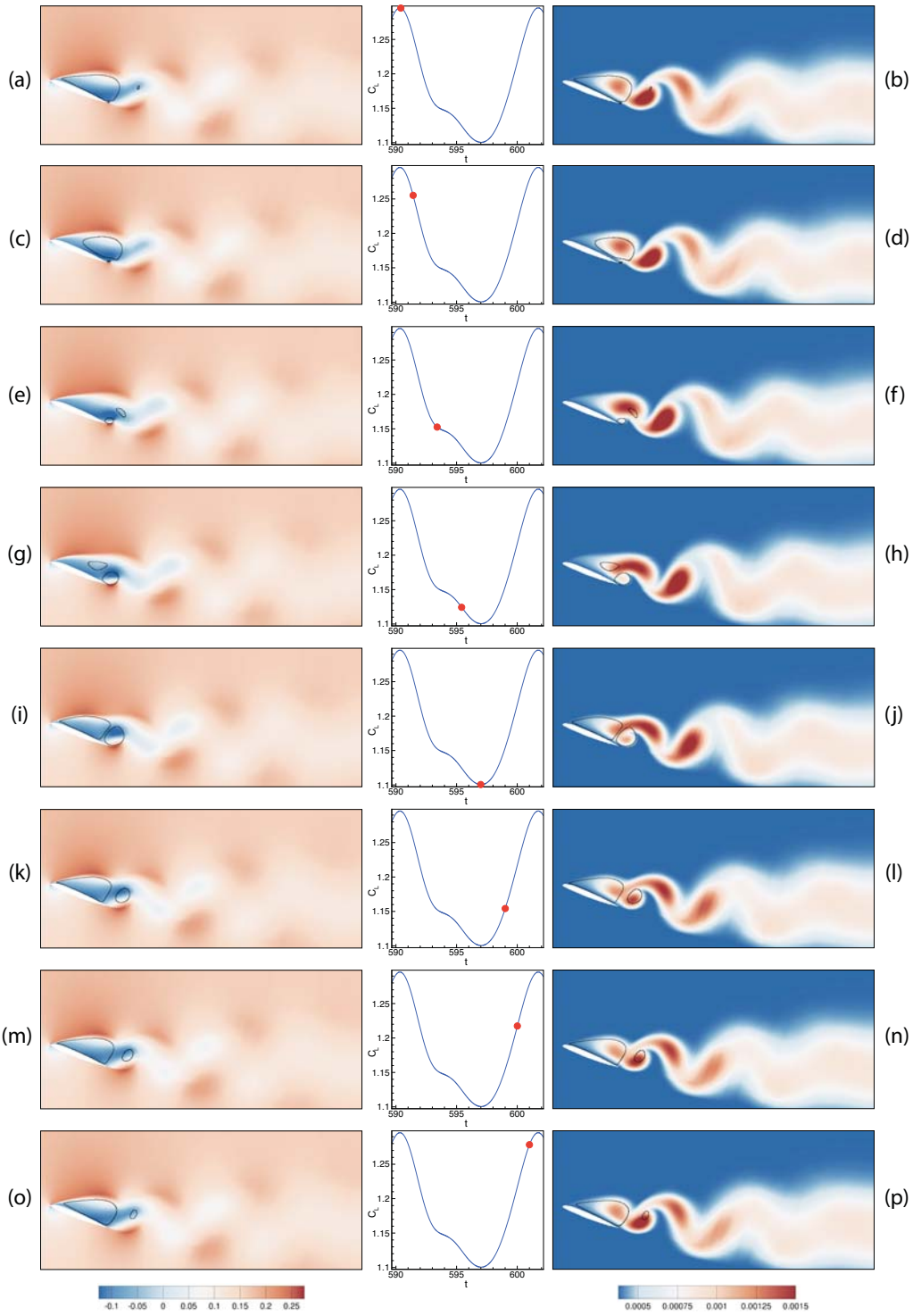

FIGURE 6.4: Flow visualisation over a period for six times t such as $t \in [0; T]$ and $\alpha = 22.00°$. Left : ρu field. Right : $\tilde{\nu}$ field. Middle : evolution of the lift coefficient over a period. Red dot : position of the visualized flow on the polar curve.

at the trailing edge becomes bigger and a second recirculation bubble appears again on the suction side of the airfoil (pictures (g), (h), (i) and (j)). The lowest lift value over

the period is reached when the size of the recirculation bubble located at the trailing edge reaches a maximum (pictures (i) and (j)). Afterwards, the lift starts increasing again as another vortex starts being formed again at the trailing edge (pictures (k) and (l)). The turbulence level in it is getting higher as it is getting extracted from recirculation bubble and while the turbulence level of the other vortices decreases (pictures (m), (n), (o), (p)). Finally, the state of maximum lift is reached again. To summarize, vortices are created alternatively each half-period from the bottom and from the top of the recirculation bubble. These vortices are convected upstream and slowly vanish after reaching a maximum value of turbulence level. Such a formation of vortices is very typical of a bluff-body vortex shedding behavior. Similarly to the low frequency oscillations associated with the stall mode, the behavior observed in Figure (6.4) is very close to that approximated in section 5.2.4.2 and depicted in Figure (5.8).

6.2 Tracking the limit cycles for other angles of attack

The case of limit cycles developing from unstable steady solutions has been investigated. It revealed two different limit cycles, which were introduced for particular angles of attack ($\alpha = 18.49°$ for the low frequency oscillations and $\alpha = 22.00°$ for the vortex shedding mechanism). If the limit cycle associated with the vortex shedding mechanism was identified from several steady solutions, the limit cycle associated with the low frequency oscillations could only be identified from steady solutions at $\alpha = 18.49°$. However, it is still possible that this limit cycle exists for different angles of attack but could not be reached from other steady solutions. In order to verify whether or not this is the case for the limit cycle identified close to stall, a continuation of this limit cycle is performed. As briefly mentioned in section 1.5, dedicated continuation methods exist in bifurcation theory for limit cycles tracking. However, in order to avoid the development of an additional tools, the range of existence of this limit cycle was investigated by performing Unsteady RANS computations with the appropriate initialization (detailed at the beginning of the present chapter).

The results found when tracking the limit cycles are presented in Figure (6.5). Picture (a) exhibits the whole polar curve with the two limit cycles identified while picure (b) presents a zoom in close to stall. The limit cycle associated with the vortex shedding mechanism is depicted in Figure (6.5)(a) mostly for comparison matters. One shall note that for this limit cycle, the tracking approach did not provide additional information compared to the unsteady computations initialized with steady solutions. Indeed, this limit cycle could be identified only for angles of attack corresponding to unstable steady solutions. This seems to indicate that the Hopf bifurcation, occurring when the vortex shedding mode becomes unstable, is supercritical. On the contrary, the low frequency limit cycle is identified for several values of α with this approach whereas it could be identified only from steady solutions for one particular angle of attack. It appears to exist for a range of approximately $\Delta\alpha = 0.045°$, as illustrated in Figure (6.5)(b), in which it always surrounds the steady solutions existing (three in the hysteresis area, one otherwise). It characterizes one of the main feature of this limit cycle compared to the vortex shedding one: a very large amplitude ($\Delta C_L \approx 0.45$ by comparison to $\Delta C_L \approx 0.2$ for the vortex shedding limit cycle). For this reason,

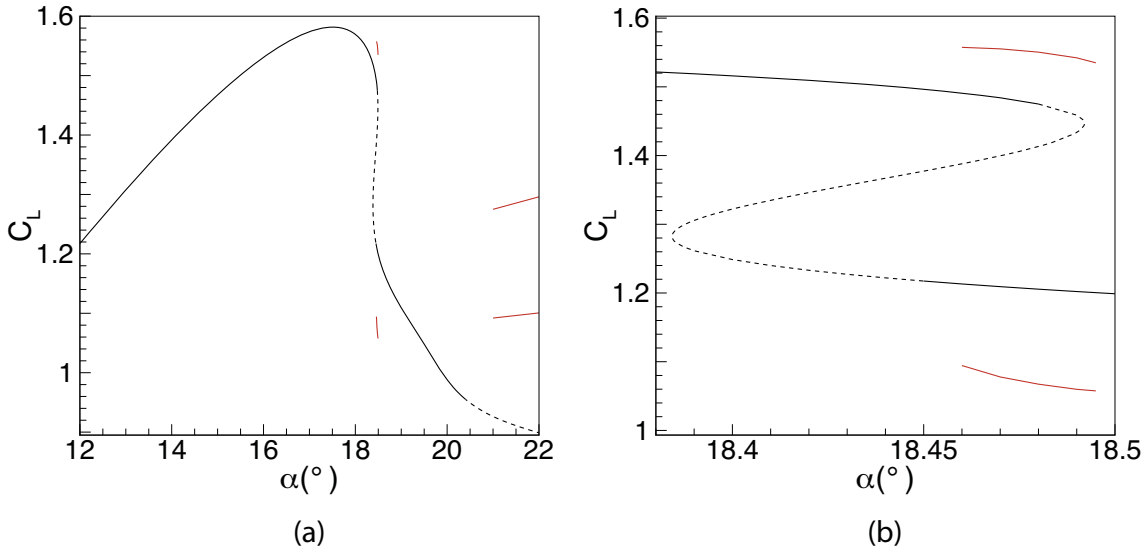

FIGURE 6.5: Superimposition of the polar curve made of steady solutions (black lines for stable solutions and dashed lines for unstable solutions from chapter 5) and extreme values of stable limit cycles (red lines). The limit cycles are represented with the highest and lowest values of the lift coefficient reached over a period for each angle of attack. The highest red line corresponds to the values of lift coefficient encountered at the top peak of the time oscillations and the lowest red line to the values of lift coefficient at the bottom peak of the time oscillations. (a) All the polar curve with two limit cycles. (b) Zoom in close to stall with one limit cycle only.

the limit cycle associated with low frequency oscillations is sometimes referred to as the *large* limit cycle in the remainder of the manuscript. Another feature of this limit cycle is the variation of the number and the state of the steady solutions coexisting with this limit cycle. In particular, in the hysteretic region, this limit cycle coexist with a varying number of stable and unstable steady states while when it bypasses the hysteretic region it coexists with only one stable steady solutions on the lower branch. This raises several questions such as: when several stable states coexist, which one is preferentially reached and based on which condition? Why do some unstable steady states fail to reach this limit cycle while other succeed? Why do the limit cycle vanish for the particular angles of attack identified?

6.3 Proposition of a stall scenario

The tracking of the limit cycles raised some questions, all related to the low frequency limit cycle appearing close to stall. In this section, we intend to focus on the phenomenon occuring in this region, in an attempt to answer the aforementioned questions. The retained approach is to perform additional unsteady RANS computations in this particular area and observe how the initial conditions affect the results. Seven regions of interest, depicted in Figure (6.6)(a), are defined based on the number of

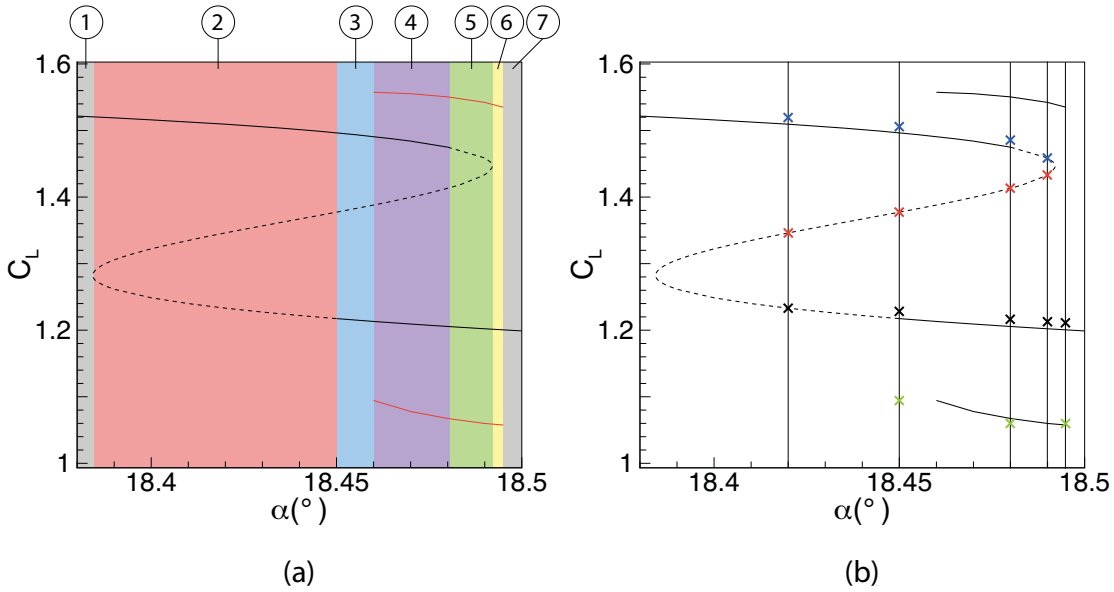

FIGURE 6.6: (*a*) Visualisation of the seven regions of interest identified close to stall. Each region exhibits a different number of coexisting solution or a different linear behaviour of the steady solutions. (*b*) solutions used to initialize the unsteady computations. One angle of attack (marked by a vertical black line) is chosen in each region between 2 and 5. Crosses indicate the solutions used as initializer. Blue crosses correspond to steady solutions from the upper branch. Red crosses correspond to steady solutions from the middle branch. Black crosses correspond to steady solutions from the lower branch. Green crosses correspond to solutions from an extrema value of large limit cycle detected for a different angle of attack.

steady solutions, their linear stability and the existence or not of a limit cycle. They are characterized by the following properties:

- 1: one stable steady solution on the upper branch (furthest left grey region in Figure (6.6))(*a*)

- 2: one stable steady solution on the upper branch and two unstable steady solutions on the middle and lower branches (red region in Figure (6.6))(*a*)

- 3: two stable steady solution on the upper and lower branches and an unstable steady solution on the middle branch (blue region in Figure (6.6))(*a*)

- 4: two stable steady solution on the upper and lower branches and an unstable steady solution on the middle branch and a large limit cycle (violet region in Figure (6.6))(*a*)

- 5: one stable steady solution on the lower branch and two unstable steady solutions on the middle and upper branches and a large limit cycle (green region in Figure (6.6))(*a*)

- 6: one stable steady solution on the lower branch and a large limit cycle (yellow region in Figure (6.6))(a)

- 7: one stable steady solution on the lower branch (furthest right grey region in Figure (6.6))(a)

Unsteady RANS computations are performed for one particular angle of attack in each region (except the first and seventh region that are not investigated as of few interest and quite obvious). For each angle of attack investigated, as many unsteady RANS computations as there are existing solutions (i.e. steady solutions and limit cycle) are performed. Each unsteady computation is initialized with a different solution as summarized in Figure (6.6)(b), which presents the chosen angles of attack (vertical black line) and the solutions used as initializer (crosses). Note that the crosses associated with linearly stable solutions are willingly shifted from the polar curve to express the use of slightly perturbed solutions as initializer as described at the beginning of the present chapter. The same observation can be made for the limit cycle, which corresponds to the initialization used in the tracking process. In the end, fifteen unsteady RANS computations are performed from five different angles of attack: $\alpha = 18.42°$ (from zone 2 in red), $\alpha = 18.45°$ (from zone 3 in blue), $\alpha = 18.48°$ (from zone 4 in violet), $\alpha = 18.49°$ (from zone 5 in green) and $\alpha = 18.495°$ (from zone 6 in yellow).

Figure (6.7) presents the results of the unsteady RANS computations, for the five different angles of attack investigated, from two different manners. The left pictures present the evolution of the lift coefficient as a function of time while the right pictures present the evolution of the solutions in the plane (C_M, C_L). The arrows indicate the direction of a positive time evolution. In each figure, the results of all the unsteady computations performed for a same angle of attack (with different initialization) are represented. The first angle of attack investigated is $\alpha = 18.42°$ ((a) and (b)). Three different computations are performed and all converge to the only linearly stable steady solution identified : the one on the upper branch. For $\alpha = 18.45°$ ((c) and (d)), it is legitimate to wonder which stable state the unsteady computations will reach as two linearly stable steady solutions coexist contrary to the previous case $\alpha = 18.42°$. It appears that only the computation initialized with the slightly modified steady solution on the lower branch converges to a low lift solution. The two other computations converge to the high lift stable solution. It is worth noticing how the temporal solution from the middle branch bypass the low lift steady solution before reaching the upper branch: in the (t,C_L) plane, it corresponds to the red curve that, first, decreases and reaches a lift value lower than the low lift steady solution and, afterwards, goes to the upper branch. In the (C_M, C_L) plane, it is characterized by the red curve that surrounds the low lift and low pitching moment steady solution, before reaching the steady solution of high lift and high pitching moment. It raises the first question of this analysis : why such a behavior is observed whereas a one similar to results obtained for $\alpha = 18.42°$ could have been expected? (i.e. the computation from the middle branch going straight to the steady state on the upper branch). The third angle of attack considered is $\alpha = 18.48°$ ((e) and (f)). The computation initialized with a solution from a limit cycle leads to a limit cycle of slightly different shape. One can observe how this limit cycle encapsulates the three steady solutions in the (C_M,C_L) plane. The computations started from the steady solutions lead to the same final result that the

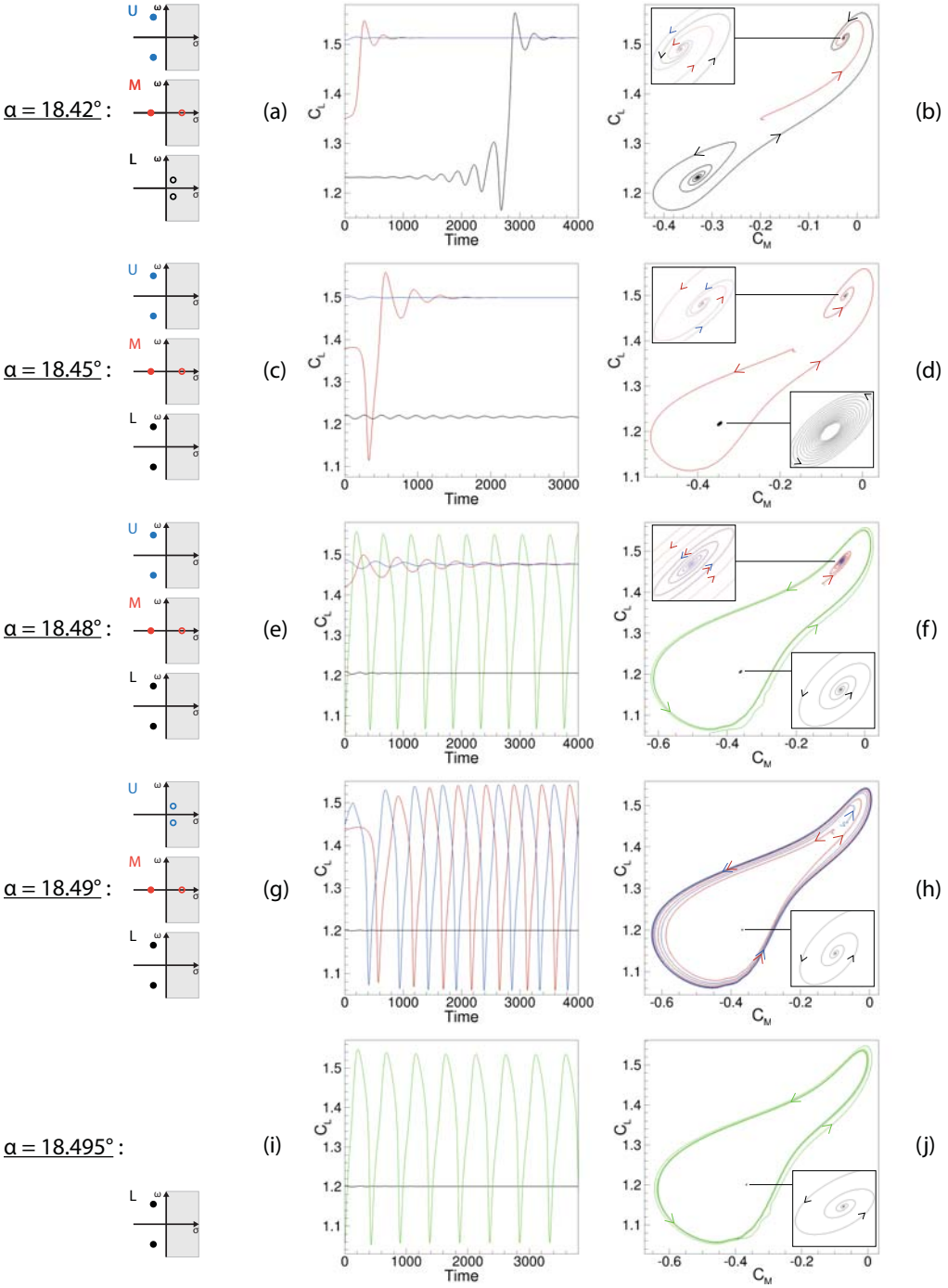

FIGURE 6.7: Temporal solutions represented in two different planes (t,C_L) (left pictures) and (C_M,C_L) (right pictures, also often called phase portrait) for different initial conditions and angles of attack. (a) and (b): $\alpha = 18.42°$. (c) and (d): $\alpha = 18.45°$. (e) and (f): $\alpha = 18.48°$. (g) and (h): $\alpha = 18.49°$. (i) and (j): $\alpha = 18.495°$. For each angle of attack, the color of the curve refers to the color of the cross in Figure (6.6)(b), marking the solution used to initialize the unsteady computation indicated. The linear behavior of the steady solutions is recalled next to the temporal solutions, as well as the angles of attack.

computation for $\alpha = 18.45°$ although the temporal solution from the middle branch (red curve) does not bypass the low lift low pitching moment solution, but goes straight to the high lift steady solution similarly to the case $\alpha = 18.42°$. The case $\alpha = 18.49°$ ((f) and (g)) presents three computations: two from linearly unstable steady solutions (upper and middle branch), which reach the large limit cycle by oscillating around the three steady solution for several periods and one from the slightly perturbed linearly stable steady solution on the lower branch, which returns to its stable steady state. Finally, the last angle of attack investigated is $\alpha = 18.495°$ ((i) and (j)) for which two time-stepping computations are performed: one from a limit cycle and one from a low lift solution. They respectively converge to a limit cycle and to a linearly stable steady solution on the lower branch.

A few observations can be made from all these unsteady computations. First, the results are qualitatively in perfect agreement with the linear stability analysis (one can refer to appendix D for more details on the comparison between linear stability analysis and Unsteady RANS computations):

- The steady solutions for which a stable unsteady mode was found, are attractors around which the temporal solutions oscillate before converging towards it.

- The steady solutions for which an unstable unsteady mode was found, are repellers around which the oscillations of the temporal solution grow in time[1].

- The steady solutions for which an unstable steady mode was found (mostly on the middle branch) are repellers for which the temporal solutions directly diverge from this solution without oscillating around it

Second, one can observe several noticeable features:

- Among all the time-stepping computations performed, the only ones that reach a steady low lift state are the ones initialized with a low lift steady solution. Neither the computations initialized with steady solutions from the upper and middle branches nor the ones initialized with solutions from the limit cycle reach a low lift steady state. In other words, all the time-stepping computations initialized with linearly unstable steady solutions converge either to a high lift solution or to a large amplitude limit cycle.

- The results of the time-stepping computations initialized with steady solutions from the middle branch are also quite interesting. These steady solutions are linearly unstable and temporal solutions diverge from them towards a stable state. It seems that as long as a linearly stable steady solution exists on the upper branch, the computations converge to this state ($\alpha = 18.42°$, $\alpha = 18.45°$ and $\alpha = 18.48°$) while, when the steady solutions on the upper branch become unstable, the time computations initialized from the middle branch reaches the stable limit cycle. Also, it is legitimate to wonder why the computations started

[1]It is not obvious for the computation initialized with the high lift unstable steady solution for $\alpha = 18.49°$ ((g) and (h)). However, two explanations can be proposed. First, the angular frequency of the stall mode associated with this steady solution is very low and, consequently, the oscillations are too slow to develop. Second, there is not a perfect match between the Unsteady RANS computations and the linear stability analysis and the initialization would actually correspond to a steady solution in the region labelled 3 in Figure 5.14 of chapter 5.

from the middle branch sometimes reach the steady state after surrounding the solution on the lower branch (for example $\alpha = 18.45°$) and sometimes not (for example $\alpha = 18.42°$ and $\alpha = 18.48°$)

6.4 Conclusion

Although several differences between the time stepping methods in *elsA* and the continuation methods were highlighted in chapter 4, the method detailed in appendix C was proven to successfully reconcile the results from the two approaches. Indeed, in the present chapter, a very good agreement was shown between the linear behavior of steady solutions and the growth in time of the instabilities identified (also illustrated in appendix D). The two unstable modes identified appeared to develop into limit cycles for several values of angles of attack. In particular, the large limit cycle is identified for several angles of attack at which very different steady states exist. A detailed investigation is carried out in the stall area. Although the perfect agreement between the linear stability analysis and unsteady RANS computations is again highlighted, this investigation seems to raise more questions than answers: why does the limit cycle suddenly vanish for particular angles of attack? Why is there no consistency in the way the time-stepping computations starting from the middle branch reaches a stable state? Why is it impossible to reach the limit cycle from steady solutions apart from angles of attack at which an unstable steady solution exist on the upper branch? Why is it impossible to reach a low lift steady state from any unstable steady state? A possible answer to several of those questions could be the existence of unstable limit cycles, which cannot be detected with the approach considered in this chapter. The objective of the next chapter is to investigate this possibility and try to obtain a more complete bifurcation scenario.

Chapter 7

A static stall model based on the linear analysis of RANS solutions

Contents

The linear stability analysis of the steady solutions revealed a complex scenario close to stall (chapter 5). This scenario was confirmed by studying the nonlinear behavior of the flow with unsteady RANS computations, which also revealed a low frequency limit cycle of large amplitude. However, several points, detailed at the end of chapter 6, remain unclear. For instance, the appearance and disappearance of the limit cycle or the impossibility to reach a low lift steady state from an unstable steady solution are two phenomena that cannot be explained with the available data. One of the possible

reason could be the existence of unstable limit cycles. Indeed, one of the limitation of tracking limit cycle with time steppers is the impossibility to identify unstable limit cycles. Specific tools exist in bifurcation theory to track these unstable limit cycles. However, their development in the RANS framework is not trivial and would be time consuming. Instead an alternative approach is considered: a one-equation nonlinear model, named *static stall model* is created. This model reproducing the linear behavior observed with the stability analysis is created and calibrated based on the steady RANS solutions and their linear behavior. Then, by studying the nonlinear behavior of this model, it is expected to gain an understanding of the nonlinear mechanisms that could not be identified with unsteady RANS computations. The philosophy leading to the considered form of the one-equation model is detailed in appendix E. Note that, the final form of the model is similar to a particular case of the more general Pernarowski's model [126] used in biophysics to study pancreatic beta cells. More details can be found in the works of De Vries [35] and Fallah [52] in which curves very similar to the ones introduced in this chapter can be encountered. In the end, the development of such a model should allow us to have a better understanding of the nonlinear mechanisms at a reduced computational cost.

The first part of the chapter is dedicated to the calibration of the static stall model. Then, the nonlinear behavior of the calibrated model is studied and a bifurcation scenario is proposed. Finally, other possible scenarios are discussed.

7.1 Calibration of the one-equation static stall model

7.1.1 Equation considered

The equation of the model to be calibrated is presented in equation (7.1). The general form of the equation remains the same as that introduced in equation (E.16) but the parameters B and C becomes higher order polynomials.

$$\frac{d^2C_L}{dt^2} + p_1(C_L) \cdot \frac{dC_L}{dt} + c \cdot (\Delta\alpha + p_2(C_L)) = 0 \tag{7.1}$$

where :

- $p_1(C_L) = \sum_{i=0}^{N_1} b_i \cdot C_L^i$, with N_1 the order of the polynomial $p_1(C_L)$
- $p_2(C_L) = \sum_{i=1}^{N_2} a_i \cdot C_L^i$, with N_2 the order of the polynomial $p_2(C_L)$
- $\Delta\alpha = \alpha - \alpha_s$, with α_s an arbitrary defined *stall angle*
- $C_L = c_l - c_{l_s}$, with c_{l_s} the lift value associated to α_S

Considering the decomposition $C_L = C_{L_0} + C'_L$, we obtain the equations at order zero (ϵ^0) and one (ϵ^1).

$$\epsilon^0 \quad : \quad \Delta\alpha + p_2(C_L) = 0 \tag{7.2}$$

$$\epsilon^1 \quad : \quad \frac{d^2C'_L}{dt^2} + p_1(C_{L_0}) \cdot \frac{dC'_L}{dt} + c \cdot (\frac{dp_2}{dC_L}(C_{L_0})) \cdot C'_L = 0 \tag{7.3}$$

By similarity with the case of the damped harmonic oscillator presented in subsection E.2.2, we define:

$$B = p_1(C_{L_0}) \tag{7.4}$$

$$C = c \cdot \frac{dp_2}{dC_L}(C_{L_0}) \tag{7.5}$$

$$\Delta = B^2 - 4 \cdot C \tag{7.6}$$

7.1.2 Calibration of the steady states

The first step is to arbitrary define a *stall point* (α_s, c_{l_s}), then we choose N points $(\alpha_i, C_{L_{0_i}})$ to fit and we solve the system (7.7) to find the N coefficients of the polynomial $p_2(x)$.

$$\begin{bmatrix} C_{L_{0_1}} & C^2_{L_{0_1}} & \dots & C^N_{L_{0_1}} \\ \vdots & \vdots & & \vdots \\ C_{L_{0_N}} & C^2_{L_{0_N}} & \dots & C^N_{L_{0_N}} \end{bmatrix} \cdot \begin{bmatrix} a_1 \\ \vdots \\ a_N \end{bmatrix} = \begin{bmatrix} -\Delta\alpha_1 \\ \vdots \\ -\Delta\alpha_N \end{bmatrix} \tag{7.7}$$

A good fit is obtained with a 4^{th} order polynomial and consequently no higher orders are investigated. The result of the calibration is presented in Figure (7.1).

7.1.3 Calibration of the linear behavior

7.1.3.1 Link between linear stability of RANS solutions and model parameters

In the spirit of what was done for the simplest version of the one-equation model (see appendix E), the parameters B and Δ are used to calibrate the linear behavior of the model. As a reminder, B drives the position of the Hopf bifurcations (labelled H in chapter 5) while Δ drives the position of the steady solution with two identical eigenvalues (labelled D in chapter 5). However, the result of the linear stability analysis of the steady RANS solutions did not provide values for B and Δ but a pair of eigenvalue $\lambda_{1/2}$ for each angle of attack, characterized by their angular frequencies $\omega_{1/2}$ and their growth rates $\sigma_{1/2}$. First a link is established between the eigenvalues and the model parameters B and Δ.

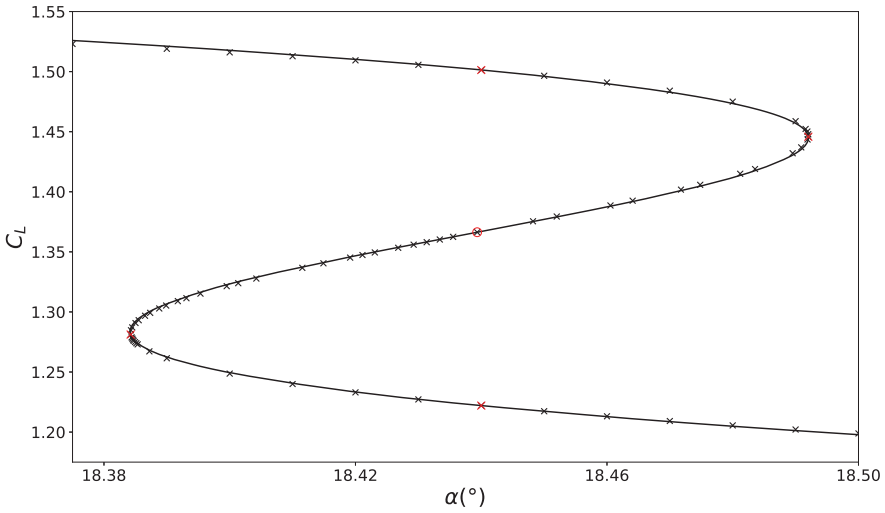

FIGURE 7.1: Calibration of the steady states. The black crosses mark the steady solutions from the RANS computations. The four red crosses are the steady solutions used for the fitting. The arbitrary stall angle and its associated lift coefficient is circled in red. The result of the fitting operation is plotted in full black line.

- When the modes are steady, their angular frequencies are null ($\omega_{1/2} = 0$). This leads to:

$$\lambda_{1/2} = \sigma_{1/2} = \frac{-B \pm \sqrt{\Delta}}{2} \tag{7.8}$$

- When the modes are unsteady, one is the complex conjugate of the other and therefore they have the same growth rates ($\sigma_1 = \sigma_2$) and opposite angular frequencies ($\omega_1 = -\omega_2$). This leads to:

$$\lambda_{1/2} = \sigma_{1/2} + i \cdot \omega_{1/2} = \frac{-B \pm i \cdot \sqrt{-\Delta}}{2} \tag{7.9}$$

From equations (7.8) and (7.9), we can deduce the following link between the parameters B and Δ and the components of the eigenvalues $\lambda_{1/2}$:

$$\begin{cases} \text{If } \omega_{1/2} = 0 : \\ \qquad B = -(\sigma_1 + \sigma_2) \\ \qquad \Delta = (\sigma_1 - \sigma_2)^2 \\ \\ \text{If } \omega_{1/2} \neq 0 : \\ \qquad B = -(\sigma_1 + \sigma_2) \\ \qquad \Delta = -(\omega_1 - \omega_2)^2 \end{cases} \tag{7.10}$$

with equations (7.10) it is now possible to determine a value of B and Δ for each angle of attack. Let us designate by B_{comp} and Δ_{comp} the values of B and Δ deduced from the results presented in chapter 5. The objective is now to find the best coefficients b_i and c, which appears in the parameters B and Δ in order to minimize the gap between the experimental values B_{comp}, Δ_{comp} and the model values B, Δ. The mean least square error is defined for each parameter :

$$B_{LMS} = \sum_{i=1}^{M} [p_1(C_{L_0}^i) - B_{comp}(\lambda_{1/2}^i)]^2 \tag{7.11}$$

$$\Delta_{LMS} = \sum_{i=1}^{M} [p_1(C_{L_0}^i)^2 - 4 \cdot c \cdot \frac{dp_2}{dC_L}(C_{L_0}^i) - \Delta_{comp}(\lambda_{1/2}^i)]^2 \tag{7.12}$$

where M is the number of data from the computations considered for the calibration.

7.1.3.2 Non-dominated Sorting Genetic Algorithm II (NSGA-II)

The goal is now to minimize two objective functions at the same time for several parameters (depending on the order N of the polynomial $p_1(x)$ considered). The main difficulty in solving these kinds of problems is that there is no single solution that minimizes both objective functions. Instead, several admissible solutions are found depending on how one objective function is weighted compared to the other. Indeed, most of the time, a solution which minimizes an objective function will give poor results on another objective function: the objective functions are defined as conflicting [50]. In such a case, several *Pareto* optimal solutions exist. They correspond to the solutions for which the value of an objective function cannot be improved without degrading the values of the others.

A first approach to solve this multi-objectives problem could be to build a single objective function made of these two objective functions. This is the spirit of the objective weighting approach, distance functions or min-max formulation. However, all these methods offer a single optimal solution to the problem heavily dependent on the formulation used to build the scalar objective function. Moreover, it is difficult to prioritize the multiple objective functions *a priori*, during the building of the single objective function. One can find a summary of all these approach in the paper of Srinivas and Deb [153]. An alternative to such methods is to try to obtain several

Pareto solutions in a single computation in order to be able to choose the solution the most adapted to the situation. This ensemble of solutions is called a Pareto front. Genetic Algorithms allow us to compute the solutions of this front. The particular case of the Non-dominated Sorted Genetic Algorithm II (NSGA-II) [37] used in our case is presented in more detail in appendix F.

7.1.3.3 Results of the calibration

The NSGA-II algorithm is used to calibrate the coefficients of the polynomial $p_1(x)$ and c. A third order polynomial is chosen for $p_1(x)$. The first reason for this choice is to have the same number of parameters and, thus, a similar precision on the calibration of steady states and their linear stability. Also, it appears that higher order does not significantly improve the results. The Pareto front obtained (see appendix F for more details) is presented in Figure (7.2). Three particular solutions are highlighted to be presented in more detail: the blue point minimizes the error B_{LMS}, the red point minimizes the error Δ_{LMS} and the green point is a compromise between the two.

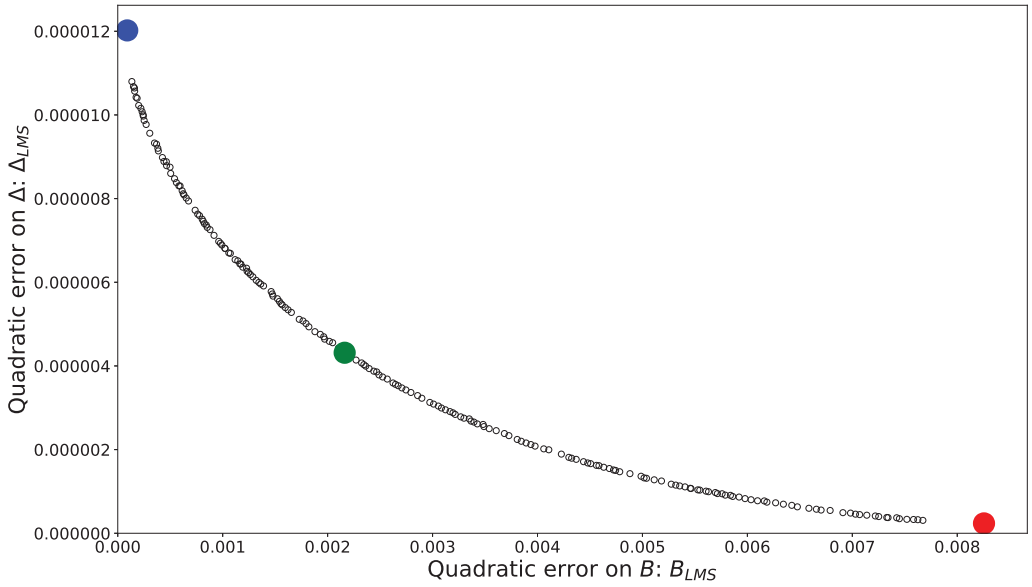

FIGURE 7.2: Pareto front obtained for the calibration of the linear behavior. Three solutions are highlighted to be presented in more detail.

Figure (7.3) compares the evolution of four variables as a function of the angle of attack between different calibration of the model and the results of the RANS computations: B (picture a), Δ (picture b), σ (picture c) and ω (picture d). Figure (7.3)(a) confirms that the blue solution, which minimizes the least mean square error on B, is the best fit for B, while the red solution, which maximizes the least mean square error on B, is the worst fit. Figure (7.3)(b) shows the exact opposite for the parameter Δ. For both variables, the green solution, stands in between these two extrema, representing a compromise between the two solutions. Figures (7.3)(c) and (d) show that a better fit on B (blue solution) corresponds to a better fit on the growth rate, while

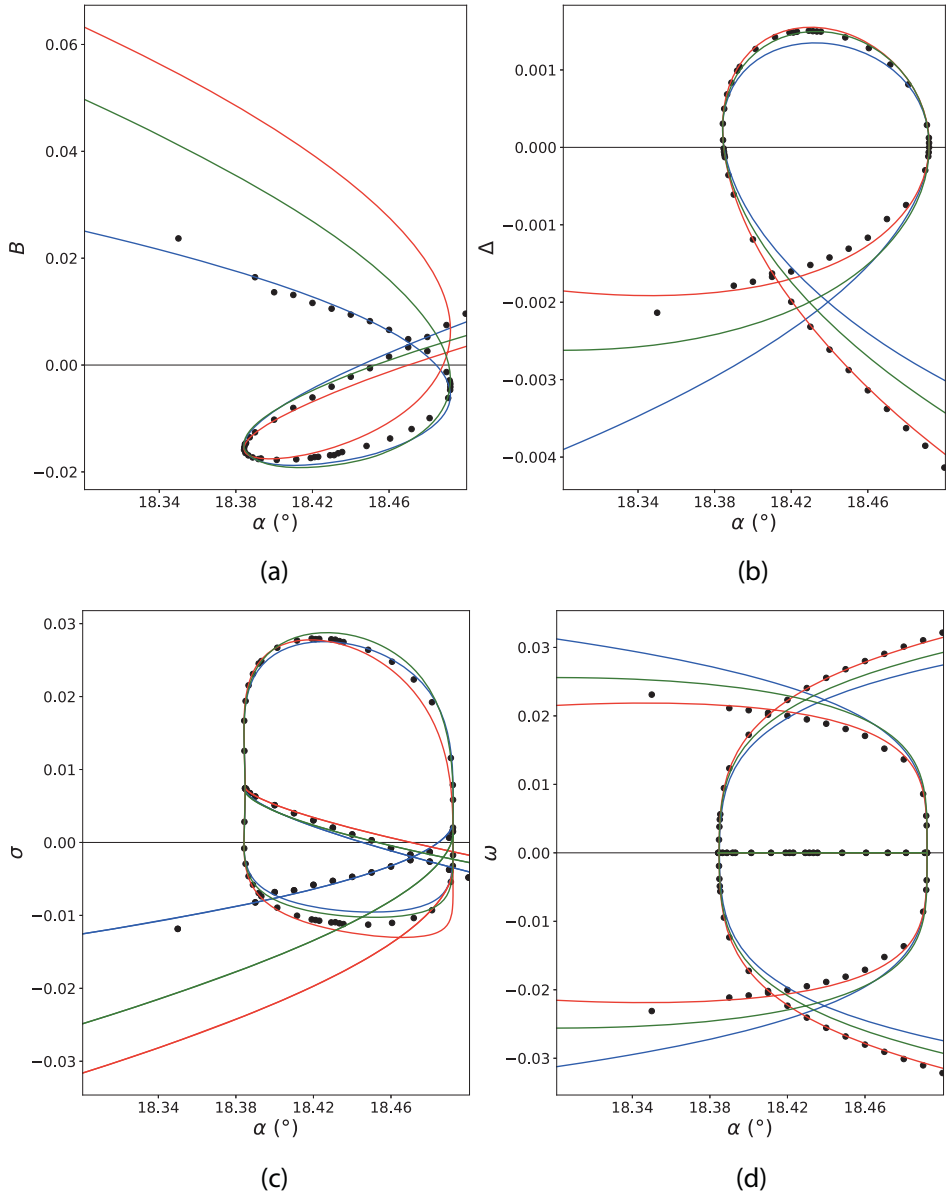

FIGURE 7.3: Evolution of four variables as a function of the angle of attack. (a): B. (b): Δ. (c): σ. (d): ω. Three different calibrations obtained with the NSGA-II algorithm are presented. The colors of the curves correspond to the solutions highlighted in Figure (7.2). The evolutions of the variables from the model are compared with the associated variables obtained from the stability analysis of steady RANS solutions (black dots).

a better fit on Δ ensures a better fit on the angular frequency.

Figure (7.4) presents the superimposed spectra obtained for the three calibrations. The blue solution, which minimizes the error on B and on the growth rate σ seems to correctly reproduce the positions where the eigenmodes switch from steady to unsteady but fails to reproduce the parabolas made by the eigenmodes. On the other hand, the red solution perfectly reproduces the parabolas of the spectrum but fails to

catch the position at which the mode switches from unsteady to steady on the upper branch (furthest left parabola). The green solution offers very decent results on the two features. Note that the eigenvalues on the upper branch (furthest left parabola) are more sensitive to the different solutions than the lower branch (furthest right parabola).

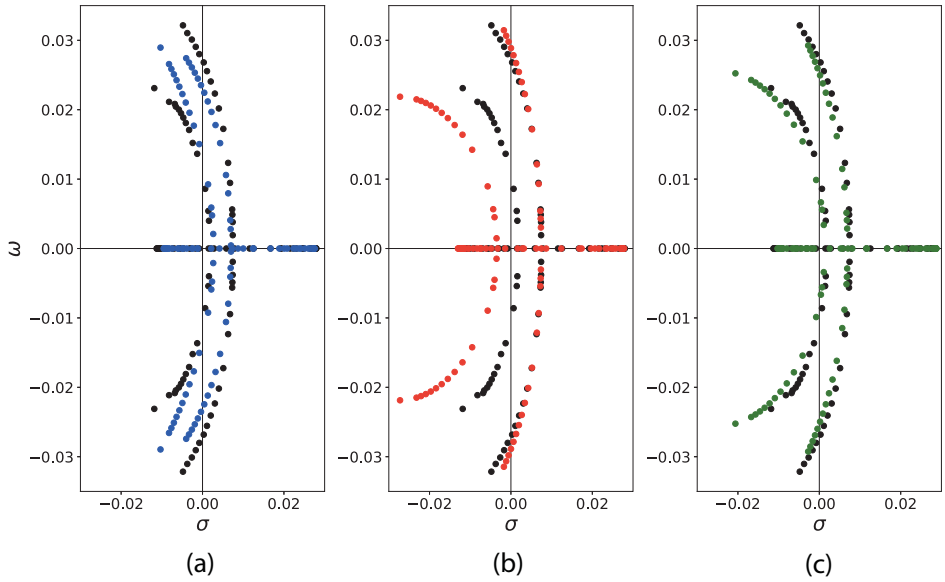

FIGURE 7.4: Comparison of the superimposed spectra obtained for different calibration of the model (color dots) with the superimposed spectra obtained from the stability analysis of steady RANS solutions presented in Figure (5.13) in section 5 (black dots). The colors of the spectra correspond to the solutions highlighted in Figure (7.2).

Based on these observations, the solution represented in green in the Pareto front plotted in Figure (7.2) is chosen. The corresponding coefficients, used for the study of the nonlinear behavior of the model, are presented in Table 7.1.

Coeff	Value	Coeff	Value	Coeff	Value
α_s	18.4381	a_1	-1.0049	b_0	-1.8359×10^{-2}
C_{L_s}	1.3651	a_2	-1.2304×10^{-1}	b_1	6.9644×10^{-2}
c	2.8708×10^{-4}	a_3	51.7158	b_2	1.4837
		a_4	19.7393	b_3	1.2870

TABLE 7.1: Values of the different coefficients corresponding to the chosen solution.

7.1.4 Comparison of the position of the particular points of the system

Table 7.2 presents the positions of some specific points obtained from the one-equation static stall model and from the RANS computations (introduced in Table 5.3 of chapter 5). For each branch, the three points considered are the Hopf bifurcations (noted H), the solutions with two identical eigenvalues (noted D) and the saddle-node bifurcations (noted SN). In order to compare the results a relative error on the position is introduced. The following characteristic scales are used:

- Saddle-node bifurcations: the range of the hysteresis (i.e. $\Delta\alpha$ between the two saddle-node bifurcations)
- Hopf bifurcations: the range in which unstable modes exist on the considered branch (i.e. the gap between the Hopf bifurcation and the closest saddle-node bifurcation)
- Two identical eigenvalues point: the range in which steady modes exist on the considered branch (i.e. the gap between the two identical eigenvalues point and the closest saddle-node bifurcation)

First, one can observe that the positions of the saddle-node bifurcations are well reproduced by the model with a very low relative error on the estimation of their positions. Indeed, the calibration of the steady states (from which the position of the saddle-nodes is determined) is more accurate than the one of the linear behavior. Second, the points H and D are better estimated on the lower branch than on the upper branch. This result was expected based on the observations made during the analysis of the spectra from different calibration in the Pareto front presented in Figure (7.2). On the upper branch, the points are closer to the saddle-node bifurcations for the model than for the RANS computations. The consequence is that the point with two identical eigenvalues is almost superposed with the saddle-node bifurcation. On the lower branch, the position of the Hopf bifurcation is pretty well estimated while the position of the solution with two identical eigenvalues exhibits a non negligible relative error. Generally speaking, the range of existence of the two unstable steady eigenvalues is very tiny (as shown in Figure (5.13) in chapter 5), which explains why a small difference of positioning leads to a large relative error.

7.2 Nonlinear behavior of the static stall model

A set of parameters offering the best fit between the linear behavior of the model and the linear behavior of the steady RANS solutions is found. The nonlinear behavior of the model is investigated with this set of parameters to gain an understanding of the nonlinear behavior of the RANS computations. Matcont [39], a Matlab Plug-in made for numerical continuation and bifurcation study of parametrized dynamical systems, is used to perform this study. It offers a fast and easy way to obtain solutions in time and compute steady states and limit cycles with continuation methods. The numerical aspect of Matcont is not described but all the techniques used in this study

		RANS	Model	$\mathcal{L}$	Error (%)
Upper branch	H	18.4867	18.4912	0.00533	84.43
	D	18.4919	18.4920267	0.00013	97.46
	SN	18.49203	18.4920274	0.1078	$\mathcal{O}(10^{-3})$
Lower branch	H	18.4527	18.4529	0.06847	0.29
	D	18.3846	18.3847	0.00037	27.03
	SN	18.38423	18.38417	0.1078	$\mathcal{O}(10^{-2})$

TABLE 7.2: Comparison of RANS computations and the static stall model for three particular points: Hopf bifurcation H, two identical eigenvalues D and saddle-node bifurcation SN. $\mathcal{L}$ designates the characteristic scale used to compute the relative error in %.

(definition of the stall model in Matcont, steady solutions computation, time-stepping computations, limit cycle identification, limit cycle tracking,...) are detailed in tutorials [103] and [104]. The results of the analysis are depicted in Figure (7.5), which presents: (a) the polar curve zoomed in close to stall angle and the existing limit cycles (providing a bifurcation diagram close to stall) and (b) schematic phase diagrams for nine values of α (representation freely inspired from the ones found in the book of Kuznetsov about bifurcation theory [89]).

Starting from the lowest value of α on the upper branch, one can observe, in phase diagram 1, a single stable steady solution to which all trajectories converge. Close to the steady point, the trajectories form a focus, indicating that a pair of complex conjugate eigenvalues is stable. By increasing the angle of attack, three steady solutions coexist: the stable focus on the upper branch and two unstable steady solutions. As seen in the phase diagram 2, the steady solution on the middle branch is a saddle point, indicating the existence of two steady eigenvalues, one stable and one unstable. On the other hand, the steady solution on the lower branch is a focus, indicating that a pair of complex eigenvalues is unstable. Obviously, all the trajectories converge towards the only stable solution on the upper branch. By further increasing α, a Hopf bifurcation occurs on the lower branch of steady solutions as the unstable unsteady pair of eigenvalues become stable on this branch. Moreover, an unstable branch of limit cycles emerges for higher angles of attack from this Hopf bifurcation, indicating that it is subcritical. Phase diagram 3 illustrates the existence of the unstable limit cycle. It surrounds the stable steady solution on the lower branch, dividing the solution field into two parts: inside the limit cycle, the trajectories converge to the lower branch and, outside, to the upper branch. For higher angles of attack, a homoclinic bifurcation is encountered as illustrated in phase diagram 4. It is characterized by a trajectory which starts from the middle branch and ends to the same solution, circling the two other steady solutions. Further increasing the angle of attack, it appears that this homoclinic orbit actually results from the collision of a large limit cycle (visible in phase diagram 5) with the saddle point on the middle branch of steady solutions. Note that the collision occurs via a shrink of the limit cycle in the direction $\dot{C}_L$. This explains why it is not visible in the bifurcation diagram shown in (a), which displays C_L as a function of α. In the phase diagram 5, two limit cycles coexist, the large one being stable while the small one surrounding the lower steady state is still unstable. Between these two

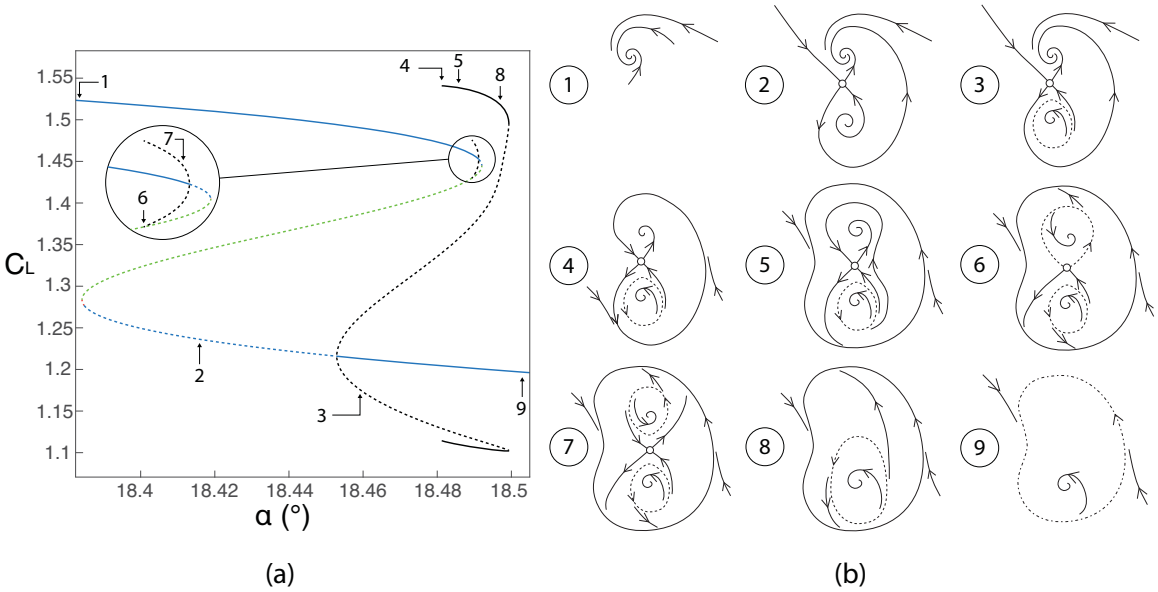

FIGURE 7.5: (a) Bifurcation diagram from the calibrated stall model (parameters presented in table parameters). The color code of the steady states is similar to the one used in Figure (5.13) (i.e. Blue: two unsteady eigenvalues. Red: two steady unstable eigenvalues. Green: two steady eigenvalues, one stable and one unstable). The limit cycles are represented with black lines corresponding to the evolution of their extreme values. Steady solutions and limit cycles are represented such that: full lines indicate stable states and dashed lines indicate unstable states. (b) Schematic phase diagrams in the plane $(\dot{C_L}, C_L)$ for different values of α referenced in the bifurcation diagram (a). The arrows in the phase diagram indicate a positive evolution of time.

limit cycles, the trajectories can either converge to the large limit cycle or to the upper steady solution. When α is further increased, a second homoclinic bifurcation occurs (phase diagram 6 and 7) via the collision of an unstable upper limit cycle with the middle sadde point. For this second homoclinic bifurcation, the unstable limit cycle emerges from the subcritical Hopf bifurcation on the upper branch of steady solutions. Examining phase diagrams 6 and 7, one can observe a shrink of the limit cycle in the C_L (vertical) direction which makes it clearly visible in the bifurcation diagram (a). Further increasing the angle of attack, the unstable upper limit cycle vanishes at a Hopf bifurcation on the upper branch. Once going through the saddle-node bifurcation on the upper branch, there are only two limit cycles remaining in phase diagram 8, coexisting with the stable lower steady solution. Finally, the size of the unstable lower limit-cycle grows until it collides with the large stable limit cycle in phase diagram 9. This is a saddle-node bifurcation of periodic orbits that leads to their disappearance. Thus, only the lower steady solution exists for larger values of α.

7.3 Comparison of the bifurcation scenario with the RANS approach

This section is dedicated to the comparison between the bifurcation scenario suggested by the static stall model and the results of the unsteady RANS computations. The features of the stable large limit cycle are discussed, the time evolution of the lift coefficients are compared and the phase diagrams presented in Figure (7.5)(b) are confronted to the ones presented in Figure (6.7) of chapter 6. Throughout the whole analysis process, answers to the questions raised by the unsteady RANS computations are proposed. Finally, the limitations of the model such as calibrated are discussed.

7.3.1 Comparison of the range of existence of the limit cycles

Figure (7.6) shows the complete bifurcation scenario obtained with the model : the steady states and the limit cycles. The limit cycles obtained with the unsteady RANS computations are superimposed to this diagram for comparison matters. One can note that the stable limit cycle observed with the unsteady RANS computation is qualitatively similar to the one observed with the static stall model. Indeed, in both cases, the smallest value of α for which it exists is associated with stable steady solutions on the upper and lower branches and unstable on the middle branch (states 3 and 4 of Figure (6.6 of chapter 6) and the highest value of α for which it exists is associated to the existence of a unique steady solution on the lower branch (states 6 and 7 of Figure (6.6 of chapter 6). However, the one caught with the unsteady RANS computations is larger than the one predicted by the model ($\Delta C_L \approx 0.5$ and $\Delta C_L \approx 0.4$ respectively), wider ($\Delta\alpha \approx 0.035°$ and $\Delta\alpha \approx 0.02°$ respectively) and slightly shifted to the left (smallest angle of attack at which it exists: $\alpha \approx 18.46°$ and $\alpha \approx 18.482$ respectively). In the end, the nonlinear behavior of the model, although not being in perfect agreement with unsteady RANS computations, qualitatively well predicts the main features of the stable limit cycle. This indicates that it is meaningful to investigate and study in more detail the unstable limit cycles revealed by the static stall model.

7.3.2 Comparison of the time evolution of the lift coefficient

In chapter 6, five different areas (presented in Figure (6.6)) were considered and, for each one, unsteady computations were performed for a particular angle of attack. For each angle of attack considered, computations were initialized with different solutions (i.e. each steady solution existing for this particular value of α and, if existing, from an extremum point of a limit cycle as presented in Figure (6.7)). As a reminder, the five zones considered are listed below :

- 2: one stable steady solution on the upper branch and two unstable steady solutions on the middle and lower branches
- 3: two stable steady solutions on the upper and lower branches and an unstable steady solution on the middle branch
- 4: two stable steady solutions on the upper and lower branches and an unstable steady solution on the middle branch and a large limit cycle

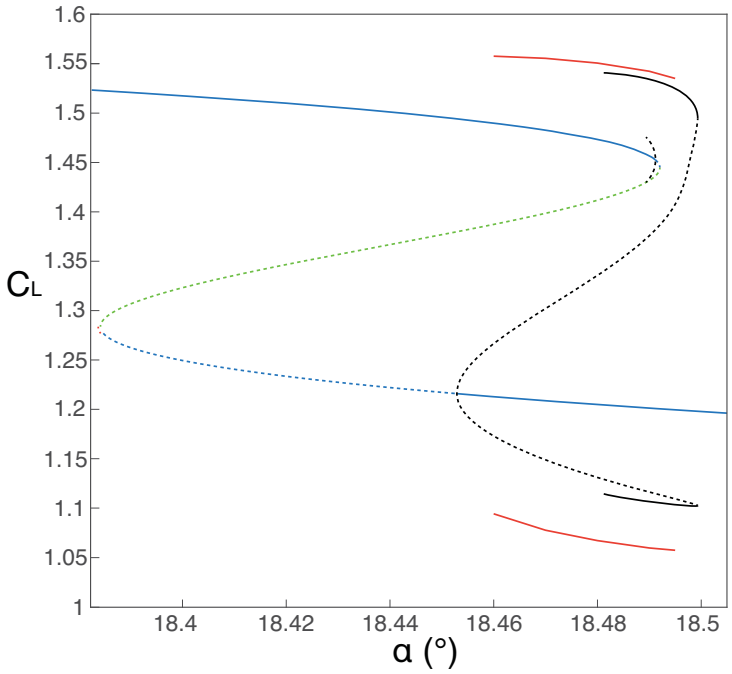

FIGURE 7.6: Comparison of the nonlinear behavior of the model and the results of unsteady RANS computations. The full red lines correspond to the extreme values of the limit cycles identified with unsteady RANS computations.

- 5: one stable steady solution on the lower branch and two unstable steady solutions on the middle and upper branches and a large limit cycle
- 6: one stable steady solution on the lower branch and a large limit cycle

A similar division can be considered in the bifurcation diagram of the static stall model (although the range of each zone will be slightly shifted due to the calibration) and time-stepping computations of the static stall model are performed for: $\alpha = 18.42°$ (2), $\alpha = 18.46°$ (3), $\alpha = 18.485°$ (4), $\alpha = 18.4915°$ (5) and $\alpha = 18.495°$ (6). The angles of attack considered are different from the ones chosen for the unsteady RANS computations but there is still one in each area to compare each other. The results obtained, presented in Figure (7.7), are to be compared to the ones obtained with unsteady RANS computations and presented in Figure (6.7) in chapter 6. For each case, the time evolution of the lift coefficient is qualitatively very similar for the static stall model and for the unsteady RANS computations. The only difference comes from the amplitude of the oscillations as already illustrated in Figure (7.6) and the exact angles of attack considered.

The main advantages of this static stall model are its very low computational cost, which, for instance, allows us to perform a detailed influence of the initial condition, and its capacity to detect unstable limit cycles. Several phenomena, very difficult to identify with unsteady RANS computations, can be easily identified with time-stepping computations of the static stall model. In order to describe them, zone 4 is studied in more detail. By applying the method used to define the zones, it appears that this zone

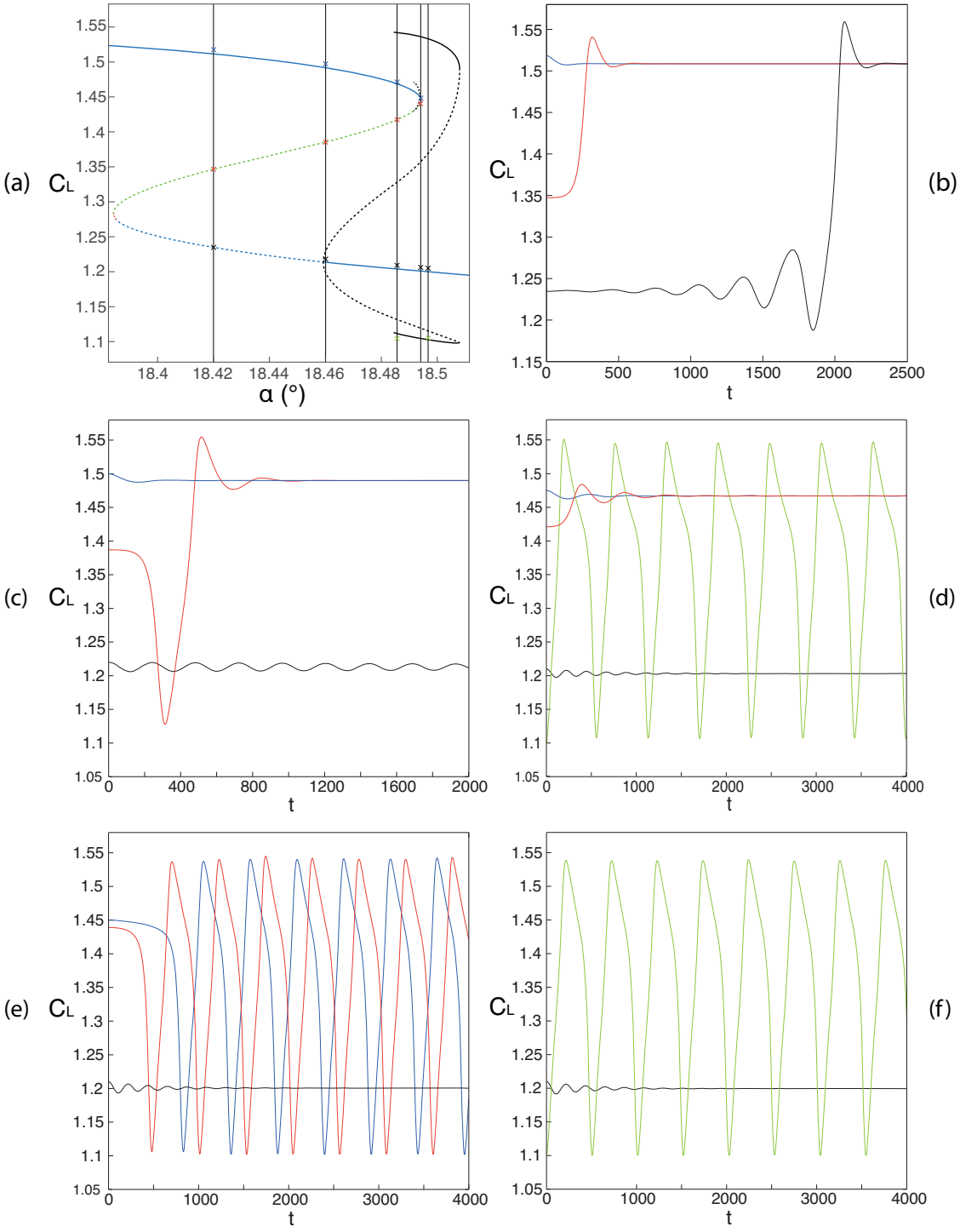

FIGURE 7.7: Time evolution of the lift coefficient obtained with the static stall model from different values of α. The crosses correspond to the steady solutions used to initialize the unsteady computations. (a) Bifurcation diagram from Figure (7.5) and angles of attack considered. (b) $\alpha = 18.42°$. (c) $\alpha = 18.46°$. (d) $\alpha = 18.485°$. (e) $\alpha = 18.4915°$. (f) $\alpha = 18.495°$. The color code of the crosses in (a) matches the one of the curves in (b), (c), (d), (e) and (f).

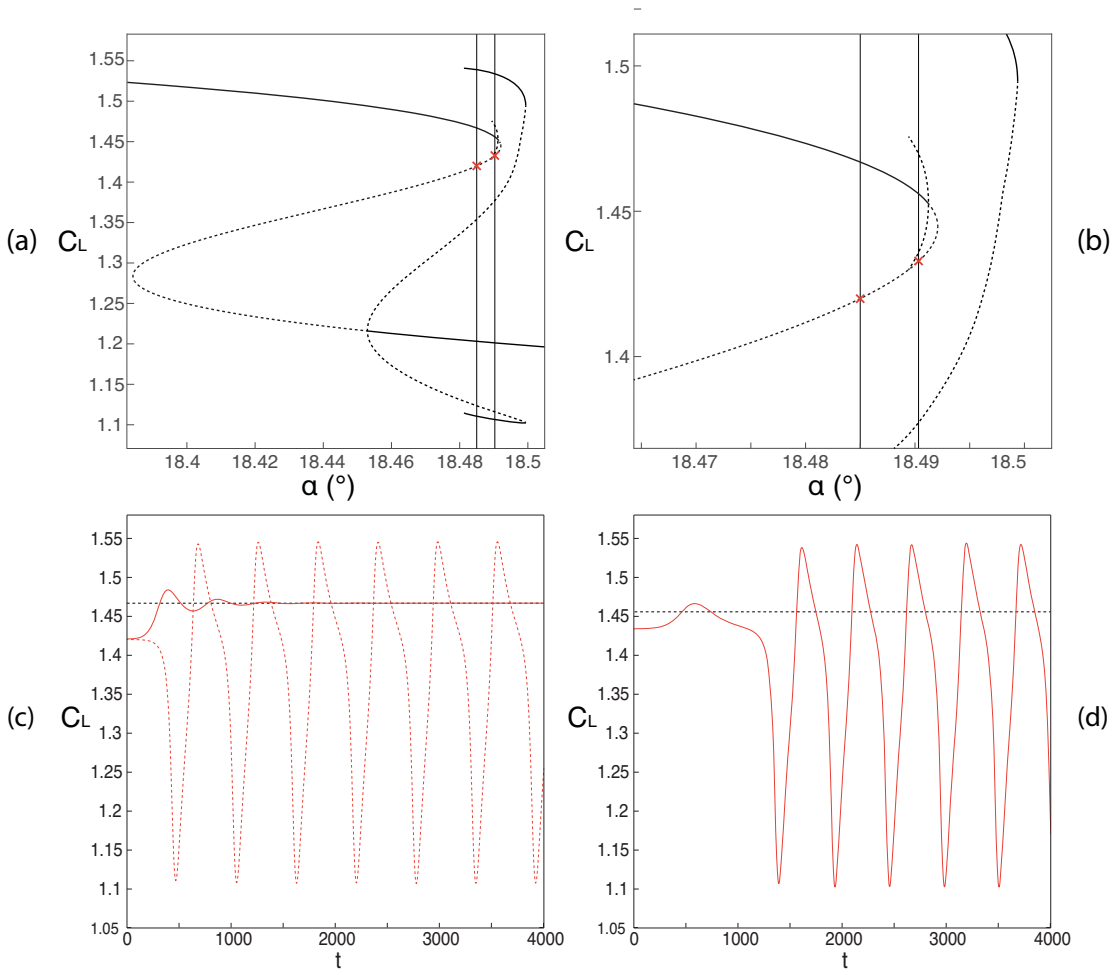

FIGURE 7.8: Time evolution of the lift coefficient obtained with the static stall model from different values of α. The crosses correspond to the steady solutions used to initialize the unsteady computations. (a) Bifurcation diagram from Figure (7.5) and angles of attack considered. (b) (a) Bifurcation diagram from Figure (7.5) zoomed in area 4 and angles of attack considered. (c) $\alpha = 18.485°$. (d) $\alpha = 18.4905°$. The color code of the crosses in (a) and (b) matches that the curves in (c) and (d).

can actually be split into two different zones because of the existence of the unstable limit cycle emerging from the Hopf bifurcation on the upper branch. A first subregion $4a$ can be defined from the lowest angle of attack for which the stable limit cycle exist to the point where the unstable limit cycle from the upper branch ends (i.e. when it collides with the middle branch of steady solutions in a homoclinic bifurcation). A second subregion $4b$ can be defined in all the range of existence of this unstable limit cycle, from the homoclinic bifurcation to the Hopf bifurcation. The difference between those two subregions is illustrated in Figure (7.8), which presents results for time-stepping computations at $\alpha = 18.485°$ (in area $4a$, already presented in Figure (7.7)) and $\alpha = 18.4905$ (in area $4b$). The only difference between the two zones is encountered for temporal computations starting from the middle branch, consequently, only this case is presented in Figure (7.8).

Figures (7.8)(a) and (b) present the position of the steady solutions considered for the initializations of the two computations and Figure (7.8)(c) and (d) the evolution of the lift coefficient as a function of time for the associated computations ($\alpha = 18.485°$ and $\alpha = 18.4905$ respectively). One can observe how the unstable limit cycle existing in zone $4b$ acts as a repeller. It prevents the temporal solution to reach the stable steady state on the upper branch and forces it to converge to the stable limit cycle while, without the existence of this limit cycle (zone $4a$), the solution converges to the stable steady solution on the upper branch (full red line). The deviation generated by the unstable limit cycle is clearly between $t \approx 500$ and $t \approx 700$ in Figure (7.8)(d). Based on these results and assuming that the static stall model correctly predicts the existence of unstable limit cycles, one can deduce that $\alpha = 18.48°$ is located in the area $4a$, before the appearance of the unstable limit cycle. Indeed, it would have been impossible to reach the upper branch from the middle branch if it was located in $4b$, when this unstable limit cycle exists (see Figure (6.7) in chapter 6). The second information is deduced by slightly modifying the steady solution on the middle branch used to initialize the computation (a variation of lift of $\Delta C_L = 10^{-3}$ is considered). The results are presented in Figure (7.8)(c), which compares the time evolution previously described (full red line) to a computation initialized with a slightly modified steady solution (dashed red line). A tiny modification of the initial condition leads to a major change of result as, instead of converging towards the stable steady state on the upper branch, the large limit cycle is reached. To understand this behavior, we can refer to the phase diagram number 5 presented in Figure (7.5). If the time-stepping computation is initialized with a solution located in the area delimited by the two lines that converge to the steady solution on the middle branch, it will converge to the upper branch, otherwise, it will converge to the limit cycle. Explained in a simpler manner: for $\dot{C_L} = 0$ a computation initialized with a solution slightly above the steady solution on the middle branch will converge to the upper branch whereas a computation initialized slightly below will reach the stable large limit cycle. This sensitivity to the initial conditions is also probably at the origin of a phenomenon identified in Figure (6.7): unsteady RANS computations initialized from the middle branch sometimes converged straight to steady solution on the upper branch ($\alpha = 18.42°$ and $\alpha = 18.48°$) and sometimes went around the low lift solution before converging to the steady solution on the upper branch ($\alpha = 18.45°$). These observations enlighten us on the fact that the unsteady RANS computations could have given very different results if started with slightly different flow topologies of angles of attack, especially in area 4.

7.3.3 Phase diagrams comparison

In Figure (6.7) of chapter 6, the results of the unsteady computations were plotted in the plane (C_M, C_L), which is very similar to the phase diagrams describing the stall model in Figure (7.5). This subsection is dedicated to the comparison of the phase diagrams from the unsteady RANS computations with phase portraits from the static stall model for the different zones identified.

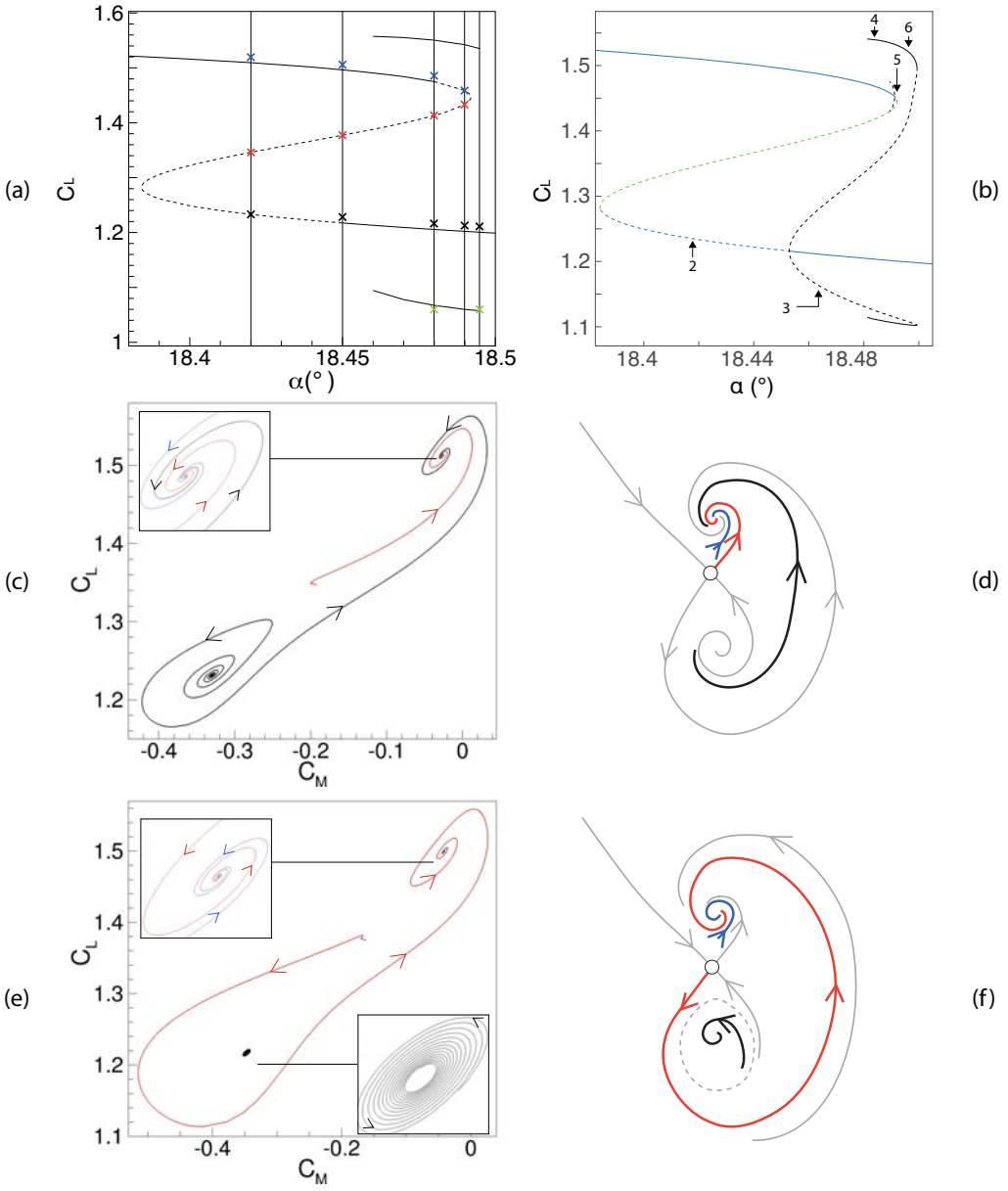

FIGURE 7.9: Comparison of phase diagrams (1/2). Polar curve and extreme values of limit cycle from unsteady RANS computations (a) and from the static stall model (b). Vertical lines in (a) mark the angles of attack considered and the crosses, the solutions used to initialize the unsteady RANS computations. The five cases considered for the model are marked by arrows and referenced by the number of the area in (b). Results of the unsteady RANS computations presented in the plane (C_M, C_L) for (c) $\alpha = 18.42°$ and (e) $\alpha = 18.45°$. Corresponding schematic phase diagram in the plane $(\dot{C_L}, C_L)$ determined with the static stall model for (d) zone 2 and (f) zone 3. The colors used to mark the initial point in the polar curve and to draw the lines in the corresponding phase diagrams all match. The grey lines in the schematic phase diagrams are the results observed with the model but not confirmed with unsteady RANS computations.

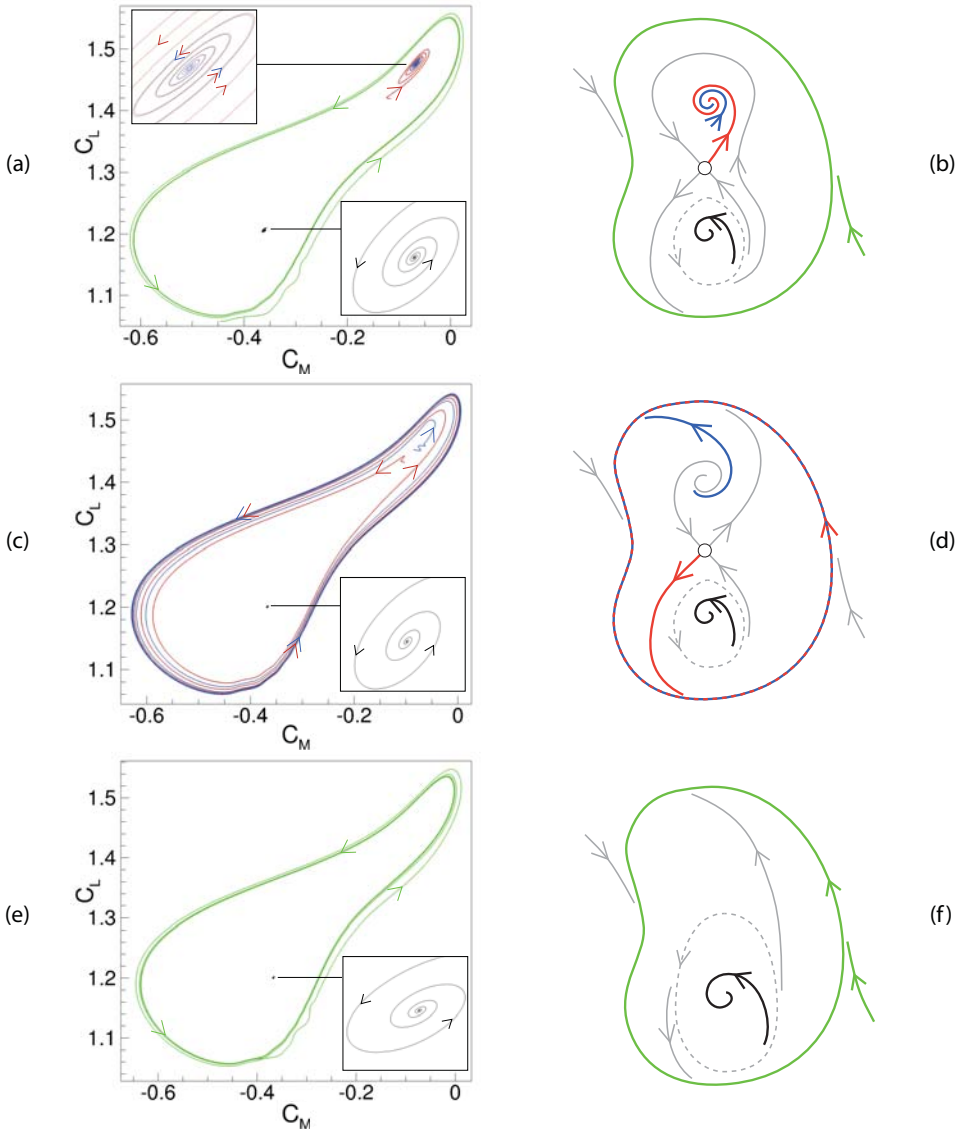

FIGURE 7.10: Comparison of phase diagrams (2/2). Results of the unsteady RANS computations presented in the plane (C_M, C_L) for (a) $\alpha = 18.48°$ (c) $\alpha = 18.49°$ and (e) $\alpha = 18.495°$. Corresponding schematic phase diagram in the plane $(\dot{C}_L, C_L)$ determined with the static stall model for (b) zone 4, (d) zone 5 and (f) zone 6. The colors used to mark the initial point in the polar curve and to draw the lines in the corresponding phase diagrams all match. The grey lines in the schematic phase diagrams are the results observed with the model but not confirmed with unsteady RANS computations.

The results of the comparison between the two approaches are depicted in Figures (7.9) and (7.10). Figure (7.9)(a) presents the incomplete bifurcation diagram obtained in the RANS framework in which the angles of attack considered are indicated as well as the initializer of the unsteady computations. Figure (7.9)(b) presents the corresponding zones in the bifurcation diagram from the static stall model. Figures (7.9)(c) and

(e) and (7.10)(a), (c) and (e) exhibit the results of the unsteady RANS computations in the plane (C_M, C_L), already presented in Figure (6.7) of chapter 6. Figures (7.9)(d) and (f) and (7.10)(b), (d) and (f) exhibit schematic phase diagrams from the study of the static stall model. The colored lines correspond to the trajectories identified with unsteady RANS computations while grey lines correspond to information not detected with unsteady RANS computations. The first thing to notice is that, in the schematic representation of the model, the three steady solutions (when existing) have the same $\dot{C_L}$ value (horizontal axis) and are aligned. This is not the case for the results from unsteady RANS computations, which exhibits different values of pitching moment coefficient C_M for each steady solution. This difference is due to the fact that the static stall model was calibrated based on lift coefficient evolution only and, consequently, only the C_L variable has a non-null steady state. A possible improvement of the model would be to take the pitching moment into account in the calibration process. Second, note that all the trajectories identified with the unsteady RANS computations are spotted with the study of the static stall model.

Moreover, the additional information provided by the static stall model, inaccessible with unsteady RANS computations (or at a very high computational cost), allows us to answer most of the questions raised at the end of chapter 6.

- Regarding the appearance and disappearance of the stable limit cycle, it is actually a homoclinic bifurcation for the lowest values of α at which it exists and a saddle-node bifurcation of periodic orbits for the highest values of α at which it exists. The criticaliity of the Hopf bifurcations is also determined: they are subcritical. The unstable limit cycle emerging from the Hopf bifurcation on the upper branch disappears in a homoclinic bifurcation, while the unstable limit cycle emerging from the Hopf bifurcation on the lower branch is directly related to the stable limit cycle in the aforementioned saddle-node bifurcation of periodic orbits.

- The impossibility to reach a steady solution on the lower branch from any other branch is attributed to the presence of the unstable limit cycle surrounding the lower branch of steady solutions and clearly visible in Figures (7.9) (f) and (7.10)(b) and (d).

- The different trajectories identified for computations initialized from the middle branch were attributed to the sensitivity of the initial condition in this region (section 7.3.2). It is clearly confirmed in Figures (7.9)(d) and (f) and (7.10)(b) and (d), where two trajectories depart from the steady solution on the middle branch in opposite directions. Furthermore, it appears that the choice of initial condition can affect not only the trajectory but also the stable state reached as illustrated in Figure (7.10)(b), which was not considered based on the results of unsteady RANS computations.

- The unsteady RANS computations performed tended to prove that the stable limit cycle could be reached from unstable steady solutions only in zone 5 (Figure (7.10)(c) and (d)). However, the static stall model demonstrates that it is also possible to reach this limit cycle from the middle branch in zones $4a$ (Figure (7.10)(a) and (b)) and $4b$.

7.3.4 Conclusion on the calibrated model

Finally, the static stall model, which appears to be in excellent agreement with the unsteady RANS computations, provides a complete bifurcation diagram. Based on all these information, it is possible to determine towards which stable state a time-stepping computation would converge based on its initialization. This is summarized in Figure (7.11) in which four distinct areas are identified :

- The yellow area, in which computations converge to the upper branch. This area covers most of the hysteresis and is stopped by the appearance of the unstable limit cycle from the lower branch and the large stable limit cycle. There is also a pocket inside the unstable limit cycle from the Hopf bifurcation on the upper branch.

- The orange area, in which the computations converge either to the upper branch or the stable limit cycle. This area is located inside the unstable limit cycle from the Hopf bifurcation on the lower branch and expands when the large limit cycle vanishes.

- The pink area, in which the computations converge either to the stable limit cycle or to the upper branch. This area is located inside the large limit cycle, before the appearance of the unstable limit cycle from the Hopf bifurcation on the upper branch.

- The violet area, in which computations converge to the lower branch. This area is located outside the large limit cycle when it exists and between the large limit cycle and the unstable limit cycles when the unstable limit cycle from the Hopf bifurcation on the upper branch appears.

However, it was shown that although providing results qualitatively in good agreement with unsteady RANS computations, the static stall model suffers from some limitations regarding a quantitative comparison. Two main reasons can be responsible for the differences noticed. The first one is attributed to the calibration process, which involves a multi-objective minimisation that ends up being a compromise between two objective functions. The main drawback of this approach is to have to choose one solution among the others on the Pareto front, which are all, according to the optimization process, similarly "good" solutions. As a reminder, one objective function mostly drives the evolution of the angular frequency of the eigenvalues while the other mostly drives the evolution of the growth rate of the eigenvalues. Thus, the Hopf bifurcations require a correct estimation of the change of sign of the growth rate to be well estimated while the solution with two identical eigenvalues requires a correct estimation of the moment the angular frequency becomes null. Consequently, by definition of a compromise, it will not be possible to exactly estimate the position of these two particular points on the two branches at the same time. This error in the calibration of the linear states of the model probably leads to differences on the nonlinear behavior of the model. One can suppose that a better calibration or formulation of the linear states of the model could improve the modeling of the nonlinear behavior. The second reason is that, as explained in chapter 4 and developed in appendix C, there is a difference between the steady solutions obtained with continuation methods and the ones obtained with a local time stepping approach. It was identified that the main difference between the

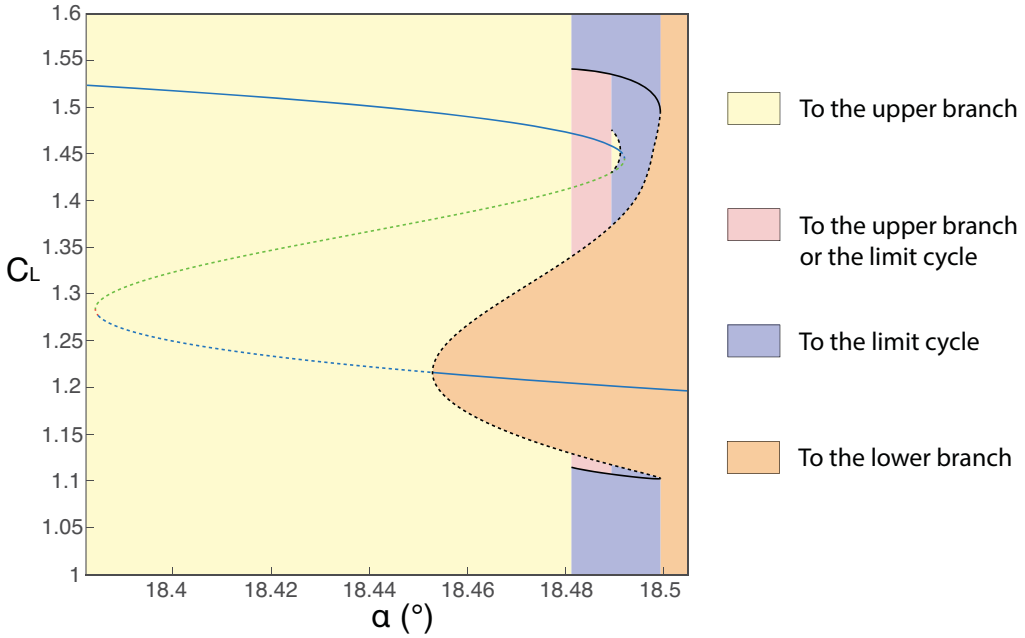

FIGURE 7.11: Presentation of the four basins of attraction that affect the result of the unsteady computations based on the position of the initial solution in the plane (C_L, α) for $\dot{C}_L = 0$.

two approaches is the presence of cutoffs in one case and not in the other. These cutoffs are also implemented and active in the unsteady RANS equations solver. It was demonstrated that a slight modification of one cutoff ensures a better match between the steady solutions obtained with the two methods (see appendix C) and, supposedly, it ensures a good match between the linear behavior of those steady solutions and unsteady RANS computations. However, the correction proposed does not provide perfect results and a tiny error still remains. Due to the small range of angles of attack in which all these phenomena occur, this error can be non negligible. Ideally, one would have wanted to modify the formulation of the Spalart–Allmaras turbulence model in *elsA* in order to remove the cutoffs. However, this would be highly time consuming and possibly tricky to achieve, which explains why the compromise of the modification of one cutoff was adopted. In the end, the two sources of differences between the model and the RANS computations lead to one main question: how do those errors influence the results of the nonlinear behavior? Indeed, it was argued that they only affect the values of the results but not the general behavior of the bifurcation scenario. However, it is legitimate to wonder to what extent this statement is true. The next section tries to provide an answer to this question.

7.4 Discussion of other possible scenarios

7.4.1 Approach and objectives

In order to evaluate to what extent an error in the calibration process could affect the bifurcation scenario, the simplest form of the static stall model is considered and the

influence of a reduced number of parameters on the nonlinear behavior is studied. The equation considered, given in (E.16), is recalled in (7.13) and corresponds to the most basic form for which the main features of the linear behavior are reproduced:

$$\frac{d^2c_l}{dt^2} + (2 \cdot b + c_l^2) \cdot \frac{dc_l}{dt} + c \cdot (\alpha + d \cdot c_l + c_l^3) = 0 \tag{7.13}$$

The objective is to identify the influence of the parameters of the model on the nonlinear behavior. Three parameters drive the whole model: b, c and d. The parameter d is responsible for the appearance of hysteresis in the steady solutions. In appendix E, it is set to $d = -1$ to ensure the appearance of this particular "S" shaped curve characterizing the hysteretic area. The study of the influence of the parameters is performed in two steps: first, the influence of b and c is investigated with the parameter d set to $d = -1$ and, afterwards, the influence of the parameters b and c with $d = 1$ is performed. Note that with such a shape, the point $(0, 0)$ is the center of symmetry of the steady solutions and their associated linear behavior.

7.4.2 Study of the nonlinear behavior in the case with hysteresis

The five scenarios are presented in Figures (7.12) to (7.16). For each figure, the branches of steady-state and limit-cycle solutions are shown in (a) by displaying the lift coefficient c_l as a function of the angle of attack α. The colored curves represent the steady state solutions while the black curves correspond to the extreme values of the limit-cycle solutions. In (b), several solutions are displayed in the phase space $(\frac{dc_l}{dt}, c_l)$ for particular values of α corresponding to the numbers indicated in (a). The values of the parameters b and c are tested in ranges defined in (E.27) to ensure that the linear behavior of the one equation model is coherent with the linear behavior of the steady RANS solutions. Five different behaviors are observed and presented in the following. For each scenario, the general behavior of the steady solutions and their linear stability is similar. The difference comes from the exact position of the Hopf bifurcation (labelled H in chapter 5), the point where the eigenvalues switch from complex to real (labelled D in chapter 5) and the growth of the limit cycles.

7.4.2.1 First scenario: $b = -0.42$ and $c = 0.1$

Reading the bifurcation diagram of Figure (7.12) from left to right, one can first observe one steady stable solution. In the corresponding phase diagram, this stable steady solution is a focus point to which all trajectories converge. Then, by increasing the value of α, three steady solutions coexist: one stable solution on the upper branch and two unstable solutions on the middle and lower branches shown with dots. The associated phase diagram (number 2) shows that all the trajectories converge to the stable solution no matter the initial point in the phase space. Further increasing the angle of attack, the steady unstable eigenvalue of the steady solution on the lower branch becomes an unsteady unstable eigenvalues. Instead of diverging straight from this point, the temporal solutions are now orbiting around it as they diverge, as shown in the phase diagram 3. However, all trajectories converge towards the upper branch.

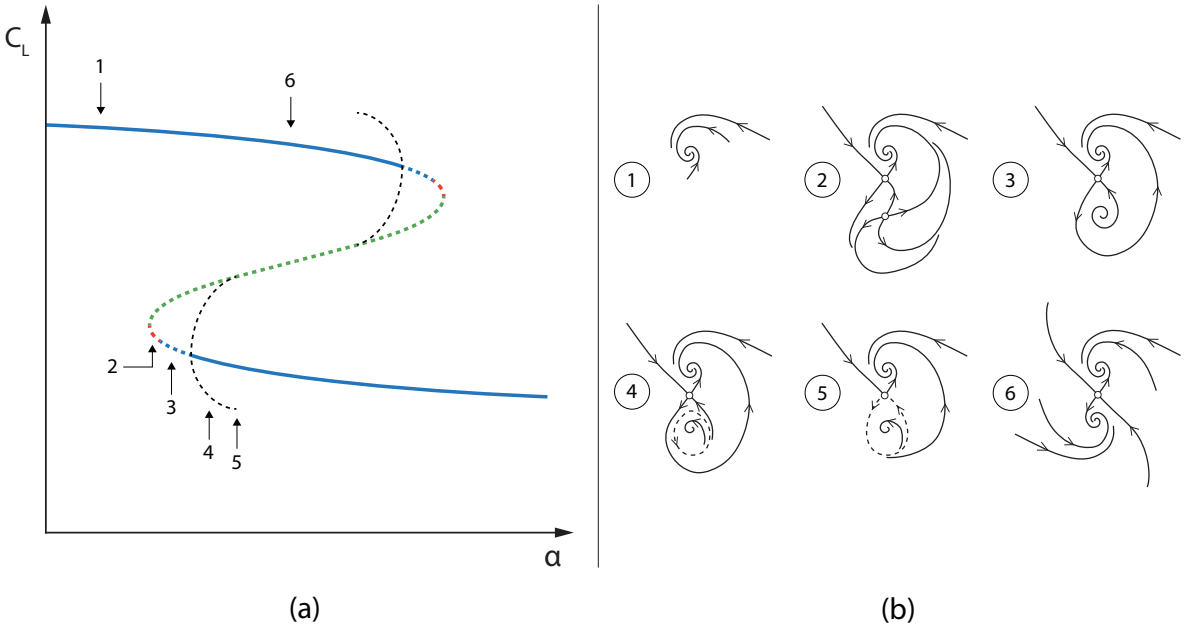

FIGURE 7.12: First stall scenario. (a) Schematic bifurcation diagram including steady solutions (in colored lines) and extreme values of limit cycles (black lines) in the plane (c_l, α). (b) Schematic phase diagrams in the plane $(\dot{c_l}, c_l)$ for different values of α referenced on the bifurcation diagram.

Then, the Hopf bifurcation on the lower branch gives birth to an unstable limit cycle when the steady solution on the lower branch is stabilized (phase diagram 4). All the computations started inside the limit cycle will converge to the lower branch whereas all the other ones will converge to the steady solution of the upper branch. When increasing the parameter α, the radius of the limit cycle grows until the limit cycle collides with the steady solution of the lower branch, as shown in the phase diagram 5. This collision is characteristic of a homoclinic bifurcation and leads to the disappearance of the limit cycle. The phase diagram number 6 exhibits two stable steady solutions on the upper and lower branches and an unstable steady solution on the middle branch. Each stable solution can be reached depending on the point in the phase space chosen for the initialisation. Finally, when further increasing the angle of attack, a similar scenario is observed, but in reversed order (from 6 to 1) and by replacing the role of the lower and upper branches. In this first reference scenario, the Hopf bifurcations lead to the appearance of unstable limit cycles, but no stable limit cycle is observed.

7.4.2.2 Second scenario: $b = -0.42$ and $c = 0.5$

The second stall scenario found with the one-equation stall model is described in Figure (7.13). Similarly to this first scenario, the Hopf bifurcation is subcritical and lead to the appearance of an unstable limit cycle that is destroyed by an homiclinic bifurcation. However, there are narrow ranges of α for which the upper and lower unstable limit cycles overlap, thus leading to the appearance of a new stable limit cycle, surrounding the upper and lower unstable limit cycles (full black lines on the bifurcation diagram).

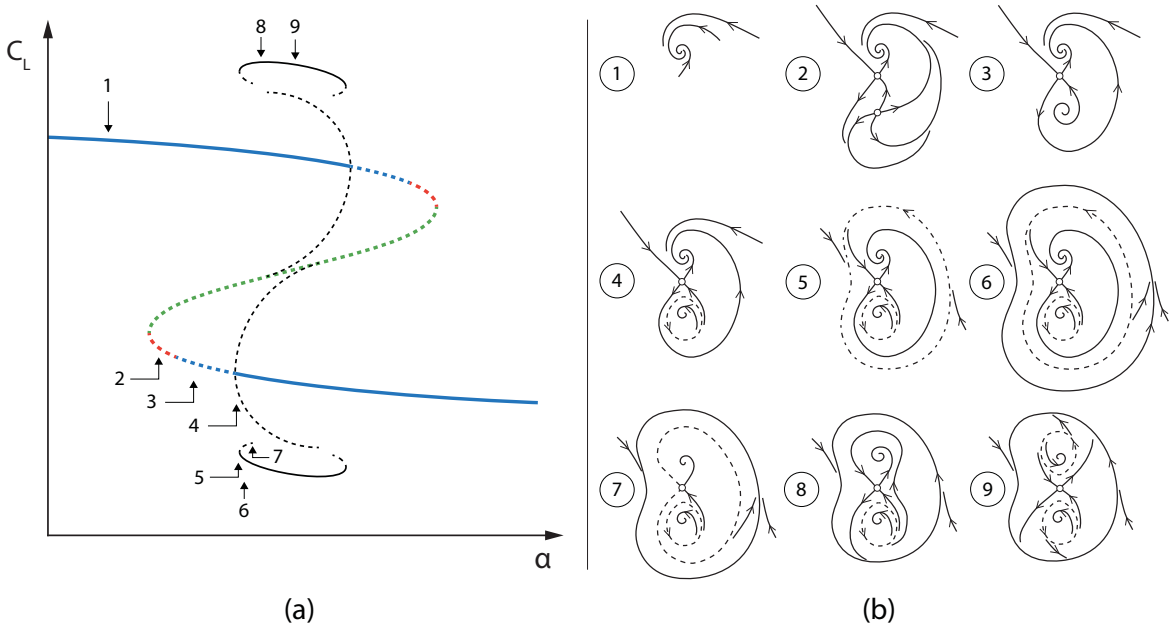

FIGURE 7.13: Second stall scenario. Same legend as in Figure (7.12).

The formation and destruction of this large limit cycle detailed in the following. Reading the bifurcation diagram in Figure (7.13) from left to right, one can observe that the four first phase diagrams are similar to the ones described for the first scenario in Figure (7.12). The phase diagram 5 exhibits a half stable large limit cycle (which acts like an attractor for the solutions outside and like a repeller for the solutions inside) that surrounds the three steady solutions. It corresponds to a limit cycle bifurcation and the unstable limit cycle of small radius surrounding the lower branch. By increasing α, the half-stable limit cycle splits into two limit cycles of large radius, as shown in phase diagram 6. The limit cycle of smaller (resp. larger) radius is unstable (resp. stable). Every computation initialized with a point located outside the unstable limit cycle will converge towards the stable limit cycle, of larger radius. The evolution between the phase diagram 6 and 7 allows the reader to have an understanding of the disappearance of the large unstable limit cycle. We can note that it shrinks in the $\frac{dc_l}{dt}$ direction (horizontal in the phase diagram) until it collides with the steady solution of the middle branch. Thus, the disappearance of these unstable limit cycle is still due to an homoclinic bifurcation, that results here from an evolution of the limit cycle's size in the $\frac{dc_l}{dt}$ direction, instead of the c_l direction in the first scenario. That explains why the previous one was visible on the representation of the bifurcation diagram in the (c_l, α) plane (the collision between the limit cycle and the middle branch is quite explicit) whereas, in the present case, the unstable limit cycle just seems to vanish when observing the bifurcation diagram in the (c_l, α) plan. However, it is just a matter of representation and the same type of bifurcation is occurring as shown on the phase diagram. In phase diagram number 8, the unstable limit cycle has completely disappeared and the solutions can either converge to the large limit cycle or to the stable solution on the upper branch if they are initialized with a point located outside the small unstable limit cycle surrounding the stable lower steady state, otherwise it converges towards this steady state. As the value of α further increases, an homoclinic

bifurcation occurs first on the unstable limit cycle from the Hopf bifurcation on the upper branch. The associated phase diagram would be between the states 8 and 9 and is not represented. This homoclinic bifurcation would be similar to the one observed in the first scenario and depicted in the phase diagram 5 of Figure (7.12). Finally, a state where two small unstable limit cycles are coexisting inside a large stable limit cycle is represented in phase diagram 9. Every computation initialized with a point located outside the unstable limit cycle will converge to the stable limit cycle. As for the first scenario, a similar succession of phase diagrams is observed in reversed order (from 9 to 1) when further increasing the angle of attack, the role of the upper and lower steady and limit cycle solutions being switched.

7.4.2.3 Third scenario: $b = -0.49$ and $c = 0.5$

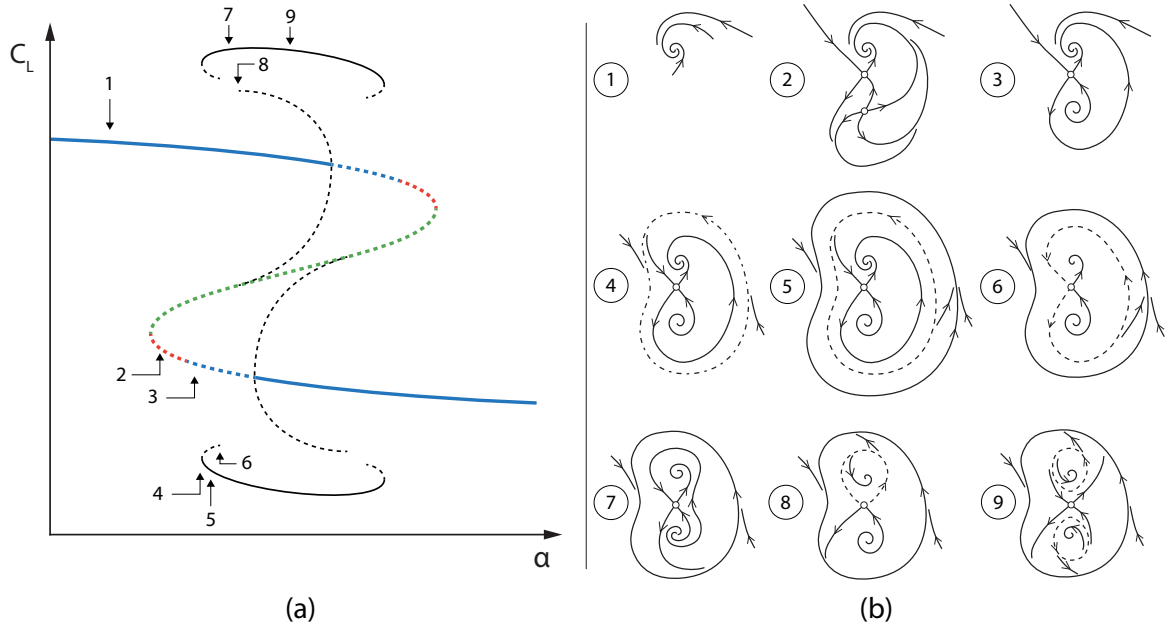

FIGURE 7.14: Third stall scenario. Same legend as in Figure (7.12).

This third reference scenario is slightly different compared to the second one but it has a lot of similarities. One can observe two unstable limit cycles starting from the Hopf bifurcations and a large stable limit cycle. In the second reference scenario, the homoclinic bifurcation of a small unstable limit cycle occurs while the other limit cycle still exists. However, on the third reference scenario when one of the two small unstable limit cycles vanishes, the other one no longer exists. This small difference leads to a slightly different bifurcation scenario. The three first phase diagrams are similar to the ones introduced in the first and second reference scenarios. The phase diagram number 4 shows the formation of a half stable large limit cycle. Unlike for the second scenario, it occurs while there is no small unstable limit cycle on the lower branch. Afterwards, the half stable limit cycle splits into one stable and one unstable limit cycle as visible in phase diagram 5. The phase diagram number 6 presents the destruction of the unstable large limit cycle in an homoclinic bifurcation, exactly as described in

the second reference scenario. In the phase diagram number 7, the only limit cycle existing is the large stable limit cycle. Temporal computations can either converge to the stable limit cycle or to the stable solution on the upper branch. Afterwards, an homoclinic bifurcation occurs on the small limit cycle from the Hopf bifurcation on the upper branch as shown in the phase diagram number 8. Finally, the phase diagram number 9 is similar to the one introduced in the second reference scenario. As for the previous scenarios, a similar succession of phase diagrams is observed in reversed order (from 9 to 1) when further increasing the angle of attack, the role of the upper and lower steady and limit cycle solutions being switched.

7.4.2.4 Fourth scenario: $b = -0.42$ and $c = 1$

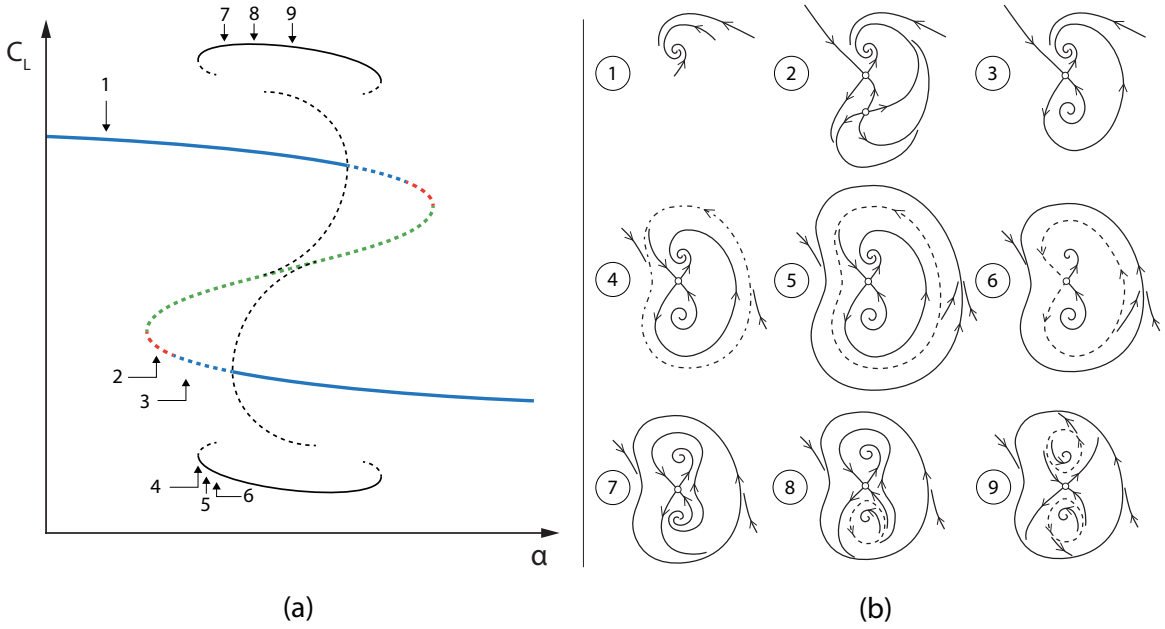

FIGURE 7.15: Fourth stall scenario. Same legend as in Figure (7.12).

The fourth reference scenario is only briefly discussed as it is simply a combination of the second and third reference scenarios and all the phase diagrams presented in the fourth scenario are described in details in the previous cases. On can observe that the small limit cycles behave as in the second reference scenario and the large limit cycle is similar to the one observed in the third reference scenario.

7.4.2.5 Fifth scenario: $b = -0.52$ and $c = 1$

One shall note that the value of b used for this scenario $b = -0.52$ is slightly out of the range of recommended values for b defined in appendix E. However, this scenario is introduced as very helpful to understand the behavior of the calibrated model. The fifth reference scenario exhibits a different behavior in the sense that no homoclinic bifurcation occurs. However, there are still some similarities with the previous scenarios:

the existence of a large stable limit cycle, unstable limit cycles from the Hopf bifurcations and limit cycle bifurcations. Reading the bifurcation diagram in Figure (7.16) from left to right, one can first observe one unsteady stable solution represented in the phase diagram number 1. It is similar to the first state of all the reference scenarios previously described. The phase diagram 2 shows the existence of a marginally stable limit cycle which results from the sub-critical Hopf bifurcation on the upper branch of steady solutions. By increasing α, the half-stable limit cycle splits into two limit cycles visible in phase diagram 3. The small limit cycle centered around the upper steady solution is unstable while the large limit cycle surrounding the upper and lower steady solutions is stable. In phase diagram 4 these two limit cycles still exist and two unstable steady solutions have appeared on the middle and lower branches. A time-stepping computation initialized with a solution located outside of the unstable limit cycle will necessarily converges to the large limit cycle. The phase diagram 5 is similar to the phase diagram 4 except that steady unstable eigenvalue of the steady solution on the lower branch gets unsteady, which implies that the temporal solution are now orbiting around it. Finally, the phase diagram 6 is similar to the last phase diagram of the second, third and fourth scenarios. Two unstable limit cycles surround two stable steady solutions, and are separated by an unstable steady solution. All these solutions are surrounded by a large stable limit cycle.

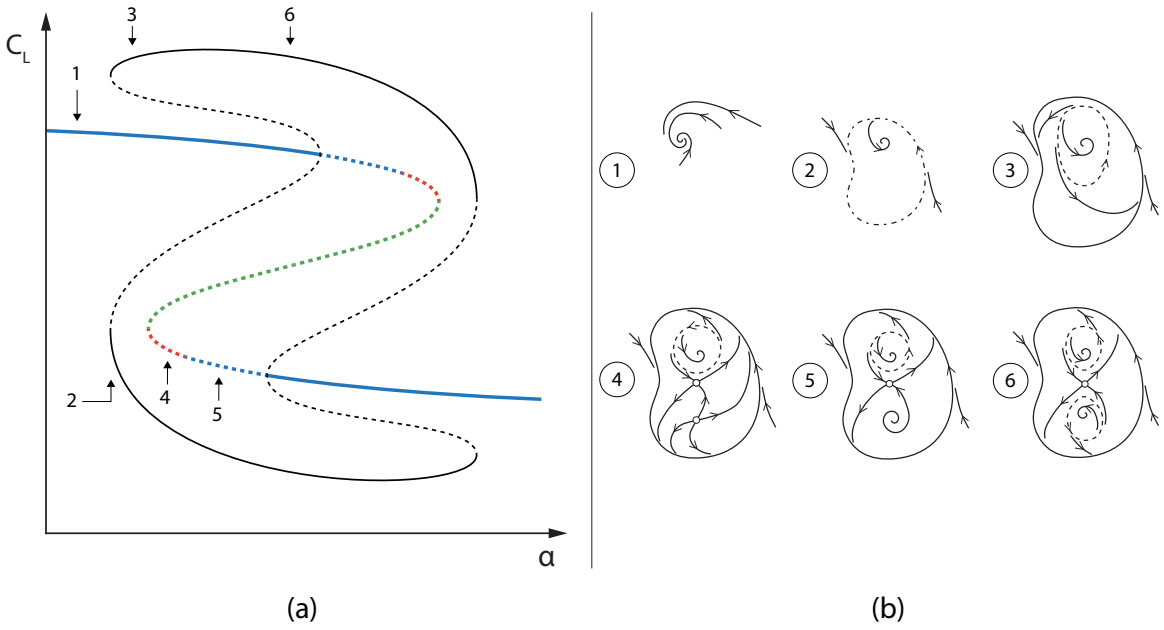

FIGURE 7.16: Fifth stall scenario. Same legend as in Figure (7.12).

7.4.2.6 Synthesis on the reference scenarios

With the range of parameters used (see equation (E.27)), at least five notable bifurcation scenarios can be encountered depending on the value of parameters b and c. Although all different, these scenarios have a lot of common points. First, in every scenario, the Hopf bifurcations give birth to unstable limit cycles. The main difference

between all these scenarios is the position at which these unstable small limit cycles collide with the steady solution on the middle branch in a homoclinic bifurcation. If the unstable limit cycles vanishes before overlapping, no other limit cycle is encountered (First reference scenario). However, if the limit cycles overlap it gives birth to a large stable limit cycle and two family of reference cases are to be distinguished: when the unstable limit cycles collide with the middle branch and when they do not. The first family includes the second, third and fourth scenarios, which are slightly different but are built the same way: the small unstable limit cycle vanishes in a homoclinic bifurcation and the large stable limit cycle bifurcates in an unstable large limit cycle that also vanishes in a homoclinic bifurcation. In the second family, corresponding to the fifth reference scenario, the unstable limit cycle never collides with the middle branch and simply just grow until bifurcating into a stable limit cycle which surrounds all three steady solutions.

Based on these observations, one can conclude that the nonlinear behavior is dictated by the position of the Hopf bifurcation and the slope of the unstable limit cycles emerging from the Hopf bifurcations. Indeed, these two characteristics will drive the existence and, if so, the position of the homoclinic bifurcations of the small unstable limit cycles. It was demonstrated in the previous section E.2.4 that the parameter b is directly responsible for the position of the Hopf bifurcations. The study of the reference cases also revealed that the parameter c is, at first order, responsible for the slope of the unstable limit cycle and the position of the limit cycle bifurcations (this can be observed by comparing the first, second and fourth scenario, which have the same positions of Hopf bifurcation ($b = -0.42$) but different positions of homoclinic bifurcations due to the variation of slope of the unstable limit cycles). Finally, with these reference scenarios, we have a better understanding on the possible formation and destruction of a large stable limit cycle.

7.4.3 Study of the nonlinear behavior in the case without hysteresis

The study of the one-equation static stall model was performed by setting the parameter $d = -1$. It ensured the presence of an hysteresis of the steady solutions. Five different scenarios were identified by modifying the parameters b and c. Among those five scenarios, four revealed a large stable limit cycle. Several papers in the literature revealed the presence of Low Frequency Oscillations (to which this limit cycle is associated) for airfoils and aerodynamic conditions which did not generate hysteresis of the steady or mean solutions. A very interesting point is to investigate whether or not the appearance of the large limit cycle identified with unsteady RANS computations and reproduced in the static stall model is linked to the hysteresis of the steady solutions. It appears that by switching the parameter d to a positive value, the stall phenomenon is still modeled but the hysteresis phenomenon disappears. First, the new linear behavior of the steady solutions along the curve is described. Then, the nonlinear behavior and the associated scenarios are introduced.

The schematized linear behavior of the steady solutions is depicted in Figure (7.17), which exhibits, a schematized polar curve zoomed in close to the stall angle (a) and

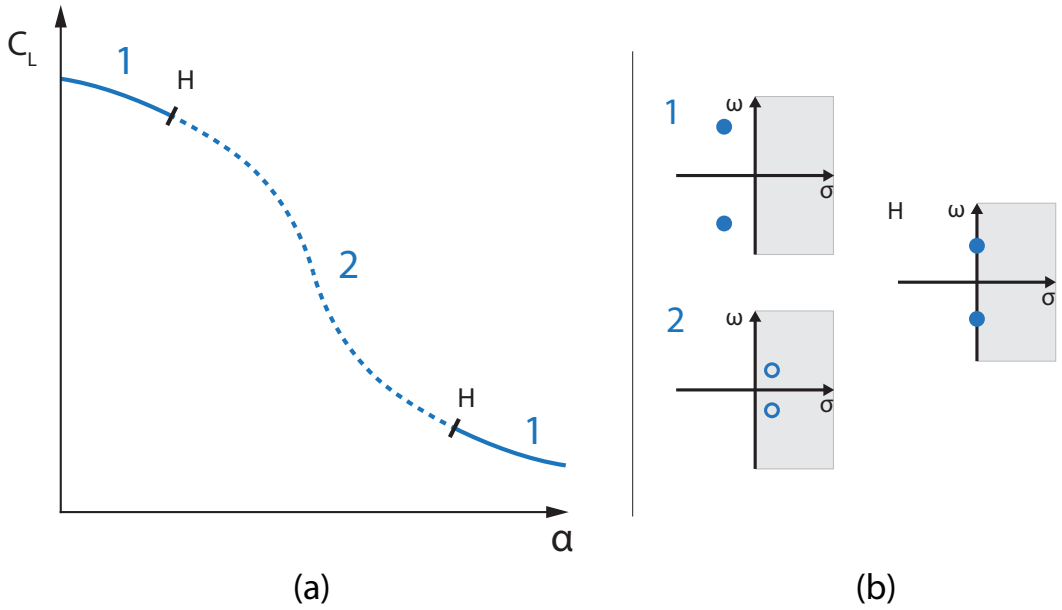

FIGURE 7.17: (a) Schematized evolution of the lift coefficient as a function of the angle of attack. (b) Associated schematized temporal behavior of the leading mode in the complex plane. The color code is similar to the one used in Figure (5.14) of chapter 5: on the polar curve, state 1 plotted in full blue line represents a stable ($\sigma < 0$) unsteady ($\omega \neq 0$) eigenvalue for the associated steady solutions and state 2 plotted in full blue line represents an unstable ($\sigma > 0$) unsteady ($\omega \neq 0$) eigenvalue for the associated steady solutions.

schematized representations of the eigenvalues in the complex planes (σ,ω), respectively growth rate σ and angular frequency ω of the eigenvalue λ (b). Two different states, numbered 1 and 2 are identified. In between, two Hopf bifurcations labelled H exist: one occurring for high lift values and the other for low lift values similarly to the case $d = -1$. However, this is the only common point as this case is much simpler and does not exhibit saddle-node bifurcations or switch between steady and unsteady eigenvalues. Starting from the upper branch and following the polar curve, a stable unsteady eigenvalue and its complex conjugate are first encountered (state 1). As the drop of lift gets closer, these eigenvalues become less stable as their growth rates increases. They finally become unstable (state 2), leading to a Hopf bifurcation at the point noted H on the polar curve.

An approach similar to the one performed for $d = -1$ is repeated and several values of b and c are tested. Two different scenarios are identified and depicted in Figure (7.18). It exhibits two schemas of the steady states made of colored lines in the plane (c_l, α) and corresponding to the the sixth scenario (a) and the seventh scenario (b). The extreme values of the limit cycles are represented in black lines. Schemas of phase diagrams are plotted for different values of α in (c). Each phase diagram is represented in the plane $(\frac{dc_l}{dt}, c_l)$, similarly to what was done in section 7.4.2.

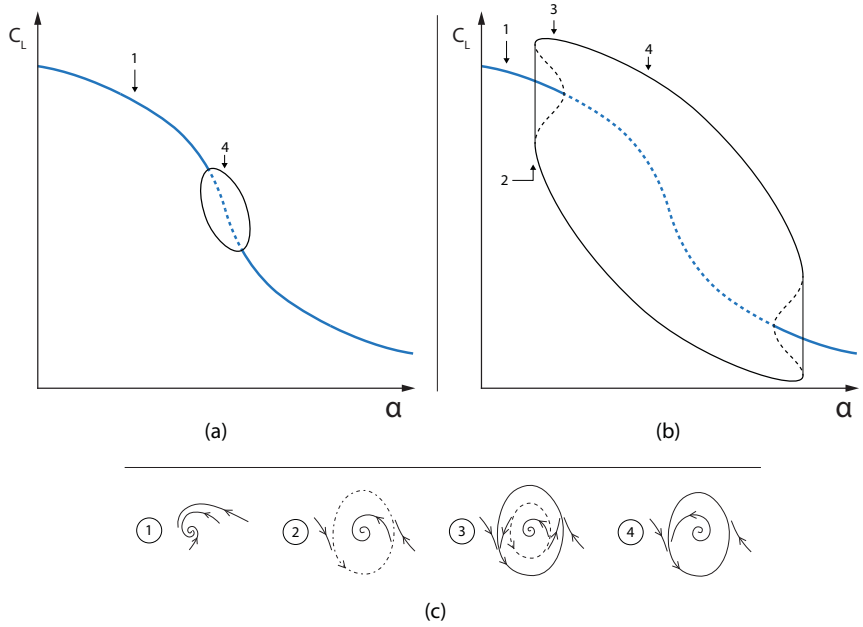

FIGURE 7.18: Sixth and seventh stall scenarios. (a) and (b) Schematic bifurcation diagram including steady solutions (in colored lines) and extreme values of limit cycles (black lines) in the plane (c_l, α). (c) Schematic phase diagrams in the plane $(\dot{c_l}, c_l)$ for different values of α referenced on the bifurcation diagram. The color code used is similar to the one used in Figure (7.12). .

The main difference between the two cases is the type of Hopf bifurcation : supercritical for the sixth scenario and subcritical for the seventh scenario. It appears that the type of the bifurcation is driven by the position of the Hopf bifurcation: if the Hopf bifurcations are inside the two points of maximum curvature, they are supercritical, otherwise, they are subcritical. For the sixth scenario (top left picture of Figure (7.18)), reading the bifurcation diagram from left to right, one can observe one unsteady stable solution represented in the phase diagram number 1. Then, by increasing the value of α, a supercritical Hopf bifurcation is reached. This bifurcation generates a stable limit cycle that surrounds the unstable solution. This state is presented in the phase diagram number 4 in which every solution will converge to this stable limit cycle. Then, as for the previous scenarios, a similar succession of phase diagrams is observed in reversed order (4 and 1) when further increasing the angle of attack, the bifurcations being reversed. For the seventh scenario (top right picture of Figure (7.18)), the behavior is the same than the sixth scenario for the states represented in phase diagrams 1 and 4. However, due to the subcriticaliity of the Hopf bifurcation, two new states presented in phase diagrams 2 and 3 appear in between. Reading the bifurcation diagram from left to right, one can observe one unsteady stable solution represented in the phase diagram number 1. Then, by increasing the value of α, one encounters a limit cycle bifurcation presented in phase diagram 2. At this point, all the computations converge to the stable solution. From this point, one unstable limit cycle and one stable limit cycle coexist as shown in the phase diagram number 3. The size of the unstable limit cycle will reduce until is vanishes at the Hopf bifurcation point while the stable limit

cycle will grow as α is increased. Then, the same behavior is repeated backwards. In the end, the model such as defined tends to indicate that the appearance of a large limit cycle is not linked to the presence of an hysteresis of the steady solutions.

7.5 Conclusion

In this chapter, it was demonstrated how the static stall model (introduced in appendix E) can be calibrated to reproduce the steady states and linear behavior of the stall of an OA209 airfoil at $\mathrm{Re} = 1.8 \times 10^6$ and $\mathrm{M} = 0.16$ computed with the Spalart–Allmaras turbulence model. Moreover the nonlinear behavior of this model appears to be in excellent agreement with the results of the unsteady RANS computations. Consequently, the capacity of the static stall model to reach unstable limit cycles is used to determine a bifurcation scenario, which provide answers for all the questions raised by unsteady RANS computations (chapter 6). Furthermore, a parametric study of the simplest form of the static stall model (i.e. before calibration), introduced in equation (7.13) in chapter E, is conducted. Different reference scenarios are identified by varying the parameters of the model and it appears that the results of the calibrated model are a combination of several of those reference scenarios. It remains to be seen whether those different scenarios would be realistic for other airfoils and flow configurations. In this spirit, the next chapter proposes to investigate a different Reynolds number and a different airfoil with an approach similar to the one described in chapters 5, 6 and 7 and verify if different bifurcation scenarios are obtained.

Chapter 8

Discussion of the possible scenarios observed

Contents

In this chapter, two additional configurations are presented. The objective is to verify if a bifurcation scenario similar to the one described in section 7.2 can be identified and, if not, if the reference scenarios detailed in section 7.4 are representative of the configurations presented. At first, the case of an OA209 airfoil at a lower Reynolds number $\mathrm{Re} = 0.5 \times 10^6$ is presented (the case $\mathrm{Re} = 1.0 \times 10^6$ is also investigated but, as it reveals a scenario strictly similar to the one presented in chapters 5 to 7, it is just briefly introduced). Then, a different airfoil is tested : a NACA0012 at $\mathrm{Re} = 1.0 \times 10^6$. This choice of configuration is motivated by the numerical study of Wales *et al.* [166] and the experimental study of Hristov and Ansell [70]. For this case, the whole approach could not be carried out due to a lack of time. However, the available data reveal a similar behavior, although more complex. Finally, the results obtained in these different configurations are compared to the case of the OA209 airfoil at Reynolds number $\mathrm{Re} = 1.8 \times 10^6$.

8.1 Influence of the Reynolds number on the stall of an OA209 airfoil

Two computations are performed for an OA209 airfoil at different Reynolds numbers: $\mathrm{Re} = 1.0 \times 10^6$ and $\mathrm{Re} = 0.5 \times 10^6$. These values are intentionally high enough to ensure that the RANS approach, considering a fully turbulent boundary layer, is still pertinent and the solutions are still meaningful from a physical point of view. The method used is similar to the one performed and presented through the different chapters: first the steady solutions are computed using continuation methods, second the stability analysis of each solution is performed and finally a bifurcation scenario is deduced fromunsteady RANS computations and the static stall model.

8.1.1 Steady solutions

The polar curves of the lift coefficient corresponding to the two additional values of Reynolds number tested are plotted with the polar curve of the case at $\mathrm{Re} = 1.8 \times 10^6$ in Figure (8.1). In Figure (8.1)(a), which presents the three polar curves, one can observe how an increase of the Reynolds number (direction of the black arrow) increases the maximum lift coefficient value and the stall angle. Moreover, in Figures (8.1)(b), (c) and (d), which present zooms close to stall for the three cases, one can also observe how it affects the appearance of the hysteresis area close to stall: for the smallest Reynolds number, no hysteresis is identified and for the two others, the higher the Reynolds number, the larger the range of coexisting solutions.

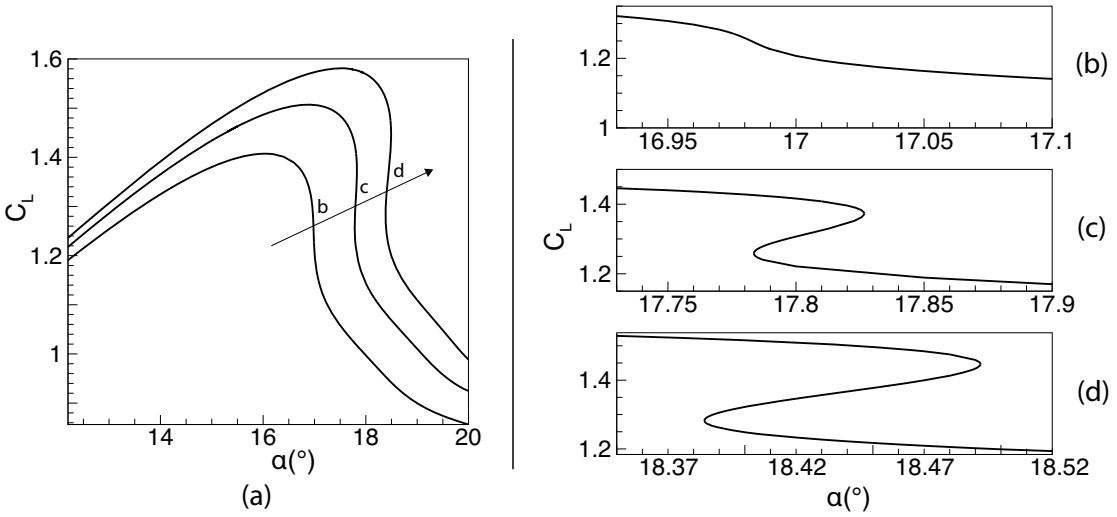

FIGURE 8.1: (a) Evolution of the lift coefficient as a function of the angle of attack for the flow around an OA209 airfoil at Mach number $\mathrm{M} = 0.16$ and for three different Reynolds numbers: $\mathrm{Re} = 0.5 \times 10^6$ (labelled b), $\mathrm{Re} = 1.0 \times 10^6$ (labelled c) and $\mathrm{Re} = 1.8 \times 10^6$ (labelled d). (b), (c) and (d): zooms on the polar curves close to stall for $\mathrm{Re} = 0.5 \times 10^6$, $\mathrm{Re} = 1.0 \times 10^6$ and $\mathrm{Re} = 1.8 \times 10^6$ respectively (letters matching the ones used in (a)).

The flow topology of the steady solutions is similar to the one presented in Figure (5.1) of section 5.1 for the three cases tested: a recirculation bubble appears at the trailing edge for low angles of attack and the separation point moves toward the trailing edge as the angle of attack increases.

8.1.2 Linear stability analysis

This section is dedicated to the stability of steady solutions obtained for $\mathrm{Re} = 0.5 \times 10^6$ for which no hysteresis is observed when varying the angle of attack (the results obtained for $\mathrm{Re} = 1.0 \times 10^6$ exhibit a scenario similar to the one obtained for $\mathrm{Re} = 1.8 \times 10^6$ and described in section 5.2). Similarly to the case $\mathrm{Re} = 1.8 \times 10^6$, two complex eigenmodes are found unstable in the explored range of angles of attack. A low-frequency stall eigenmode is unstable in a small range of angles of attack where the lift coefficient drops suddenly. A high-frequency vortex-shedding eigenmode becomes unstable for higher angles of attack $\alpha > 19.50°$, in the post-stall regime. The temporal features and the structures of these modes are similar to the ones described in sections 5.2.3 and 5.2.4.1 respectively for the case at Reynolds number $\mathrm{Re} = 1.8 \times 10^6$. As a reminder, the vortex shedding mode, existing for high angles of attack, when the flow is detached, has a Strouhal number $\mathrm{St} \approx 0.2$. The topology of this mode, which is made of large structures convected upward, is represented in Figures (5.6)(b) and (d) of chapter 5. The stall mode, has a lower Strouhal number $\mathrm{St} \approx 0.05$. The topology of this mode, which is made of a large pulsating structure located on the suction side of the airfoil, is depicted in Figures (5.6)(a) and (c). The main difference for the case at Reynolds number $\mathrm{Re} = 0.5 \times .10^6$ is the evolution of the low frequency mode as a function of the angle of attack.

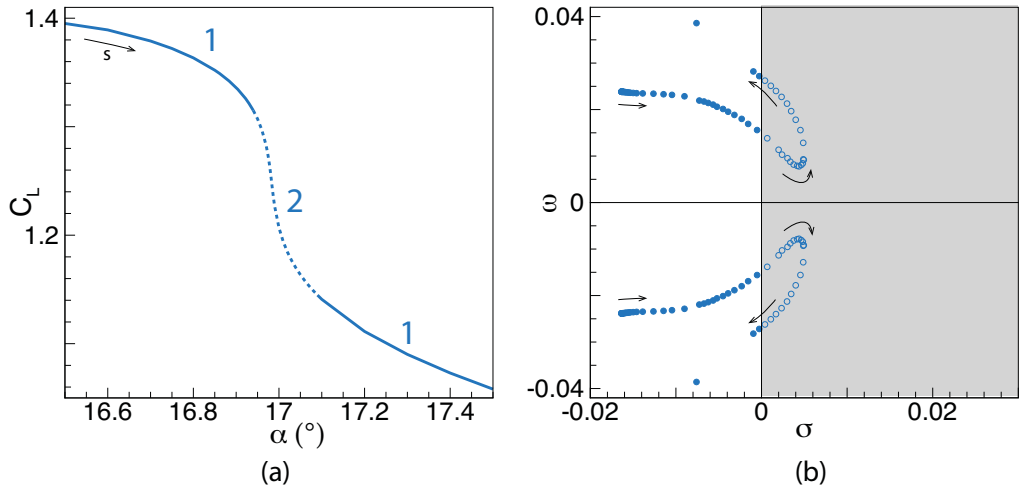

FIGURE 8.2: Real evolution of the temporal behavior of the leading mode. (a) polar curve zoomed in close to stall and associated temporal behavior. (b) Superimposition of the spectra obtained from each steady solution along the polar curve (the black arrows indicate the direction of an increasing curvilinear abscissa). The color code is similar to the one of Figure (7.17) in chapter 7. The grey area corresponds to the zone in which the modes are unstable.

Figure (8.2) shows a superposition of all the eigenspectra (b) computed for angles of attack in the range $12.00° \leq \alpha \leq 17.30°$ (a). The displacement of the leading complex eigenvalues (blue points) in the plane (σ, ω) clearly shows that they get first unstable (dashed line on the polar curve and grey area in the complex plan) when increasing the angle of attack above $\alpha = 16.95°$ and then get stable for $\alpha \geq 17.08°$. The identification of the unstable region $16.95° \leq \alpha \leq 17.08°$ is clear when examining the growth rate as a function of the angle of attack displayed in Figure (8.3) (a). The change of slope for the growth rate occurs around $\alpha = 16.98°$ and is associated to an increase of the frequency, as seen in Figure (8.3) (b). The angular frequency $\omega = 0.015$ at the second Hopf bifurcation is slightly larger than $\omega = 0.026$, the angular frequency at the first Hopf bifurcation. Note that this scenario is in perfect agreement with the one predicted by the model in the case without hysteresis (parameter d of the model set to $d = 1$) and whose a schematized representation is proposed in Figure (7.17) of chapter 7.

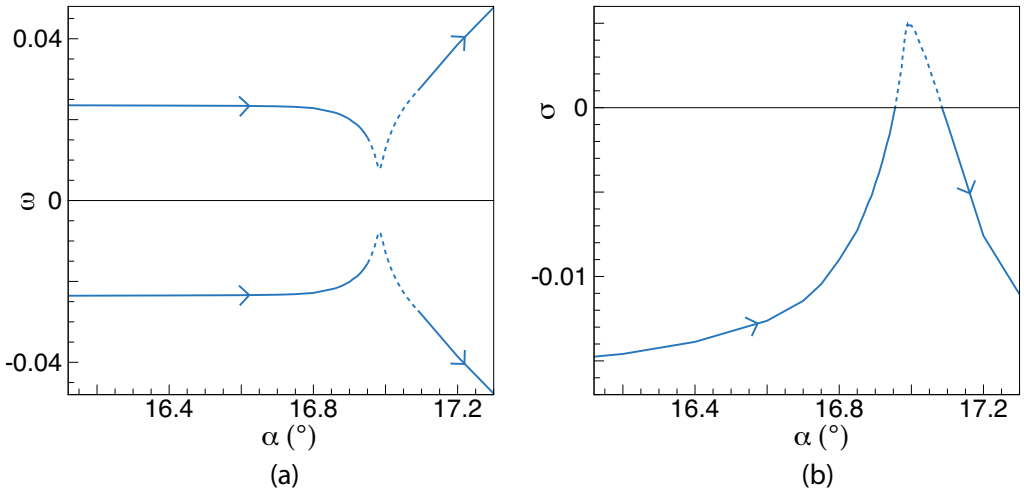

FIGURE 8.3: Evolution of the angular frequency (a) and the growth rate (b) as a function of the angle of incidence. The direction of the arrows refers to increasing curvilinear abscissa.

8.1.3 Unsteady RANS computations

As identified in section 4.3.1, a difference between the solutions obtained with continuation methods and local time stepping methods exists. A solution is proposed in appendix C and validated in appendix D and chapter 6. It consists in slightly modifying the cutoff value on the turbulent variable and allows us to obtain a good agreement between the linear stability of steady solutions obtained with continuation methods and unsteady RANS computations. For the case $\mathrm{Re} = 0.5 \times 10^6$, the unsteady RANS computations were actually performed before identifying the modification of the cutoff as a solution to reconcile RANS computations and continuation methods. In order to avoid performing additional time costly unsteady RANS computations, it was decided to live with the small shift between the two approaches. It was verified for a few steady solutions that the stability analysis is qualitatively similar in both cases. Consequently, the results of the unsteady RANS computations presented in Figure (8.4) are slightly

shifted compared to the bifurcation scenario calibrated on the steady states from continuation methods and their linear behavior (presented in Figure (8.5)).

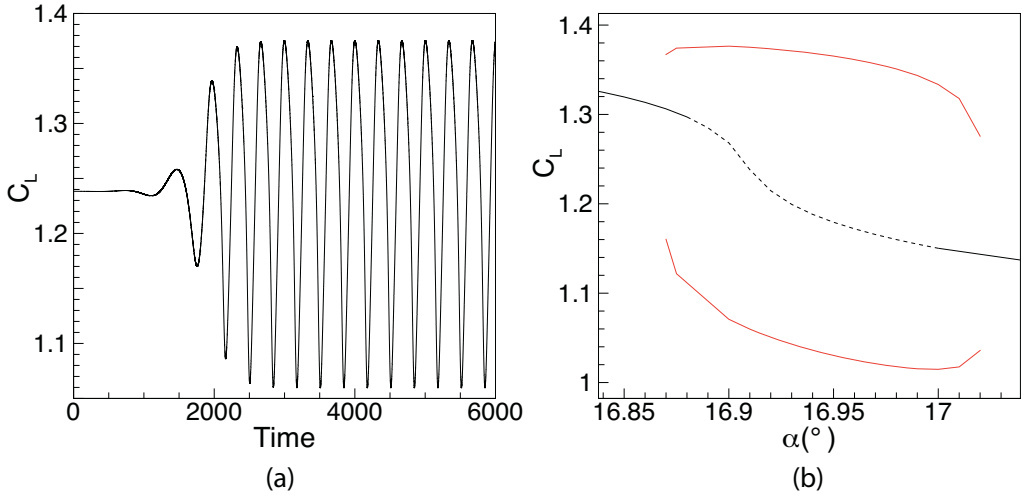

FIGURE 8.4: Results of the unsteady RANS computations. (a) Time evolution of the lift coefficient for an angle of attack of $\alpha = 16.91°$. Computation initialized with a steady solution at the same angle of attack. (b) Evolution of the lift coefficient for the steady states (full black lines and dashed black line) and visualisation of the extreme values of the limit cycle (full red lines). The linear behavior of the steady states is indicated by a dashed line for the linearly unstable ones and by a full line for the linearly stable ones.

Figure (8.4)(a) shows the evolution of the lift coefficient as a function of the time for the particular case of $\alpha = 16.91°$. This curve is obtained from an unsteady RANS computation initialized with the steady solution at the same angle of attack. For this angle of attack the linear stability analysis of the steady solution revealed an unsteady unstable mode. The lift coefficient fast diverges from the lift value of the steady state. It oscillates until it reaches a limit cycle of large amplitude ($\Delta C_L \approx 0.3$). The analysis of the structure of the unsteadiness reveals a recirculation bubble pulsating from the trailing edge, which is similar to the mechanism presented in Figure (6.2) in chapter 6 for the case at higher Reynolds number. It generates a high lift state (corresponding to the maximum value of the limit cycle) when the recirculation bubble is tiny and located at the trailing edge and a low lift state (corresponding the minimum value of the limit cycle) when the recirculation bubble is large and extends on the whole suction side. The Strouhal number associated with this unsteady phenomenon is St = 0.00545. Such a value is two orders of magnitude lower than the classic bluff body vortex shedding Strouhal number $St \approx 0.2$ and in good agreement with the Strouhal number of the unstable mode identified with the linear stability analysis St = 0.00296. All these observations (large amplitude oscillations at a low Strouhal number and structure made of a pulsating recirculation bubble on the suction side of the airfoil) tend to indicate that this phenomenon is similar to the one observe at higher Reynolds number when there is an hysteresis (presented in chapter 6) and described in the literature as low frequency oscillations (see section 1.3.2). The study of the possible different scenarios

with the static stall model showed that the appearance of such a limit cycle was conditioned by the positions of the Hopf bifurcations and the position of the intersection of the unstable limit cycle with the middle branch of steady solutions. Thus, it was supposed that the Hopf bifurcations played a more significant role in the formation of this limit cycle than the saddle-node bifurcations. This case confirms this hypothesis and, even more, highlights the fact that the existence of this limit cycle of high amplitude and low frequency is independent of the existence of saddle-node bifurcations and a hysteresis of the steady solutions.

Limit cycle solutions have been tracked when varying the angle of attack using a simple parameter continuation (as described in chapter 6). The full red lines in Figure (8.4)(b) are the maximal and minimal values of the limit cycles obtained when varying the angle of attack. For comparison, the branch of steady solutions (obtained with steady RANS computations) is reproduced in this figure with a solid (resp. dashed) curve when it is stable (resp. unstable). Interestingly, the limit cycle branch exists in the range of angle of attack $16.87° \leq \alpha \leq 17.20°$ that is larger than the range of instability $16.88° \leq \alpha \leq 17.00°$ found for the steady solutions. Consequently, the Hopf bifurcations at $\alpha = 16.88°$ and $\alpha = 17.00°$ are both sub-critical. Limit cycle solutions thus exist for values of the angle of attack for which the steady solutions are stable, approximatively in the range $16.87° \leq \alpha \leq 16.88°$ (resp. $17.00° \leq \alpha \leq 17.20°$) for the first (resp. second) Hopf bifurcation.

8.1.4 Application of the one-equation static stall model to the case without hysteresis

At first, one shall note that the steady states presented in subsection 8.1.1 were computed with continuation methods, which implies that the cutoffs on the turbulent variable implemented into the solver are not taken into account (see section 4.3.1). The linear stability analysis presented in section 8.1.2 is based on these steady solutions obtained with a continuation method. However, the unsteady RANS computations (presented in subsection 8.1.3) were performed with the standard version of the Spalart–Allmaras turbulence model in the sense of elsA, which means that several cutoffs were active. The static stall model, which requires results from the linear stability analysis, will be calibrated using results obtained with continuation methods. Consequently, it will not be possible to quantitatively compare the results from the static stall model and from the unsteady RANS computations. However, a qualitative comparison will be possible and will provide interesting insights about the criticaliity of the Hopf bifurcations and the width of the limit cycle.

Section 7.4 was dedicated to the study of different scenarios based on the values of the one-equation static stall model. The sixth and seventh scenarios detailed in subsection 7.4.3 of chapter 7 were for cases without hysteresis of the steady solutions. As a reminder, a low frequency large amplitude limit cycle is found in the two cases. The difference between the two scenarios is the type of Hopf bifurcation, supercritical or subcritical, which is driven by their positions. If the Hopf bifurcations are inside the two points of maximum curvature, they are supercritical, otherwise, they are subcritical. At first, note that the results of the linear stability analysis and the unsteady

RANS computations for the case $\mathrm{Re} = 0.5 \times 10^6$ are in agreement with this observation made on simplified scenarios as the Hopf bifurcations identified are located outside the two points of maximum curvature and seem to be sub-critical.

The point is now to calibrate the model in order verify if this behavior is confirmed. We recall the equation of the static stall model:

$$\frac{d^2 C_L}{dt^2} + p_1(C_L) \cdot \frac{dC_L}{dt} + c \cdot (\Delta\alpha + p_2(C_L)) = 0 \tag{8.1}$$

where :

- $p_1(C_L) = \sum_{i=0}^{N_1} b_i \cdot C_L^i$, with N_1 the order of the polynomial $p_1(C_L)$
- $p_2(C_L) = \sum_{i=1}^{N_2} a_i \cdot C_L^i$, with N_2 the order of the polynomial $p_2(C_L)$
- $\Delta\alpha = \alpha - \alpha_s$, with α_s an arbitrary defined *stall angle*
- $C_L = c_l - c_{l_s}$, with c_{l_s} the lift value associated to α_S

The calibration process, which consists in determining a_i, b_i, c, c_{l_s} and α_S, is similar to the one used for the case $\mathrm{Re} = 1.8 \times 10^6$ and presented in section 7.1.3 of chapter 7. As a reminder, the calibration of the parameters a_i, b_i and c is based on two objective functions and a Pareto front of optimal solutions is found. Each extremity of the front corresponds to the best fit for each objective function. All the solutions in between correspond to compromises between the two objective functions. The results of the calibration presented below are obtained for one compromise. Table 8.1 presents the values of the coefficients obtained in that case.

Coeff	Value	Coeff	Value	Coeff	Value
α_s	16.985366	a_1	2.5706×10^{-1}	b_0	-9.4346×10^{-3}
C_{L_s}	1.240135	a_2	-2.3221	b_1	8.3811×10^{-2}
c	2.4658×10^{-4}	a_3	8.3774×10^{1}	b_2	2.5296
		a_4	1.6206×10^{2}	b_3	4.9003

TABLE 8.1: Values of the different coefficients corresponding to the chosen solution.

Figure (8.5) presents the bifurcation scenario obtained with such coefficients. This bifurcation scenario exhibits two subcritical Hopf bifurcations. It is coherent with the observations made during the analysis of unsteady RANS computations results, which highlighted such a type of bifurcations as well as with the seventh reference scenario

depicted in Figure (7.18)(*b*). The range of existence of the limit cycle is similar between the static stall model ($\approx 0.12°$) and the unsteady RANS computations ($\approx 0.16°$). The model slightly underestimates the range of existence of the limit cycle, similarly to what was observed for the case at $\mathrm{Re} = 1.8 \times 10^6$. Finally, the similarities between the static stall model and the unsteady RANS computations prove that the model, which was created based on a hysteresis behavior, successfully reproduces the nonlinear behavior observed when there is no hysteresis.

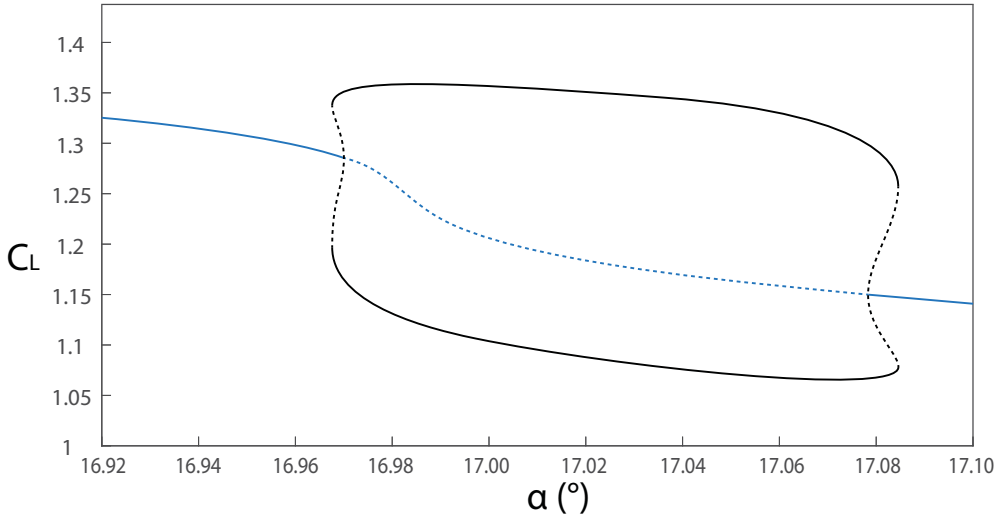

FIGURE 8.5: Bifurcation diagram of the model calibrated on the linear behavior observed during RANS computations. The color code is similar to the one of Figure (7.5). The steady solutions are plotted in blue and the black lines represent the extreme values of the surrounding limit cycle. The unstable solutions are plotted with dashed lines while the stable ones are associated to full lines.

8.1.5 Comparison of the cases at $\mathrm{Re} = 1.8 \times 10^6$ and $\mathrm{Re} = 0.5 \times 10^6$

It is interesting to compare this scenario with the one described in chapter 5. At first sight, they might seem very different as this one is much simpler. However, their behaviors are strongly linked. They both start with an unsteady stable mode that becomes unstable and less unsteady at the same time. The only difference is that, in the case with hysteresis, the angular frequency decreases enough to become null. When it happens, the new unstable steady mode splits into two steady modes and when one of these two modes becomes stable, the saddle-node bifurcation occurs. On the other hand, in the case without hysteresis ($\mathrm{Re} = 0.5 \times 10^6$), the angular frequency of the mode never becomes null and starts increasing before reaching the axis $\mathrm{St} = 0$ (Figure 8.2).

In the end the complete scenario makes sense: there is an unsteady mode responsible for stall that becomes unstable around the stall angle. The complexity of the

scenario depends on the temporal behavior of this mode: a saddle-node occurs when a steady mode crosses the axis $\sigma = 0$. When there is no hysteresis, and consequently no saddle-node bifurcation, the unsteady mode never becomes steady whereas with hysteresis, the unsteady mode becomes null and split into two steady modes, which might lead to a saddle-node bifurcation.

The model originally created for the most complicated case with a hysteresis is actually robust and works well without extra efforts for the simplest case without hysteresis. The study of this model reveals that both cases generate low frequency oscillations around the stall angle even though the appearance and disappearance of the limit cycle in the case with hysteresis is more complicated. These observations are confirmed with unsteady RANS computations for the two scenarios.

Finally, one shall note that an attempt to link the evolution of hysteresis as a function of the Reynolds number from a bifurcation theory point of view was proposed by Cui *et al.* [34]. A similar approach could be very useful to identify the critical Reynolds number for which hysteresis disappears and could provide very interesting insight on how the limit cycles evolve from the case with hysteresis to the case without and, particularly, close to the critical point.

8.2 Investigation of the stall for a NACA0012 airfoil

The bifurcation scenario of a NACA0012 at Reynolds number $\mathrm{Re} = 1.0 \times 10^6$ is investigated. First, several results that can be found in the literature are introduced. The possibility to compare as much as possible to these results is the main motivation that have led to the choice of this configuration. Afterwards, the steady solutions obtained with continuation methods and their linear stability are introduced. Two different cases are actually investigated for this configuration: one with the Spalart–Allmaras model and one with a modified version of the Spalart–Allmaras model [46]. This choice is motivated by the aforementioned literature review. Due to a lack of time, the non linear behavior could not be investigated for this airfoil.

8.2.1 Literature review and motivations

In a recent paper, Hristov and Ansell [70] investigated experimentally the static stall phenomenon around the symmetric NACA0012 airfoil at the Reynolds number $\mathrm{Re} = 1.0 \times 10^6$. The polar curves obtained by Hristov and Ansell are presented in Figure (8.6), which exhibits the evolution of the lift (a) and the pitching moment (b) as a function of the angle of attack. One can identify two branches in the area where the lift coefficient decreases : the blue one is obtained by increasing α while the red one is obtained by decreasing α. The existence of two solutions based on the history of the flow is characteristic of a hysteresis phenomenon. However, note that in the present case, these lift coefficient values are time-averaged while the hysteresis described in this manuscript for the OA209 is obtained from steady lift values. The hysteresis identified by Hristov and Ansell implies different limit cycles for the two branches.

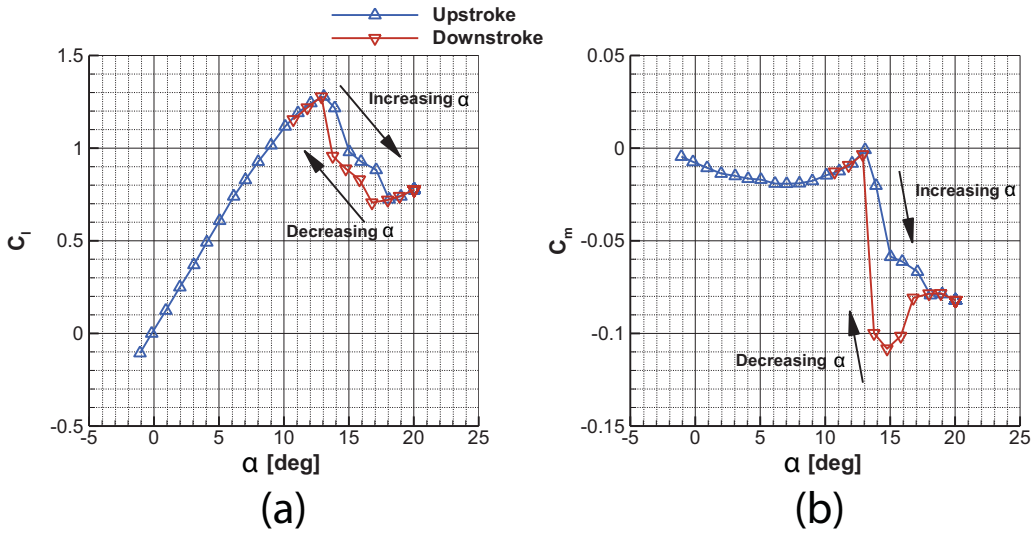

FIGURE 8.6: Evolution of the lift coefficient (a) and the pitching moment (b) for several angles of attack for a NACA0012 at Re $= 1.0 \times 10^6$ from Hristov and Ansell [70].

They also measured the unsteady surface pressure and, from it, deduced the Strouhal number[1] of the phenomena involved. Figure (8.7) presents a map of the Strouhal number as a function of the position on the airfoil (made nondimensional with the chord c.). Three angles of attack are investigated for each solution of the hysteresis: $\alpha = 14.00°$ (a) and (d), $\alpha = 15.00°$ (b) and (e) and $\alpha = 16.00°$ (c) and (f). The high lift solutions (labelled upstroke in the legend of Figure (8.6)) are on the left (a), (b) and (c) and the low lift solutions (labelled downstroke in the legend of Figure (8.6)) are on the right (e), (f) and (g). From this spectral analysis, one can observe two very distinct phenomena: one of very low Strouhal number $St \approx 0.01$ of large amplitude near the leading edge ($0 \leq x/c \leq 0.2$) and one of Strouhal number St ≈ 0.2 of large amplitude more upstream ($0.2 \leq x/c \leq 0.9$). Hristov and Ansell describe the unsteadiness close to the leading edge as a low frequency oscillations mechanism as its Strouhal number and location are in good agreement with the studies more extensively presented in section 1.3.2. Also, they argued that the Strouhal number of the higher frequency phenomenon observed downstream is in agreement with classic bluff-body shedding such as the one identified by Roshko [142]. With time resolved particle image velocimetry (not presented here but visible in detail in the PhD of Hristov [69]) they confirmed that the low frequency phenomenon is a movement of the separation point characteristic of the LFO described in the literature. However, one should note that the amplitude of the separation point displacement is quite small ($\approx 15\%$ of the chord) compared to the displacement of the separation point encountered in this study (Figure (6.2)) or in the literature (Figure (1.9) from Broeren [23]). The difference between these studies and the one of Hristov seems to be the simultaneous existence of a vortex shedding unsteadiness and low frequency oscillations. Finally, the amplitude of these phenomena evolves with the angle of attack as illustrated in Figure (8.7): the upper branch is mostly dominated by the low frequency unsteadiness (the vortex shedding mechanism

[1]Based on the chord length weighted by the sine of the angle of attack: St $= \frac{f \cdot c \cdot \sin(\alpha)}{U_\infty}$

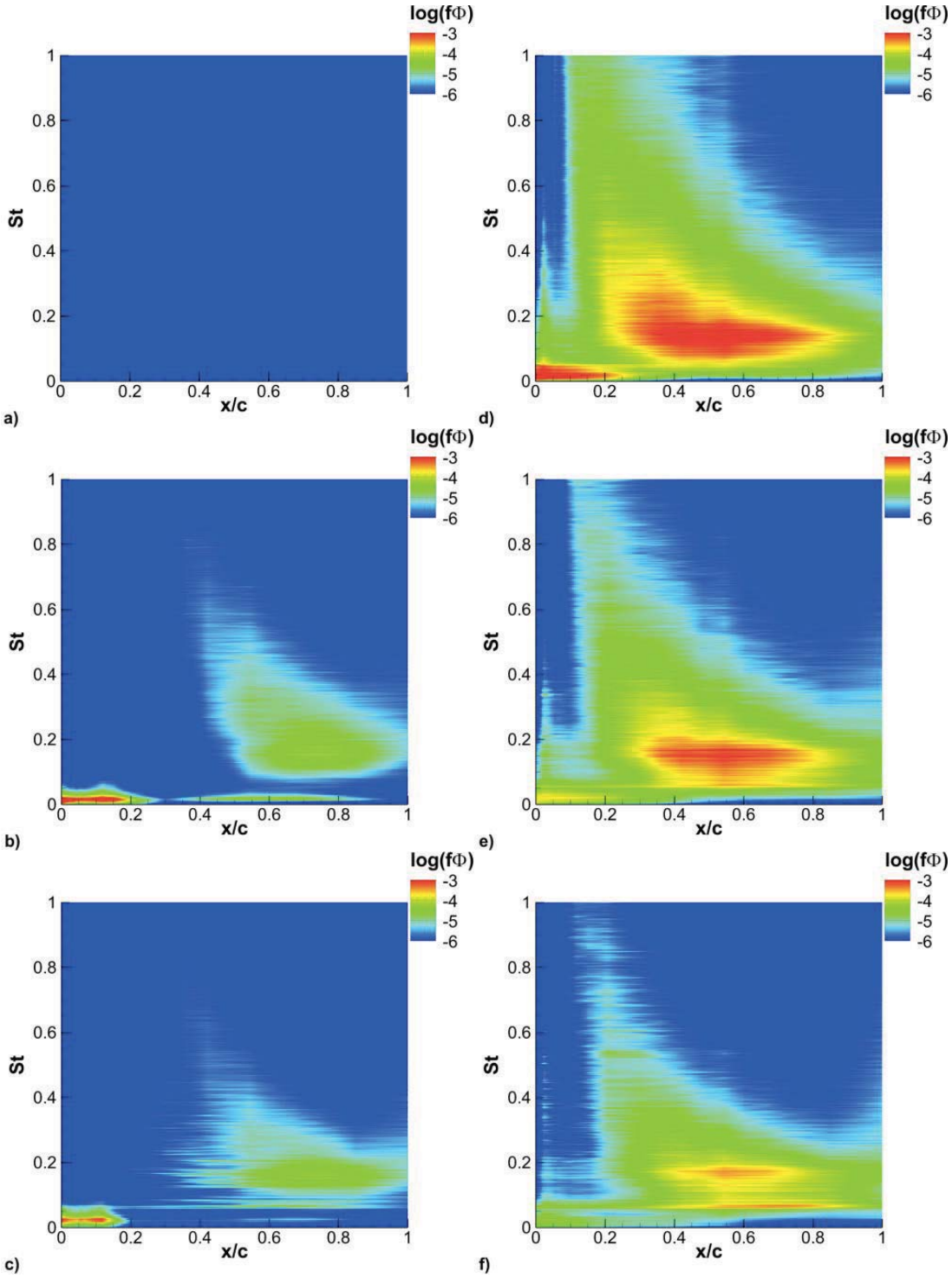

FIGURE 8.7: Maps representing the Strouhal number of unsteady phenomena as a function of their position along the suction side of the airfoil. On the upper branch : $\alpha = 14.00°$ (a), $\alpha = 15.00°$ (b) and $\alpha = 16.00°$ (c). On the lower branch : $\alpha = 14.00°$ (d), $\alpha = 15.00°$ (e) and $\alpha = 16.00°$ (f). From Hristov and Ansell [70].

is also identified but is very weak). On the contrary, the lower branch is driven by the vortex shedding phenomenon mostly, even if one can notice that for $\alpha = 14.00°$, both

phenomena seem to coexist. In the end, Hristov and Ansell observed the following regarding the unsteady mechanisms in the hysteresis area:

- The low frequency oscillations are dominant at the end of each branch (Figures (8.7)(b), (c) and (d))
- The vortex shedding mechanism is dominant at the end of the lower branch (Figures (8.7)(d) and (e)). On this branch, the amplitude of this unsteadiness decreases as the angle of attack increases
- The two phenomena coexist for $\alpha = 14.00°$ on the lower branch (Figure (8.7)(d))

Several numerical studies on a NACA0012 at high Reynolds number can also be found in the literature. Mittal [110] identified a hysteresis between $17.00° < \alpha < 19.00°$ with unsteady RANS computations coupled with the Baldwin-Lomax turbulence model at Reynolds number $\mathrm{Re} = 1.0 \times 10^6$. Although the stall angle is higher than the experimental one identified by Hristov and Ansell (probably due to the limitations of the RANS modeling detailed in section 1.4), the range of hysteresis identifed by Mittal [110] matches the one of Hristov and Ansell [70]. Wales *et al.* [166] conducted a numerical study that consisted in computing steady solutions with continuation methods for a flow at high Reynolds number ($\mathrm{Re} \geq 1.85 \times 10^6$). Particularly, they investigated the influence of the Edwards–Chandra modification of the Spalart–Allmaras model [46] (this modification is introduced in section 2.1.4) and the influence of the turbulent variable boundary condition. Figure (8.8) exhibits the steady solutions obtained for four different cases : with two values of the boundary condition ratio $\left(\frac{\mu_t}{\mu}\right)_\infty$ (3.0 and 10.0) and with/without the Edwards–Chandra modification of the Spalart–Allmaras model. This figure shows that the level of freestream turbulent has a direct effect on the appearance of a hysteresis steady solutions with the Spalart–Allmaras. This obervation is coherent with the one made by Marchman [94] who noted that the freestream turbulence level had an impact on the appearance of hysteresis in wind tunnel. Moreover, Figure (8.8) also shows that the original Spalart–Allmaras model fails to catch hysteresis in the case of a NACA0012 while the modification proposed by Edwards and Chandra [46] succeed to identify a hysteresis of steady solutions.

In the end, the NACA0012 airfoil at high Reynolds number seems to be able to combine simultaneously a hysteresis and low frequency oscillations [70], which are the two main features of the bifurcation scenario identified for the OA209 airfoil at Reynolds number $\mathrm{Re} = 1.8 \times 10^6$. In that sense, it is the perfect candidate to investigate the robustness of the bifurcation scenario. Moreover, based on the numerical computations carried out by Wales *et al.* [166], it is very likely that at $\mathrm{Re} = 1.0 \times 10^6$, the Spalart–Allmaras turbulence model fails to catch a hysteresis while the Edwards–Chandra modification of the model might be able to. Consequently, it appears interesting to study both cases as it would allow us to obtain one case without hysteresis to be compared to the scenario identified for the OA209 at $\mathrm{Re} = 0.5 \times 10^6$ and one with hysteresis to be compared to the scenario identified for the OA209 at $\mathrm{Re} = 1.8 \times 10^6$. It must be noted that contrary to what is done by Wales *et al.* and what is presented in Figure (8.8) the boundary condition of the turbulent variable, set by the ratio $\frac{\mu_t}{\mu}$ will not be changed and will remain equal to 3.0 in agreement with the value suggested by Spalart

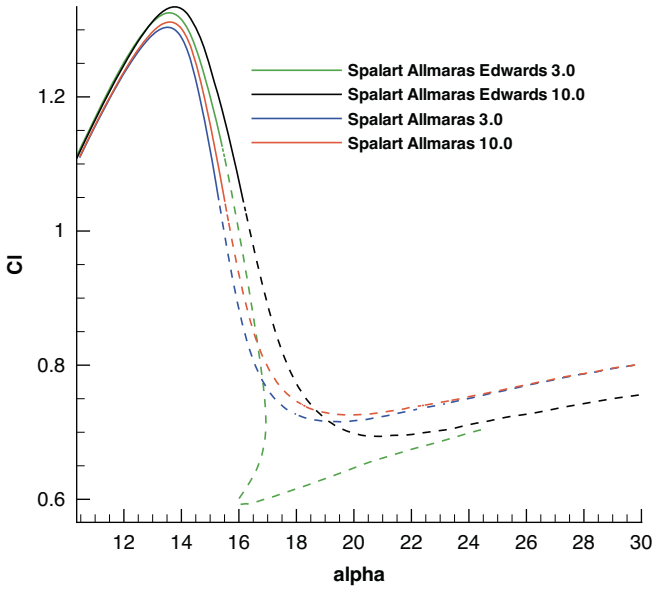

FIGURE 8.8: Influence of the turbulent boundary condition on the steady solutions around a NACA0012 at Mach number M = 0.3 and Reynolds number Re = 1.85×10^6 from Wales *et al.* [166].

and Rumsey [152] and to the boundary conditions used for the OA209. Finally, a comparison of the results with the aforementioned studies should give us insights on the validity of our approach and its capacity to correctly identify the phenomena observed experimentally.

8.2.2 Results with the Spalart–Allmaras model

First, the case of the flow around a NACA0012 airfoil at Reynolds number Re = 1.0×10^6 modelled with the original version of the Spalart–Allmaras turbulence model is investigated. Based on the results of Wales *et al.*, an evolution of the steady states similar to the one obtained with the OA209 at Re = 0.5×10^6 is expected and a similar bifurcation scenario is supposed at first. The evolution of the lift coefficient as a function of the angle of attack is presented in Figure (8.9):(a) depicts a general overview and (b) a zoom close to stall. As expected, the polar curve does not exhibit any hysteresis. Moreover, if the stall angle is overestimated compared to the experiment of Hristov and Ansell [70], the maximum lift value is in good agreement with the one they observed. This figure also presents the areas where a linearly unstable mode is identified with the global stability analysis: they are highlighted with dashed lines. Similarly to the cases of the OA209, two unstable modes are encountered: one low frequency mode close to stall and one of higher frequency when the flow is massively separated. The second one, is a very classic bluff-body mode of Strouhal number St = 0.2.

Figure (8.10) presents the structure of the eigenmode: (a) depicts the real part of the streamwise velocity component ρu and (b) the real part of the turbulent variable $\rho\tilde{\nu}$. The structure of the low frequency mode is very similar to the structure of the mode identified in the cases of the OA209 airfoil (see Figure (5.6)): the main structure

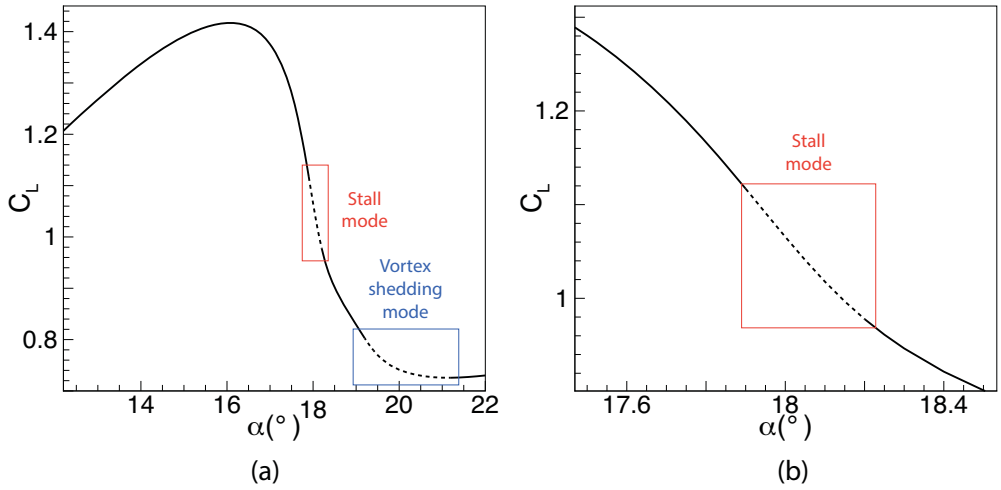

FIGURE 8.9: Evolution of the lift coefficient as a function of the angle of attack for an NACA0012 airfoil at Re $= 1.0 \times 10^6$ and M $= 0.16$ with a RANS approach coupled with the original version of the Spalart–Allmaras turbulence model. (a) Full polar curve. (b) Zoom close to stall angle. Dashed lines indicate the solutions for which an unstable mode is encountered.

is located just above the recirculation bubble. However, in the case of the NACA0012, the flow seems to be more massively separated and consequently, the main structure of the mode is located more upstream than in the case of the OA209.

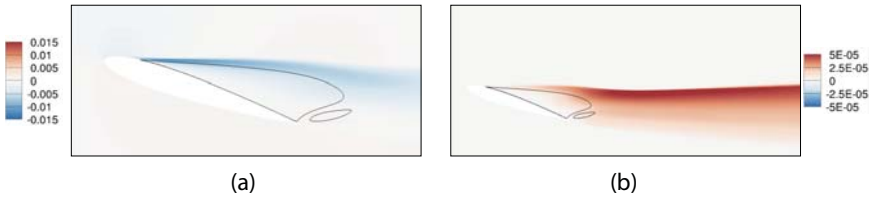

FIGURE 8.10: Visualisation of the structure of the eigenmodes. (a) Real part of the $\hat{\rho u}$ field of the stall eigenmode ($\alpha = 18.05°$). (b) Real part of the $\hat{\rho\tilde{\nu}}$ field of the stall eigenmode ($\alpha = 18.05°$).

Then, the evolution of the eigenmode along the polar curve is investigated. The superimposition of the spectra is presented in Figure (8.11): (a) shows the evolution of the lift coefficient as a function of the angle of attack (the areas where an unstable mode is found are highlighted by dashed lines) and (b) the superimposition of the spectra computed for every angle of attack (only the stall mode, introduced in Figure (8.10), is represented). At first sight, the evolution seems different from the one observed for the OA209 airfoil at Reynolds number Re $= 0.5 \times 10^6$ and for which a schematic representation of this behavior is represented in Figure (7.17). However, close to stall, the behavior is actually very similar (for $17.90° < \alpha < 18.20$ in the (α, C_L) plane and for $\omega < 0.05$ in the complex plane (σ, ω)). Indeed, starting from the most left blue dots, which correspond to the stall mode and its complex conjugate obtained for $\alpha = 12.00°$,

as the angle of attack increases, this mode becomes less and less stable until it finally becomes unstable. Then, while its angular frequency increases, the mode is stabilized again. So far, the evolution is indeed identical to the one described in section 8.1.2 for the OA209 at Reynolds number $\mathrm{Re} = 0.5 \times 10^6$. The main difference appears for higher angles of attack ($\alpha > 19.20°$ in the (α, C_L) plane and $\omega > 0.05$ in the complex plane (σ, ω)): instead of staying stable, the mode describes a Z shape and becomes unstable again for a very few angles of attack before finally getting stable while its angular frequency increases.

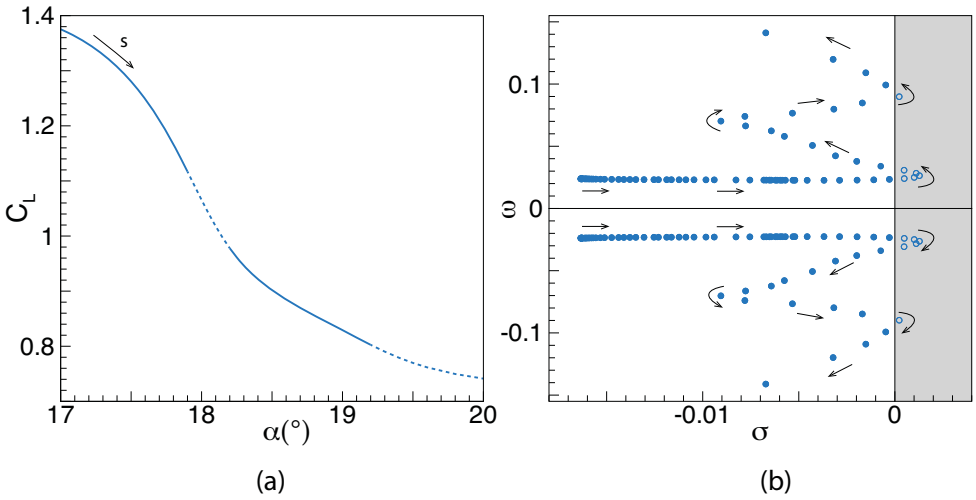

FIGURE 8.11: Real evolution of the temporal behavior of the leading mode in the case of a NACA0012 at $\mathrm{Re} = 1.0 \times 10^6$ with the original Spalart–Allmaras model. (a) Polar curve zoomed in close to stall and associated temporal behavior. (b) Superimposition of the spectra obtained from each steady solution along the polar curve. Color code similar as the one of Figure (5.13). The grey area corresponds to the zone in which the modes are unstable.

To have a better understanding of the origins of this particular Z shape, the evolution of the angular frequency and of the growth rate are studied in more detail for the two unstable modes (stall mode and vortex shedding mode) . The evolutions of the angular frequencies as a function of the angle of attack are depicted in Figures (8.12)(a) and (c) and the evolutions of the growth rates as a function of the angle of attack are depicted in Figures (8.12)(b) and (d). Focusing on the evolution of the growth rate of the stall mode, one can observe on the first part of the curve ($\alpha < 18.50°$) a behavior similar to the one of the OA209 airfoil at Reynolds number $\mathrm{Re} = 0.5 \times 10^6$ (presented in Figure (8.3)). For larger angles of attack ($\alpha \geq 18.50°$), the growth rate of the stall mode increases again and event gets unstable in a narrow range of angle $19.20° \leq \alpha \leq 19.40°$ with a peak for $\alpha = 19.30°$. Examining the growth rate of the vortex-shedding eigenmode depicted in Figure (8.12)(d), it appears that this mode becomes unstable for the angle of attack $\alpha = 19.30°$ corresponding to the peak of growth rate of the stall mode during the second destabilization (this value is marked by dashed line linking Figures (8.12)(b) and (d)). Also, the angle of attack for which the vortex shedding mode becomes unstable seems to correspond to a break in the slope of the

evolution of the Strouhal number as illustrated by a dashed line in Figures (8.12)(a) and (c). Finally, note that the angle of attack for which the vortex shedding mode is first identified seems to correspond to a break of slope in the evolution of the stall mode's growth rate (marked by dashed line linking Figures (8.12)(b) and (d)). In the end, it seems that the behavior of the stall mode is similar to the one observed for the OA209 at Reynolds number $\mathrm{Re} = 0.5 \times 10^6$ at stall but is then affected by the appearance of the vortex shedding mode which appears right after stall, for angles of attack smaller than in the case of the OA209.

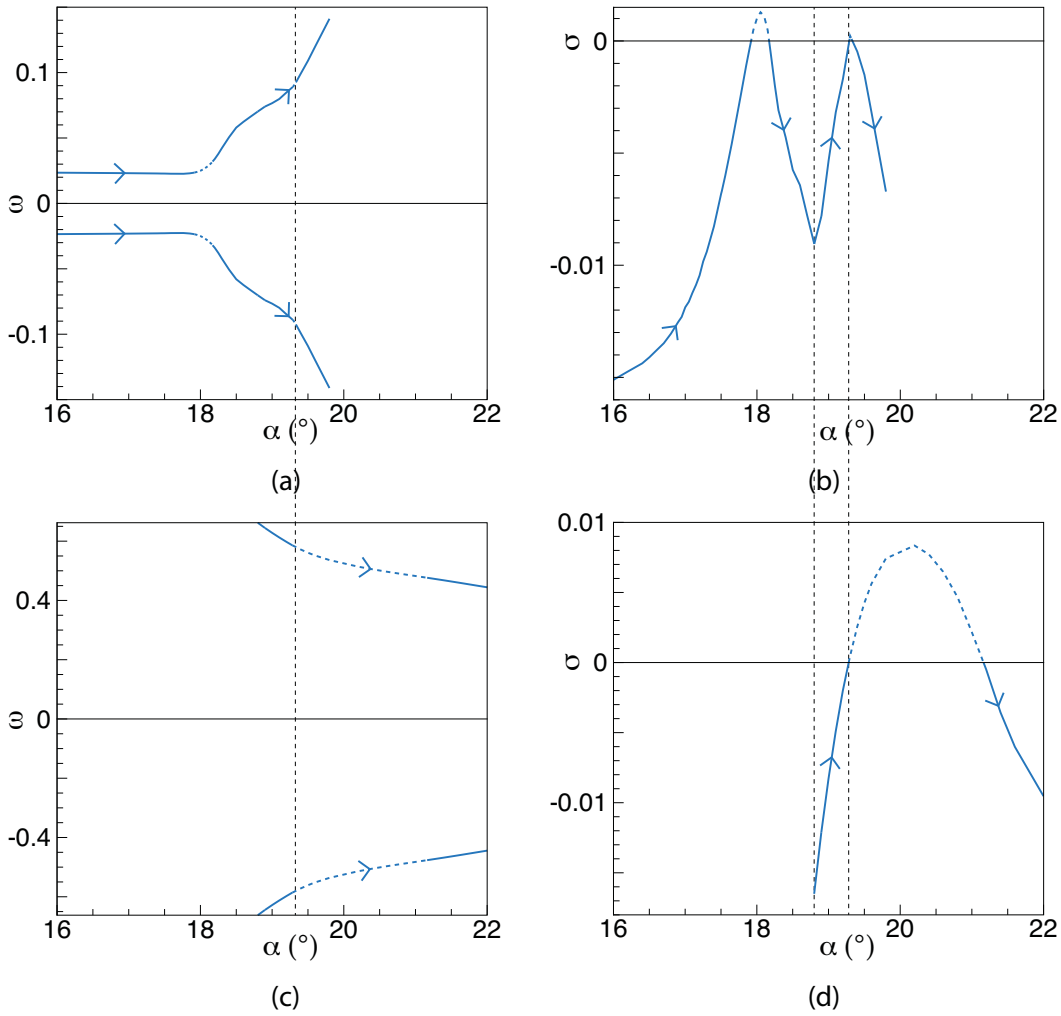

FIGURE 8.12: Evolution of the eigenvalues as a function of the angle of attack in the case of a NACA0012 at $\mathrm{Re} = 1.0 \times 10^6$ with the original Spalart–Allmaras model. (a) and (c): evolution of the angular frequency as a function of the angle of attack. (b) and (d): evolution of the growth rate as a function of the angle of attack. (a) and (b): stall mode. (c) and (d): vortex shedding mode.

8.2.3 Results with the Edwards–Chandra modification

Based on the results of Wales *et al.*, it is expected that, by using the Edwards–Chandra modification of the Spalart–Allmaras turbulence model, a hysteresis of the steady solutions could be identified for the flow around a NACA0012 at Reynolds number $\mathrm{Re} = 1.0 \times 10^6$. Such a scenario could be compared to the results obtained without the modification of the turbulence model, to the results obtained for the OA209 airfoil at $\mathrm{Re} = 1.8 \times 10^6$, and to the results of the experimental study of Hristov and Ansell [70].

The polar curve obtained with continuation methods is presented in Figure (8.13): (a) depicts the general overview of the evolution of the lift coefficient as a function of the angle of attack and (b) shows the same evolution zoomed in close to stall angle. As expected regarding the results obtained by Wales *et al.* [166] with the Edwards–Chandra modification of the Spalart–Allmaras model, a hysteresis existing for a large range of angles of attack is identified. Note that for this airfoil, the hysteresis is much larger than the one found for the OA209 airfoil : $\Delta\alpha_{Hyst} \approx 2.8°$ for the NACA0012 and $\Delta\alpha_{Hyst} \approx 0.1°$ for the OA209. The areas where an unstable mode is found are highlighted with dashed lines. Similarly to the cases of the OA209 at various Reynolds numbers and of the NACA0012 with the original Spalart–Allmaras model, the stall eigenmode and the vortex shedding mode are encountered. The structure of the stall mode is similar to the one of the mode found for the NACA0012 with the original Spalart–Allmaras turbulence model and presented in Figure (8.10).

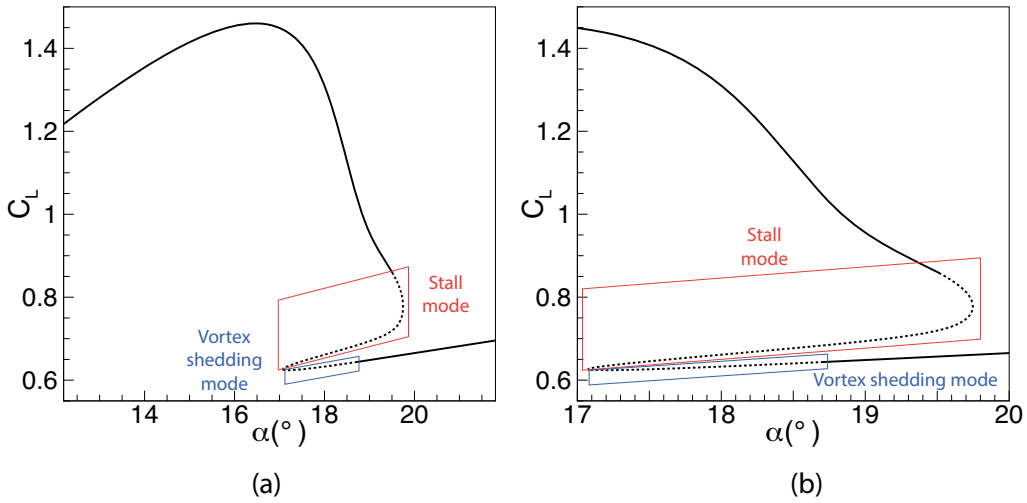

FIGURE 8.13: Evolution of the lift coefficient as a function of the angle of attack for an NACA0012 airfoil at $\mathrm{Re} = 1.0 \times 10^6$ and $\mathrm{M} = 0.16$ with a RANS approach coupled with the Edwards–Chandra modification of the Spalart–Allmaras turbulence model. (a) General overview of the polar curve. (b) Zoom close to stall angle.

Figure (8.14)(a) shows the evolution of the lift coefficient as a function of the angle of attack (the areas where an unstable mode is found are highlighted by dashed lines) and Figure (8.14)(b) the superimposition of the spectra computed for every angle of attack. Schematically, the behavior observed for the NACA0012 at Reynolds number

$\mathrm{Re} = 1.0 \times 10^6$ with the Edwards–Chandra modification of the Spalart–Allmaras turbulence model is very similar to the scenario depicted for the OA209 airfoil at Reynolds number $\mathrm{Re} = 1.8 \times 10^6$. The two blue dots the closest of the abscissa axis correspond to $\alpha = 12.00°$ on the upper branch, to the most left blue dots corresponding to $\alpha = 18.40°$ on the lower branch. For higher angles of attack the mode is difficult to track as it evolves quite fast and surrounded by a lot of spurious modes. More generally, the smallest circular arc of blue dots describes the evolution on the upper branch whereas the largest circular arc describes the evolution on the lower branch. From a global point of view, the superimposition of the eigenspectra shows results mostly similar to the case of the OA209 at Reynolds number $\mathrm{Re} = 1.8 \times 10^6$

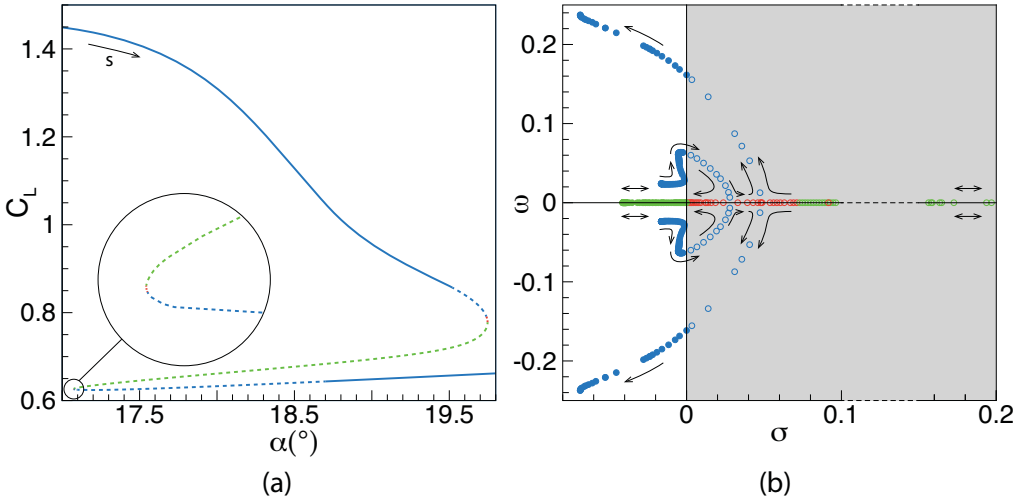

FIGURE 8.14: Real evolution of the temporal behavior of the leading mode in the case of a NACA0012 at $\mathrm{Re} = 1.0 \times 10^6$ with the Edwards–Chandra modification of the Spalart–Allmaras model. (*a*) Polar curve zoomed in close to stall and associated temporal behavior. (*b*) Superimposition of the spectra obtained from each steady solution along the polar curve. Color code similar to the one of Figure (5.13). The grey area corresponds to the zone in which the modes are unstable.

Even though the evolution of the eigenmode along the polar curve is mostly similar, a few slight differences with the case of the OA209 airfoil exist. First, the value of the growth rate of the most unstable mode found is much higher in the case of the NACA0012 (furthest right green dot). It seems to be correlated with the size of the hysteresis area, which is also much wider in that case. Second, starting from $\alpha = 12.00°$ and tracking the mode as the angle of attack is increasing, at some point, one can observe a sudden increase of the Strouhal number and slight decrease of the growth rate of the unsteady stable mode. This sudden change in the evolution of the eigenmode was not observed in the case of the OA209 airfoil and seems to be characteristic of the NACA0012 airfoil.

A more detailed investigation of the particular behavior of the mode is carried out by studying the evolutions of the angular frequencyand the growth rate as a function of the angle of attack. The results are plotted in Figure (8.15) for the two modes.

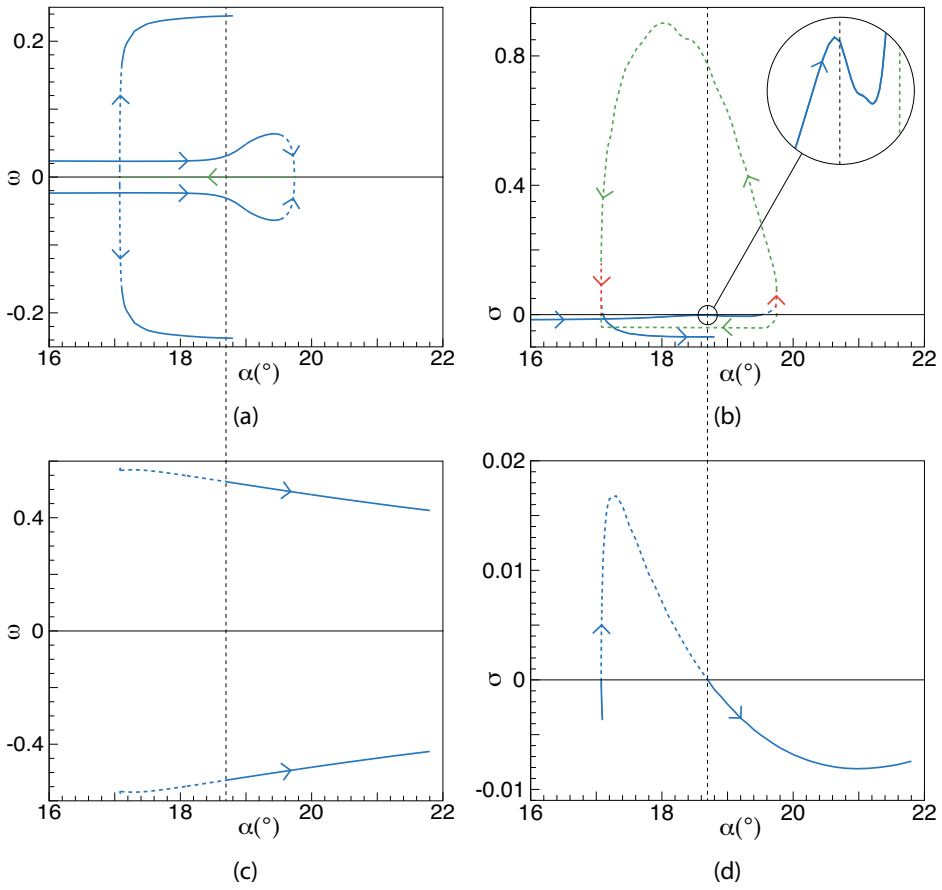

FIGURE 8.15: Evolution of the eigenvalues as a function of the angle of attack in the case of a NACA0012 at Re $= 1.0 \times 10^6$ with the Edwards–Chandra modification of the Spalart–Allmaras model. (a) and (c): evolution of the angular frequency as a function of the angle of attack. (b) and (d): evolution of the growth rate as a function of the angle of attack. (a) and (b): stall mode. (c) and (d): vortex shedding mode. The direction of the arrows refers to increasing curvilinear abscissa.

First, note that, for the stall mode (pictures (a) and (b)[2].), the evolutions of the angular frequency and the growth rate are very similar to the one described in section 5.3.1. The vortex shedding mode (pictures (c) and (d)) appears for $\alpha \approx 17.05°$ on the lower branch. as can be observed in Figure (8.15)(d), it becomes almost instantaneously unstable before its growth rate starts to slowly decrease and the mode finally becomes stable again. The angular frequency of the mode remains almost constant as illustrated in Figure (8.15)(c). Second, similarly to the case of the NACA0012 with the original version of the Spalart–Allmaras turbulence model, the two modes appear to

[2]One can note that the evolution of the stall mode's growth rate on the middle branch is completely flat (lowest green part of the curve corresponding to steady stable state of the mode). It is actually not representative to the real evolution of the growth rate, but just due to a glitch in the extraction of the mode. Indeed, the more the mode is stable, the more it is surrounded by spurious mode and consequently the more it is complicated and costly to find it. The stable steady mode was exactly in that case and as it could not be found for several angles of attacks. Note that this observation also affects Figure 8.14

be identified simultaneously for several angles of attack on the lower branch. However, if a coupling between the two modes seems to appear in the case without hysteresis (see Figure 8.12), no obvious evidence of a coupling can be observed in the present case with an hysteresis. Finally, the sudden change in the evolution of the eigenmode observed in Figure (8.14)(b) is characterized by a sudden change of slope of the angular frequency visible in Figure (8.15)(a) and an oscillation in the evolution of the growth rate visible in Figure (8.15)(b). Surprisingly, the value of α at which those phenomena occur is similar to the angle of attack at which the vortex shedding mode is stabilized again: $\alpha = 18.35°$.

8.2.4 Discussion of the case of the NACA0012 at Re $= 1.0 \times 10^6$

The unsteady behavior of the NACA0012 could not be investigated either with URANS computations or with the static stall model. However, based on the linear behaviors described in sections 8.2.2 and 8.2.3, a few observations and assumptions can be made. First, the simultaneous existence of the stall mode and the vortex shedding mode for several angles of attack seems to be characteristic of the NACA0012 airfoil as it is observed independently of the turbulence model. In particular, a strong coupling seems to occur for the case without hysteresis (original version of the Spalart–Allmaras model). Second, because of this coexistence of the modes and the possible couplings occurring, it seems probable that it would require an improvement of the model to correctly reproduce the nonlinear behavior of the flow and catch the limit cycles for the NACA0012 airfoil in this flow configuration. Finally, although no information on the unsteady behavior of the flow are available, it is interesting to guess general tendencies by extrapolating the results obtained with the OA209 at Reynolds number $\mathrm{Re} = 1.8 \times 10^6$. By doing so, a cautiously conducted comparison with the experimental results of Hristov and Ansell [70] is possible. As expected, based on the results of Wales, the case with the Edwards–Chandra modification of the Spalart–Allmaras turbulence model seems to be the most appropriate to be compared with the experiment. For this case, note that, on the upper branch, the general behavior is mostly similar to the one of the OA209 at Reynolds number $\mathrm{Re} = 1.8 \times 10^6$. Consequently, it is probable that the linearly unstable steady solutions at the end of the upper branch develops into a low frequency high amplitude limit cycle. Such a scenario would be in agreement with the results from Hristov [70] that exhibits a low frequency phenomenon located at the leading edge for angles of attack at the end of the upper branch (illustrated in Figures (8.7)(b) and (c)). On the lower branch, on the contrary, the scenario is very different from the one obtained with the OA209. Indeed, in this case, the vortex shedding mode appears in the hysteresis area, at the end of the lower branch and even appears to be unstable while the stall mode is still unstable. Although rending an extrapolation from the case of the OA209 difficult, this observation is in agreement with the observations of Hristov and Ansell who observed the simultaneous existence of low frequency oscillations and vortex shedding at the end of the lower branch (illustrated in Figure (8.7)(d)) and the existence of the vortex shedding for several angles of attack on the lower branch (illustrated in Figures (8.7)(d), (e) and (f)). Finally, Hristov and Ansell noticed that the vortex-shedding unsteadiness loses amplitude as the angle of attack increases (illustrated in Figures (8.7)(d), (e) and (f)) which would be coherent with

the fact that the mode is stabilized again after having been unstable.

In the end, the results obtained for the NACA0012 airfoil at Reynolds number $\mathrm{Re} = 1.0 \times 10^6$ are very interesting as they confirm that the scenarios observed for the OA209 airfoil are globally replicable for another airfoil although they exhibited a slightly more complicated behavior. Moreover, if the cautious comparison with the experimental results of Hristov and Ansell [70] seems very promising, this also highlights the need for a finest analysis, which would require an improved version of the model and multiple unsteady RANS computations.

8.3 Conclusion

In this chapter, different configurations are investigated and their bifurcation scenarios compared with the one of the OA209 airfoil at $\mathrm{Re} = 1.8 \times 10^6$ and $\mathrm{M} = 0.16$, defined as the reference scenario. First, a variation of the Reynolds number is considered and two lower Reynolds numbers are studied : $\mathrm{Re} = 1.0 \times 10^6$ and $\mathrm{Re} = 0.5 \times 10^6$. The first scenario resembles the reference scenario, while the second scenario is different in that it exhibits no hysteresis. However, the stall mode is still revealed by the linear stability analysis. Similarly, low frequency oscillations of large amplitude are revealed with unsteady RANS computations. It indicates that a hysteresis of steady solutions is not a necessary condition to the existence of the low frequency oscillations. Moreover, it is shown that the two behaviors are actually linked and that the stall model correctly predicts the behavior of that case without hysteresis. Second, a NACA0012 airfoil is considered instead of the OA209. The Reynolds number retained for the study is $\mathrm{Re} = 1.0 \times 10^6$ based on the work of Hristov and Ansell [70]. When using the original version of the Spalart–Allmaras model no hysteresis is found while the modification of the model proposed by Edwards and Chandra [46] allows us to observe a hysteresis of the steady solutions (in agreement with the work of Wales *et al.* [166]). Consequently two different scenarios are considered depending on the turbulence model and each one appears to be mostly similar to respectively each scenario observed for the OA209 airfoil. One of the main difference compared to the scenarios observed for the OA209 is the appearance of the vortex shedding mode very close to stall and, even, for several angles of attack, the coexistence of the two modes (while it appears only in deep stall configuration for the OA209 airfoil). The nonlinear behavior of the flow around the NACA0012 was not investigated, however the results of the linear stability analysis in the case with hysteresis, although incomplete, seems to be in agreement with the flow behavior described by Hristov and Ansell [70] in a similar configuration. These preliminary results are not sufficient to properly compare the numerical results we have obtained with an experiment and further investigations including unsteady RANS computations and the improvement and use of the stall model would be required to achieve such a comparison but they are very promising.

Chapter 9

Conclusion and perspectives

Contents

9.1 Summary

The aim of this study is to gain understanding of static stall and the phenomena that sometimes appear when it occurs. The study was conducted on a two dimensional OA209 airfoil at Reynolds number $\mathrm{Re} = 1.8 \times 10^6$ and Mach number $\mathrm{M} = 0.16$ (corresponding to a retreating blade configuration) in the RANS framework.

In chapter 3 it is proven that static stall, hysteresis and low frequency oscillations can be successfully captured with the Spalart–Allmaras turbulence model for this particular flow configuration. These results are in good agreement with the works of Richez *et al.* [133] and Iorio *et al.* [76] who identified respectively hysteresis on the same configuration with the $k-\omega$ model and low frequency oscillations for a NACA0012 at higher Reynolds number. The identification of the upper and lower branches, which characterize the hysteresis of steady solutions close to stall, strongly suggests the existence of a middle branch linking them similarly to that which Wales *et al.* [166] observed for a different flow configuration. However, the identification of such a branch is impossible with the local time stepping approach and requires the development of dedicated tools: continuation methods.

The mathematical framework and the numerical implementation of continuation methods (naive continuation and pseudo arclength) are presented in chapter 4. They were developed as part of an already-existing tool dedicated to the linear stability of flows coupled with *elsA*. The validation process of these methods is also presented in this chapter, as well as a discussion regarding the differences between the steady solutions obtained with the local time stepping approach and with continuation methods. A difference is observed between the two approaches and the error is attributed to the presence of cutoffs in the case of the time stepping approach. This discussion is further

extended in appendix C.

With the use of the continuation methods developed, a middle branch of steady solutions, joining the upper and lower branches, is identified (chapter 5). The existence of this middle branch demonstrates that the evolution of the steady solutions at stall is continuous and not characterized by a sudden change of flow topology as could be supposed based on the results presented in chapter 3. By carrying out a systematic linear stability analysis of all the steady solutions computed, two modes are revealed: a *vortex shedding* mode, unstable when the flow is massively separated and a *stall* mode, unstable when stall occurs. The first one is characterized by a very standard Strouhal number[1] St ≈ 0.2 while the Strouhal number of the second is one order of magnitude lower St ≈ 0.02. The stall mode consists of a large structure located just above the recirculation bubble, which affects the size of this bubble and makes it pulse. These two features of the stall mode (Strouhal number and structure) strongly suggest that this mode is linked to the low frequency oscillation phenomenon, which has the same features. The stall mode and its associated adjoint mode are used to identify the most sensitive regions of the flow at stall: the leading edge and the separation point are designated by the wavemaker approach [59] and the local contribution approach [95] [122]. Finally, the evolution of the stall eigenmode is investigated thoroughly along the polar curve in an attempt to draw a bifurcation diagram. Although the structure of the mode remains always the same, its growth rate and angular frequency vary depending on the steady solution considered and the evolution of these quantities reveal a very particular bifurcation scenario with several noticeable points:

- a Hopf bifurcation occurring when the unstable mode and its complex conjugate become unstable;
- the merging of the unstable unsteady mode and its complex conjugate to form a single unstable steady mode;
- the splitting of the single unstable steady mode into two unstable steady modes, one more unstable and the other less unstable;
- a saddle-node bifurcation occurring when one of the two unstable steady mode becomes stable;
- the exact same points appearing in reverse order in the second part of the polar curve.

In chapter 6, unsteady RANS computations are performed to understand the possible formation of the low frequency oscillations limit cycle identified in chapter 3 and the switch of the flow from one branch to the other. The computations carried out are also used to consolidate the results of the linear stability analysis (also briefly developed in appendix D). The low frequency oscillations limit cycle is found from two unstable steady solutions only, whereas many more steady solutions appear to be unstable. However, starting from an already-developed form, this limit cycle can be tracked for other values of α and appears to exist in almost half of the hysteresis area. Nevertheless, the unsteady RANS approach is insufficient to explain the sudden vanishing of

[1] Based on the chord length weighted by the sine of the angle of attack: $\mathrm{St} = \frac{f \cdot c \cdot \sin(\alpha)}{u_\infty}$

this limit cycle as well as the possibility of reaching it from particular steady solutions only.

The approach retained to answer these questions (among others) is the development of a one equation *stall* model. The aim is to define a single equation that reproduces the evolution of the steady solutions as a function of the angle of attack as well as their linear behavior (as introduced in appendix E). The model is then calibrated (using a Non-Dominated Sorting Genetic Algorithm, NSGA-II) based on the results of the steady RANS computations and their linear stability (as presented in chapter 7). Afterwards, the nonlinear behavior of the model is studied assuming that it is similar to the one of the flow in the configuration studied. The relative simplicity of the model and the use of a tool dedicated to bifurcation continuation of dynamical systems [39] make it possible to identify features unaccessible with unsteady RANS computations and to deduce a complete bifurcation diagram:

- the two Hopf bifurcations are subcritical and two unstable limit cycles emerge from them;
- the unstable limit cycle from the upper branch vanishes in a homoclinic bifurcation when the orbit collides with a steady solution of the middle branch;
- the stable low frequency limit cycle actually does not vanish:
    - One side of the limit cycle disappears because of a homoclinic bifurcation when the orbit collides with a steady solution on the middle branch;
    - The other side of the limit cycle is directly linked to the unstable limit cycle emerging from the lower branch in a limit cycle saddle-node bifurcation.

The use of the model appears to be crucial to understanding this complex scenario, whose all the features could not have been identified with time steppers. In addition to this bifurcation scenario, the stall model is used to study the influence of the parameters of the model and propose several other scenarios in order to evaluate uncertainties in the calibration process. This extended study reveals that as long as the two unstable limit cycles *overlap*, a large limit cycle is created. This highlights the fact that several different scenarios could lead to the appearance of low frequency oscillations.

Finally, in chapter 8, different flow configurations are investigated. The flow around an OA209 airfoil at Reynolds number $\mathrm{Re} = 0.5 \times 10^6$ exhibits no hysteresis of the steady solutions. However, the stall model (which appears to be also perfectly adapted to this case) and unsteady RANS computations still reveal the existence of a low frequency limit cycle. This seems to indicate that the appearance of this limit cycle is not linked to the existence of an hysteretic behavior but to the existence of an unstable mode at stall. The flow around a NACA0012 at Reynolds number $\mathrm{Re} = 1.0 \times 10^6$ is also investigated. In this configuration, the appearance of hysteresis is conditioned by the use of the Edwards–Chandra modification of the Spalart–Allmaras turbulence model (similarly to the work of Wales *et al.* [166]). The two cases (with and without the modification of the model) are studied and the results are very similar to the ones found for the OA209 airfoil. The main difference comes from the fact that the vortex shedding mode appears closer to stall and coexist with the stall mode. Moreover, the

results of the linear stability analysis seem to be qualitatively in good agreement with the experiment of Hristov and Ansell [70] carried out on the same airfoil in the same flow configuration.

9.2 Conclusion

In summary, the present study shows how stall, hysteresis and low frequency oscillations can be linked in a bifurcation diagram. The mechanisms responsible for their respective appearances are also suggested. This is of first interest when trying to gain understanding and control stall. Furthermore, the main features of this diagram are identified for different flow configurations proving that it is not configuration-dependent.

However, the approach is more phenomenological than predictive due to the use of the Spalart–Allmaras turbulence model in the RANS framework. First, the use of this specific turbulence model must be seen as the first step of a larger study, mostly dedicated to the development of the methodology and the tools. The use of other turbulence model is, at least, a necessary step to prove that this scenario is not turbulence model dependent and, possibly, the opportunity to obtain more quantitative results. Second, the use of the RANS framework raises the question of the comparison between the bifurcation diagram obtained and a *real flow*.

In the next section, future studies that could help consolidate the results as well as other paths that seem interesting to explore are proposed.

9.3 Future work and perspectives

Several additional studies could be conducted to validate the robustness of the scenario identified for the OA209 airfoil at Reynolds number $\mathrm{Re} = 1.8 \times 10^6$ and determine to what extend it is representative of a real flow and obtain more quantitative results.

First, several improvements could be made on the unsteady RANS computations to improve the quality of the results. As mentioned in chapter 4 and appendix C, the cut-offs implemented in the Spalart–Allmaras model generate some differences between the solutions obtained with time steppers and the ones obtained with continuation methods. In the present work, a solution was proposed in order to obtain similar results with both approaches at a reasonable cost. However, a direct modification of the *elsA* source code could improve the quality of the results and particularly the link between the linear stability analysis and unsteady RANS computations and, as a consequence, the match between the unsteady RANS computations and the results of the stall model.

Second, in order to verify that the bifurcation scenario observed is not related to the use of the Spalart–Allmaras model, the study could be conducted with a different turbulence model, eventually coupled with a transition model. The objective would be double: first, provide information regarding the robustness of the bifurcation scenario with respect to the turbulence model, second, provide results more representative of

the real flow topology. The $k-\omega$ turbulence model is probably the best candidate as very decent results can be obtained in the case of stall. Furthermore, lately, transition models have become much better at modeling the transition from laminar to turbulent flows on airfoils, and even at identifying laminar separation bubbles (see for instance the work of Bernardos *et al.* [16]). In the end, even with a RANS approach, solutions more representative of the real flow could be obtained and the corresponding bifurcation scenario would be less questionable than the one obtained with the Spalart–Allmaras turbulence model.
However, this approach is also much more challenging from a technical point of view. The method used to compute the Jacobian matrix and perform continuation methods or linear stability analysis is, in theory, well adapted to the use of a different turbulence model as the solver is used as a black box [108]. However, in fact, the formulation of most of the turbulence and transition models is complex and Bonne [17] demonstrated that the computation of a Jacobian matrix might not be possible for some turbulence and transition models because of the way they are implemented in *elsA*. He also proposed an alternative solution to compute a Jacobian but it implies a reformulation of the turbulence model directly in the source code of the solver, which is not a trivial operation and completely cancels the benefits of using the solver as a blackbox.
In the end, in the present work, the Spalart–Allmaras was used for its simplicity and is to be considered only as the first step of a more global study dedicated to gain an understanding of stall. However, the second step, which consists in using a different turbulence model coupled with a transition model, might not be so simple.

Third, experimental studies or more accurate numerical studies (LES, DNS) could be conducted to look specifically for the phenomena described in the bifurcation diagram. Several studies were already conducted on this airfoil in this aerodynamic conditions [121] [125] [135]. However, none of them really focused on the identification of hysteresis or low frequency oscillation. Furthermore, in this study the range of existence of these two phenomena was demonstrated to be very thin (a few tenth of angular degrees). Consequently, the fact that they were not identified might just mean that the angles of attack at which they exist were not investigated. New studies dedicated to the search of these particular phenomena are necessary to conclude on their existence.
In the event of the low frequency oscillations do not naturally appear, an alternative solution to verify the existence of the bistable region is to trigger the oscillations by forcing the system.
An alternative to the setup of a new experiment or time costly computations is to use the already-existing experimental data of Hristov and Ansell [70] on the NACA0012 at Reynolds number $\mathrm{Re} = 1.0 \times 10^6$ and compare it to the associated bifurcation diagram. However, it would require to extend the work already done in this configuration. Particularly, it would be necessary to perform the stability analysis one more time to correctly track the stable steady mode on the middle branch, perform unsteady RANS computations and, last but not least, improve the stall model to take the vortex shedding mode into account.

Additionally, several studies could be dedicated to the stall model in order to improve our global understanding of the phenomena occurring at stall.

First, a more detailed and systematic study of the simplest form of the model (see appendix E) could provide a better understanding of the stall model. The study of the reference scenarios presented in section 7.4.2 was a first step limited to certain values of the parameters and there are many more reference scenarios to be identified and which could help understanding the different possibilities in the calibrated model. Also, it was discovered lately that similarities might exist between the present stall model and the Pernarowski's model [126] used in the modeling of pancreatic beta-cells [35] [52]. A deeper investigation of this model might reveal to paths to explore in order to improve the stall mode.

Second, several bifurcations were identified by considering the angle of attack as the parameter of the study. However, in the case of the OA209 airfoil, it was shown that by varying the Reynolds number, the size of the hysteresis area, and even its existence changes. Cui *et al.* [34] proposed to study the evolution of the size of the hysteresis based on experimental data. They considered three polar curves at different Reynolds number and identified that the evolution as a function of the Reynolds number is driven by pitchfork bifurcations. This scenario could be easily investigated and confirmed with the simplest form of the stall model (as the parameter d of the model is clearly identified as the one driving the size and existence of the hysteresis), which would provide interesting insights on the formation of this bifurcation and the possible evolution of the low frequency limit cycle with respect to the Reynolds number. Ultimately, this could also be investigated in the particular case of the OA209 airfoil by studying additional Reynolds numbers between $0.5 \times 10^6 < \mathrm{Re} < 1.8 \times 10^6$. This would lead to a more complete bifurcation scenario including the Reynolds number.

Finally, one of the motivation of the present work is to improve helicopters' performance. One way to achieve such a goal is to increase the static stall angle, which can be done by considering different paths. First, passive control could be investigated: either based on the direct and adjoint modes computed in the present work (in the spirit of what was done by Hill [66] or Marquet *et al.* [97] in the case of the flow past a cylinder) or by directly modeling the control devices (similarly to the work of Gardner *et al.* [55] for instance). Second, active control, which is already widely used in helicopters' blade (see for instance the work of Le Pape *et al.* [124]) could be explored. Finally, shape optimization is surely worth study. Particularly, recent studies proposed an adjoint based shape optimization method in which the growth rate of an unstable mode is considered as the objective function (see for instance the works of Nakazawa and Azegami [116] or Brewster and Juniper [21]).

Appendix A

Definition of the aerodynamical forces and coefficients

It was explained in chapter 1 how the difference of pressure between the flow on the suction and pressure sides of the airfoil generates lift. More generally, the flow around an airfoil generates a local force per surface unit $\boldsymbol{f}$ on each point of the airfoil. Its normal component is noted p and its tangential component is noted τ, such as $\boldsymbol{f} = -p\boldsymbol{n}+\tau\boldsymbol{t}$. The resulting forces and moments generated by these local forces per surface unit are referred to as $\boldsymbol{R}$ and $\boldsymbol{M}$ (with $\boldsymbol{M} = M\boldsymbol{z}$ and M positive in the clockwise direction). Expressed in the flow reference frame, the longitudinal and perpendicular components of $\boldsymbol{R}$ correspond respectively to the drag and lift forces. Two particular reference frames are chosen: the reference frame of the airfoil $(\boldsymbol{x_0}, \boldsymbol{y_0})$ and the reference frame $(\boldsymbol{x}, \boldsymbol{y})$ of the flow. In the first one, the $\boldsymbol{x_0}$ component is named D_0 and the $\boldsymbol{y_0}$ is named L_0. They correspond respectively to the drag and lift forces generated by the fluid on the airfoil with an inclination of $\alpha = 0°$. In the second reference frame, the $\boldsymbol{x}$ component is named D and the $\boldsymbol{y}$ is named L. They correspond respectively to the drag and lift forces generated by the fluid on the airfoil with an inclination $\alpha \neq 0$. All these forces and reference frames are summarized in Figure (A.1) (a). The pitching moment is the moment associated with the resultant $\boldsymbol{R}$ with respect to any point of coordinate (x_p, y_p). The point of this section is to introduce the mathematical definitions of L, D and M and the associated non-dimensionalized coefficients C_L, C_D and C_M in the case of a two dimensional airfoil. The quantities are defined as follow:

$$C_L = \frac{L}{q_\infty c} \quad ; \quad C_D = \frac{D}{q_\infty c} \quad ; \quad C_M = \frac{M}{q_\infty c^2} \tag{A.1}$$

Where $q_\infty = \frac{1}{2}\rho U_\infty^2$ is the freestream dynamic pressure based on the freestream speed U_∞ and c is the chord of the airfoil.

In order to define the quantities L, D and M in the flow reference frame, the quantities L_0, D_0 and M_0 are first defined in the airfoil reference frame. A small element dl of the airfoil's outline, whose normal is denoted $\boldsymbol{n}$ and tangent $\boldsymbol{t}$ is isolated. The pressure exerted over dl will generate a resultant force along $\boldsymbol{n}$, while the friction will generate a resultant force along $\boldsymbol{t}$. Consequently, the resulting force $\boldsymbol{R}$ generated on the airfoil is:

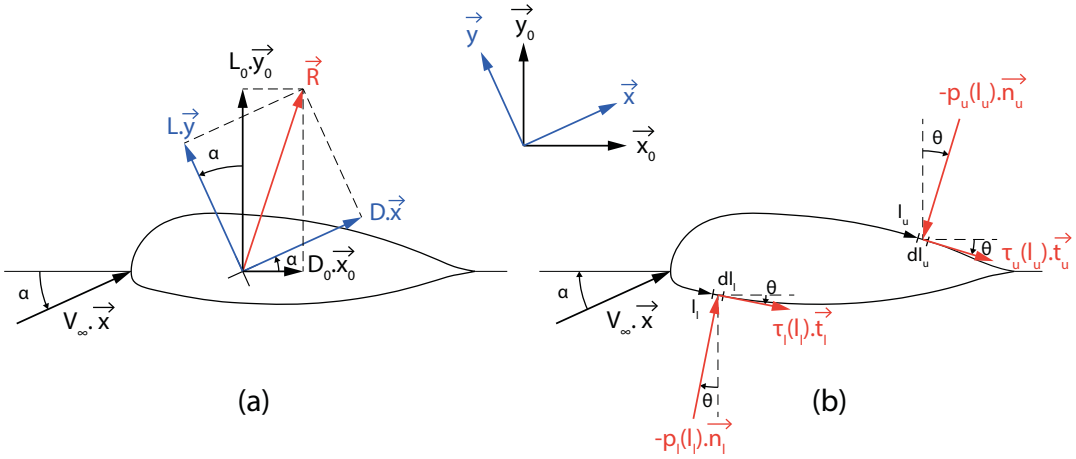

FIGURE A.1: Diagrams of the aerodynamic forces exerted on an airfoil inclined at an angle α. (a) Expression of the lift, drag and pitching moment in different reference frames. (b) Expression of the forces exercised on a small element dl on the suction side (or upper side) and the pressure side (lower side) of the airfoil.

$$\boldsymbol{R} = \oint_{airfoil} (-p\boldsymbol{n} + \tau\boldsymbol{t})dl \tag{A.2}$$

Where the pressure p is deduced from the variable ρE, with the equations of the total energy (2.2) and ideal gas law (2.4). In order to compute this integral, we split the airfoil outline into an upper and a lower part (corresponding respectively to the suction side of the airfoil, $y_0 > 0$ and the pressure side of the airfoil $y_0 < 0$) such as presented in Figure (A.1) (b). The integration is performed from the leading edge (l_{LE}) to the trailing edge (l_{TE}).

$$\boldsymbol{R} = \int_{l_{LE}}^{l_{TE}} (-p_u\boldsymbol{n_u} + \tau_u\boldsymbol{t_u})dl_u + \int_{l_{LE}}^{l_{TE}} (-p_l\boldsymbol{n_l} + \tau_l\boldsymbol{t_l})dl_l \tag{A.3}$$

Which, by expressing the vectors $\boldsymbol{t_u}$, $\boldsymbol{n_u}$, $\boldsymbol{t_l}$ and $\boldsymbol{n_l}$ in the $(\boldsymbol{x_0}, \boldsymbol{y_0})$ reference frame, becomes:

$$\begin{aligned}\boldsymbol{R} = &[\int_{l_{LE}}^{l_{TE}} (-p_u\sin(\theta) + \tau_u\cos(\theta))dl_u + \int_{l_{LE}}^{l_{TE}} (p_l\sin(\theta) + \tau_l\cos(\theta))dl_l]\boldsymbol{x_0} \\ &+ [\int_{l_{LE}}^{l_{TE}} (-p_u\cos(\theta) - \tau_u\sin(\theta))dl_u + \int_{l_{LE}}^{l_{TE}} (p_l\cos(\theta) - \tau_l\sin(\theta))dl_l]\boldsymbol{y_0}\end{aligned} \tag{A.4}$$

The component over the axis $\boldsymbol{x_0}$ is the drag D_0 in the airfoil reference frame and the component over the axis $\boldsymbol{y_0}$ is the lift L_0 in the airfoil reference frame. Note that the small element dl is linked with the small elements dx_0 and dy_0 by the relations: $\cos(\theta)dl = dx_0$ and $\sin(\theta)dl = -dy_0 = -\frac{dy_0}{dx_0}dx_0$, which leads to the following expressions of the drag D and the lift L in the flow reference frame (c being the chord of the

airfoil):

$$\begin{aligned} D = \cos(\alpha) \left[\int_0^c \left(p_u \frac{dy_{0_u}}{dx_0} - p_l \frac{dy_{0_l}}{dx_0} + \tau_u + \tau_l \right) dx_0 \right] \\ + \sin(\alpha) \left[\int_0^c \left(p_l - p_u + \tau_u \frac{dy_{0_u}}{dx_0} + \tau_l \frac{dy_{0_l}}{dx_0} \right) dx_0 \right] \end{aligned} \tag{A.5}$$

$$\begin{aligned} L = \cos(\alpha) \left[\int_0^c \left(p_l - p_u + \tau_u \frac{dy_{0_u}}{dx_0} + \tau_l \frac{dy_{0_l}}{dx_0} \right) dx_0 \right] \\ + \sin(\alpha) \left[\int_0^c \left(p_l \frac{dy_{0_l}}{dx_0} - p_u \frac{dy_{0_u}}{dx_0} - (\tau_u + \tau_l) \right) dx_0 \right] \end{aligned} \tag{A.6}$$

Moreover, the friction contribution to the lift is considered negligible:

$$\begin{aligned} D = \cos(\alpha) \left[\int_0^c \left(p_u \frac{dy_{0_u}}{dx_0} - p_l \frac{dy_{0_l}}{dx_0} + \tau_u + \tau_l \right) dx_0 \right] \\ + \sin(\alpha) \left[\int_0^c \left(p_l - p_u + \tau_u \frac{dy_{0_u}}{dx_0} + \tau_l \frac{dy_{0_l}}{dx_0} \right) dx_0 \right] \end{aligned} \tag{A.7}$$

$$L = \cos(\alpha) \left[\int_0^c (p_l - p_u) dx_0 \right] + \sin(\alpha) \left[\int_0^c \left(p_l \frac{dy_{0_l}}{dx_0} - p_u \frac{dy_{0_u}}{dx_0} \right) dx_0 \right] \tag{A.8}$$

A similar approach based on the moments leads to the following expression of the pitching moment (assuming that the contribution of the friction to this moment is negligible):

$$M = \int_0^c \left[p_u \left(x_0 - x_p + (y_{0_u} - y_p) \frac{dy_{0_u}}{dx_0} \right) - p_l \left(x_0 - x_p + (y_{0_l} - y_p) \frac{dy_{0_l}}{dx_0} \right) \right] dx_0 \tag{A.9}$$

Note that this moment is usually expressed at a quarter chord location, which in terms of coordinate in the airfoil reference frame corresponds to the point: $(x_p, y_p) = (\frac{c}{4}, 0)$. Also, note that by substituting the expression of the lift (A.11) into the expression of the lift coefficient (A.1) and by considering that $\frac{dy_{0_u}}{dx_0} \approx \frac{dy_{0_l}}{dx_0} \approx \frac{dy_0}{dx_0}$, the following relation appear:

$$C_L = \frac{1}{c} \left\{ \cos(\alpha) \left[\int_0^c \frac{p_l - p_u}{q_\infty} dx_0 \right] + \sin(\alpha) \left[\int_0^c \frac{p_l - p_u}{q_\infty} \frac{dy_0}{dx_0} dx_0 \right] \right\} \tag{A.10}$$

Where $\frac{p_l - p_u}{q_\infty} = c_{p_u} - c_{p_l}$, with c_p, the pressure coefficient defined as the difference between the local static pressure and the far field static pressure normalized by the dynamic pressure : $c_p = \frac{p - p_\infty}{q_\infty}$, which leads to the following expression of the lift coefficient:

$$C_L = \frac{1}{c} \left\{ \cos(\alpha) \left[\int_0^c (c_{p_u} - c_{p_l}) dx_0 \right] + \sin(\alpha) \left[\int_0^c (c_{p_u} - c_{p_l}) \frac{dy_0}{dx_0} dx_0 \right] \right\} \tag{A.11}$$

With such a definition, the lift coefficient is directly linked to the pressure coefficient and can be seen as the difference of area under the curves $c_{p_u}(x_0)$ and $c_{p_l}(x_0)$ or under the curves $c_{p_u}(y_0)$ and $c_{p_l}(y_0)$.

Appendix B

Schematized description of the continuation methods

This appendix presents three schemas which summarizes the different steps of the two continuation methods from a simplified point of view. It also includes the interfaces between the different tools and softwares used as well as the data exchanged. Figure B.3 describes the naive continuation method while Figures B.1 and B.2 describe the pseudo arclength method (the first one focusing on the predictor step and the second one on the corrector step). In each case, one external tool is used to compute the Jacobian matrix and the CFD software *elsA* is called anytime a residual needs to be computed. Otherwise, all the operations are performed by the continuation methods tool. Although the continuation tools (blue boxes) and the computing Jacobian tool are two separated tools, they are actually two parts of a same bigger code dedicated to linear stability analysis.

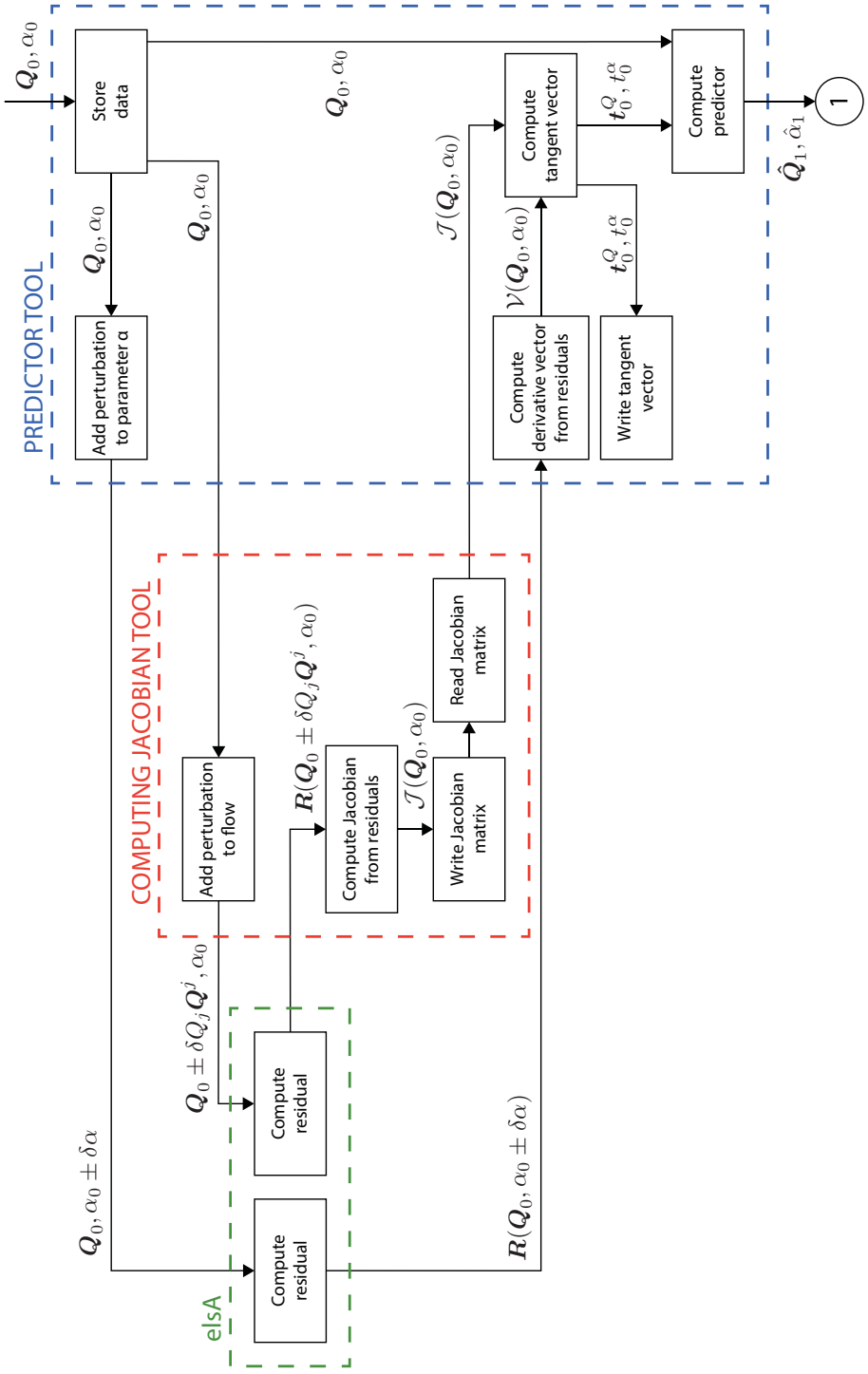

FIGURE B.1: Schematized representation of the different tools used in the predictor step of the pseudo arclength method: the predictor tool (blue box), the computing Jacobian tool (red box) and *elsA*, the CFD software (green box). The arrows indicate the data exchanged and the boxes the operations performed. This is step 1/2 of the pseudo arclength method.

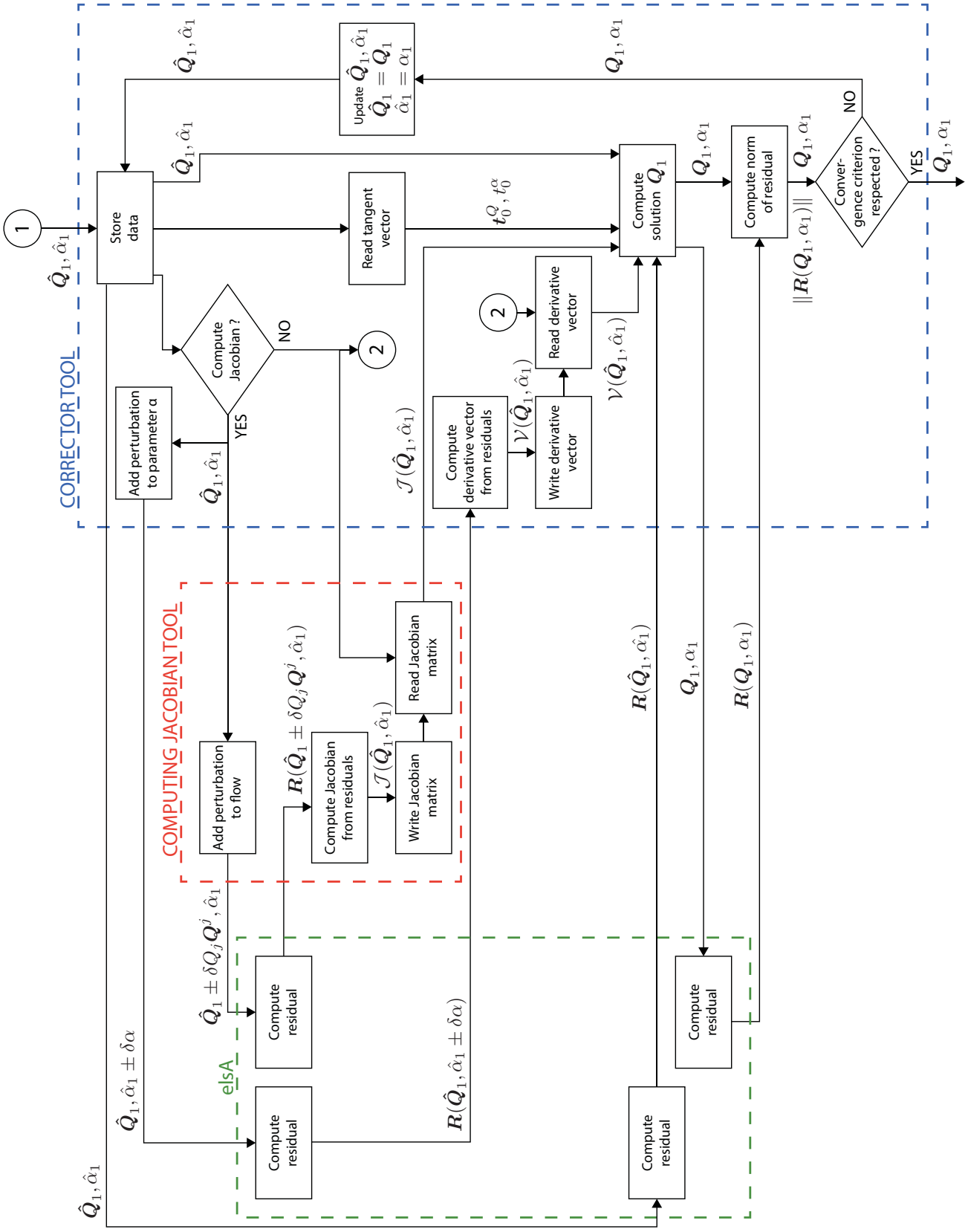

FIGURE B.2: Schematized representation of the different tools used in one iteration of the corrector step of the pseudo arclength method: the corrector tool (blue box), the computing Jacobian tool (red box) and *elsA*, the CFD software (green box). The arrows indicate the data exchanged and, the boxes, the operations performed. This is step 2/2 of the pseudo arclength method.

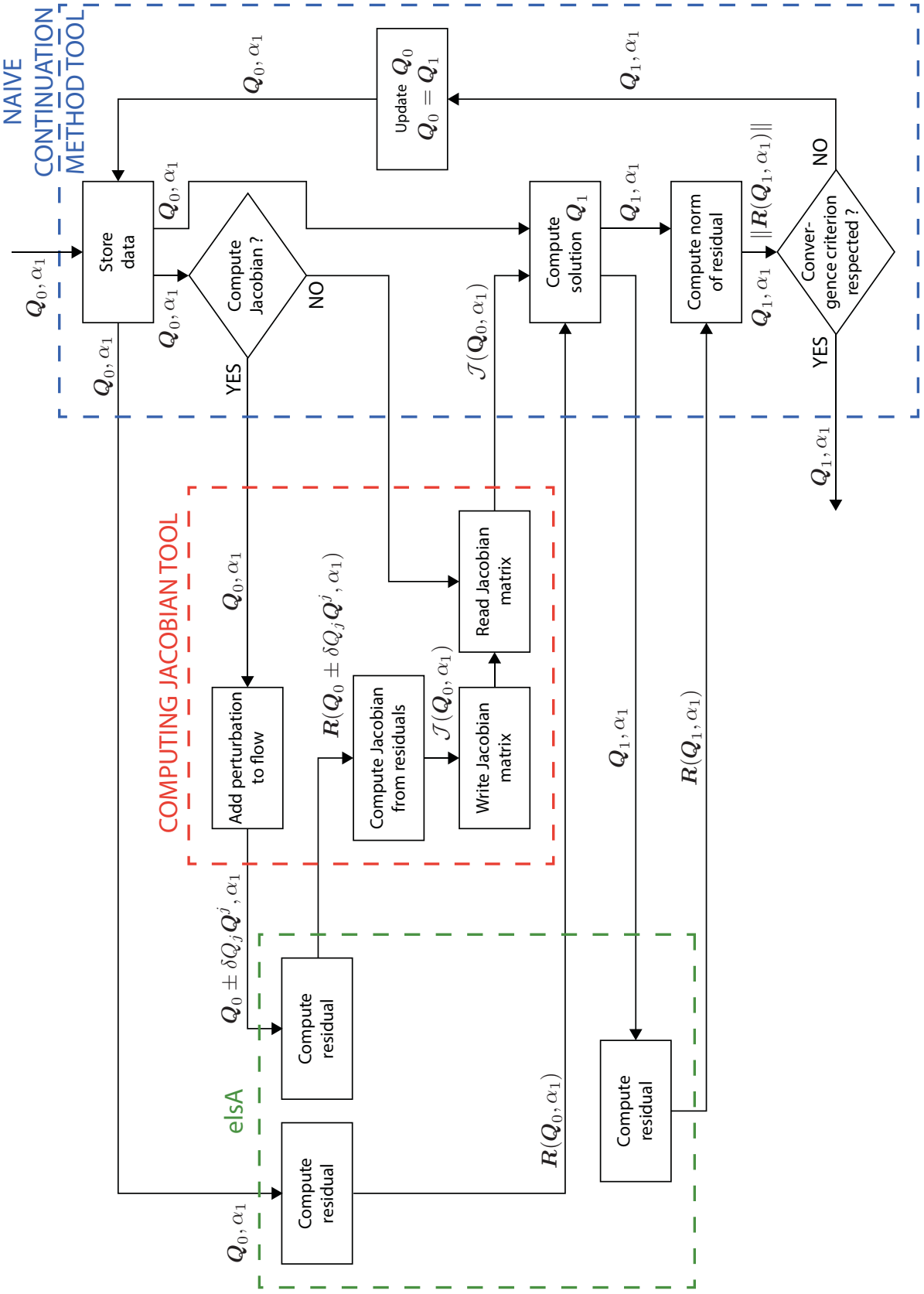

FIGURE B.3: Schematized representation of the different tools used in the different steps of one iteration of the naive continuation method: the naive continuation method tool (blue box), the computing Jacobian tool (red box) and *elsA*, the CFD software (green box). The arrows indicate the data exchanged and the boxes the operations performed.

Appendix C

Continuation methods and (U)RANS computations in *elsA*

Contents

C.1 Context

Section 4.3.1 in chapter 4 highlighted the fact that the steady solutions obtained with a local time stepping approach and the ones obtained with continuation methods are slightly different. As a reminder, this was due to non-removable cutoffs in the local time stepping approach that could not be taken into account in continuation methods. It is not a problem in itself if the objective is only to compute steady states and perform a linear stability analysis of these solutions. It is impossible, however, to compute a middle branch with a local time stepping approach and consequently identify a complete scenario and compare it to the one described in chapter 3. However, the linear stability analysis performed on the available solutions obtained with a local time stepping approach reveals, for these solutions, an evolution of the eigenvalues similar to the one described in section 5.3 of chapter 5.

However, one objective of this work is to obtain the complete nonlinear scenario occurring at stall and, as much as possible, we intend this nonlinear scenario to match the linear one described in chapter 5. To do so, unsteady RANS computations must be performed with the solver *elsA*. The observations made on the cutoffs during the computation of steady solutions remain true during the computation of unsteady solutions. In these conditions it is unrealistic to expect that the linear scenario obtained from steady solutions that does not take cutoffs into account to match a nonlinear scenario based on unsteady RANS computations that does take cutoffs into account.

An ideal solution would be to remove all the internal cutoffs in the elsA source code to ensure that the equations solved during the unsteady RANS computations are similar to the ones solved in the computation of steady states with the continuations

method. However, it has two main drawbacks. First, it is not an easy task and also very time consumming. Second, some of the cutoffs implemented are applied to ensure a correct physical behavior of the model but some others are present to ensure the convergence and stability of the numerical schemes. Removing this second kind of cutoffs could lead to the impossibility for the unsteady RANS computations to converge. In the end, it is a complicated and risky task to accomplish.

C.2 Proposed solution

An alternative solution, less elegant but easier to implement, consists in slightly modifying the admissible minimal value of the turbulent variable $\rho\tilde{\nu}$. Originally, this cutoff is set equal to the value imposed at the farfield boundary condition. Indeed, Spalart and Rumsey [152] demonstrated that, due to numerical dissipation, the turbulent level tends to decay in the far field and the ambient value near the airfoil might be much smaller than the imposed boundary condition. Such a cutoff ensures that the value in the farfield remains the same as the boundary condition. However, it appears that a small diminution of this cutoff (less than 5%) gives solutions very similar to the ones obtained with the naive continuation method.

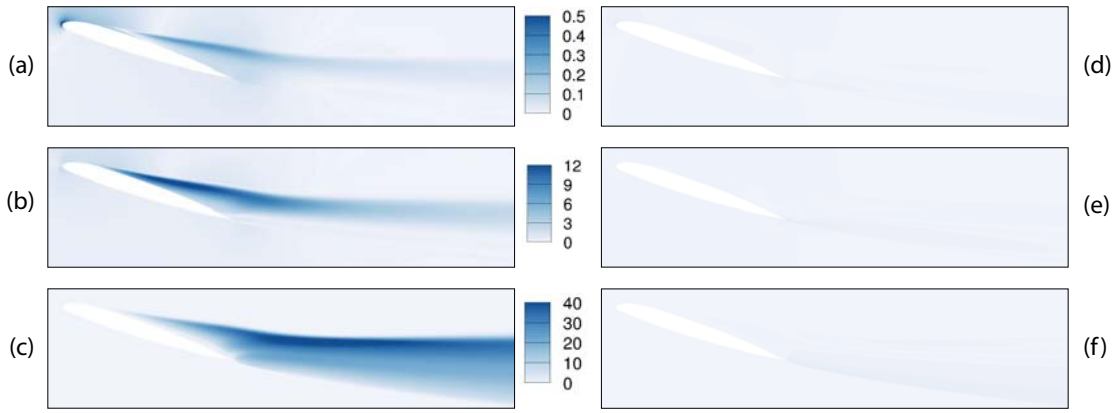

FIGURE C.1: Local relative error in % between the solution obtained with the naive continuation method and solutions obtained with a local time stepping approach ($\alpha = 18.41°$) for three variables ρ (a and d), ρu (b and d) and $\rho\tilde{\nu}$ (c and f). Left (a, b, c) : with standard cutoff on the turbulent variable. Right (d, e, f) : with modified cutoff on the turbulent variable.

The results obtained with this approach are first presented for a single angle of attack and then for the entire polar curve. Figure (C.1) presents the local errors between the solution obtained with the local time stepping approach and the naive continuation method on the left, and between the solution obtained with the local time stepping approach with a slight modification of the cutoff on the turbulent variable and the naive continuation method on the right for the particular angle of attack $\alpha = 18.41°$ chosen for being in the stall area for the two computations. The errors are plotted for

three different variables : the density ρ at the top, the streamwise velocity ρu in the middle and the turbulent viscosity $\rho\tilde{\nu}$ at the bottom. One can observe that the turbulent variable exhibits the largest error. As explained in chapter 4, it is due to the fact that the cutoffs responsible for the differences of solutions between the two approaches are directly applied to this variable before being propagated to the other variables. The slight modification of the cutoff on the turbulent variable (right pictures) shows a drastic reduction of the error with the naive continuation method. The maximum error switches from 1.5% to 0.1% for the density ρ, from 13% to 2% for the streamwise velocity ρu and from 45% to 2% for the turbulent variable $\rho\tilde{\nu}$.

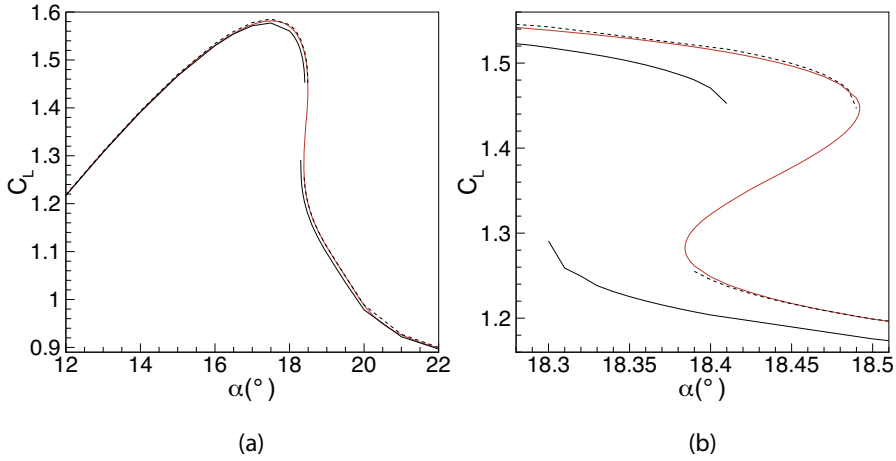

FIGURE C.2: Lift coefficient polar curves for three different steady solution computations: local time stepping approach with standard cutoff on the turbulent variable (full black curve), local time stepping approach with modified cutoff on the turbulent variable (dashed black line) and naive continuation method approach (red line). Right : complete polar curve. Left : zoom in close to stall.

Figure (C.2) shows the comparison of the lift coefficient polar curves obtained with the three methods : local time stepping approach with standard cutoff (full black line), local time stepping approach with modified cutoff (dashed black line) and continuation methods (red line). The left picture presents the whole polar curve while the right picture exhibits a zoom in close to the stall area. The two curves obtained with a local time stepping approach (black curves) only have upper and lower branches as it is impossible to reach the middle branch with these approaches. The evolution of the lift coefficient is very similar for the three curves. The only difference comes from the position of the curve : the black one is shifted from the two other ones. One can observe that the gap between the black curve and the two other ones increases with the angle of attack as the turbulence level becomes higher. This observation explains why the error presented in Figure (C.1) for $\alpha = 18.41°$ is bigger than the one presented in in Figure (4.4) in chapter 4 for $\alpha = 12.00°$. In the stall area, the gap between the curves reaches approximately $\Delta = 0.1°$, which is not very significant if the point of the study is only to approximate a stall angle. However, it is the same order of magnitude as the hysteresis area so, with the objective of determining a stall scenario with unsteady RANS computations that matches the results of the linear stability analysis of steady

solutions, it becomes a major issue. The slight modification of the cutoff on the turbulent variable shows very good results and major reduction of the gap. The two curves are not perfectly similar but at least the error between the red and the dashed black curve is significantly reduced and several orders of magnitude lower than the range of coexisting solutions.

Appendix D

Validation of the linear stability with URANS computations

Contents

In this appendix, we intend to validate the results obtained with the linear stability analysis of steady solutions with unsteady RANS computations. The point is to, first, verify if the unsteady behaviour of the flow (stable or unstable) is in agreement with the prediction of the linear stability analysis. Then, compare the linear angular frequency and growth rate with the nonlinear angular frequency and growth rate.

D.1 Initialization of the unsteady RANS computations

Two cases are to be distinguished: one when the linear stability analysis reveals a stable solution and the other when the linear stability analysis reveals an unstable solution. In the first case, under the effect of any small perturbation, the flow shall return to its stable steady state. To observe such a phenomenon, it is necessary to create a slightly perturbed solution to initialize an unsteady RANS computation. Then, it is possible to observe whether or not the computation evolves towards the steady stable solution and matches the linear stability analysis. There are several ways of generating perturbed initialized solution, particularly when the eigenmodes of the steady solutions are known. For instance, an approach similar to that used to compute an approximated solution in section 5.2.4.2 (detailed in equation (5.8)) may provide good candidates for initialization if B is correctly set to ensure a small enough perturbation of the steady state. However, this procedure implies the computation of a new state. In order to avoid this step, a much simpler protocol is used: for a stable steady solution $\boldsymbol{Q}(\alpha)$ at α, the steady solution $\boldsymbol{Q}(\alpha + \delta\alpha)$ at $\alpha + \delta\alpha$ is considered to be equivalent to the solution $\boldsymbol{Q}(\alpha)$ on top of which a small perturbation $\delta\boldsymbol{Q}$ would have been added

: $\boldsymbol{Q}(\alpha + \delta\alpha) \approx \boldsymbol{Q}(\alpha) + \delta\boldsymbol{Q}$. Visually, this approximation makes perfect sense as, if $\delta\alpha$ is small enough, the aerodynamic coefficients as well as the flow topology are very close. In the end, the solution $\boldsymbol{Q}(\alpha + \delta\alpha)$ (with $\delta\alpha$ small) is used to initialize the unsteady RANS computation for the angle of attack α. Practically speaking, this solution $\boldsymbol{Q}(\alpha + \delta\alpha)$ is computed during the continuation process with a $\delta\alpha$ small enough due to the requirements of the continuation methods. Consequently, such an an approach does not require an additional step to initialize the unsteady RANS computation. In the second case, when the linear stability analysis predicts an unstable steady solution, the instabilities will naturally grow and the initialization is much simpler : the unsteady RANS computation for an angle of attack α is initialized with the steady solution computed for α : $\boldsymbol{Q}(\alpha)$.

D.2 Application of the validation method to two solutions at $\alpha = 18.42°$

First, the results of the linear stability analysis are presented in Table D.1 as a reminder. The main result is that the steady solution on the upper branch is stable while the steady solution on the lower branch is unstable.

	Upper branch	Lower branch
Growth rate σ	$-5.81155109 \times 10^{-3}$	$3.03396274 \times 10^{-3}$
Angular frequency ω	$-2.00180695 \times 10^{-2}$	$-2.23286983 \times 10^{-2}$
Linear state	STABLE	UNSTABLE

TABLE D.1: Reminder of the results of the linear stability analysis obtained for $\alpha = 18.42°$ for two different steady solutions on the upper and lower branches.

Two unsteady RANS computations are performed with two different initializations. To validate the linearly stable state of the steady solution on the upper branch, the unsteady RANS computation is initialized with a slightly perturbed solution. Factually, the steady solution obtained for $\alpha = 18.43°$ is used as explained in subsection D.1. On the other hand, to validate the unstable state of the steady solution on the lower branch, the exact steady solution obtained for $\alpha = 18.42°$ is used as an initializer of the unsteady RANS computation. The results of the two unsteady RANS computations are presented in Figure (D.1) that shows the evolution of the lift coefficient as a function of the time for the angle of attack $\alpha = 18.42°$. Picture (a) presents the results for the computation starting from the upper branch while picture (b) presents the results for the computation starting from the lower branch. One can observe that the computation started from the upper branch (a), starts with a high lift coefficient, slightly oscillates and converges to a constant value of high lift after a long time. The computation started from the lower branch (b) starts with some oscillations around the low lift steady solution. These oscillations seem to exponentially grow, going away from the unstable steady solution on the lower branch. In the end, these unsteady computations are in agreement with the unstable or stable behaviour of the steady

solutions predicted by the linear stability analysis.

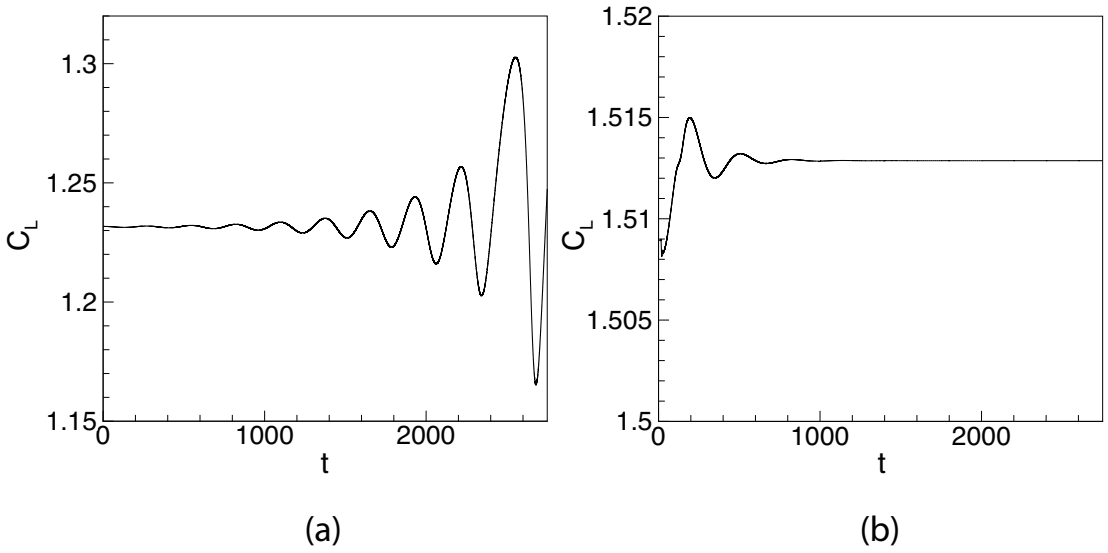

FIGURE D.1: Time evolution of the lift coefficient for $\alpha = 18.42°$ for unsteady RANS computations. As a reminder, at this angle of attack, the low lift steady solution is linearly unstable and the high lift steady solution is linearly stable. Left: computation initialized with the steady solution obtained with $\alpha = 18.42°$ on the lower branch. Right: computation initialized with the the steady solution obtained with $\alpha = 18.43°$ on the upper branch.

The second set of information given by the linear stability analysis is the angular frequency (or associated Strouhal number) and the growth rate of the oscillations. These quantities can also be compared to the nonlinear ones obtained with the unsteady RANS computations. To illustrate the comparison, the case initialized with the steady solution from the lower branch is chosen. Indeed, it exhibits a larger number of oscillations that make the quantification of the growth rate and the Strouhal number more accurate. To compute the growth rate, the points of the envelope of the oscillations are extracted for the oscillations around the low lift solution. The notion of envelope of a sinusoidal curve is introduced in Figure (D.2) which exhibits the time evolution of the function $f(t) = \mathrm{e}^{0.006t}\sin(0.1t)$. The curve of the function f is plotted in black and the envelope of the curve is highlighted in red. The periods T^i_{up} (respectively T^i_{low}) is also introduced as the value of the period between the i^{th} and $i+1^{th}$ upper (resp. lower) peaks of the curve of the function f.

The equation of the envelope is supposed to be in the following form:

$$C_L = C_{L_S} \pm \mathrm{e}^{\sigma t + K} \tag{D.1}$$

where σ is the nonlinear growth rate, K a constant to be determined and C_{L_S} the lift value of the steady solution. The plus or minus sign depends on whether the upper

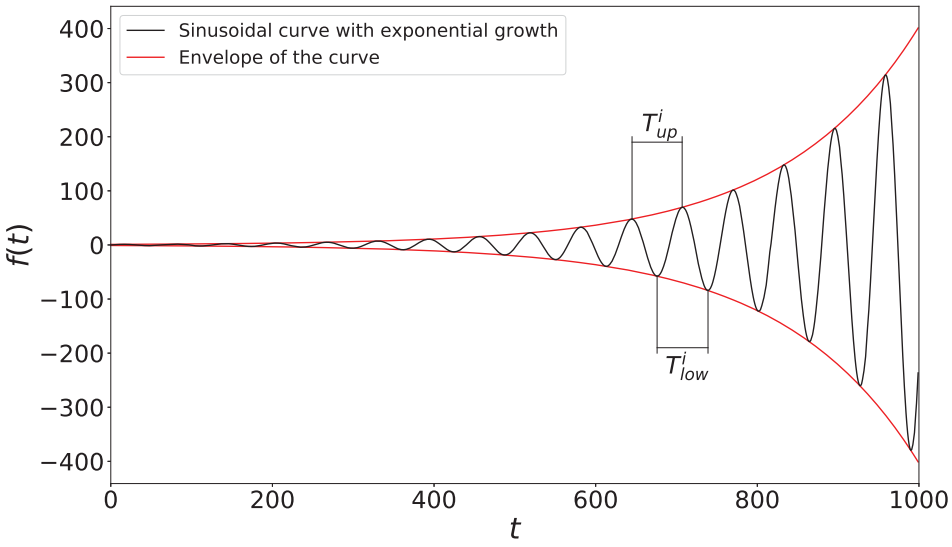

FIGURE D.2: Definition of the envelope (red curve) and the i^{th} periods computed from high peaks (T^i_{up}) and from low peaks (T^i_{low}) of a sinusoidal curve with an exponential growth.

or the lower part of the envelope is considered. To identify σ and K, the following equation is considered:

$$\ln(|C_L - C_{L_S}|) = \sigma t + K \tag{D.2}$$

Then, σ and K are determined by a linear regression. Figure (D.3)(a) shows the points of the envelope used for the linear regression and the associated results of the fit. The top picture shows the results for the upper part of the envelope and the bottom picture, the results for the lower part of the envelope. Figure (D.3)(b) presents the results of the linear regression in the form presented in equation (D.1). In both cases, the non linear growth rate is the same and equal to $\sigma = 0.0022$, which is in good agreement with the growth rate $\sigma = 0.002092$ provided by the linear stability analysis (the results are summarized in Table D.2). Although one can observe that the approximation of the shape of the envelope (based on the linear stability theory) starts becoming less accurate as the time dependent solution departs from the steady solution. It illustrates the fact that a key point in the stability analysis theory is to consider a small perturbation around the steady state in order to linearize the equations. Consequently, the results obtained with this theory are accurate only close to the steady solution.

Figure (D.4) presents the evolution of the period as a function of the index of the period (which is equivalent to its evolution as a function of the time). The value of the period remains almost constant except for the last two periods, independently if they are computed from the high peaks (T^i_{up}) or from the low peaks (T^i_{low}) of the curve. Considering the eleven first points, a mean period value is estimated at : $T = 275.95$, which correspond to a frequency of $f = 3.624 \times 10^{-3}$. The associated Strouhal number is St $= 0.007156$. This value that is to be compared with the value of the linear Strouhal

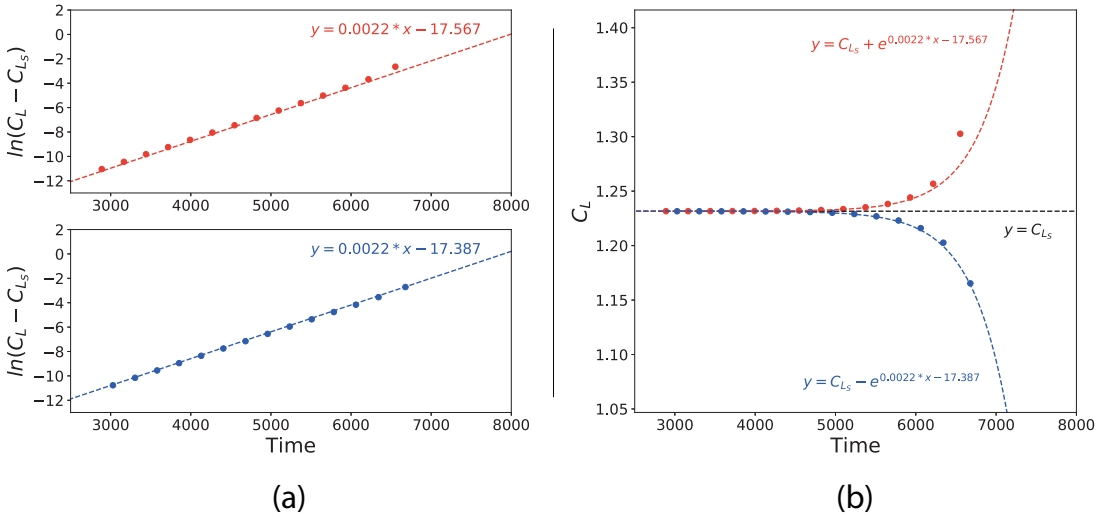

FIGURE D.3: Determination of the growth rate. Left : logarithmic evolution of the lift coefficient of the envelope's points. Red dots : points of the upper part of the envelope. Blue dots : points of the lower part of the envelope. Dashed lines : linear regression to fit the evolution of the points. Right : Evolution of the lift coefficient as a function of the time. Red : envelope points and fit of the upper part of the envelope. Blue : envelope points and fit of the lower part of the envelope.

number is St = 0.00758. The prediction based on the linear stability analysis is in good agreement with the non linear results as there is a discrepancy of approximately 5% between the two. Moreover, one can also observe how, similarly to what was observed with the comparison of the growth rates, the value of the period starts becoming less close to the one estimated with the linear stability analysis as the temporal solution departs from the steady solution. Table D.2 summarizes the values of growth rate and Strouhal number for the linear stability analysis and the unsteady RANS computations. An approximated 5% error is found between the two methods. It indicates that the linear stability analysis correctly predictes the temporal behavior of the oscillations.

	From linear stability analysis	From unsteady computations	Error (%)
St	0.00758	0.00715	5.7
σ	0.002092	0.0022	5.1

TABLE D.2: Comparison of the temporal behavior (Strouhal number and growth rate) from unsteady RANS computations and from linear stability analysis of steady RANS solutions.

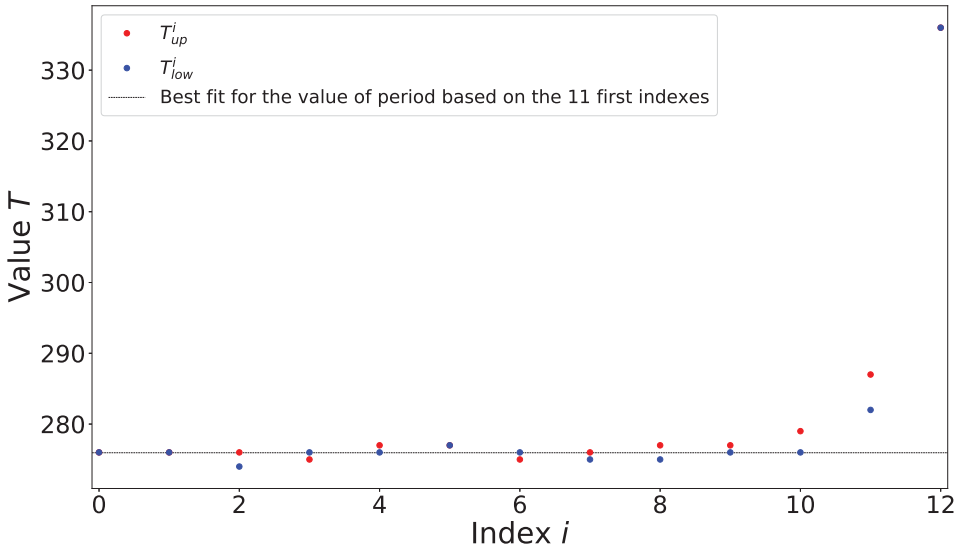

FIGURE D.4: Evolution of the value of the period T as a function of the index of the period. The red dots correspond to values computed from high peaks (T^i_{up}) and the blue dots to values computed from low peaks (T^i_{low})

Appendix E

Design of the one-equation static stall model

Contents

This section is dedicated to the design of a one-equation static stall model, which follows three objectives. The first one is to create a dynamical model whose steady states reproduce the evolution of the steady lift coefficient as a function of the angle of attack, as computed with the RANS equations in chapter 5. The second objective is to make the linear stability of each steady state from the one-equation model similar to the linear stability of the steady solutions of the RANS equations presented in chapter 5. The last objective is to include nonlinearity in the one-equation model in order to ensure that if growing instabilities develop into periodic solutions, they are of finite-amplitude .

E.1 Modeling the steady solutions

A very typical "S" shaped curve characterizing the existence of a hysteresis of the steady solutions was observed close to stall in chapter 5 when plotting the evolution of the lift coefficient as a function of the angle of attack. In one dimension, the usual equation of such a shape is:

$$\alpha + d \cdot c_l + c_l^3 = 0 \tag{E.1}$$

where c_l, the variable of the equation, represents the lift value of the steady state and α, the parameter, the angle of attack. The parameter d is key in the appearance of

hysteresis and shall be set such that $d < 0$. Note that, a nonlinear term of the form $\dot{c_l} = \alpha + d \cdot c_l - c_l^3$ with $d > 0$ would also work but the S shape would be inverted. Actually, the requirement for several coexisting solutions to appear is that the coefficients of the c_l and c_l^3 terms have opposite signs. The case where they have the same sign is discussed in chapters 7 and 8. Moreover, the value of the parameter d drives the size of the hysteretic area. At first, this parameter is set to $d = -1$ in order to simplify the study. The result is plotted in Figure (E.1). One can observe the coexistence of several solutions for a range of angles of attack and the two saddle-node bifurcations characteristic of such a shape. At the moment, on its simplest form, equation (E.1) provides a curve for which the point (0,0) is a rotational symmetry centre.

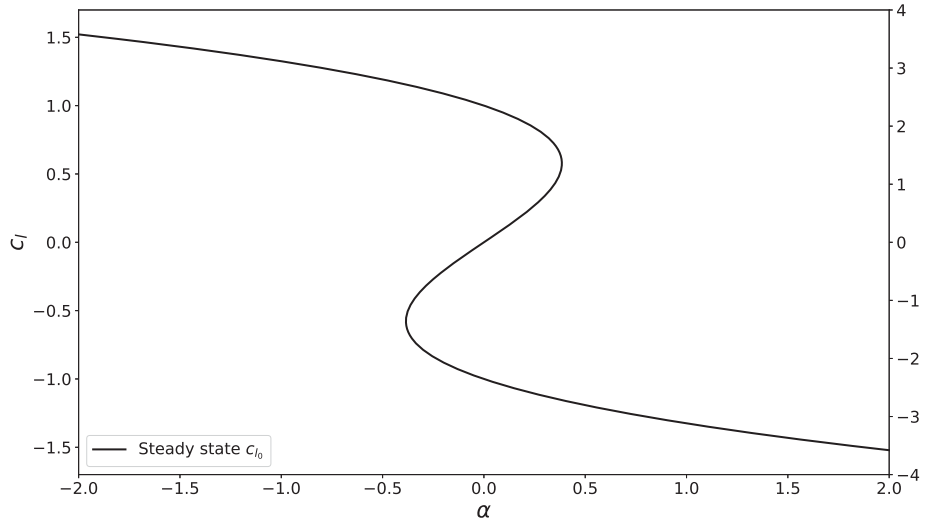

FIGURE E.1: Evolution of the lift coefficient as a function of the parameter α for equation (E.1)

E.2 Modelling the linear stability

E.2.1 Reminder

The linear stability analysis of the steady RANS solutions of an airfoil close to stall (presented in chapter 5) revealed several different states: identical eigenvalues, stable or unstable and steady or unsteady. The objective is to have the different states observed appearing in the following exact order as the curvilinear abscissa of the steady solution curve increases:

- State 1: 2 different stable unsteady modes
- State 2: 2 different unstable unsteady modes
- State 3: 2 identical unstable steady mode

- State 4: 2 different unstable steady modes
- State 5: 1 unstable steady mode and 1 stable steady mode
- State 6-10: Same in the opposite order...

E.2.2 Linear stability analysis of a damped harmonic oscillator

This subsection describes the linear behaviour of a damped harmonic oscillator and highlights the similarities with the linear behavior of the steady solutions from RANS equations presented in chapter 5. The equation of such an oscillator can be written as:

$$\frac{d^2c_l}{dt^2} + 2 \cdot b \cdot \frac{dc_l}{dt} + c \cdot c_l = 0 \tag{E.2}$$

The steady state c_{l_0} is defined such as $\frac{d^2c_{l_0}}{dt^2} = \frac{dc_{l_0}}{dt} = 0$. It is considered that the solution c_l can be written as the sum of this steady state plus a small time dependent perturbation: $c_l = c_{l_0} + \epsilon c'_l$. By replacing this solution in equation (E.2), we obtain two equations at orders ϵ^0 and ϵ^1.

$$\epsilon^0 : c_{l_0} = 0 \tag{E.3}$$

$$\epsilon^1 : \frac{d^2c'_l}{dt^2} + 2 \cdot b \cdot \frac{dc'_l}{dt} + c \cdot c'_l = 0 \tag{E.4}$$

The shape of the small perturbation c'_l is imposed: $c'_l = A\mathrm{e}^{rt}$ and the equation at order ϵ^1 becomes :

$$r^2 + 2 \cdot b \cdot r + c = 0 \tag{E.5}$$

The solutions of equation (E.5) depend on three parameters: b, c and $\delta = 4b^2 - 4c$.

$$\bullet\ \delta > 0 : r_1 = -b - \sqrt{b^2 - c} \tag{E.6}$$

$$r_2 = -b + \sqrt{b^2 - c} \tag{E.7}$$

$$\bullet\ \delta = 0 : r_1 = r_2 = -b \tag{E.8}$$

$$\bullet\ \delta < 0 : r_1 = -b - i\sqrt{c - b^2} \tag{E.9}$$

$$r_2 = -b + i\sqrt{c - b^2} \tag{E.10}$$

The real part of the solution r determines if c_l is stable or unstable and the imaginary part of the solution r determines if c_l is steady or unsteady:

- $\mathcal{I}(r) = 0 :$ c_l is steady
- $\mathcal{I}(r) \neq 0 :$ c_l is unsteady
- $\mathcal{R}(r) < 0 :$ c_l is stable

- $\mathcal{R}(r) > 0$: c_l is unstable

		$\delta > 0$	$\delta = 0$	$\delta < 0$
$b > 0$	$c > 0$	2 Stable	1 Stable	2 Stable
$b < 0$	$c > 0$	2 Unstable	1 Unstable	2 Unstable
$b < 0$	$c < 0$	1 Stable and 1 Unstable	1 Unstable	2 Unstable
$b > 0$	$c < 0$	1 Stable and 1 Unstable	1 Stable	2 Stable

TABLE E.1: State of x according to the parameters b, c and δ. For gray cells, x is steady and for white cells, x is unsteady.

Table E.1 summarizes the different states of the solutions according to parameters b, c and δ. One can note that most of these states can be obtained from different combinations of the coefficients b, c, and δ. For instance, state 1, which is defined as two stable unsteady modes, can be obtained either with the combination $b > 0$, $c > 0$, $\delta < 0$ or with $b < 0$, $c < 0$, $\delta < 0$. The only state that can be obtained with one combination is the state 4, characterized by two unstable steady modes, and obtained with $b < 0$, $c > 0$ and $\delta > 0$. Starting from this combination for state 4, all the other states can be reached in the specified order by changing only one of the coefficient at the time, as shown in Table E.2. For instance, state 5 is obtained by changing the sign of c to a negative value, as highlighted with the blue color. State 3 is reached by setting the value of δ to zero (highlighted with the red color), and so on.

State	1	2	3	4	5
Eigenvalues .	2 different Stable	2 different Unstable	2 identical Unstable	2 different Unstable	1 Stable and 1 Unstable
	Unsteady	Unsteady	Steady	Steady	Steady
Parameters value	$b > 0$ $c > 0$ $\delta < 0$	$b < 0$ $c > 0$ $\delta < 0$	$b < 0$ $c > 0$ $\delta = 0$	$b < 0$ $c > 0$ $\delta > 0$	$b < 0$ $c < 0$ $\delta > 0$

TABLE E.2: States of c_{l_0} according to the parameters b, c and δ and corresponding states identified during the linear stability analysis of RANS equations close to stall.

The influence of each coefficient is now straightforward. The coefficient b drives the Hopf bifurcation (from state 1 to state 2, in green in Table E.2) since its change of

sign destabilizes the two unsteady modes. The coefficient δ drives the steady/unsteady nature of the state including the particular point $\delta = 0$ for which the two eigenvalues of similar (from state 2 to 4 through 3, in red in Table E.2). And the coefficient c drives the saddle-node bifurcation, since its change of sign stabilizes one steady mode (from state 4 to state 5, in blue in Table E.2).

In the above discussion, we recall that the coefficients b and c are independent, unlike the coefficient δ which depends on the other two as $\delta = 4 \cdot (b^2 - c)$. Let us define the coefficients b and c as a function of a single parameter denoted α, as follow

$$b = 0.1 \cdot \alpha^2 - 2.5 \tag{E.11}$$
$$c = 0.5 \cdot \alpha^2 - 2 \tag{E.12}$$

This specific choice allows us to obtain the successive states, from state 5 to state 1, by increasing the value of α. Indeed, let us examine the evolution of the coefficients b, c and δ as a function of α, plotted in Figure (E.2) with the dashed, dash-dotted and solid curves, respectively. Around $\alpha = 0$, the coefficient δ is positive while the coefficients b and c are positive. Therefore, the trivial solution $c_{l_0} = 0$ is unstable (dashed line) and characterized by one stable steady and one unstable steady mode (state 5). This stability state is marked from now using a green dashed line. Increasing α, the coefficient c (dash-dotted curve) changes its sign and the stability state switches from state 5 to state 4, which is marked with a red dashed line. Further increasing α, the coefficient δ gets to zero and then negative, thus going to state 3 for a single value of α to state 2, marked in the figure with a blue dashed line. Note that the color code used to identify the different states in Figure (E.2) is similar to the one used to identify the different states in chapter 5. Finally, further increasing α, the coefficient b changes its sign and the two unstable modes are stabilized, switching to state 1, denoted with a solid blue line, as the trivial solution is now stable. Due to the parabolic dependence of equations (E.11) and (E.12) on α, this evolution is symmetric with respect to this parameter and consequently, the same behavior is observed backward for negative values of α.

E.2.3 Modification of the steady state

Although offering the possibility to obtain all the linear states in the exact same order as the one observed in chapter 5, the simplest form of a damped harmonic oscillator (equation (E.2)) implies a steady solution $c_{l_0} = 0$ for any value of α. In order to obtained the "S" shaped curve very typical of the hysteresis of the steady solutions, it is necessary to modify the steady state of the equation and make it dependent on the parameter α. Equation (E.1) modelling the hysteretic behavior of the steady solutions is implemented in equation (E.2) of the damped harmonic oscillator. Equation (E.13) is obtained:

$$\frac{d^2 c_l}{dt^2} + 2 \cdot b \cdot \frac{dc_l}{dt} + c \cdot (\alpha - c_l + c_l^3) = 0 \tag{E.13}$$

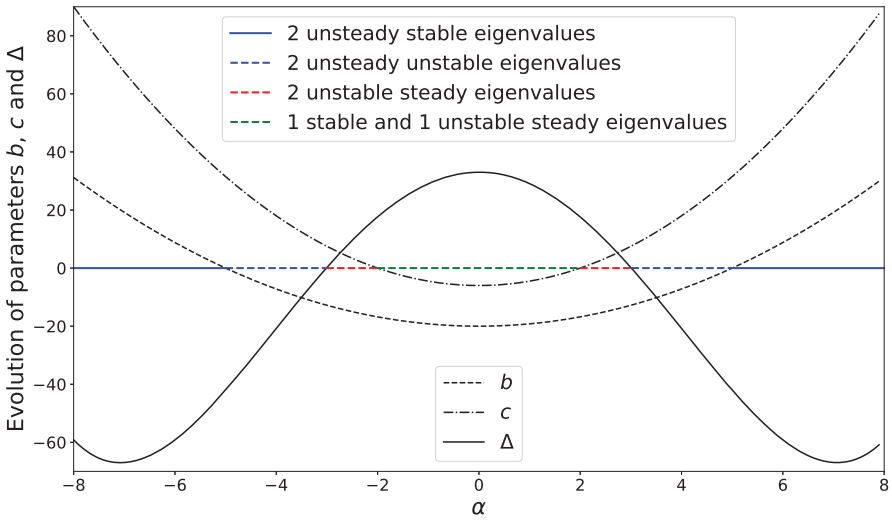

FIGURE E.2: Representation of the steady state $c_{l_0} = 0$ with the linear behavior associated for each value of α (see associated color code in legend). This linear behavior is based on the evolution of parameters b, c and δ also plotted. Every time that one of these parameters changes of sign, the linear behavior of the steady state evolves (as described in Table E.2. b is represented with a factor 8 and c with a factor 3 for visualization purpose.

The linearization of the solution $c_l = c_{l_0} + \epsilon c'_l$ in equation (E.13) gives the two following equations at orders ϵ^0 and ϵ^1.

$$\epsilon^0 : \alpha - c_{l_0} + c_{l_0}^3 = 0 \tag{E.14}$$

$$\epsilon^1 : \frac{d^2 c'_l}{dt^2} + 2 \cdot b \cdot \frac{dc'_l}{dt} + c \cdot (3 \cdot c_{l_0}^2 - 1) \cdot c'_l = 0 \tag{E.15}$$

One can observe that the steady state (order ϵ^0) is now dependent of the parameter α. From now, the computation of the steady state is less obvious than the previous case and requires a numerical resolution as there is no exact solution. A pseudo arc-length method is developed with python for this simple one-equation model.

E.2.4 Modelling limit cycles

Equation (E.13) has the ability to replicate the shape of the steady states as well as their linear behavior with wisely chosen parameters. However, with such an equation, the unstable unsteady eigenvalues would generate unsteadiness that would grow to infinity. To avoid such a nonphysical behavior, it is necessary to add nonlinear saturation. The case of the Van der Pol oscillator is considered to ensure such a behavior. Equation (E.13) becomes :

$$\frac{d^2 c_l}{dt^2} + (2 \cdot b + c_l^2) \cdot \frac{dc_l}{dt} + c \cdot (\alpha - c_l + c_l^3) = 0 \tag{E.16}$$

The linearization of the solution $c_l = c_{l_0} + \epsilon c'_l$ in equation (E.16) gives the two following equations at order ϵ^0 and ϵ^1.

$$\epsilon^0 \ : \ \alpha - c_{l_0} + c_{l_0}^3 = 0 \tag{E.17}$$

$$\epsilon^1 \ : \ \frac{d^2 c'_l}{dt^2} + (2 \cdot b + c_{l_0}^2) \cdot \frac{dc'_l}{dt} + c \cdot (3 \cdot c_{l_0}^2 - 1) \cdot c'_l = 0 \tag{E.18}$$

By similarity with the case of a simple oscillator, the terms previously designated as b, c and δ become B, C and Δ and are defined as following in equation (E.19):

$$\begin{cases} B = 2 \cdot b + c_{l_0}^2 \\ C = c \cdot (3 \cdot c_{l_0}^2 - 1) \\ \Delta = (2 \cdot b + c_{l_0}^2)^2 - 4 \cdot c \cdot (3 \cdot c_{l_0}^2 - 1) \end{cases} \tag{E.19}$$

The main difference with the case of a simple oscillator is that, to ensure the correct linear behavior of the steady solutions we previously had to define b and c as functions of α. However, by adding the previously described nonlinearities, it appears that B, C and Δ are now functions of the steady solution c_{l_0}, which depends on α. Consequently, these parameters naturally evolve as functions of α, which simplifies the choice of parameters b and c.

The equation of a damped harmonic oscillator (E.2) could be analytically resolved. However, the new form of the equation (E.16) requires a numerical resolution. Nevertheless, it is possible to determine the expression of some particular points and have a better understanding of the model. We recall that the Hopf bifurcations occurs when $B = 0$. The corresponding values of the steady lift coefficients are $c_l^{H\pm} = \pm\sqrt{(}-2b)$, showing that the coefficient b should be negative to obtain the Hopf bifurcations of the steady states in the model. They occur for the values $\alpha = c_l^{H\pm} - (c_l^{H\pm})^3$.

The saddle-node bifurcations arise when $C = 0$. The corresponding steady state are thus defined by $c_c^{SN\pm} = \pm\sqrt{(}1/3)$, showing that their value is independent of any parameter. They occur for the angle of incidence $\alpha = c_l^{SN\pm} - (c_l^{SN\pm})3$.

The transition from steady to unsteady states is obtained for $\Delta = 0$. The values of the lift coefficient are then $c_l^{D\pm} = 2 \cdot (b - 3 \cdot c) \pm 2 \cdot \sqrt{9 \cdot c^2 - 6 \cdot b \cdot c - c}$ and are obtained for the angle of incidence $\alpha^{D\pm} = c_l^{D\pm} - c_l^{D\pm 3}$.

The existence of Hopf bifurcations and steady to unsteady transition in the model constrains the choice of the values of the parameters b and c as follows:

$$b < 0 \tag{E.20}$$

$$9 \cdot c^2 - 6 \cdot b \cdot c - c > 0 \tag{E.21}$$

Morever, we would like to have Hopf bifurcations located on the upper or lower branches of the steady states, not on the middle branches. This additional constrain is written:

$$c_l^{H+} > c_l^{SN+} \tag{E.22}$$

It leads to the following restriction in the choice of the coefficient b:

$$b < -1/6 \tag{E.23}$$

Similarly, we would like to have $C < 0$ on the middle branch only. It means, $c \cdot (3 \cdot c_{l_0}^2 - 1) < 0$. We already know that $3 \cdot c_{l_0}^2 - 1$ is negative for $c_l^{SN-} < c_{l_0} < c_l^{SN+}$. Precisely, the domain of existence of the middle branch is for $c_l^{SN-} < c_{l_0} < c_l^{SN+}$, so we want the parameter C to have a sign evolution similar to the sign evolution of $3 \cdot c_{l_0}^2 - 1$. The condition to ensure that is:

$$c > 0 \tag{E.24}$$

Another requirement is to have the Hopf bifurcation on the upper branch appearing for higher values of α than the Hopf bifurcation on the lower branch. This conditions is satisfied if:

$$\alpha^{H+} > \alpha^{H-} \tag{E.25}$$

It yields to the following restriction in the choice of the coefficient b:

$$b > -1/2 \tag{E.26}$$

To summarize, the parameters b and c are subject to the following restrictions in order to replicate the linear behaviour wished:

$$\begin{cases} -\dfrac{1}{6} > b > -\dfrac{1}{2} \\ \\ c > 0 \end{cases} \tag{E.27}$$

One can also notice that with such ranges of existence, the condition $9 \cdot c^2 - 6 \cdot b \cdot c - c > 0$ is completely fulfilled.

Figure (E.3) shows the evolution of the steady states with the associated linear behavior and the evolution of the parameters B, C and Δ (respectively dashed, dotted-dashed and full lines) in the particular case of $b = -0.45$ and $c = 0.1$ as an example. In this particular case, the parameters respect the aforementioned conditions: one can note the appearance of the different linear state in the order detailed in subsection

E.2.1. By following the linear abscissa of the curve, one encounters first state 1 with two stable unsteady eigenvalues (full blue line), state 2 with two with two unstable unsteady eigenvalues (dashed blue line), state 3 with two unstable steady eigenvalues (dashed red line) and state 4 with one stable steady and one unstable steady eigenvalues. The point (0,0) is a rotational symmetry centre of the curve and consequently, the same behavior is repeated on the other half of the curve.

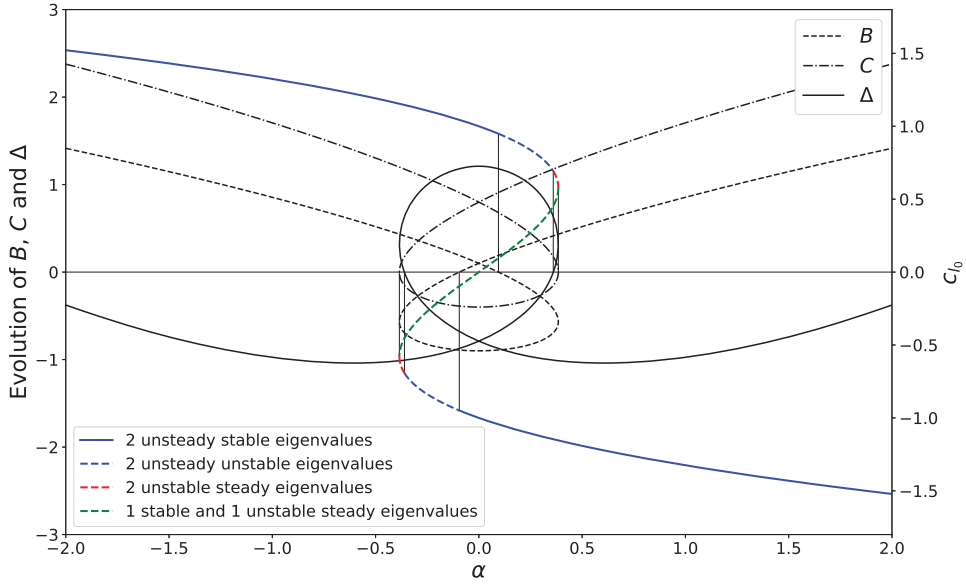

FIGURE E.3: Representation of the steady state c_{l_0} as a function of α with the linear behavior associated for each value of α (see associated color code in legend). This linear behavior is based on the evolution of parameters B, C and Δ also plotted. Every time that one of these parameters changes of sign, the linear behavior of the steady state evolves (as described in Table (E.2). Similar to Figure (E.2) but with non-null steady states and parameters B, C and Δ functions of the steady states.

Appendix F

Non-dominated Sorted Genetic Algorithm

Contents

The Non-dominated Sorting Genetic Algorithm II (NSGA-II) [37], is a genetic algorithm named after the method used to rank and select the solutions. NSGA-II uses the same principle as NSGA but the computation time is reduced and a better diversity of the population is ensured in this version. This chapter is dedicated to the presentation of the algorithm : first, the different steps and the specific vocabulary are introduced, then a simple example is presented (also used to validate the code developed in python).

F.1 Introduction

The principle of genetic algorithms is fundamentally different from the gradient based methods. Indeed, genetic algorithms are based on the evaluation of a large number of solutions to identify the best ones while gradient based methods consists in finding a descent direction to reach the best solution [153].

Genetics algorithms often refer to a very specific vocabulary, based on natural selection:

- The term *individuals* refers to a solution to the considered problem. However, this is not necessarily a solution that minimizes the objective functions
- The term *population* refers to a set of individuals
- The term *parents* is used to characterized an individual which is considered to generate new individuals
- The term *offsprings* is used to characterized the new individuals generated from the parents
- The term *generation* refers to the number of time the offsprings have been generated. It can be seen as an iteration.

The approach of genetic algorithms is the following. A large *population* of randomly set *individuals* is used to evaluate the two (or more) objective functions. First, a part of the population is selected to become *parents*. These parents generate *offsprings* by genetic modification (*crossover* [36] or *mutation*). More practically, this means that some parents are mixed with others to create offsprings (crossover) while other parents are slightly modified to generate other offsprings (mutation). Then, the initial population and the offsprings are evaluated and ranked based on the value of the objective functions. The best solutions based on this ranking are used to become the next *generation*. The process is repeated with this new population until convergence. In the end, a *Pareto* front of solutions is obtained: it offers a large population of solutions that fits more or less each objective function.

Let us consider a case with two objective functions $\boldsymbol{Obj_1}$ and $\boldsymbol{Obj_2}$ as an example. The Pareto front would be made of a solution that is an excellent fit for $\boldsymbol{Obj_1}$ but a poor fit for $\boldsymbol{Obj_2}$, of another solution that is, on the contrary, an excellent fit for $\boldsymbol{Obj_2}$ and a poor fit for $\boldsymbol{Obj_1}$ and, in between, a large choice of solutions that are compromises between these two extrema. This kind of algorithm is named after the particular way to consider the problem as the evolution of a species that would naturally select the individuals which are the most adapted for certain conditions and has the advantage of offering several solutions that can be chosen.

F.2 Steps and specific vocabulary

F.2.1 Non-dominated sorting

This is the method used to rank the solutions. Let us consider the objective function vector $\boldsymbol{Obj}(\boldsymbol{p})$, which gives the value of each objective function associated to the solution $\boldsymbol{p}$. A solution $\boldsymbol{p}$ is dominated by $\boldsymbol{q}$ if for each component i of the the vector $\boldsymbol{Obj}$, $Obj(\boldsymbol{p})_i < Obj(\boldsymbol{q})_i$ is never true and for at least one component $Obj(\boldsymbol{p})_i > Obj(\boldsymbol{q})_i$. The point of the method, is to evaluate the whole population and determine the non-dominated solutions which means that dominated by no other solutions. They are

gathered into the *front* number one and removed from the population. The same process is repeated and this time the non-dominated solutions are gathered into the front number two and so one until the whole population is ranked in fronts. A solution is not necessary dominated or non-dominated by another solution but can also be neutral compared to another solution. For example, if we consider the objective vectors associated to three solutions $\boldsymbol{a}$, $\boldsymbol{b}$ and $\boldsymbol{c}$: $\boldsymbol{Obj}(\boldsymbol{a}) = (2, 1)$, $\boldsymbol{Obj}(\boldsymbol{b}) = (1, 2)$ and $\boldsymbol{Obj}(\boldsymbol{c}) = (2, 2)$. $\boldsymbol{a}$ and $\boldsymbol{b}$ dominates $\boldsymbol{c}$ and so $\boldsymbol{c}$ is dominated by $\boldsymbol{a}$ and $\boldsymbol{b}$. However, $\boldsymbol{a}$ does not dominate $\boldsymbol{b}$ and neither the invert. Consequently, $\boldsymbol{a}$ and $\boldsymbol{b}$ are ranked in the first front and $\boldsymbol{c}$ in the second front.

Note that this method of evaluation, used in the original version of NSGA [153], can be quite long as we have to compare each solution to all the others and do it until they are all ranked. The updated version NSGA-II [37] actually performs the comparison only once and, for each solution $\boldsymbol{i}$, the number of other solutions that dominate $\boldsymbol{i}$ are stored as well as the indices of the solutions that are dominated by $\boldsymbol{i}$. Consequently, by only performing the comparison once, all the data needed to rank the solutions are stored.

F.2.2 Crowding distance

This criteria is used to compare the solutions from a same front to ensure the diversity of the population. Indeed, it is preferable that the population does not converge to a particular solution but covers the whole field of possible solutions. To do so, the crowding distance, which evaluates the distance to other solutions, is developed and used to ensure that between two solutions from the same front, the one with the largest crowding distance is selected first (i.e. the solution the furthest from other solutions). This is a new feature of the NSGA-II as in the previous version, a user parameter was used to maintain diversity of solutions which was more complex and less efficient.

F.2.3 Parents selection

The parents are selected using a tournament method: two individuals are randomly selected from the population and compared. The best one is chosen to become a parent and removed from the population. The other one stays in the population. The selection is made, first by comparing the front of the two individuals : the one in the lowest front is the best. If they are from the same front, their crowding distance is compared : the one with the largest crowding distance is the best. With this method, half of the population is selected to become parents.

F.2.4 Genetic modifications

The point of this step is to create new solutions from the parents selected until the size of population has doubled. The offsprings are created by means of Simulated Binary Crossover (SBX) and polynomial mutation with 90% chance of performing a SBX and 10% of performing a mutation.

F.2.4.1 Crossover

Each crossover actually generates two children from two parents. The k^{th} element of each offspring is defined as in equation (F.2):

$$Child_k^1 = \frac{1}{2}[(1-\beta_k)\cdot Par_k^1 + (1+\beta_k)\cdot Par_k^2] \quad \text{(F.1)}$$

$$Child_k^2 = \frac{1}{2}[(1+\beta_k)\cdot Par_k^1 + (1-\beta_k)\cdot Par_k^2] \quad \text{(F.2)}$$

where β_k is a distribution obtained by generating a random number u for each component k in the law presented in equations (F.3) and (F.4). μ_c is a parameter that allow the user to define how different the children is from the parents. In our case, we set $\mu_c = 5$.

$$u \leq 0.5 \quad , \quad \beta_k(u) = (2\cdot u)^{\frac{1}{\mu_c+1}} \quad \text{(F.3)}$$

$$u > 0.5 \quad , \quad \beta_k(u) = \frac{1}{[2\cdot(1-u)]^{\frac{1}{\mu_c+1}}} \quad \text{(F.4)}$$

F.2.4.2 Mutation

The mutation generates only one child from one parent by modifying the parent using the law presented on equation (F.5):

$$Child_k = Par_k + \delta_k \quad \text{(F.5)}$$

with δ_k a distribution obtained by generating a random number u for each component k in the law presented in equation (F.7). μ_m is a parameter that allow the user to define how different the child is from the parent. In our case, we set $\mu_m = 10$.

$$u < 0.5 \quad , \quad \beta_k(u) = (2\cdot u)^{\frac{1}{\mu_m+1}} - 1 \quad \text{(F.6)}$$

$$u \geq 0.5 \quad , \quad \beta_k(u) = 1 - [2\cdot(1-u)]^{\frac{1}{\mu_m+1}} \quad \text{(F.7)}$$

F.2.5 Candidates for next generation

The new population of size N made of initial population and the offsprings generated is ranked and only the best half is kept for next generation. The non-dominated sorting coupled with the crowding distance criteria is used. However, to avoid useless computations, the population for next generation is selected as following. Let us designate by n_j the number of individuals of the j^{th} front. K is the first front for which $\sum_{j=1}^{K} n_j > \frac{N}{2}$. All the individuals of the $K-1$ fronts are kept for next generation. For the elements of the K^{th} front a ranking based on the crowding distance is necessary : the individuals of the K^{th} front with the largest crowding distance are selected until $\frac{N}{2}$ individuals are selected. With such an approach the crowding distance is evaluated only for the individuals in the front that has to be split.

F.2.6 Summary

All the steps described are summarized in the schema presented in Figure (F.1) (adapted from [37]).

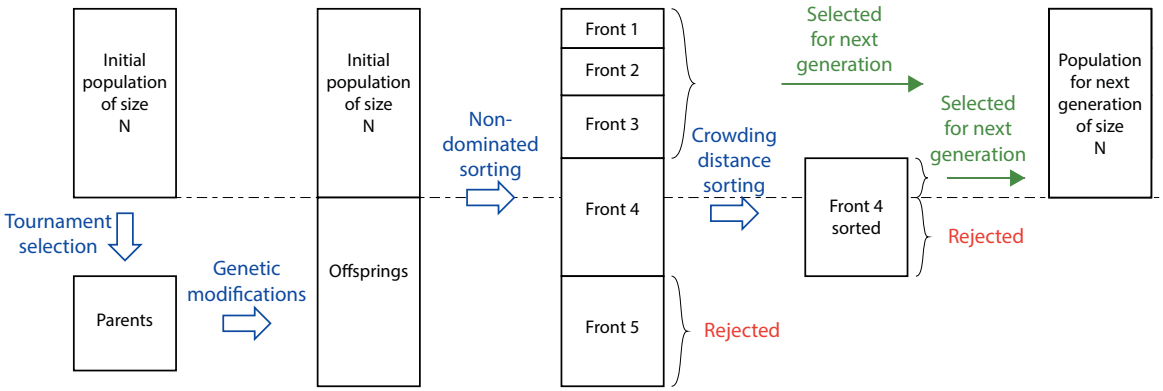

FIGURE F.1: Schema of the various steps of the NSGA-II during a generation. Adapted from [37]

F.3 Application to a simple case

We want to find the best solutions (x, y) minimizing these two functions f and g.

$$f = (x-1)^2 + (y-1)^2 \tag{F.8}$$
$$g = (x+1)^2 + (y+1)^2 \tag{F.9}$$

The analytical solutions of this minimization problem are:

$$S = \{(x, y) \in [-1, 1] \times [-1, 1] \mid x = y\} \tag{F.10}$$

F.3.1 Selection for the next generation

Figure (F.2) presents the different steps of the selection process of the population that is conserved from generation n to generation $n + 1$.

The results of the tournament selection are depicted in Figure (F.2)(a). The initial population is represented by black circles in the plane $(f(x, y), g(x, y))$. The individuals with a white cross are selected as parents. Note that with the tournament method, not only the best individuals are selected. This method, although presenting the drawback of missing a few good individuals, offers the advantage of preserving the diversity of the population as two "bad" parents not necessarily generate a "bad" offspring. The children generated by the selected parents are presented in Figure (F.2)(b) by white circles. Finally, in Figure (F.2)(c), the individuals of the population chosen for next generation are highlighted in red. Visually this corresponds to the individuals the most on the bottom/left part of the curve, which minimizes both objective functions.

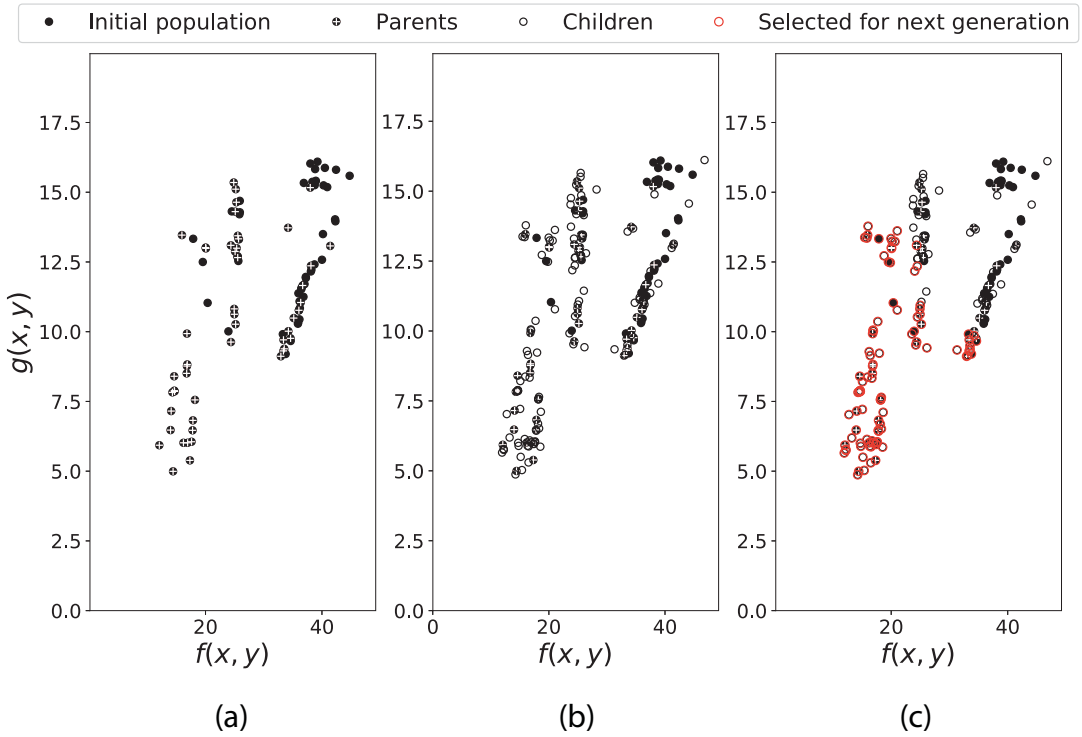

FIGURE F.2: Evolution of the population at the different stages of a generation. (*a*) Selection of parents. (*b*) Creation of offsprings. (*c*) Selection of best parents and offsprings for the next generation.

F.3.2 Evolution of the Pareto front

This selection process is repeated during 50 generations and the results are presented in Figure (F.3), which exhibits the population for different generations in red circles and the theoretical Pareto front by a black line. One can observe how the population get closer and closer to the Pareto front as the number of generations is increasing and how the population is well spread on this front at the last generation.

One shall note that randomness is a big part of genetic algorithm (initial population, parents selection and genetic modifications). Consequently, running two times the same optimization problem might lead to two different ways to reach the Pareto front and the number of generations needed for convergence might be different.

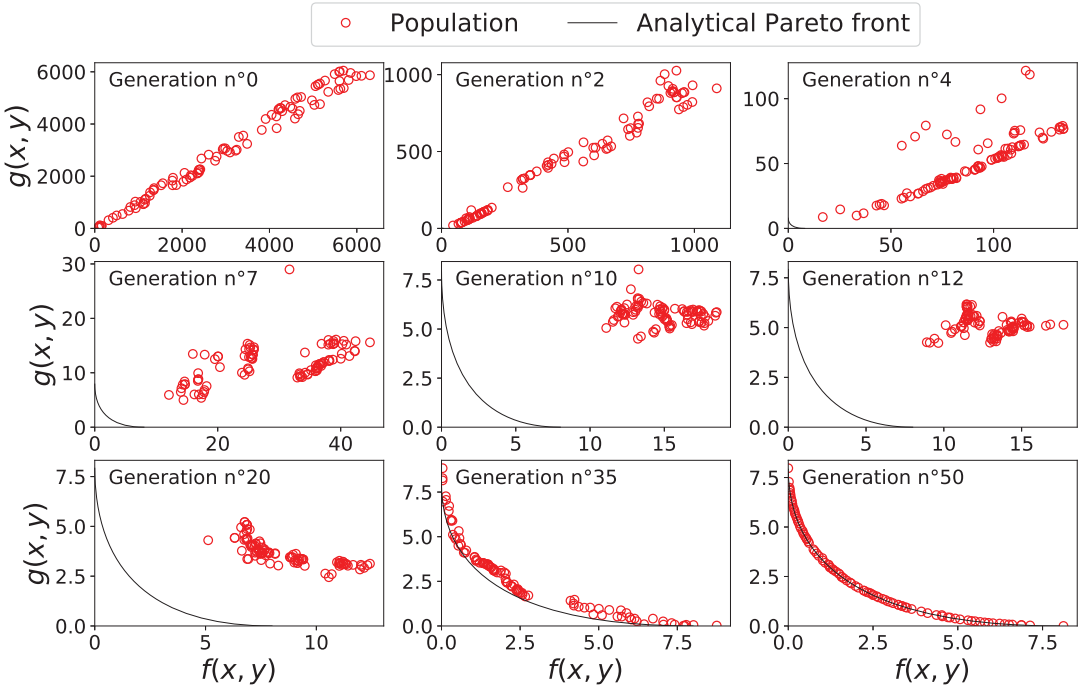

FIGURE F.3: Visualization of the population (red circles) in the $(f(x,y), g(x,y))$ plane for several generations. Each circle corresponds to a couple (x,y). The theoretical Pareto front is represented by a black line.

Bibliography

[1] S. Abhyankar, J. Brown, E. Constantinescu, D. Ghosh, B. F. Smith, and H. Zhang. PETSc/TS: A Modern Scalable ODE/DAE Solver Library. *arXiv preprint arXiv:1806.01437*, 2018.

[2] J. Almutairi and I. Alqadi. Large-eddy simulation of natural low-frequency oscillations of separating-reattaching flow near stall conditions. *AIAA Journal*, 51(4):981–991, 2013.

[3] J. Almutairi, I. Alqadi, and E. M. ElJack. Large eddy simulation of a NACA-0012 airfoil near stall. *Direct and Large-Eddy Simulation IX*, 20, 2015.

[4] H.B. An, J. Wen, and T. Feng. On finite difference approximation of a matrix-vector product in the Jacobian-free Newton-Krylov method. *Journal of Computational an Applied Mathematics*, 236:1399–1409, 2011.

[5] P. J. Ansell and M. B. Bragg. Characterization of ice-induced low-frequency flowfield oscillations and their effect on airfoil performance. *AIAA Journal*, 2673, 2013.

[6] P. J. Ansell and M. B. Bragg. Characterization of low-frequency oscillations in the flowfield about an iced airfoil. *AIAA Journal*, 53(3):629–637, 2015.

[7] P. J. Ansell and M. B. Bragg. Unsteady modes in flowfield about airfoil with horn-ice shape. *Journal of Aircraft*, 53(2), 2016.

[8] S. Bagheri, P. Schlatter, P. J. Schmid, and D. S. Henningson. Global stability of a jet in crossflow. *Journal of Fluid Mechanics*, 624(33–44), 2009.

[9] B. S. Baldwin and T. J. Barth. A one-equation turbulence transport model for high Reynolds number wall bounded flows. *NASA Technical Memorandum*, 102847, 1990.

[10] D. Barkley. Linear analysis of the cylinder wake mean flow. *Europhysics Letter*, 75(5):750–756, 2006.

[11] D. Barkley, L. S. Tuckerman, and M. Golubitsky. Bifurcation theory for three-dimensional flow in the wake of a circular cylinder. *The American Physical Society*, 61(5):5247–5252, 2000.

[12] G. K. Batchelor and A. E. Gill. Analysis of the stability of axisymmetric jets. *Journal of Fluid Mechanics*, 14(4):529–551, 1962.

[13] S. Beneddine. Global stability analysis of underexpanded screeching jets. *European Journal of Mechancs B/Fluids*, 49:392–399, 2014.

[14] S. Beneddine. *Characterization of unsteady flow behavior by linear stability analysis*. PhD thesis, Ecole Polytechnique, 2017.

[15] S. Beneddine, D. Sipp, A. Arnault, J. Dandois, and L. Lesshafft. Conditions for validity of mean flow stability analysis. *Journal of Fluid Mechanics*, 798:485–504, 2016.

[16] L. Bernardos, F. Richez, V. Gleize, and G. A. Gerolymos. Algebraic nonlocal transition modeling of laminar separation bubbles using $k-\omega$ turbulence models. *AIAA Journal*, 57(2), 2019.

[17] N. Bonne. *Stabilité de l'interaction onde de choc/couche limite laminaire*. PhD thesis, Université Paris-Saclay - Ecole Polytechnique, 2018.

[18] J. L. Bonnet and C. Gleyzes. Etude expérimentale de la transition dans des bulbes de décollement laminaire au bord d'attaque des profils d'aile. *Rapport Technique OA*, 23(5018), 1983.

[19] M. B. Bragg, D. C. Heinrich, F. A. Balow, and K. B. M. Q. Zaman. Flow oscillation over an airfoil near stall. *AIAA Journal*, 34(1):199–201, 1996.

[20] M. B. Bragg and K. B. M. Q. Zaman. Flow oscillation over airfoils near stall. *International Council of the Aeronautical Sciences*, 4(5):1639–1648, 1994.

[21] J. Brewster and M. P. Juniper. Shape sensitivity of eigenvalues in hydrodynamic stability, with physical interpretation for the flow around a cylinder. *European Journal of Mechancs B/Fluids*, 80:80–91, 2019.

[22] A. P. Broeren. Phase-averaged LDV flowfield measurements about an airfoil in unsteady stall. *AIAA Journal*, 2494:921–931, 1996.

[23] A. P. Broeren and M. B. Bragg. Flowfield measurements over and airfoil during natural low-frequency oscillations near stall. *AIAA Journal*, 37(1):130–132, 1998.

[24] A. P. Broeren and M. B. Bragg. Low frequency flowfield unsteadiness during airfoil stall and the influence of stall type. *AIAA Paper*, 2517(196–209), 1998.

[25] A. P. Broeren and M. B. Bragg. Spanwise variation in the unsteady stalling flowfields of two-dimensional airfoil models. *AIAA Journal*, 37(1):130–132, 2001.

[26] A. P. Broeren, B. S. Woodard, J. M. Diebold, and F. Moens. Low-Reynolds number aerodynamics of an 8.9 percent scale semispan swept wing for assessment of icing effects. *NASA Technical Memorandum*, 219533, 2017.

[27] L. Cambier, M. Gazaix, S. Heib, S. Plot, M. Poinot, J.-P. Veuillot, J.-F. Boussuge, and M. Montagnac. An Overview of the Multi-Purpose elsA Flow Solver. *AerospaceLab*, pages 1–15, 2011.

[28] P. Chassaing. *Turbulence en mecanique des fluides*. Cepadues-Editions, 2000.

[29] J.-M. Chomaz. Global instabilities in spatially developping flows: non-normality and nonlinearity. *Annual Review of Fluid Mechanics*, 37:357–392, 2005.

[30] C. Cossu, G. Pujals, and S. Depardon. Optimal transient growth and very large-scale structures in turbulent boundary layers. *Journal of Fluid Mechanics*, 619:79–94, 2009.

[31] D. Crighton and M. Gaster. Stability of slowly diverging jet flow. *Journal of Fluid Mechanics*, 77(2):397–413, 1976.

[32] J. D. Crouch, A. Garbaruk, and D. Magidov. Predicting the onset of flow unsteadiness based on global instability. *Journal of Computational Physics*, 224:924–940, 2007.

[33] J. D. Crouch, A. Garbaruk, D. Magidov, and A. Travin. Origin of transonic buffer on aerofoils. *Journal of Fluid Mechanics*, 628:357–369, 2009.

[34] T. Cui, W. Liao, and D. Yu. Topological approach for analyzing and modeling the aerodynamic hysteresis of an airfoil. *Computer Modeling in Engineering and Sciences*, 45(3):273–293, 2009.

[35] G. de Vries. Multiple bifurcations in a polynomial model of bursting oscillations. *Journal of Nonlinear Sciences*, 8:281–316, 1998.

[36] K. Deb and R. B. Agarwal. Simulated Binary Crossover for Continuous Search Space. *Complex Systems*, 9:115–148, 1995.

[37] K. Deb, A. Pratap, S. Agarwal, and T. Meyarivan. A Fast and Elitist Multiobjective Genetic Algorithm: NSGA-II. *IEEE Transactions on Evolutionnary Computation*, 6(2), 2002.

[38] S. Deck. *Simulation numérique des charges latérales instationnaires sur des configurations de lanceur*. PhD thesis, Université d'Orléans, 2002.

[39] A. Dhooge, W. Govaerts, Y. A. Kuznetsov, H. G. E. Meijer, and B. Sautois. New features of the software MatCont for bifurcation analysis of dynamical systems. *Mathematical and Computer Modelling of Dynamical Systems*, 14(2):147–175, 2008.

[40] K. I. Dickson, C. T. Kelley, I. C. F. Ipsen, and I. G. Kevrekidis. Condition estimates for pseudo-arclength continuation. *SIAM Journal on Numerical Analysis*, 45(1):263–276, 2006.

[41] H. A. Dijkstra, F. W. Wubs, A. K. Cliffe, E. Doedel, I. F. Dragomirescu, B. Eckhardt, A. Y. Gelfgat, A. L. Hazel, V. Lucarini, A. G. Salinger, E. T. Phipps, J. Sanchez-Umbria, H. Schuttelaars, L. S. Tuckerman, and U. Thiele. Numerical bifurcation methods and their application to fluid dynamics: analyysis beyond simulation. *Communication on Computational Physics*, 15(1):1–45, 2014.

[42] G. Dimitriadis and J. Li. Bifurcation behavior of airfoil undergoing stall flutter oscillations in low-speed wind tunnel. *AIAA Journal*, 47(11):2577–2596, 2009.

[43] S. Diwan, S. Chetan, and O. Ramesh. On the bursting criterion for laminar separation bubbles. *IUTAM Symposium on Laminar-Turbulent Transition*, pages 401–407, 2006.

[44] A. V. Dovgal. Development of vortical disturbances in flow with laminar separation. *Laminar-Turbulent Transition, Proceedings of the IUTAM-Symposium*, pages 359–366, 1985.

[45] P. G. Drazin. On a model of instability of a slowly-varying flow. *The Quarterly Journal of Mechanics and Applied Mathematics*, 27(1):69–86, 1974.

[46] J. R. Edwards and S. Chandra. Comparison of eddy viscosity-transport turbulence models for three-dimensional, shock-separated flowfields. *AIAA Journal*, 34(4):756–763, 1996.

[47] J. R. Edwards and M.-S. Liou. Low-diffusion flux splitting methods for flows at all speeds. *AIAA Journal*, 36:1610–1617, 1998.

[48] J. A. Ekaterinaris and F. R. Menter. Computation of oscillating airfoil flows with one- and two-equation turbulence models. *AIAA Journal*, 32(12):2359–2365, 1994.

[49] E. M. ElJack and J. Soria. Bursting and reformation cycle of the laminar separation bubble over a NACA-0012 aerofoil: the underlying mechanism. *arXiv*, 2018.

[50] H. A. Eschenauer. Multicriteria optimization for highly accurate focusing systems. *Multicritera Optimization in Engineering and Sciences - Mathematical Concepts and Methods in Science and Engineering*, 37(309-354), 1988.

[51] D. Fabre, F. Auguste, and J. Magnaudet. Bifurcations and symmetry breaking in the wake of axisymmetric bodies. *Physics of Fluids*, 20(051702):1–4, 2008.

[52] H. Fallah. Symmetric fold/super-Hopf bursting, chaos and mixed-mode oscillations in Pernarowski model of pancreatic beta-cells. *International Journal of Bifurcation and Chaos*, 26(09), 2016.

[53] A. Favre. Equations des gaz turbulents compressibles, part 1: formes générales. *Journal de Mécanique*, 4:361–390, 1965.

[54] A. Favre. Equations des gaz turbulents compressibles, part 2: méthode des vitesses moyennes; méthode des vitesses moyennes pondérées par la masse volumique. *Journal de Mécanique*, 4:391–421, 1965.

[55] A. D. Gardner, K. Richter, and H. Rosemann. Nuerical investigation of air jets for dynamic stall control on the OA209 airfoil. *CEAS Aeronautical Journal*, 1:69–82, 2011.

[56] M. Gaster. The structure and behaviour of separation bubbles. *A.R.C. Reports and Memoranda*, 3595, 1967.

[57] T. B. Gatski and J.-P. Bonnet. *Compressibility, turbulence and high speed flow.* Elsevier, 2009.

[58] D. E. Gault. A correlation of low-speed, airfoil-section stalling characteristics with Reynolds number and airfoil geometry. *NACA Technical Note*, 3963, 1957.

[59] F. Giannetti and P. Luchini. Structural sensitivity of the first instability of the cylinder wake. *Journal of Fluid Mechanics*, 581:167–197, 2007.

[60] R. Gilmore. *Catastrophe theory for scientists and engineers*. Dover Publications, 1993.

[61] V. Gleize, J. Szydlowski, and M. Costes. Numerical and physical analysis of turbulent viscous flow around a NACA0015 profile at stall. *European Congress on Computational Methods in Applied Sciences and Engineering*, 2004.

[62] C. Gleyzes, C. Cousteix, and J. L. Bonnet. Theoretical and experimental study of low Reynolds-number transitional separation bubbles. In *Conference on Low Reynolds Number Airfoil Aerodynamics*, Notre Dame, IN, 137-152, 1985.

[63] W. Govaerts. *Numérical methods for bifurcations of dynamical equilibria*. Siam, 2000.

[64] A. Harten and J. M. Hyman. Self adjusting grid methods for one-dimensional hyperbolic conservation laws. *Journal of Computational Physics*, 50(2):235–269, 1983.

[65] A. Hatman and T. Wang. Separated-Flow transition. PART 1 - Experimental methodology and mode classification. PART 2 - Experimental results. PART 3 - Primary modes and vortex dynamics. *ASME Paper*, 98(461–462–463), 1998.

[66] D. C. Hill. A theoretical approach for analyzing the restabilization of wakes. *NASA Technical Memorandum*, 103858, 1992.

[67] J. A. Hoffman. Effects of freestream turbulence on the performance characteristics of an airfoil. *AIAA Journal*, 29(9):1353–1354, 1991.

[68] H. P. Horton. *Laminar separation bubbles in two and three dimensional incompressible flow*. PhD thesis, University of London - Queen Mary College - Department of Aeronautical Engineering, 1968.

[69] G. Hristov. *Post-stall hysteresis and flow field unsteadiness on a NACA0012 airfoil*. PhD thesis, University of Illinois ar Urbana-Champaign, 2017.

[70] G. Hristov and P. J. Ansell. Post-stall hysteresis and flow field unsteadiness on a NACA0012 airfoil. *AIAA SciTech Forum*, 55th AIAA Aerospace Sciences Meeting, 2017.

[71] H. Hu, Z. Yang, and H. Igarashi. Aerodynamic hysteresis of a low-Reynolds-number airfoil. *Journal of Aircraft*, 44(6):2083–2086, 2007.

[72] P. Huerre and P. A. Monkewitz. Absolute and convective instabilities in free shear layers. *Journal of Fluid Mechanics*, 159(151–168), 1985.

[73] P. Huerre and P. A. Monkewitz. Local and global instabilities in spatially developing flows. *Annual Review of Fluid Mechanics*, 22:473–357, 1990.

[74] M. Illsley. https://bigsynthesis.com/understandingaerospace/index.php/6-why-are-helicopters-so-slow/. *Website*, 2014.

[75] M. C. Iorio, L. M. Gonzalez, and E. Ferrer. Direct and adjoint global stability analysis of turbulent transonic flows over a NACA0012 profile. *International Journal for Numerical Methods in Fluids*, 76:147–168, 2014.

[76] M. C. Iorio, L. M. Gonzalez, and A. Martinez-Cava. Global stability analysis of a compressible turbulent flow around a high-lift configuration. *AIAA Journal*, 54(2):373–385, 2015.

[77] Richard P. Dwight Jacques E. V. Peter. Numerical sensitivity analysis for aerodynamic optimization: a survey of approaches. *Computers and Fluids*, 39:373–391, 2010.

[78] R. Jain, A. Le Pape, A. Grubb, M. Costes, F. Richez, and M. Smith. High-resolution computational fluid dynamics predictions for the static and dynamic stall of a finite-span OA209 wing. *Journal of Fluids and Structures*, 78:126–145, 2018.

[79] B. M. Jones. An experimental study of the stalling of wings. *R. & M.*, 1588, 1933.

[80] B. M. Jones. Stalling. *Journal of the Royal Aeronautical Society*, 38(285):753–770, 1934.

[81] W. P. Jones and B. E. Launder. The calculation of low-Reynolds-number phenomena with a two-equation model of turbulence. *Journal Heat Mass*, 16:1119–1130, 1973.

[82] M. P. Juniper and B. Pier. The structural sensitivity of open shear flows calculated with a local stability analysis. *European Journal of Mechancs B/Fluids*, 49:426–437, 2015.

[83] T. Von Kármán. Ueber den Mechanismus des Widerstandes, den ein bewegter Körper in einer Flüssigkeit erfährt. *Nachrichten von der Gesellschaft der Wissenschaften zu Göttingen, Mathematisch-Physikalische Klasse*, pages 509–511, 1911.

[84] T. Von Kármán. Ueber den Mechanismus des Widerstandes, den ein bewegter Körper in einer Flüssigkeit erfährt. *Nachrichten von der Gesellschaft der Wissenschaften zu Göttingen, Mathematisch-Physikalische Klasse*, pages 547–556, 1912.

[85] K. Kaufman, M. Costes, F. Richez, A. D. Gardner, and A. Le Pape. Numerical investigation of three-dimensional static and dynamic stall on a finite wing. *Journal of the American Helicopter Society*, 60, 2015.

[86] H. B. Keller. *Lectures on numerical methods in bifurcation problems.* H. Goctzc, Springer-Verlag, 1986.

[87] C. T. Kelley. *Solving nonlinear equations with Newton's method.* Society for Industrial and Applied Mathematics, 2003.

[88] D.A. Knoll and D.E. KEYES. Jacobian-free Newton-Krylov methods: a survey of approaches and applications. *Journal of Computational Physics*, 193:357–397, 2004.

[89] Y. A. Kuznetsov. *Elements of applied bifurcation theory, second edition.* Springer, 2004.

[90] B. Van Leer. Towards the ultimate conservative difference scheme. II. Monotonicity and conservation combined in a second-order scheme. *Journal of Computational Physics*, 14(4):361–370, 1974.

[91] P. Luchini, F. Giannetti, and J. Pralits. Structural sensitivity of linear and nonlinear global modes. *AIAA Paper*, 4227, 2008.

[92] C. K. Mamun and L. S. Tuckerman. Asymmetry and Hopf bifurcation in spherical Couette flow. *Physics of Fluids*, 7:80–91, 1995.

[93] J. F. Marchman, Y. K. Chang, and R. D. Robinson. Sweep effects on low Reynolds number stall hysteresis. *AIAA Paper*, 88(4419), 1988.

[94] J. F. Marchman, V. Sumantran, and C. G. Schaefer. Acoustic and turbulence influences on stall hysteresis. *AIAA Journal*, 25(1):50–51, 1987.

[95] O. Marquet and L. Lesshafft. Identifying the acive flow regions that drive linear and nonlinear instabilities. arXiv.

[96] O. Marquet, M. Lombardi, D. Sipp, J. M. Chomaz, and L. Jacquin. Direct and adjoint global modes of recirculation bubble: lift-up and convectire nonnormalities. *Journal of Fluid Mechanics*, 622(1–21), 2009.

[97] O. Marquet, D. Sipp, and L. Jacquin. Sensitivity analysis and passive control of cylinder flow. *Journal of Fluid Mechanics*, 615:221–252, 2008.

[98] I. Mary. *Méthode de newton approchee pour le calcul d'écoulements instationnaires comportant des zones à très faibles nombres de Mach.* PhD thesis, Université Paris XI, 1999.

[99] I. Mary and P. Sagaut. Large eddy simulation of flow around an airfoil near stall. *AIAA Journal*, 40(6):1139–1145, 2002.

[100] W. J. McCroskey. Unsteady airfoil. *Annual Review of Fluid Mechanics*, 14:285–311, 1982.

[101] W. J. McCroskey and R. K. Fisher. Dynamic stall of airfoils and helicopter rotors. *AGARD R*, 595:2.1–2.7, 1972.

[102] G. B. McCullough and D. E. Gault. Examples of three representative types of airfoil section sall at low speed. *NACA Technical Note*, 2502, 1951.

[103] H. G. E. Meijer. Matcont Tutorial: ODE GUI version. 2014.

[104] H. G. E. Meijer. Matcont Tutorial: ODE GUI version. 2016.

[105] P. Meliga, J.-M. Chomaz, and D. Sipp. Global mode interaction and pattern selection in the wake of a disk: a weakly nonlinear expansion. *Journal of Fluid Mechanics*, 633:159–189, 2009.

[106] P. Meliga, J.-M. Chomaz, and D. Sipp. Unsteadiness in the wake of disks and spheres: instability, receptivity and control using direct and adjoint global stability analyses. *Journal of Fluids and Structures*, 25:601–616, 2009.

[107] F. R. Menter. Zonal two equation $k-\omega$ turbulence models for aerodynamic flows. *AIAA Paper*, 93-2906, 1993.

[108] C. Mettot, F. Renac, and D. Sipp. Computation of eigenvalue sensitivity to base flow modification in a discrete framework: Application to open-loop control. *Journal of Computational Physics*, 269:234–258, 2014.

[109] C. B. Millikan and A. L. Klein. The effect of turbulence. *Aircraft Engineering*, 5(8):169–174, 1933.

[110] S. Mittal and P. Saxena. Hysteresis in flow past a NACA 0012 airfoil. *Computer methods in applied mechanics and engineering*, 191:2179–2189, 2001.

[111] M. Mizoguchi, Y. Kajikawa, and H. Itoh. Static stall hysteresis of low-aspect-ratio wings. *32nd AIAA Applied Aerodynamic Conference*, 2014.

[112] M. V. Morkovin. Effects of compressibility on turbulent flows. *A. Favre (e), Mécanique de la turbulence*, pages 367–380, 1962.

[113] T. J. Mueller. The influence of laminar separation and transition on low Reynolds number airfoil hysteresis. *Journal of Aircraft*, 22(9):763–770, 1985.

[114] T. J. Mueller, L. J. Pohlen, P. E. Conigliaro, and B. J. Jansen. The influence of free-stream disturbances on low Reynolds number airfoil experiments. *Experiments in Fluids*, 1:3–14, 1983.

[115] M. Nagata. Three-dimensional traveling-wave solutions in plane Couette flow. *Physical Review E*, 55(2):2023–2025, 1997.

[116] T. Nakazawa and H. Azegami. Shape optimization of flow field improving hydrodynamic stability. *Japan Journal of Industrial and Applied Mathematics*, 33:167–181, 2016.

[117] I. Newton. *The Mathematical Papers of Isaac Newton*, volume 2. Cambridge University Press, 1968.

[118] M. M. O'meara and T. J. Mueller. Experimental determination of the laminar separation bubble characteristics of an airfoil at low Reynolds numbers. In *AIAA/ASME 4th Fluid Mechanics, Plasma Dynamics and Lasers Conference, Atlanta, USA*, 1986.

[119] P. R. Owen and L. Klanfer. On the laminar boundary layer separation from the leading edge of a thin airfoil. *A.R.C. Technical Report*, 220, 1955.

[120] J.-Y. L'Excellent P. Amestoy, I. Duff and J. Koster. A fully asynchronous multifrontal solver using distributed dynamic scheduling. *SIAM Journal on Matrix Analysis and Applications*, 23(1):15–41, 2001.

[121] G. Pailhas, R. Houdeville, P.Barricau, A. Le Pape, A. Faubert, P. Loiret, and F. David. Experimental investigation of dynamic stall. *31th European Rotorcraft Forum*, Florance, Italy, 2005.

[122] E. Paladini. *Insight on transonic buffet instability - Evolution from two dimensional aerofoils to three-dimensional swept wings*. PhD thesis, Ecole Nationale Superieure d'Arts et Metiers - ENSAM, 2019.

[123] E. Paladini, O. Marquet, D. Sipp, J.-C. Robinet, and J. Dandois. Various approaches to determine active regions in an unstable global mode: application to transonic buffet. *Journal of Fluid Mechanics*, 881:617–647, 2019.

[124] A. Le Pape, C. Lienard, and J. Bailly. Active flow control for helicopters. *AerospaceLab Journal*, 6, 2013.

[125] A. Le Pape, G. Pailhas, F. David, and J. M. Deluc. Extensive wind tunnel measurements of dynamic stall phenomenon for the OA209 airfoil including 3D effects. In *33rd European Rotocraft Forum, Kazan, Russia*, 2007.

[126] M. Pernarowski. Fast subsystem bifurcations in a slowly varying Liénard system exhibiting bursting. *SIAM Journal of Applied Mathematics*, 54:814–832, 1994.

[127] E. Piot, G. Casalis, F. Muller, and C. Bailly. Investigation of the PSE approach for subsonic an supersonic hot jets. Detailed comparisons with LES and linearized Euler equations results. *Internal Journal of Aeroacoustics*, 5(4), 2006.

[128] R. Piziali. 2D and 3D oscillating wing aerodynamics for a range of angles of attack including stall. *NASA Technical Memorandum*, 4632(USAATCOM Technical Report 94-A-011), 1994.

[129] L. J. Pohlen and T. J. Mueller. Boundary layer characteristics of the Miley airfoil at low Reynolds numbers. *Journal of Aircraft*, 21(9):658–664, 1984.

[130] D. C. Sorensen R. B. Lehoucq and C. Yang. ARPACK Users Guide : Solution of Large Scale Eigenvalue Problems by Implicitly Restarted Arnoldi Methods. *Philadelphia: SIAM*, 1998.

[131] J. Raphson. *Analysis aequationum universalis*. Tho. Braddyll, 1697.

[132] O. Reynolds. On the dynamical theory of incompressible viscous fluids and the dermination of the criterion. *Proceedings of the Royal Society of London*, 56:40–45, 1895.

[133] F. Richez, M. Leguille, and O. Marquet. Selective Frequency Damping method for steady RANS solutions of turbulent separated flows around an airfoil at stall. *Computers and Fluids*, 132:51–61, 2016.

[134] F. Richez, I. Mary, V. Gleize, and C. Basdevant. Zonal RANS/LES coupling simulation of a transitional and separated flow around an airfoil near stall. *Theoretical and Computational Fluid Dynamics*, 22:305–315, 2008.

[135] F. Richez, A. Le Pape, and M. Costes. Zonal detached-eddy simulation of separated flow around a finite-span wing. *AIAA Journal*, 53(11):3157–3166, 2015.

[136] F. Richez, A. Le Pape, M. Costes, and R. Gavériaux. Zonal detached-eddy simulation (ZDES) of the three dimensional stalled flow around a finite span wing. In *42nd AIAA Fluid Dynamics Conderence and Exhibit, New Orleans, Louisiana*, 2012.

[137] K. Richter, A. Le Pape, T. Knopp, M. Costes, V. Gleize, and A. D. Gardner. Improved two-dimensional dynamic stall prediction with structured and hybrid numerical methods. *Journal of the American Helicopter Society*, 45, 2011.

[138] K. Rinoie and N. Takemura. Oscillating behaviour of laminar separation bubble formed on an aerofoil near stall. *Aeronautical Journal*, 108(1081):153–163, 2004.

[139] D. Rodriguez, E. M. Gennaro, and M. P. Juniper. The two classes of primary modal instability in laminar separation bubbles. *Journal of Fluid Mechanics*, 734(4):1–11, 2013.

[140] I. Rodriguez, O. Lehmkuhl, R. Borrell, and A. Oliva. Direct numerical simulation of a NACA0012 in full stall. *International Journal of Heat and Fluid Flow*, 43:194–203, 2013.

[141] P. L. Roe. Approximate Riemann solvers, parameter vectors and difference schemes. *Journal of Computational Physics*, 43(2):357–372, 1981.

[142] A. Roshko. On the drag and shedding frequency of two dimensional bluff bodies. *NACA Technical Note*, 3169, 1954.

[143] Y. Saad. *Numerical methods for large eigenvalue problems*. Siam, 1992.

[144] L. Sankar, J. Zibi-Bailly, J. C. Le Balleur, D. Blaise, O. Rouzaud, and M. Rhee. A comparative study of three methodologies for modeling dynamic stall. In *28th European Rotorcraft Forum, Bristol, UK*, 2002.

[145] F. Sartor, C. Mettot, and D. Sipp. Stability, receptivity and sensitivity analyses of buffeting transonic flow over a profile. *AIAA Journal*, 53(7):1980–1993, 2015.

[146] F. W. Schmitz. Aerodynamics of the model airplane, Part I, Airfoil measurements. *NASA Technical Memorandum*, 60976, 1967.

[147] M. S. Selig, J. J. Guglielmo, A. P. Broeren, and P. Giguere. Experiments on airfoils at low Reynolds numbers. *AIAA Paper*, 0062, 1996.

[148] D. Sipp. Open-loop control of cavity oscillations with harmonic forcings. *Journal of Fluid Mechanics*, 708:439–468, 2012.

[149] D. Sipp and A. Lebedev. Global stability of base and mean flows: a general approach and its applications to cylinder and open cavity flows. *Journal of Fluid Mechanics*, 593:333–358, 2007.

[150] D. Sipp, O. Marquet, P. Meliga, and A. Barbagallo. Dynamics and control of global instabilities in open-flows: a linearized approach. *Applied Mechanical Review*, 63, 2010.

[151] P. R. Spalart and S. R. Allmaras. A one-equation turbulence model for aerodynamic flows. *La recherche aérospatiale*, 1:5–21, 1994.

[152] P. R. Spalart and C. L. Rumsey. Effective inflow conditions for turbulence models in aerodynamic calculations. *AIAA Journal*, 45(10):2544–2553, 2007.

[153] N. Srinivas and K. Deb. Multiobjective Optimization Using Nondominated Sorting in Genetic Algorithms. *Evolutionnary Computations*, 2(3):221–248, 1994.

[154] G. R. Srinivasan, J. A. Ekaterinaris, and W. J. McCroskey. Evaluation of turbulence models for unsteady flows of an oscillating airfoil. *Computers and Fluids*, 24(7):833–861, 1995.

[155] S. H. Strogatz. *Nonlinear dynamics and chaos: with applications to physics, biology, chemistry and engineering*. Addison-Wesley Publishing Company, 1994.

[156] J. Szydlowski and M. Costes. Simulation of flow around a static and oscillating pitching NACA0015 airfoil using URANS and DES. *ASME Transfer/Fluids Engineering Summer Conference*, 2004.

[157] H. Tanaka. Flow visualization and PIV measurements of laminar separation bubble oscillating at low frequency on an airfoil near stall. In International Council of the Aeronautical Sciences Paper, editor, *24th Congress of International Council of the Aeronautical Sciences*, 2004.

[158] I. Tani. Low-speed flows involving bubble separations. *Progress in Aerodynamical Sciences*, 5:70–103, 1964.

[159] A. Tezuka and K. Suzuki. Three-dimensional global linear stability analysis of flow around a spheroid. *AIAA Journal*, 44:1697–1708, 2006.

[160] V. Theofilis. Advances in global linear instability of nonparallel and three-dimensional flows. *Progress in Aerospace Sciences*, 39(4):249–315, 2003.

[161] V. Theofilis. Global linear instability. *Annual Review of Fluid Mechanics*, 43:319–352, 2011.

[162] V. Theofilis, S. Hein, and U. Dallmann. On the origins of unsteadiness and three-dimensionality in a laminar separation bubble. *Philosophical Transactions of the Royal Society of London*, 358, 2000.

[163] J. J. Thibert, M. Grandjacques, and L. H. Ohman. Experimental database for computer program assessment. *AGARD Advisory Report*, 138(A1), 1979.

[164] E. Torenbeek. *Synthesis of subsonic airplan design*. Delft University Press, 1982.

[165] L. S. Tuckerman and D. Barkley. Bifurcation analysis for timesteppers. Numerical methods for bifurcation problems and large-scale dynamical systems. *IMA Volumes in Mathematics and its Applications*, 119:453–466, 2000.

[166] C. Wales, A. L. Gaitonde, D. P. Jones, D. Avitabile, and A. R. Champneys. Numerical continuation of high Reynolds number external flows. *International journal for numerical methods in fluids*, 68:135–159, 2012.

[167] J. H. Watmuff. Evolution of a wave packet into vortex loops in a laminar separation bubble. *Journal of Fluid Mechanics*, 119–169, 397.

[168] D. C. Wilcox. Reassessment of the scale-determining equation for advanced turbulence models. *AIAA Journal*, 26(11):1299–1310, 1988.

[169] Z. Yang, H. Igarashi, M. Martin, and H. Hu. An experimental investigation on aerodynamic hysteresis of a low-Reynolds number airfoil. *AIAA Paper*, 315, 2008.

[170] S. Yon and J. Katz. Study of the unsteady flow features on a stalled wing. *AIAA Journal*, 3(305–312), 36.

[171] S. Yoon and A. Jameson. An LU-SSOR scheme for the Euler and Navier-Stokes equations. *NASA Contractor Report*, 179556, 1986.

[172] K. B. M. Q. Zaman, A. Bar-Sever, and S. M. Mangalam. Effect of acoustic excitation over airfoils near stall. *Journal of Fluid Mechanics*, 182:127–148, 1987.

[173] K. B. M. Q. Zaman, D. J. McKinzie, and C. L. Rumsey. A natural low-frequency oscillation of the flow over an airfoil near stalling conditions. *Journal of Fluid Mechanics*, 54:403–442, 1989.

INSTITUT POLYTECHNIQUE DE PARIS

Titre: Étude d'un écoulement turbulent à haut nombre de Reynolds autour d'un profil proche du décrochage; une approche couplant formalisme RANS et théorie de la bifurcation

Mots clés: décrochage, stabilité globale, théory de la bifurcation, RANS, écoulement turbulent

Résumé: Le phénomène de décrochage est souvent décrit comme une chute soudaine de portance lorsque l'angle d'incidence augmente, ce qui est préjudiciable aux avions et aux hélicoptères. Plusieurs études numériques et expérimentales ont révélé des phénomènes apparaissant proche de l'angle de décrochage : plusieurs angles d'attaque pour lesquels l'écoulement est bistable et des oscillations basses fréquences à un nombre de Strouhal particulier de St ~ 0.02. L'objectif de cette thèse est d'avoir une meilleure compréhension de l'origine du décrochage et de ces deux phénomènes grâce à des simulations numériques d'écoulements turbulents modélisés par une approche RANS. Une combinaison de diverses approches numériques et théoriques (simulations instationnaires, continuation de solutions stationnaires, stabilité linéaire et analyse de bifurcation) est développée et appliquée dans le cas du décrochage d'un profil 2D de pale d'hélicoptère, le OA209, à bas nombre de Mach (M ~ 0.2) et haut nombre de Reynolds (Re $\sim 1.8 \times 10^6$).
Des solutions stationnaires sont calculées pour différents angles d'attaque en considérant le modèle de turbulence de Spalart-Allmaras et en utilisant des méthodes de continuation. Les résultats mettent en évidence la bistabilité de l'écoulement pour plusieurs angles proches du décrochage. Des analyses de stabilité linéaire réalisées autour de ces états d'équilibres révèlent l'existence d'un mode instable basse fréquence associé au décrochage. L'évolution des valeurs propres associées à ce mode le long des branches stationnaires nous permet d'établir une première version du diagramme de bifurcation. Afin de le compléter, des calculs RANS instationnaires sont réalisés et des cycles limites basse fréquence de large amplitude sont identifiés sur une plage réduite d'angles d'attaque proches du décrochage. Pour clarifier la formation et la disparition de ces cycles limites basse fréquence et permettre une meilleure compréhension du scénario de bifurcation, un modèle à une équation reproduisant les caractéristiques linéaires du phénomène est proposé. Ce modèle non-linéaire du décrochage statique est calibré sur les états stationnaires, et leur comportement linéaire, obtenus par calculs RANS. Une étude du comportement non-linéaire de ce modèle révèle un scenario possible qui pourrait conduire à l'apparition et à la disparition de cycles limites basse fréquence. Finalement, le cas d'un NACA0012 à nombre de Reynolds Re $\sim 1.0 \times 10^6$ est considéré pour valider la robustesse du scenario identifié.

Title: Study of a high Reynolds number flow around a two dimensional airfoil at stall; an approach coupling a RANS framework and bifurcation theory

Keywords: stall, global stability, bifurcation theory, RANS, turbulent flow

Abstract: Airfoil stall is commonly described as a sudden drop of lift when increasing the angle of attack, which is detrimental to aircraft and helicopters. Past experimental and numerical investigations have clearly identified two phenomena which can appear close to the stall angle: several angles of attack for which the flow is bistable and low frequency oscillations at the particular Strouhal number of St ~ 0.02.
The objective of this thesis is to better understand the origin of stall and of these two phenomena using numerical simulations of turbulent flows modeled in the RANS framework. A combination of numerical and theoretical approaches (unsteady simulations, continuation of steady solutions, linear stability and bifurcation analyses) have been developed and applied to the case of a 2D OA209 airfoil at low Mach number (M ~ 0.2) and high Reynolds number (Re $\sim 1.8 \times 10^6$).
Steady RANS computations are performed using the Spalart-Allmaras model to obtain steady states for several angles of attack taking advantage of continuation methods. The results highlight the bistability of the flow for several angles of attack near stall. Linear stability analyses performed around these equilibrium states reveal the existence of a low-frequency unstable mode associated with stall. The evolution of the corresponding eigenvalues along the branches of steady solutions allows us to establish a first sketch of the bifurcation scenario. Unsteady RANS computations are carried out to complete it. Large amplitude low-frequency limit-cycle solutions are identified in a narrow range of angles of attack close to stall. To clarify the formation and disappearance of this low-frequency limit cycle, and thus improve our knowledge about the bifurcation scenario, a one-equation model reproducing the linear characteristics of the phenomenon is proposed. This nonlinear static-stall model is calibrated on the steady states and their linear behavior obtained with RANS computations. A study of the nonlinear behavior of this model then reveals a possible scenario leading to the appearance and collapsing of the low frequency limit cycle. Finally, the case of a NACA0012 at Re $\sim 1.0 \times 10^6$ is considered to check the robustness of the scenario identified.

Institut Polytechnique de Paris
91120 Palaiseau, France